Development of Novel Carbon Nanotubes (CNT) Reinforced Plasma Sprayed Baghdadite Coatings

Doctoral Thesis

by

"Saminderpreet Singh" (2020MMZ0013)



DEPARTMENT OF METALLURGICAL AND MATERIALS ENGINEERING

INDIAN INSTITUTE OF TECHNOLOGY ROPAR SEPTEMBER, 2024

Development of Novel Carbon Nanotubes (CNT) Reinforced Plasma Sprayed Baghdadite Coatings

A Thesis Submitted

In Partial Fulfilment of the Requirements for the Degree of

DOCTOR OF PHILOSOPHY

by

"Saminderpreet Singh" (2020MMZ0013)



DEPARTMENT OF METALLURGICAL AND MATERIALS ENGINEERING

INDIAN INSTITUTE OF TECHNOLOGY ROPAR SEPTEMBER, 2024

Copyright © "2024" by Indian Institute of Technology Ropar All Rights Reserved

DEDICATED TO MY PARENTS

Mrs. Harinder Kaur

Mr. Gurvinder Pal Singh

A father's goodness is higher than the mountain;

A mother's goodness is deeper than the sea.

- Japenese Proverb

DECLARATION

I declare that this work entitled "Development of Novel Carbon Nanotubes (CNT) Reinforced Plasma Sprayed Baghdadite Coatings" has not previously been accepted in substance for any degree and is not being simultaneously submitted in candidature for any other degree. This thesis is being submitted in partial fulfillment of the requirements for the degree of PhD in Metallurgical and Materials Engineering. This thesis is the result of my own independent investigation, except where otherwise stated. I have acknowledged all the other sources by stating the references explicitly. I declare that any idea /data /fact /source stated in my thesis has not been fabricated/ falsified/ misrepresented. All the principles of academic honesty and integrity have been followed. I understand that any violation of the above will be cause for disciplinary action by the Institute and can also evoke penal action from the sources which have thus not been properly cited or from whom proper permission has not been taken when needed. I hereby give consent for my thesis, if accepted, to be available online in the Institute's Open Access repository and for inter-library loan, and for the title and abstract to be made available to outside organizations.

Signature

Name- Saminderpreet Singh

Saminderpreet Sight

Entry Number- 2020MMZ0013

Program-PhD

Department - Metallurgical and Materials Engineering

Date- 11/09/2024

CERTIFICATE

It is certified that the work contained in the thesis titled "Development of Novel Carbon Nanotubes (CNT) Reinforced Plasma Sprayed Baghdadite Coatings" by "Saminderpreet Singh" has been carried out under my supervision and this work has not been submitted elsewhere for the award of any degree.

Mullog 2024

Signature of the Supervisor

Dr. Khushboo Rakha

Department of Metallurgical and Materials Engineering

Indian Institute of Technology Ropar

Rupnagar, Punjab 140001

Date- 11/09/2024

ACKNOWLEDGMENTS

I would like to express my sincere gratitude to my supervisor, **Dr. Khushboo Rakha**, (Assistant Professor, Department of Metallurgical and Materials Engineering, Indian Institute of Technology Ropar) for always being an inspiration and for providing a great deal of support, guidance and encouragement during this work. Her expertise, patience, and encouragement have been instrumental in shaping this work and my academic growth. I am highly grateful to **Prof. Harpreet Singh** (Professor, Department of Mechanical Engineering, Indian Institute of Technology Ropar) for the extended discussions and valuable suggestions which have contributed greatly to the improvement of the thesis. He has always been very kind, supportive, cordial and helped me throughout the entire journey of this dissertation.

I would like to thank the doctoral committee members: Dr. Ravi Mohan Prasad, Dr. Pratik K. Ray, Dr. Atharva Poundarik, and Prof. Harpreet Singh for their insightful feedback, constant support and dedication to excellence. I extend my appreciation to **Dr. Bodhisatwa Das** (Assistant Professor, Department of Biomedical Engineering, Indian Institute of Technology Ropar) and his PhD scholar Mr. Mohit for their assistance, resources, and academic support. Special thanks to Mr. Avneesh Kumar (R&D Specialist, Research and Testing Institute, Pilsen, Czech Republic) for his invaluable support, guidance and for motivating me at every stage of this work.

I would also like to express my thanks and gratitude to Prof. Rajeev Ahuja (Director, Indian Institute of Technology Ropar) and Dr. Pratik K Ray (Head, Department of Metallurgical and Materials Engineering) for providing financial, infrastructural, and administrative support in carrying out this work.

I am highly obliged and wish sincere thanks to the technical staff- Mr. Deepak Kumar, Mr. Pankaj Thakur, Mr. Ram Kumar, Mr. Jaswinder Singh, Mr. Amit Kaushal, Mr. Abhishek Sharma, Mr. Manu Rana, Mr. Damninder Singh, Mr. Kamlesh Satpute who helped in all the possible way during experimental work. I also thank Dr. Tarwinder Singh Handa, Assistant Librarian, for his prompt responses and for instantly providing the plagiarism reports.

I am indebited to my colleagues from DREAM Lab Mr. Abhinesh Verma, Mr. Maninder Jeet Singh, and Mr. Shubham Prajapati for their camaraderie, intellectual exchange and moral support. Thanks are due to Mr. Gidla Vinay and Mr. Saiful Wali Khan and all my friends who have encouraged me and made this journey more enjoyable and rewarding.

Above all, I owe my deepest gratitude to my family for their unconditional love, encouragement and belief in my abilities. Their unwavering support and sacrifices have been a constant source of strength and motivation. Lastly, I dedicate this thesis to my parents.

Thank you Almighty for blessing me with this wonderful life!

LAY SUMMARY

The human body comprises 206 bones and over 300 joints, among which the synovial joints like the knee, hip, and shoulder are remarkable bio-tribological systems. These joints encounter considerable challenges during use, as they endure high loads while facilitating a broad range of movements. Osteoarthritis is a most common joint disease that results in the degradation of cartilage and can lead to the failure of the synovial joint functionality. The temporary solutions like intra-articular steroid injection may relieve the pain but are not able to restore functionality. The other possible solution can be the whole joint replacement which consists of replacement of damaged bone and cartilage with the implant.

Bio-implant materials can be made up of metallic, ceramic, or polymeric materials with an average lifespan of 10-15 years. The different challenges in bio-implants are the corrosion, wear or toxicity within the human body environment. It can lead to the development of conditions like Alzheimer's disease or neuropathy. Hence, the manufacturing of the bio-implant is highly important for addressing these concerns.

Surface coatings are one of the widely accepted methods for modifying the surfaces of bio-implants to attain specific properties. In thermal spray techniques, plasma spray has been approved by the Food and Drug Administration (FDA) USA for depositing biomaterials on the surface of the implant. The plasma spray coatings are used in functional biomedical coatings for addressing corrosion, wear, and biocompatibility issues. The most commonly used biomaterials for commercial applications of surface modification of bio-implants are hydroxyapatite and titanium alloys. According to the literature, plasma-sprayed baghdadite has been identified as the potential substitute for hydroxyapatite owing to its superior mechanical properties. Further, carbon nanotubes can be used as the reinforcement material in the coatings to enhance the mechanical and electrochemical properties.

In the current research work, a novel material composition of baghdadite reinforced with carbon nanotubes was deposited with a plasma spray technique on titanium substrates. Further, the characterization of the coatings, mechanical, electrochemical

and biological properties were investigated. The addition of carbon nanotubes in the coatings results in an improvement in the mechanical properties and corrosion resistance without causing any cytotoxicity effects. Therefore based on the current results it can be considered that carbon nanotubes reinforced baghdadite coatings can be a promising candidate for use in the surface modification of the orthopedic implants. However, the in vivo testing of these coatings is necessary to recommend for practical use in bio-implants.

ABSTRACT

Biomaterials are natural or synthetic materials to substitute the damaged biological structure to restore its form and function. The synovial joints like hip, knee and shoulder suffers from degenerative diseases like osteoarthritis that results in the cartilage breakdown. According to published data, orthopedic implant market is experiencing significant growth. The implant life depends upon multiple factors like age, gender, and patient body mass index and it ranges from 10 to 15 years. Therefore, it is important to increase the lifespan of orthopedic implants, which will delay the need for replacement surgeries and improving the comfort of implant users.

The main requirements of load-bearing implants are mechanical properties like tensile strength, hardness, modulus, and elongation, and should be non-toxic and non-inflammatory. Apart from that, high corrosion and wear resistance are also required to enhance the life of implants which usually depends on the surface properties of the implants.

The surface modification techniques can help in improving the biocompatibility of materials like titanium by coating it with bioactive material and hence, improving the osseointegration. Amongst different coating methods, plasma-spray is the most widely used because of its high deposition rate, desired coating thickness, cost-effectiveness and reliability. Hydroxyapatite (HA) coatings by plasma spray techniques are commercially accepted and approved by the FDA (Food and Drug Administration) and used in knee, hip, shoulder, ankle, and dental implants. However, its intrinsic brittle nature and inadequate mechanical properties restrict its usage as a coating material, declaring it unreliable for load-bearing bioimplants. Another bioceramic, Baghdadite (BAG, Ca₃ZrSi₂O₉), has emerged as a highly promising biomaterial for facilitating bone and tissue regeneration. As reported in the literature, BAG exhibits superior mechanical properties compared to hydroxyapatite (HA).

Carbon nanotubes (CNT) have high tensile strength, high thermal conductivity, and excellent chemical stability. Over the past 15-20 years, CNT has emerged as a promising

reinforcement material for bioimplant coating applications, contributing significantly to advancements in both mechanical and biological properties.

In the present work, bioceramic coatings reinforced with CNT using the plasma-spray technique were developed. Four different coatings were prepared which include HA, BAG, BAG reinforced with 1wt%CNT and BAG reinforced with 2wt%CNT on titanium substrate. The developed coatings were characterized using SEM (Scanning Electron Microscopy), EDS (Energy Dispersive Spectroscopy), XRD (X-ray Diffraction), XPS (X-ray Photoelectron Microscopy), and Raman spectroscopy. The surface morphology of the coatings exhibits typical plasma spray characteristics of pores, microcracks, and irregular melting. The XRD analysis confirmed the presence of hydroxyapatite and baghdadite phases in the HA and BAG coatings respectively. Raman spectroscopy validated the presence of CNT in the coatings after the plasma spray deposition. The coatings were firmly bonded to the substrate and thickness in the range of 350-450 μm.

The porosity and surface roughness values of the coatings were also measured. The BAG coatings have higher surface roughness values than HA coatings and it increased further with CNT reinforcement. The porosity values were decreased with CNT addition due to the ability of CNT to infiltrate the inter-lamellar spaces and fill the gaps at the intersplat region.

The microhardness values increased with the reinforcement of CNT in BAG coatings by 38.7%. It can be ascribed to the reduction in porosity and effective anchoring of CNT within the BAG ceramic matrix. The scratch testing of the coatings indicated the reduction in wear volume loss and scratch rate due to the decrease in penetration depth and scratch width by the addition of 2wt% CNT in BAG coatings. The increase in critical load values in BAG-2CNT coatings demonstrated the enhancement of the cohesion strength of the coatings. The CNT provided improved interlocking and mechanical anchorage among the splats.

The electrochemical corrosion analysis of the coatings was performed by linear polarization test and Electrochemical Impedance Spectroscopy (EIS) in SBF at 37°C. The corrosion current density value was reduced by 80% for BAG-2CNT coatings as compared to the BAG coatings. Further, the EIS results showed the increase in the polarization resistance values in CNT-reinforced coatings. The post corrosion analysis

indicated the reduction of defects like pores and microcracks in the CNT reinforced coatings which leads to the enhancement of the corrosion resistance. The CNT having higher thermal conductivity and acting as an inert barrier to the SBF can be the other major reasons.

The in-vitro biocompatibility studies revealed the good cell attachment, growth and spreading of the MC3T3-E1 cells on the surface of the coatings. The filopodia development indicated the efficient colonization and spreading of the cells on the coating surface. The cell viability and proliferation analysis indicated no cytotoxicity is caused by the CNT reinforcement in the coatings. The BAG-2CNT coatings have the highest cell viability % at the end of day 1, 3 and 7. In summary, this study demonstrates how the plasma spray BAG coatings with CNT reinforcement exhibits favorable mechanical, electrochemical characteristics as well as biocompatibility.

LIST OF PUBLICATIONS

1. Saminderpreet Singh, Avneesh Kumar, Mohit Kamboj, Bodhisatwa Das, Khushboo Rakha, Harpreet Singh, "Corrosion behaviour of plasma-sprayed baghdadite bioceramic coatings reinforced with carbon nanotubes", **Journal of Alloys and Compounds**, Volume 976, 2024, 173094, ISSN0925-8388.

https://doi.org/10.1016/j.jallcom.2023.173094

2. Saminderpreet Singh, Avneesh Kumar, Mohit Kamboj, Bodhisatwa Das, Harpreet Singh, Khushboo Rakha, "Scratch Resistance and In-vitro Biocompatibility of Plasma-Sprayed Baghdadite Coatings Reinforced with Carbon Nanotubes", **Surface and Coatings Technology**, Volume 481, 2024 130670, ISSN 0257-8972.

https://doi.org/10.1016/j.surfcoat.2024.130670

3. Saminderpreet Singh, Khushboo Rakha, Harpreet Singh, "A comprehensive review on carbon-based thermal sprayed coatings for orthopedic implants", **Journal of Thermal Spray and Engineering**, 2024, 4: 126-131 ISSN (Online): 2582-1474.

https://doi.org/10.52687/2582-1474/408

4. Saminderpreet Singh, Jasmaninder Singh Grewal, Khushboo Rakha, "*Erosion wear performance of HVOF and cold spray coatings deposited on T-91 boiler steel*", Materials Today: Proceedings, Volume 62, Part 14, 2022, Pages 7509-7516, ISSN 2214-7853.

https://doi.org/10.1016/j.matpr.2022.04.277.

TABLE OF CONTENTS

DECLARATION	IV
CERTIFICATE	V
ACKNOWLEDGMENTS	VI
LAY SUMMARY	VIII
ABSTRACT	X
LIST OF PUBLICATIONS	XIII
TABLE OF CONTENTS	XIV
LIST OF FIGURES	XIX
LIST OF TABLES	XXIII
LIST OF ABBREVIATIONS	XXIV
CHAPTER 1	1
Introduction	1
1.1 Implants	1
1.1.1 Cardiovascular Implants	1
1.1.2 Dental Implants	2
1.1.3 Neural Implants	2
1.1.4 Orthopedic Implants	3
1.2 Arthritis	3
1.2.1 Solutions to Osteoarthritis	4
1.3 Biomaterials	6
1.3.1 Metallic Biomaterials	6
1.3.2 Ceramic Biomaterials	6
1.3.3 Polymeric Biomaterials	7
1.4 Problems related to Bio-implants	7

1.4.1 Biocompatibility	8
1.4.2 Corrosion	9
1.4.3 Wear	10
1.4.4 Mechanical Properties	11
1.5 Surface Modification of Bio-implants	11
1.6 Research Outline	12
CHAPTER 2	13
Literature Review	13
2.1 Introduction	13
2.2 Corrosion of Bio-implants	13
2.3 Wear of Bio-implants	15
2.4 Biocompatibility of Bio-Implants	16
2.5 Mechanical Properties of Bio-Implants	17
2.6 Surface Modification of Bio-implants	18
2.7 Thermal Spray Techniques	23
2.7.1 Electric Arc Spraying	24
2.7.2 Detonation Gun (D-Gun) Spraying	25
2.7.3 Flame Spray	25
2.7.4 High Velocity-Oxy Fuel (HVOF) Spraying	26
2.7.5 High Velocity Air Fuel (HVAF) Spraying	26
2.7.6 Cold Spraying	27
2.7.7 Plasma Spraying	29
2.8 Biomaterials used for the current study	33
2.8.1 Hydroxyapatite (HA)	33
2.8.2 Baghdadite (BAG)	36
2.9 Carbon Reinforcement	38
2.9.1 Carbon nanotubes (CNT)	38

2.9.2 Graphene	40
2.9 Problem Formulation	42
2.10 Research Objectives	43
CHAPTER 3	45
Experimental Methods	45
3.1 Introduction	45
3.2 Raw Materials	45
3.2.1 Titanium Substrate	45
3.2.2 Hydroxyapatite Powder	45
3.2.3 Baghdadite Powder	46
3.2.4 Carbon Nanotubes	46
3.3 Coatings Development	46
3.3.1 Feedstock Powder Preparation	46
3.3.2 Substrate Preparation	48
3.3.3 Coatings Deposition	48
3.4 Characterization of Plasma Spray Coatings	49
3.4.1 Metallographic Sample Preparation	49
3.4.2 Microstructural Characterization of Coatings	49
3.5 Mechanical Testing of Coatings	50
3.5.1 Surface Roughness Testing	50
3.5.2 Microhardness Testing	50
3.5.3 Scratch Testing	51
3.6 Electrochemical Corrosion Studies	52
3.6.1 Potentiodynamic Polarization Tests	52
3.6.2 Electrochemical Impedance Spectroscopy (EIS)	54
3.6.3 Post-Corrosion Analysis	54
3.7 Biocompatibility Testing of Coatings	55

3.7.1 Cells Adhesion and Growth	55
3.7.2 Cell Viability and Proliferation	56
3.7.3 Zr Toxicity Analysis	56
3.8 Summary of the Chapter	57
CHAPTER 4	58
Feedstock Powder and Coatings Characterization	58
4.1 Introduction	58
4.2 Feedstock Powder Characterization.	58
4.2.1 FESEM Analysis of Powders	58
4.2.2 XRD Analysis of Powders	60
4.3 Microstructural Characterization of Coatings	61
4.3.1 Deposition of Coatings	61
4.3.2 FESEM-EDS Analysis of Coatings	63
4.3.3 XRD Analysis of Coatings	67
4.3.4 XPS Analysis of Coatings	69
4.3.5 Raman Spectroscopy Analysis	72
4.3.6 Cross-sectional Analysis of Coatings	75
4.4 Coating Thickness Measurement	81
4.5 Porosity Analysis of Coatings	82
4.6 Summary of the Chapter	83
CHAPTER 5	85
Mechanical and Electrochemical Corrosion Studies	85
5.1 Introduction	85
5.2 Mechanical Characterization	85
5.2.1 Surface Roughness Testing	85
5.2.2 Micro-Hardness Testing	87
5.2.3 Scratch Testing	88

5.3 Electrochemical Corrosion Testing	99
5.3.1 Open Circuit Potential Measurements	99
5.3.2 Potentiodynamic polarisation studies	100
5.3.3 Electrochemical Impedance Spectroscopy (EIS) Studies	102
5.3.4 Post-corrosion analysis	106
5.4 Summary of the Chapter	109
CHAPTER 6	111
In-vitro Biocompatibility Studies	111
6.1 Introduction	111
6.2 Cell Adhesion and Growth	111
6.3 Cell Viability Analysis	115
6.4 Zr Toxicity Analysis	117
6.5 Summary of the Chapter	120
CHAPTER 7	121
Conclusion and Future Work	121
7.1 Conclusions	121
7.1.1 Coatings Development and Characterization	121
7.1.2 Mechanical and Electrochemical Behavior of the Developed G	Coatings 122
7.1.3 In-vitro biocompatibility studies of the coatings	123
7.2 Future Work	123
References	125

LIST OF FIGURES

Figure No.	Particulars	Page No.
Figure 1.1 Vario	ous types of Bio-Implants	1
Figure 1.2 Schen	ematic representation of total knee arthroplasty [20]	5
Figure 1.3 Diffe	erent reasons for implant failure leading to revision surgery	8
Figure 2.1 Fretti	ting corrosion of implanted metallic screw and plate [63]	15
Figure 2.2 Schen	ematic illustration of osteolysis and implant loosening due to	wear of
implants [65]		16
Figure 2.3 Requ	uired surface characteristics for biomedical applications [85]]19
Figure 2.4 Diffe	erent surface modification techniques used for enhancing the	e properties
of bio-implants.		20
Figure 2.5 Schen	ematic diagram showing the working principle of thermal sp	ray
processes [107]		23
Figure 2.6 Schen	ematic diagram illustrating the working principle of HVOF s	spray [120]
		26
Figure 2.7 Schen	ematic diagram of cold spray coating process [85]	28
Figure 2.8 Schen	ematic diagram representing the plasma spray coating techni	que [85] 30
Figure 2.9 Schen	ematic representation of plasma spray coating splat [133]	32
Figure 2.10 Sch	nematic diagram illustrating the buildup of plasma spray coa	iting
showing voids,	oxidized and unmelted particles [133]	33
Figure 3.1 Alph	nie powder mixer machine used for mixing the powders [200)]47
Figure 3.2 Plasm	ma Spray Gun MF-4MB [200]	48
Figure 3.3 Vicke	ters microhardness setup	51
Figure 3.4 Scrat	tch testing setup	52
Figure 3.5 Elect	trochemical Corrosion Workstation setup	53
Figure 3.6 Cell	culture incubator and hood used for biocompatibility tests	55
Figure 3.7 Work	k methodology adopted for carrying out the research	57
Figure 4.1 FESI	EM micrographs of feedstock powders (a) HA (b) BAG, and	d (c) CNT
used for the den	position of plasma-sprayed coatings on Ti substrate [190]	59

Figure 4.2 FESEM micrographs of blended (a) BAG-1CNT and (b) BAG-2CNT with
high magnification images showing CNT distribution [190]60
Figure 4.3 XRD analysis of HA and BAG powders used for plasma spray coatings61
Figure 4.4 FESEM-EDS images of (a) HA (b) BAG (c) BAG-1CNT and (d) BAG-
2CNT plasma sprayed coatings on Ti substrate [201]65
Figure 4.5 FESEM images of CNT distribution on (a) BAG-1CNT and (b) BAG-
2CNT plasma sprayed coatings and magnified images showing (c) CNT connecting
splats and (d) CNT bridging on the fracture surface of BAG-2CNT coatings [201] 66
Figure 4.6 EDS mapping of plasma sprayed BAG-2CNT coatings [190]67
Figure 4.7 XRD peaks of HA, BAG, BAG-1CNT and BAG-2CNT plasma sprayed
coatings on Ti substrate [190]69
Figure 4.8 (a) XPS peaks of HA plasma sprayed coatings on Ti substrate70
Figure 4.8 (b) XPS peaks of BAG plasma sprayed coatings on Ti substrate71
Figure 4.8 (c) XPS peaks of BAG-1CNT plasma sprayed coatings on Ti substrate71
Figure 4.8 (d) XPS peaks of BAG-2CNT plasma sprayed coatings on Ti substrate
[190]
Figure 4.9 (a). Raman spectroscopy of HA powder and coating on Ti substrates [201]
74
Figure 4.9 (b). Raman spectroscopy of BAG powder and coating on Ti substrates
[201]
Figure 4.9 (c). Raman spectroscopy of BAG-1CNT and BAG-2CNT coating on Ti
substrates [201]
Figure 4.10 Cross-sectional SEM images of a) HA coating b) BAG coatings c) BAG-
1CNT d) BAG-2CNT along with magnified images (middle) and their EDS analysis
respectively [201]
Figure 4.11 (a) Cross-sectional EDS mappings of plasma-sprayed HA coating on Ti
substrate [201]
Figure 4.11 (b) Cross-sectional EDS mappings of plasma-sprayed BAG coating on Ti
substrate [201]
Figure 4.11 (c) Cross-sectional EDS mappings of plasma-sprayed BAG-1CNT coating
on Ti substrate [201]80
Figure 4.11 (d) Cross-sectional EDS mappings of plasma-sprayed BAG-2CNT coating
on Ti substrate [201]81

Figure 4.12 Porosity analysis of plasma-sprayed HA, BAG, BAG-1CNT, and BAG-
2CNT plasma sprayed coatings on Ti substrates [201]83
Figure 5.1 Surface roughness measurement of HA, BAG, BAG-1CNT and BAG-
2CNT plasma sprayed coated samples [201]86
Figure 5.2 Microhardness values of HA, BAG, BAG-1CNT and BAG-2CNT plasma
sprayed coated samples [190]
Figure 5.3 (a) Frictional force during the progressive scratch test of HA plasma
sprayed coatings
Figure 5.3 (b) Frictional force during the progressive scratch test of BAG plasma
sprayed coatings89
Figure 5.3 (c) Frictional force during the progressive scratch test of BAG-1CNT
plasma sprayed coatings90
Figure 5.3 (d) Frictional force during the progressive scratch test of BAG-2CNT
plasma sprayed coatings [190]90
Figure 5.4 FESEM images of scratch groves on (a) HA (b) BAG (c) BAG-1CNT and
(d) BAG-2CNT plasma sprayed coatings after progressive load scratching [190]93
Figure 5.5 (a) Surface element mapping of plasma sprayed HA coatings after scratch
test94
Figure 5.5 (b) Surface element mapping of plasma sprayed BAG coatings after scratch
test94
Figure 5.5 (c) Surface element mapping of plasma sprayed BAG-1CNT coatings after
scratch test
Figure 5.5 (d) Surface element mapping of plasma sprayed BAG-2CNT coatings after
scratch test
Figure 5.6 Scratch profile of (a) HA (b) BAG (c) BAG-1CNT and (d) BAG-2CNT
plasma sprayed coatings after scratch test under progressive loading conditions [190]
97
Figure 5.7 Schematic diagram of the effect of CNT reinforcement on plasma sprayed
BAG coatings during scratch testing [190]
Figure 5.8 Open Circuit Potential (OCP) of HA, BAG, BAG-1CNT, and BAG-2CNT
plasma-sprayed coatings on Ti substrate [201]
Figure 5.9 (a) Potentiodynamic polarization curves for HA, BAG, BAG-1CNT and
BAG-2CNT plasma-sprayed coatings and Ti substrate

Figure 5.9 (b) I _{corr} and E _{corr} values for HA, BAG, BAG-1CNT and BAG-2CNT
plasma-sprayed coatings and Ti substrate [201]
Figure 5.10 (a) Nyquist plot of HA, BAG, BAG-1CNT and BAG-2CNT plasma spray
coatings on Ti substrates
Figure 5.10 (b) Bode impedance plot of HA, BAG, BAG-1CNT and BAG-2CNT
plasma-sprayed coatings on Ti substrates
Figure 5.10 (c) Bode Phase plot of HA, BAG, BAG-1CNT and BAG-2CNT plasma-
sprayed coatings on Ti substrates
Figure 5.10 (d) Equivalent circuit model for fitting of HA, BAG, BAG-1CNT and
BAG-2CNT plasma-sprayed coatings on Ti substrates [201]
Figure 5.11 Pits and crack formation in the surface of (a) HA (b) BAG (c) BAG-1CNT
and (d) BAG-2CNT coatings after corrosion [201]107
Figure 5.12 Raman spectroscopy of CNT reinforced coatings after corrosion test [201]
Figure 5.13 Schematic illustrations of corrosion inhibiting nature of CNT-reinforced
plasma-sprayed coatings [201]
Figure 6.1 FESEM images showing successful adhesion of MC3T3-E1 cells on the
surfaces of (a) HA (b) BAG (c) BAG-1CNT and (d) BAG-2CNT plasma sprayed
coatings [201]
Figure.6.2 FESEM images of MC3T3-E1 cell morphology on HA, BAG, BAG-1CNT
and BAG-2CNT plasma sprayed coatings after incubation periods of 1,3 and 7 days
[190]
Figure 6.3 Filopodia developments of MC3T3-E1 cells on the surfaces of (a) HA (b)
BAG (c) BAG-1CNT and (d) BAG-2CNT plasma sprayed coatings [190]115
Figure 6.4 Cell viability % of MC3T3-E1 cells on HA, BAG, BAG-1CNT and BAG-
2CNT plasma-sprayed coatings
Figure 6.5 Optical microscopy images (Magnification= 10X) of fibroblast cells on
plasma sprayed BAG, BAG-1CNT and BAG-2CNT coatings compared with SBF and
control
Figure 6.6 Cell viability % of BAG, BAG-1CNT and BAG-2CNT coatings compared
with SBF and control
Figure 6.7 XPS graphs of SBF extract of plasma sprayed BAG coatings immersed for
(a) 3 days and (b) 7 days

LIST OF TABLES

Table No.	Particulars	Page No.
Table 2.1 Proc	ess parameters of various	thermal spray techniques [58]24
Table 2.2 Carb	on-reinforced coatings pr	epared by various thermal spray techniques
[58]		41
Table 3.1 Spec	ifications of powder mixi	ng machine [153]47
Table 3.2 Deta	ils of plasma-spray proce	ss parameters used for the development of
coatings on Ti	substrate [154]	49
Table 3.3 Ring	er's solution reagents and	compositions [154]53
Table 4.1 Plasm	na sprayed HA, BAG, BA	AG-1CNT and BAG-2CNT coatings62
Table 4.2 Plas	ma-sprayed HA, BAG, B	AG-1CNT, and BAG-2CNT coating thickness
values [154]		82
Table 5.1 First	critical load and final cri	tical load of HA, BAG, BAG-1CNT and
BAG-2CNT pl	asma sprayed coatings [1	43]91
Table 5.2 Coef	ficient of friction (COF),	penetration depth (P _d), maximum frictional
force $(F_{T(max)})$,	maximum scratch width	(w), wear volume loss (W _{vol}), scratch rate
(W _R) and scrat	ch hardness (H _s) of HA,	BAG, BAG-1CNT, and BAG-2CNT plasma
sprayed coating	gs [143]	98
Table 5.3 Elect	trochemical parameters or	FHA, BAG, BAG-1CNT, and BAG-2CNT
coatings on Ti	[154]	101
Table 5.4 EIS	circuit element values for	plasma-sprayed HA, BAG, BAG-1CNT, and
BAG-2CNT co	oatings on Ti substrates [1	54]106

LIST OF ABBREVIATIONS

Abbreviations Description

AC Alternating Current

ASTM American Society for Testing and Materials

BAG Baghdadite

BMP Bone Morphogenetic Protein

BMSCs Bone Marrow Stromal Cells

Ca-Si Calcium-Silicates

CNT Carbon Nanotubes

CPE Constant Phase Element

CVD Chemical Vapor Deposition

D-Gun Detonation Gun

DLC Diamond-like Carbon

DMSO Dimethyl Sulfoxide Solution

EDS Energy Dispersive Spectroscopy

EIS Electrochemical Impedance Spectroscopy

FBS Fetal Bovine Serum

FDA Food and Drug Administration

FESEM Field Emission Scanning Electron Microscopy

HA Hydroxyapatite

HVOF High Velocity-oxy Fuel

IA Intra-articular

IASI Intra-articular Steroid Injections

MEM-α Minimal Essential Media Alpha

MTT 3-[4, 5-dimethylthiazol-2-yl]-2, 5-diphenyl tetrazolium bromide

MWNT Multi Wall Nanotubes

OA Osteoarthritis

OCP Open Circuit Potential

PBS Phosphate Buffer Saline

PMMA Polymethyl Methacrylate

PVD Physical Vapor Deposition

Ra Arithmetic Mean Roughness

Rq Root Mean Square Average of Profile Height

R_z Maximum Peak to Valley Heights

SBF Simulated Body Fluid

SCE Saturated Colamel Electrode

SWNT Single Wall NanotubesTCP Tri-calcium Phosphate

Ti Titanium

TKA Total Knee ArthroplastyTTCP Tetra-calcium Phosphate

XPS X-ray Photoelectron Spectroscopy

XRD X-ray Diffraction

CHAPTER 1

Introduction

1.1 Implants

Implants are medical devices that are designed to support, replace, or enhance the existing biological structures within the human body. They can be temporary or permanent and their application includes a wide range of medical fields such as cardiology, dentistry, orthopedic, and neural implants [1]. The development of implant materials has revolutionized medical treatments by providing solutions for conditions that were once considered untreatable. This progress is evident in various medical fields, where implants have significantly improved the patient outcomes and quality of life [2]. Implants can be broadly categorized based on their functions as shown in Fig.1.1.

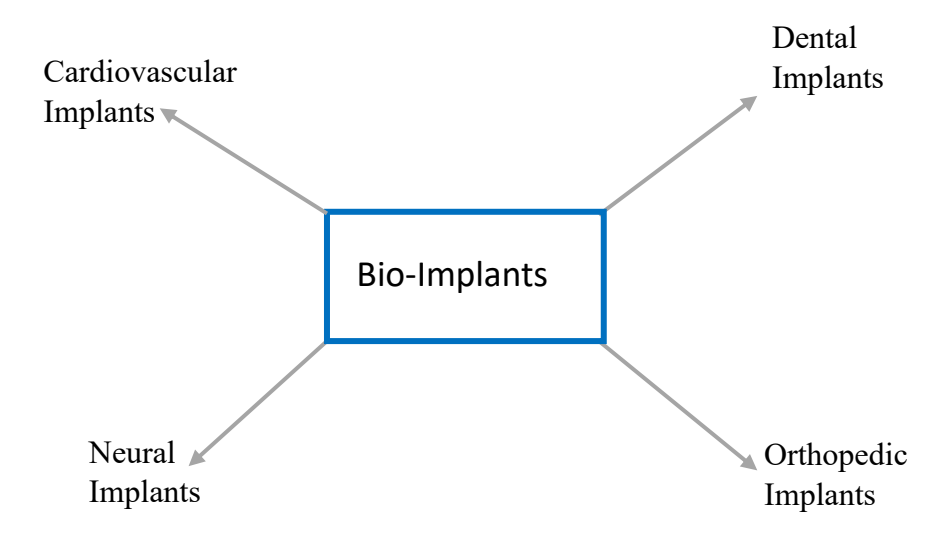


Figure 1.1 Various types of Bio-Implants

1.1.1 Cardiovascular Implants

Cardiovascular implants play a critical role in treating various cardiovascular diseases which are one of the major cause of mortality worldwide. These implants range from devices that regulate heart rhythms to those that ensure unobstructed blood flow through

arteries. The include devices like pacemakers, stents, and artificial heart valves [3]. Pacemakers are small electronic devices implanted in the chest to regulate abnormal heart rhythms and deliver electrical impulses to prompt the heart to beat at a normal rate. Stents are small mesh tubes placed inside the arteries and used to treat coronary artery disease. Artificial heart valves are used to replace damaged heart valves that are unable to open or close properly [4]. The major challenges in these implants include thrombosis and bleeding, infection, device longevity, and infection.

1.1.2 Dental Implants

Dental implants offers a reliable and long-lasting solution for replacing the missing teeth. They provide the functional, aesthetic, and biocompatible alternative to the traditional dentures and bridges. They are the artificial tooth roots which are surgically embedded into the jaw bone. It helps in improving the oral functions by restoring the full chewing capacity [5]. The benefit of dental implant is their ability to prevent bone loss. Implants stimulate the bone, similar to natural bone, helping to maintain bone density and volume. The main challenges and considerations include the bone density requirements, healing time, cost, and risk of complications. The sufficient bone density is crucial for the success of the dental implants [6].

1.1.3 Neural Implants

Neural implants are devices that interact with the nervous system either by stimulating neural tissue or by recording neural activity. These devices are designed to interfere with the brain, spinal cord or peripheral nerves to modulate or record neural signals, allowing for the restoration of sensory, motor, or cognitive functions that have been lost due to injury or disease. The different types of neural implants include deep brain stimulation, cochlear implants, retinal implants, spinal cord stimulation, peripheral nerve stimulation. Deep brain stimulation involves the implantation of the electrodes into specific areas of the brain and delivers the electrical impulses that modulate abnormal neural activity. It provides relief for conditions like Parkinson's disease, tremor, and dystonia [7]. Cochlear and retinal implants can restore lost sensory functions allowing the patient to regain hearing and vision. The major challenges in the development of neural implants include the biocompatibility and longevity, ethical considerations, invasive procedures, cost and accessibility [8].

1.1.4 Orthopedic Implants

Orthopedic implants are used in various surgical procedures to replace or stabilize bones and joints, enabling the patients to regain mobility and alleviate pain from conditions like arthritis, fractures or bone deformities. The joint replacement implants include the hip and total knee replacement. The plates, screws and intramedullary rods are used as fracture fixation devices [9]. Spinal implants helps in maintaining the alignment of spine while the vertebrae fuse together with time. Bone grafts are used to promote bone healing when bone loss has occurred due to injury or surgery. They can be autografts (from patient's own body), allografts (from a donor), or synthetic substitutes made from biocompatible materials [10].

1.2 Arthritis

Arthritis has emerged as one of the common health issues among humans. The different types of arthritis that affect the knee joints are osteoarthritis, rheumatoid arthritis, and post-traumatic arthritis [11]. Amongst these, osteoarthritis (OA) is the most common and leading to disability in 1 out of 4 adults. As per the World Health Organization's data, more than 150 million individuals are affected by OA globally [12]. For the middle-aged and older population, it is the most common joint disease and is considered as the top cause of years lived with disability in the world.

In a healthy state, the knee joint tibial and femoral component surfaces are protected by articular cartilage tissue. The tissue consists of collagen II, proteoglycans, and chondrocytes, possessing a meticulously organized matrix structure that provides viscoelastic problems, aiding in biomechanical load-bearing. Chondrocytes are the primary cell type in articular cartilage and play a pivotal role in the formation and maintenance of this tissue [13]. However, OA is characterized by the gradual deterioration of articular cartilage and ultimately leads to the failure in the functionality of synovial joints. It is considered a whole joint disease involving articular cartilage degeneration, synovial membrane hypertrophy, and osteochondral bone sclerosis. The healthy and OA knee joint. OA is more predominant in the knee, hip, and hand but can also affect any joint from spinal vertebrae to the feet. The most common symptoms of OA are pain, stiffness, swelling around the joint, and loss of movement. The risk factors of OA are classified in two major categories which include systemic and local factors. In systemic risk factors, the joint is vulnerable to damage because of the creation of the

systemic environment. It includes ethnicity, age, genetics, gender, bone density, nutrition, and obesity. However, in local factors, OA is triggered when the joint is exposed to abnormal biomechanical loading [14]. This includes joint injury, physical activity/sports, joint biomechanics, and obesity.

1.2.1 Solutions to Osteoarthritis

OA most commonly affects the knee joint and hip joints which are the largest and most complex joints in the human body. Knee joint is responsible for facilitating bending, straightening and rotation of the leg and carries the body's weight. The knee joint vulnerability to OA arises from the stress, impact of weight, and twisting and turning motions it endures. The OA knee can inflict severe pain during walking, standing, and sitting. The lifestyle modifications such as exercise, maintaining a healthy weight can reduce the risk of OA in its early stages. But once the knee joint fails, there is no potential rehabilitation solution. Nevertheless, there are temporary remedies like intra-articular steroid injections for treating OA. The other solution can be the total knee joint replacement.

1.2.1.1 Intra-articular Steroid Injections (IASI)

The drug-based treatment involves systematic analgesic medication like nonsteroidal 3 anti-inflammatory drugs, acetaminophen, and COX2 inhibitors [15]. They can be effective in providing temporary relief to the pain but can also lead to other problems like gastrointestinal bleeding. Moreover, the primary emphasis of these pharmaceutical treatments is on alleviating pain as they do not possess structural modifying effectiveness. Currently, there is a deficiency of drugs capable of modifying OA progression, and ongoing efforts in drug development are concentrated on addressing issues within the articular cartilage tissue [15].

For advanced stages of OA, treatment alternatives include hyaluronic acid and corticosteroid injections into the intra-articular (IA) space. Qvistgaard et al. reported that corticosteroids can be more beneficial in treating OA than hyaluronic acid [16]. Hyaluronic acid can help in improving the synovial fluid viscosity and gliding motion of the joint. The limitations of hyaluronic acid injections include the short duration of effectiveness as they degrade quickly due to native enzyme activity (with a half-life of approximately 24 hours) [17]. The drawbacks like potential complications at the

injection site such as leakage and their primary focus on pain relief rather than functional restoration [18]. Compatibility issues can also occur and not all the patients respond positively to these injections.

1.2.1.2 Total Knee Arthroplasty

Total Knee Arthroplasty (TKA) has been widely employed in addressing end-stage knee OA for the past 50 years. In TKA surgery, the damaged bone and cartilage surface are removed and substituted with the metal femoral and tibial components, separated by polyethylene insert. After successful TKA, a majority of patients experience a substantial reduction of pain and restoration of knee function [19]. The different components of knee implants are shown in Fig. 1.2.

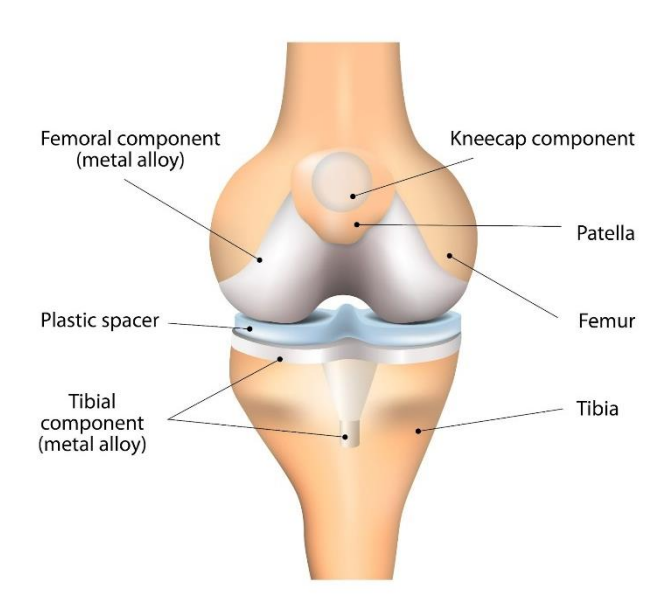


Figure 1.2 Schematic representation of total knee arthroplasty [20]

The objective of arthroplasty is not to cure an illness but rather to address a biological issue through mechanical means. In case of substantial joint injury, arthroplasties may represent the only treatment option available [21]. The obese individuals undergoing TKA experience greater functional enhancements than those with normal body mass index. TKA led to weight reduction, improved BMI and enhanced functional outcomes in 31% of cases [22]. The most common reasons for recurrent failures of TKA include aseptic loosening, instability, infection, periprosthetic fracture, and arthrofibrosis [23].

1.3 Biomaterials

Biomaterials are natural or synthetic materials that are utilized in the construction of structures or implant to replace lost or diseased biological tissue aiming to restore form and function. Consequently, biomaterials play a crucial role in enhancing the quality of life and extending the lifespan of individuals. As a result, the field of biomaterials has experienced significant growth to meet the needs of the aging population [24]. Biomaterials have applications in various regions of the human body such as artificial valves within the heart, stents in the blood vessels, and replacement implants in the knee, shoulder, hips, elbows, and dental structures [25]. Amongst these, the utilization of implants for hip and knee replacements is notably high due to degenerative diseases like OA. The different types of biomaterials used in human body are discussed below-

1.3.1 Metallic Biomaterials

Metallic implants are most widely used in total knee replacement surgeries. From the three main components of knee implants femur, tibia and patella, the femoral component and tibial tray are made up of metals like stainless steel, cobalt-chromium alloys, and titanium alloys [26]. SS316L is commonly employed in traumatological devices like screws, fracture plates, and hip nails due to its low cost, easy availability, and high strength. Cobalt-based alloys have high elastic modulus and high resistance to fatigue and cracking [27]. Ni, Cr, and Co elements are released from stainless steel and cobalt-chromium alloys due to corrosion within the body. On the other hand, Ti alloys have high corrosion resistance along with high strength, low density and complete inertness in the body environment. However, the poor wear resistance of Ti restricts its use where wear resistance is important [28].

1.3.2 Ceramic Biomaterials

The extensively used ceramics for knee and hip joint replacements are alumina (Al₂O₃) and zirconia (ZrO₂), with alumina more commonly employed [29]. These ceramics possess crystalline structures where atoms are bonded by a combination of strong ionic and covalent bonds. The strong atomic bonding contributes to the ceramics' desirable mechanical properties like high hardness, compression strength, elastic modulus as well as chemical inertness in vivo. The biocompatibility of ZrO₂ and Al₂O₃ is attributed to high chemical stability which results in high corrosion resistance and consistent in vivo

performance over time [30]. The presence of polar hydroxyl(-OH) groups on the surfaces facilitates the interaction with aqueous body fluids by lubricating layer formation.

The strong bonding of ceramics contributes to their less favourable mechanical property of brittleness which restricts its utility in orthopedic surgery. Due to the intrinsic brittle nature, ceramics typically exhibit low fracture toughness values, significantly lower than those of CoCr and Ti alloys commonly employed in orthopedic procedures [31].

1.3.3 Polymeric Biomaterials

The use of polymeric biomaterials as tibial insert and patellar components of the knee joint has increased over the years because of high load-carrying capacity and good biocompatibility. The majorly used polymers for tibial insert are - ultra-high molecular weight polyethylene (UHMWPE), highly cross-linked polyethylene (HXPE), and polyethylene ether ketone (PEEK). The key attribute of these polymers is their inertness to chemical reactions within the human body environment making them highly favourable for knee and hip implant applications. However, the major drawbacks of these polymers include insufficient wear resistance and degradation when exposed to the human body [32].

1.4 Problems related to Bio-implants

Bio-implants, when introduced into the human body, encounter various challenges such as biocompatibility, corrosion, wear, and mismatch in modulus of elasticity. Hence, it is crucial to address these concerns prior to implanting the biomaterial. Otherwise, it may lead to the revision surgery which is a very complicated process. The different reasons for failure of implant leading to revision surgery are depicted in Fig.1.3.

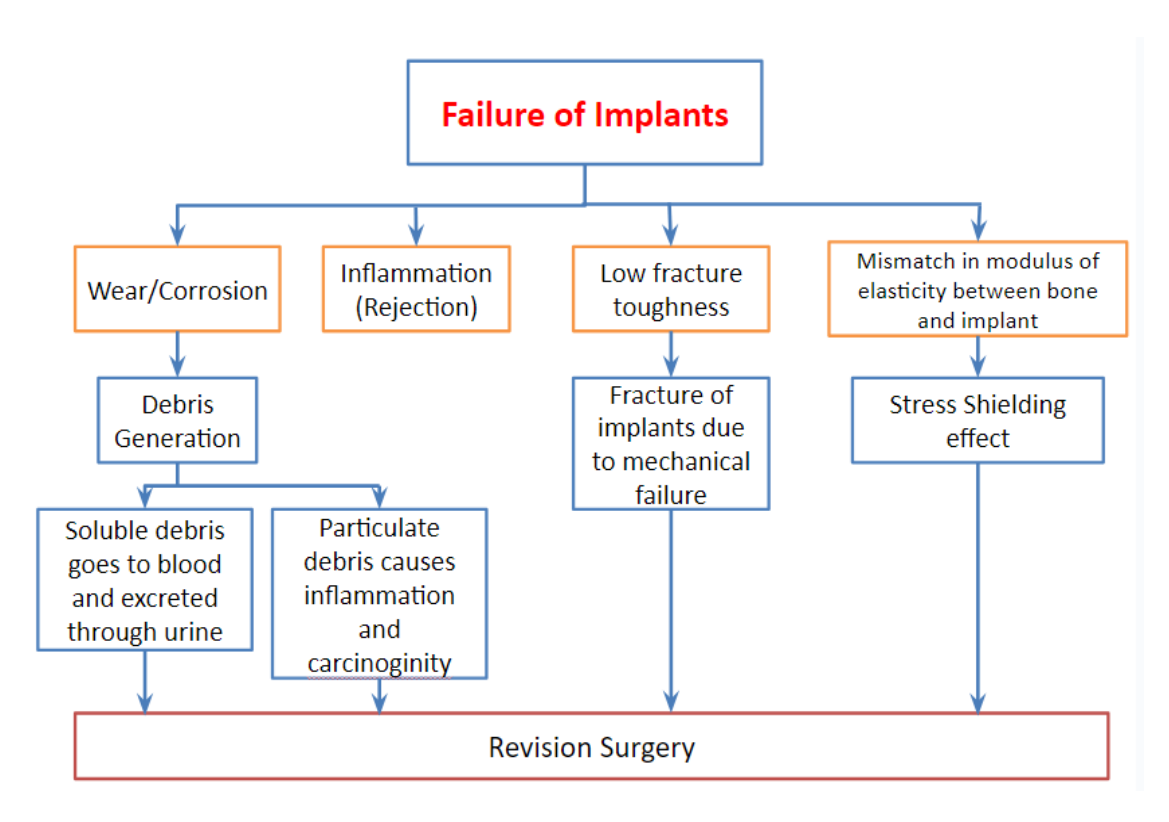


Figure 1.3 Different reasons for implant failure leading to revision surgery

1.4.1 Biocompatibility

Biocompatibility refers to the ability of the materials to be highly nontoxic and should not cause any allergic reactions or inflammation in the human body. The efficacy of biomaterial largely depends on the human body's response to the implant and this defines the biocompatibility of the material [33]. The biocompatibility of a material is primarily determined by two key factors: the response provoked by the host and the degradation of the material within the body environment. Bioactive materials are highly favored for their ability to promote strong integration with the neighboring bone. When the implant comes in contact with human fluids and tissues, various reactions occur between the implant material and the host, ultimately determining the compatibility with our system. The main concerns regarding biocompatibility include thrombosis, which involves coagulation of blood and blood platelet adhesion to the surface of biomaterial as well as the formation of fibrous tissue encapsulation around biomaterials implanted in soft tissues [28]. This results in the deterioration of the biomaterial and can create toxicity in the human body environment. The design of the implant can also affect the biocompatibility of the implant. It can impact the surgical process, affecting both patient

discomfort and the longevity of implants. Biofilm formation represents a key factor influencing implant biocompatibility. It occurs when the pathogens adhere to the surface of an implant and generate an extracellular polymeric substance. The presence of biofilm on the implant surface can significantly affect implant lifespan and contribute to health complications [34].

1.4.2 Corrosion

Corrosion refers to the degradation of materials when exposed to their surrounding environment. It is one of the major causes of the failure of metals and their alloys when used as implants within the human body [35]. The highly corrosive human body environment can result in the release of ions through chemical and electrochemical reactions. These reactions tend to progress toward a thermodynamic equilibrium which can be assessed through electrochemical behavior testing in electrochemical cells. Within these cells, oxidation and reduction processes occur at the anodic and cathodic sites respectively. At the anode, electrons are released from metals or their alloys when electric energy is provided from the external source resulting in oxidation at the anode. When equilibrium is reached, the flow of electrons on both surfaces becomes equal, thereby causing the net current flow in the cell to become zero. It signifies that the rate of oxidation and reduction become equal. The current flowing through the electrodes at an equilibrium state is called corrosion current (i_{corr}) and the corresponding potential is called corrosion potential or open circuit potential (E_{corr} or E_{ocp}) [36].

Many biomaterials release ions upon exposure to the human body environment. However, upon exposure, they develop a protective oxide layer between the metal and body fluid (electrolyte) offering resistance against corrosion. The corrosion behavior was influenced by several factors including surface properties, composition, and microstructure [37]. For example, the stainless steel having chromium forms chromium oxide on exposure to body fluid thus protecting the steel substrate from corrosion [38]. Cobalt-based alloys and Ti alloys can form chromium oxide and titanium oxide layers respectively, when exposed to body fluid. These oxide layers have a thickness in the range of several nanometres [39].

The different types of corrosion occurring in the implant biomaterials are pitting, fretting, galvanic, crevice, fatigue, and stress cracking corrosion [38]. Pitting corrosion occurs due to the breakdown of passive layers on the metal surface and is characterized

by localized corrosion [40]. Fretting corrosion arises from small amplitude vibrations caused by rubbing actions in a corrosive environment. It usually occurs at the joint interfaces in orthopedic implants [41]. Galvanic corrosion is more likely to occur when two or more metals with different nobility are exposed to the corrosive environment and electrically connected. The metal with lower nobility serves as the anode that experiences higher corrosion and leads to galvanic corrosion [42]. Crevice corrosion occurs at the gap between two surfaces, often due to stagnant electrolytes. This type of corrosion occurs at the interface of the femoral head and stem in the case of hip implants [43]. Material degradation under cyclic loading in a corrosive medium leads to fatigue corrosion which results in the formation of cracks on the implanted surfaces. Corrosion-induced pitting combined with cyclic loading is typically the cause of crack initiation in implants. Additionally, stress corrosion cracking is a frequent form of degradation in implanted biomaterials, occurring due to the tensile stress-induced cracks in the corrosive environments [44].

1.4.3 Wear

Wear is characterized as the gradual deterioration of material due to friction between two surfaces in contact. It is also considered as the leading cause of bio-implant failure. Surface wear of implants results in implant loosening and can contribute to osteolysis [45]. Thus, enhancing the wear resistance of the implants remains a critical focus area in orthopedic implant development. Metallic implants have good mechanical, chemical and biomedical properties but have poor wear resistance. The poor wear resistance can lead to the generation of wear debris. The soluble debris goes to the blood and can be secreted through urine. However, particulate debris accumulates to human tissues and can lead to inflammation, damage of cells, hypersensitivity, and carcinogenicity [45].

The various wear mechanisms occurring in the bio-implants are – abrasion, adhesion, fretting, and tribo-corrosion wear. The rubbing of two solid surfaces results in the removal of material is called abrasion wear. The primary reason for abrasion is the sliding motion of one surface against another. Following, implantation, the total joint replacements like hip or knee replacements undergo abrasive wear within the human body [46]. Adhesive wear on the other hand refers to the transfer of one material onto the surface it contacts. This occurs predominantly due to the formation of weld junctions

between contacting surfaces, induced by elevated temperature resulting from shearing action at the contact point. Metallic implants undergo the adhesive wear [47].

Fretting wear is characterized by low-amplitude, high-frequency wear resulting from rubbing action. It is unavoidable in implants both during implantation and after several years of use and occurs at the joint interfaces [41]. Tribo-corrosion represents another form of implant wear within the human body environment combining wear and corrosion mechanisms. Total joint replacements like knee, hip, and shoulder are prone to tribo-corrosion failure [48].

1.4.4 Mechanical Properties

The mechanical properties of a material determine its suitability for bio-implant applications. The key properties required include tensile strength, hardness, modulus, and elongation. The material response to repeated cyclic loads or strain is characterized by its fatigue strength which is crucial for the long-term success of implants under cyclic loading. The implant is considered biomechanically incompatible if it fractures due to insufficient strength or a mismatch in the mechanical properties between bone and implant. The material used to replace the bone should ideally have a modulus similar to natural bone which ranges from 4 to 30 GPa, depending on the type of bone and direction of measurement [49]. Implant materials that are stiffer than natural bone can prevent the necessary stress from being transferred to the surrounding bone, leading to bone resorption around the implant and causing the implant to loosen. This biomechanical incompatibility which results in the death of the bone cells, is known as the stress shielding effect. Therefore, the material with an optimal combination of high strength and a low modulus similar to that of bone should be used for implantation to prevent the implant from loosening and extend the service life, reducing the need for revision surgery [50].

1.5 Surface Modification of Bio-implants

Many researchers have worked on the surface modification of bio-implants, aiming to achieve favorable mechanical, chemical and biological responses from the surface within the human body environment. Various techniques have been investigated to enhance implant surface quality are provided in chapter-2. Three main routes- chemical, mechanical and physical have been identified for surface modification in implant

manufacturing based on their mechanisms. Plasma spraying, among various routes, has been approved by US Food and Drug Administration (FDA) for coating bio-implant surfaces [51].

1.6 Research Outline

The present research work utilized hydroxyapatite (HA), baghdadite (BAG), and carbon nanotubes (CNT) as the coating materials on the titanium substrate. Different compositions of BAG and CNT have been prepared by mechanical mixing method. Plasma spraying method is used for the deposition of feedstock powders on the Ti substrate. The developed coatings were characterized using field emission scanning electron microscopy (FESEM) along with energy dispersive spectroscopy (EDS), X-ray diffraction (XRD), X-ray photoelectron spectroscopy (XPS) and Raman spectroscopy discussed in chapter 4. Subsequently the mechanical properties such as surface roughness, microhardness and scratch resistance of the coatings have been evaluated. The electrochemical behavior of the coatings was studied in simulated body fluid environment and discussed in chapter 5 of the thesis. The chapter 6 covers the in-vitro biocompatibility studies of the developed coatings for understanding the cell growth and proliferation on the surface of the coatings.

CHAPTER 2

Literature Review

2.1 Introduction

This chapter provides an extensive review of the literature related to the current research. The studies relevant to the corrosion, wear, and biocompatibility of the implants have been discussed. The different surface modification techniques used for biomedical applications have also been explored. The working principle and deposition mechanisms of the plasma spraying technique have also been reviewed. After the comprehensive literature survey, the research problem and research objectives were formulated towards the conclusion of the chapter.

2.2 Corrosion of Bio-implants

The corrosion of metallic bio-implants is an inevitable consequence of the corrosive environment within the human body. The body fluid contains various ions such as phosphate, chloride, and bicarbonate as well as cations like K⁺, Mg⁺, Ca⁺, and Na⁺ along with high molecular weight species having dissolved oxygen [52]. These molecules can interrupt the corrosion equilibrium reactions occurring on the implanted biomaterials by altering the pH value and facilitating the transport of proteins along with metal ions. According to ISO guidelines, the acceptable threshold for the corrosion rate of implant biomaterial is 1 micron per year [53]. Corrosion can result in the erosion of biomaterials and can ultimately lead to the fracture of the implant.

Liu et al. investigated the fretting-induced crevice corrosion in SS316L under a simulated body fluid environment. The findings revealed that fretting significantly contributes to the initiation of crevice corrosion, resulting in the failure of the implant. This is attributed to the breakage of the protective passive oxide layer on the steel implant surface [54]. Aksakal et al. investigated the failure of SS316L and Ti6Al4V bio-implants between 1993 and 2002. Their metallurgical analysis revealed that corrosion was the primary cause of these implant failures [55]. Wang et al. conducted a study on failed CoCrMo hip implants to investigate the chemical nature and fretting corrosion

particles formation mechanisms [56]. Gilbert et al. analyzed a fractured Co alloy hip implant and observed the fracture originated from the grain boundaries which resulted from the intergranular corrosive attack within the microstructure [57]. Merritt and Brown conducted a study on the release of the chromium ions from SS316L and cobalt-chromium alloys and found that red blood cells rapidly convert the Cr⁶⁺ ions into Cr³⁺ ions. These Cr³⁺ ions resulted in carcinogenic and mutagenic effects on DNA. Ti-based alloys like Ti6Al4V release Al and V ions in the human body environment [58].

Walker et al. studied the impact of aluminium ions on the brain and liver structure. Their findings indicated that aluminium ions altered the structure properties of brain, potentially leading to the Alzheimer's disease [59]. Costa et al. examined the effects of vanadium ions released from the corrosion of Ti6Al4V. They proposed that vanadium ions may migrate to blood vessels from the implants and bind to human serum albumin and hyaluronic acid in synovial fluid. The presence of vanadium at the joints can lead to potentially dangerous conditions [60]. Willert et al. reported the Ti-6Al-4V and Ti6Al-7Nb femoral components undergoes crevice corrosion when implanted with bone cement [61]. Nakagawa et al. studied the in-vitro corrosion behavior of various titanium alloys and reported an increase in corrosion resistance of titanium with Pd over a wide range of pH due to palladium enrichment on the surface [62].

In another study by Santos et al. studied the degradation of metallic screws and plates by corrosion at the load-bearing areas. These implants are subjected to regular loads and there is a tendency for maximum precipitation to accumulate at the grain boundaries of metallic implants. The physical imperfections can also contribute to precipitation and localized corrosion. The load-bearing structures get weakened by the aggregation of metal-protein complexes at a specific site [63]. Moreover, these physical imperfections also result in fretting corrosion which is a combination of local imperfections and micromotion and can be observed in screw plate orthopedic implants as shown in Fig. 2.1.

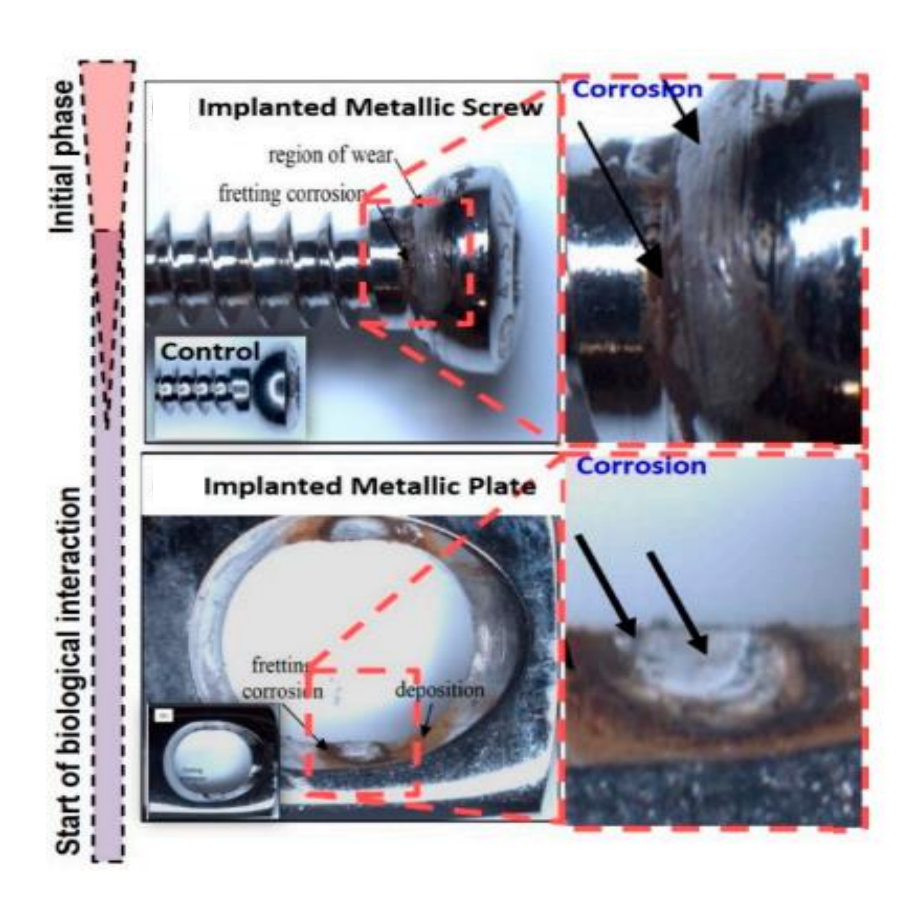


Figure 2.1 Fretting corrosion of implanted metallic screw and plate [63]

2.3 Wear of Bio-implants

The wear of bio-implants occurs due to the rubbing action of one surface over another within the joints. The various modes of wear failure of implants are- abrasion, erosion, fretting, adhesion, tribo-corrosion, and fatigue wear as described in Chapter 1. The wear debris generated by the bio-implant wear can damage the cell tissues. Cooper et al. studied the wear at the interface of bone and implant and the effect of uncemented fixation in total hip arthroplasty [64]. The generation of wear debris by uncemented fixation can cause osteolysis as represented in Fig.2.2. The cellular host response is provoked by the release of wear debris. Macrophages (type of white blood cells) interact with wear debris and lead to the release of soluble chemicals that flow between the surface of the implant and bone through the body fluid. Further, it starts deteriorating bone tissue, leading to osteolysis and failure of implants [65]. Sochart et al. reported that 14% of hip implants (235 hips) faced aseptic loosening due to wear debris generation. The breakdown and loss of bone tissue resulted in the revision surgery [66].

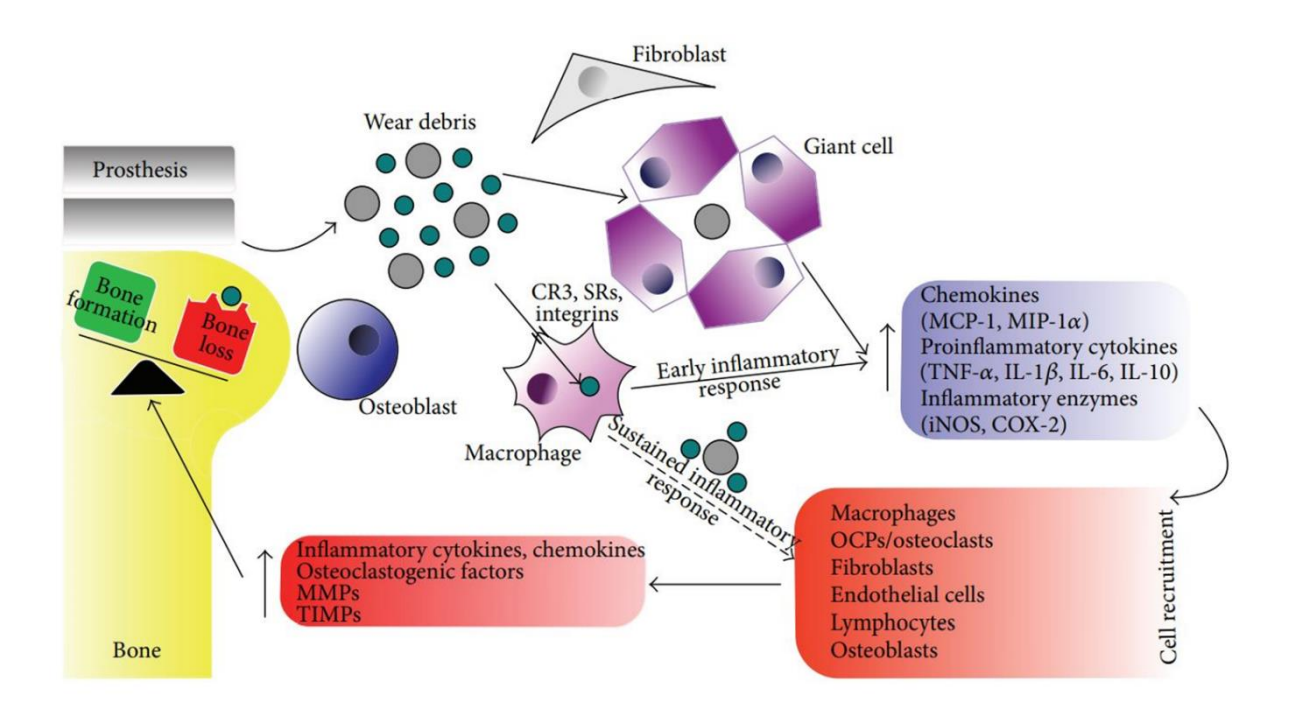


Figure 2.2 Schematic illustration of osteolysis and implant loosening due to wear of implants [65]

2.4 Biocompatibility of Bio-Implants

The biocompatibility of the implant refers to the implant's ability to not create any negative response from the host tissue while the bioactivity leads to the interaction with biological tissue in a way that promotes bone healing, integration, or regeneration. The surface properties can be altered to enhance the biocompatibility and bioactivity of the implants without compromising the mechanical properties of the bulk material. Wennerberg et al. reported that roughened surfaces on titanium implants, achieved through grit blasting, acid etching, or laser treatment have been shown to enhance bone ingrowth and stability of the implant [67]. The surface chemistry of the implants can improve the biocompatibility by enhancing protein adsorption, cell attachment and tissue integration. Hydrophilic surfaces tend to adsorb proteins more readily which can improve cell attachment and proliferation. The titanium implants with hydrophilic surface treatment have improved the osseointegration. The plasma sprayed hydroxyapatite coatings is widely used method for improving the bioactivity of orthopedic implants and has been discussed in detail in the later sections. Roe et al. studied the silver nanoparticles are effective in preventing bacterial colonization on the

implant surfaces without causing any toxicity to human cells [68]. Bone morphogenetic proteins are a group of growth factors which have the ability to induce bone formation. The coatings releasing BMPs have been shown to enhance bone regeneration and improve the integration of orthopedic implants [69]. Biodegradable materials like magnesium alloys are biocompatible and have mechanical properties similar to human bone. The degradation of the magnesium releases ions that can stimulate bone formation and have potential to be used for orthopedic implant applications [70]. The polymer-bioceramic composites such as poly(lactic-co-glycolic acid) combined with hydroxyapatite is bioactive as well as biodegradable material. These composites are used in bone graft substitutes and tissue engineering scaffolds where they support bone regeneration while gradually degrading [71]. Shape memory alloys such as Nitinol, a Ni-Ti alloy can change the shape with the change in temperature. These materials are used in stents and other implants where they provide a dynamic response to physiological conditions [72].

2.5 Mechanical Properties of Bio-Implants

The implants that are used in load-bearing applications like orthopedic and dental implants are subjected to cyclic loading and stress. The low fracture toughness is prone to crack initiation and propagation which can lead to implant failure. The bio-ceramic materials like alumina and zirconia have high wear resistance and biocompatibility but have lower fracture toughness compared to metals. These materials can undergo brittle failure under tensile stress [73]. The metallic implants like titanium and its alloys have higher fracture toughness compared to ceramics and are less prone to catastrophic failure. The fracture toughness of the material is affected by its microstructure, processing methods and presence of defects. The polycrystalline material like ceramic and metals having a smaller grain size enhances the fracture toughness by impeding crack propagation. The porous implants designed for better osseointegration can reduce the fracture toughness and act as stress concentrators and lead to crack initiations [74]. The surface flaws introduced during manufacturing or implantation can significantly lower the fracture toughness. These flaws act as crack initiation sites under stress. The composite materials with different mechanical properties such as ceramics with polymers or metals can enhance fracture toughness. Partially stabilized zirconia undergoes phase transformation under stress which increases its fracture toughness [75].

The modulus of elasticity is a measure of a material's stiffness. For implants, matching the modulus of elasticity to that of the surrounding bone is critical to avoid stress shielding effect. Titanium and its alloys, commonly used in orthopedic implants have lower modulus of elasticity (110GPa) compared to stainless steel (200GPa) and cobalt-chromium alloys (240GPa) making it more suitable for load bearing applications [76]. Rack &Qazi developed titanium alloys Ti-6Al-7Nb and Ti-13Nb-13Zr with lower modulus of elasticity closer to that of bone have reduced stiffness while maintaining strength [77]. Ryan et al. created porous titanium scaffolds within the implant and reduced the modulus of elasticity and bringing it closer to that bone and also improving the osseointegration [78]. Suresh S. designed functionally graded material with gradual variations in composition and structure, allowing transition in mechanical properties across the material. This resulted in matching the modulus of elasticity to that of the bone at different locations and resulted in stress shielding effect [79].

2.6 Surface Modification of Bio-implants

The surface properties of the implant play a major role in the long-term performance of surgical implants. Although the implant has good bulk properties for specific applications can still fail if the surface properties are not suitable [80]. Surface treatments help in improving the mechanical, electrochemical, and biological properties in the human body environment [81]. For instance, the poor wear resistance of the Ti alloys can be enhanced by coating them with the desired materials. Further, the bioactive coatings can promote the osseointegration of bioinert materials like Ti alloys. The coatings with proper adhesion to the substrate can facilitate the optimal integration with the surrounding tissues while the substrate is responsible for the load-bearing application of the implant [82].

The required surface properties for enhancing the life of the implants are represented in Fig. 2.3. The bioactive coatings can help the bone cells to grow on the surface of the implant and provoke biological responses like tissue regeneration. Bioceramics like bioactive glasses, hydroxyapatite, and composite coatings have been explored for tissue regeneration applications [83]. The implant failures due to bacterial contamination are reduced by the use of antimicrobial coatings. The bacterial adhesion can lead to the formation of biofilms on the surface of the implant and develop the risk of infection.

The frequently touched surfaces, urinary catheters and ventilators are also contaminated by the healthcare-associated infections [84].

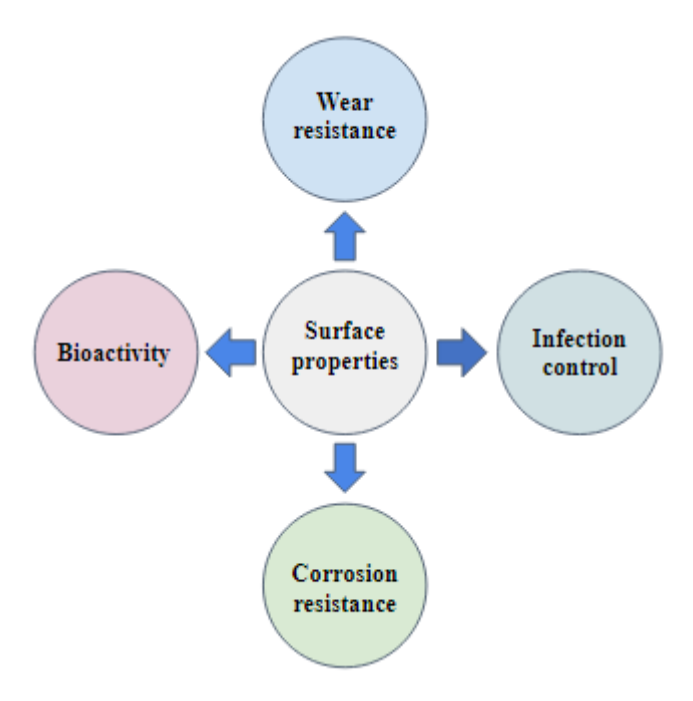


Figure 2.3 Required surface characteristics for biomedical applications [85]

Various surface modification methods have been examined by different researchers to improve the overall performance of biomedical implants [86–88]. The surface modification routes for biomedical implants are classified as mechanical, chemical, and physical based on the mechanisms as shown in Fig.2.4.

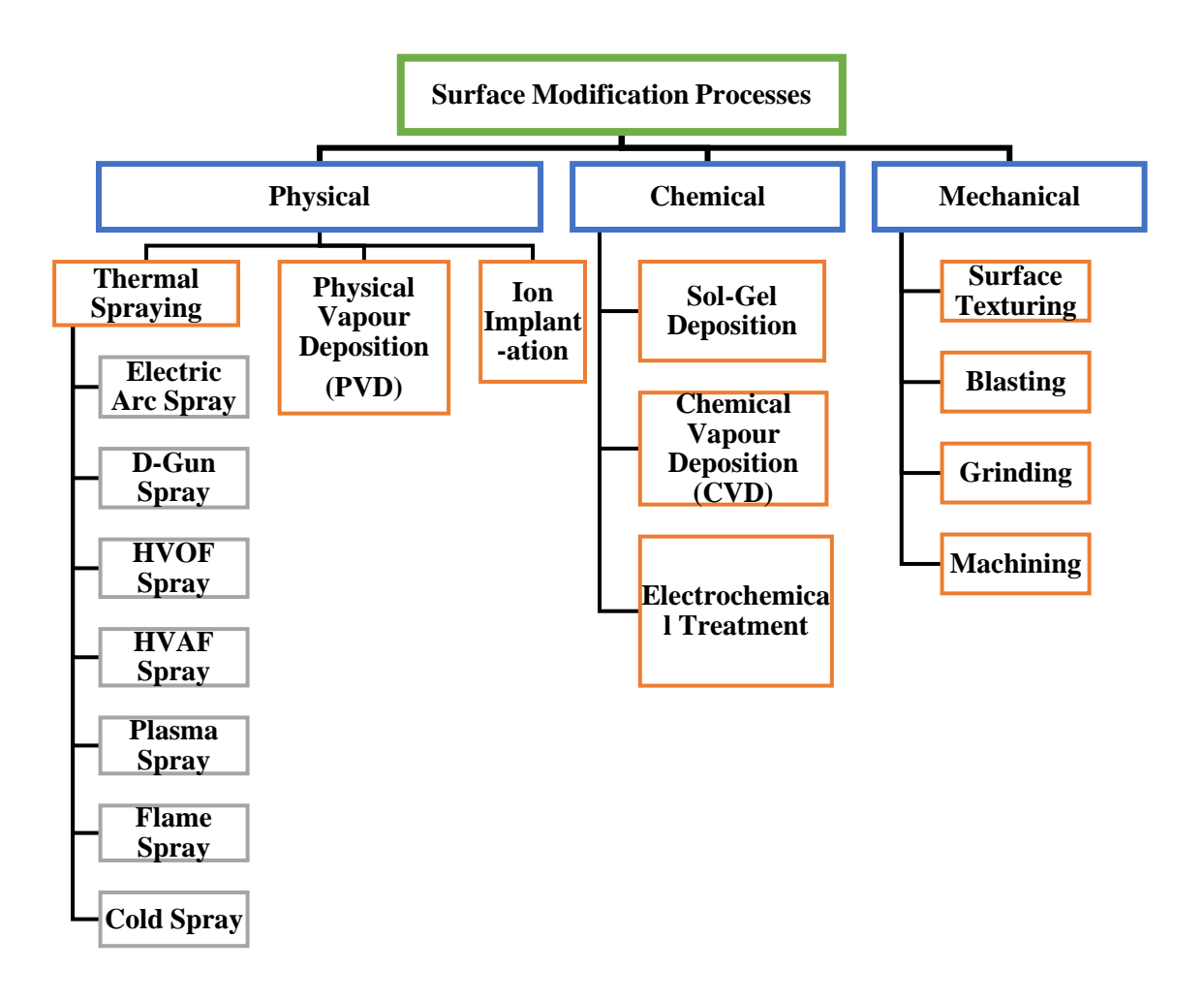


Figure 2.4 Different surface modification techniques used for enhancing the properties of bio-implants

The commonly used chemical methods for surface modification of implants are-chemical vapor deposition (CVD), sol-gel and electrochemical treatment. In CVD, the coatings are deposited by chemical reaction on the surface of the implant by the surrounding gas under a vacuum. CVD is widely used technique for producing high quality and precise thin films or coatings. This technique involves the chemical reaction of gaseous precursor material that contain the desired coating elements. The gases are introduced into a reaction chamber, where they react or decompose on the surface of a heated substrate, forming a thin film solid layer. The process can be tailored to produce different materials including metals, ceramics and composites. The CVD process can be classified based on various factors such as method of energy delivery, pressure inside reaction chamber and temperature used. The thermal CVD uses heat to drive the chemical reactions and deposits the materials like silicon, silicon nitride and silicon dioxide [89]. Plasma enhanced CVD utilizes plasma to enhance the chemical reaction

rates at lower temperature making it suitable for depositing films on temperature sensitive substrates [90]. CVD is used to enhance surface properties of biomedical implants. Corona-Gomez et al. deposited diamond-like carbon (DLC) CVD coating on Co-Cr-Mo alloy substrate and evaluated the wear response in the human body environment [91]. Lusvardi et al. developed titanium nitride and zirconium nitride CVD coatings to improved the corrosion resistance of metallic implants and reducing the risk of adverse biological reactions [92]. The CVD technique can produce uniform and high purity of coatings along with wide range of materials including metals, ceramic and polymers.

Sol-gel coating method involves the formation of a colloidal suspension solution that transforms into gel to form a thin solid coating. Ceramic coatings like hydroxyapatite, SiO₂, and TiO₂ have been deposited by this method [93]. This process is based on the hydrolysis and condensation of metal alkoxides or inorganic salts, leading to the formation of a colloidal suspension or "sol". The sol is then applied to the substrate where it undergoes condensation and polymerization to form continuous gel layer. Upon drying and heat treatment, the gel layer is transformed into a dense, uniform ceramic or glass coating [94]. The advantages of this technique include low processing temperature, versality and control over composite and structure. However, it is a time consuming method, limited thickness can be achieved and gel may undergo shrinkage and cracking during drying. Chen et al. deposited hydroxyapatite and silica based bioactive coatings by sol gel process and these coatings enhanced the bone cell attachment and proliferation [95]. Catauro et al. developed silica and titania sol-gel coatings and found the improvement in corrosion resistance of titanium implants by providing a protective barrier against corrosive body fluids [96].

The electrochemical coating is achieved by processes such as anodic oxidation, electrophoretic deposition, and cathodic treatment. It utilizes electrical energy as well as chemical reactions for coating deposition. The electrochemical cell supplies the energy to create a chemical reaction between electrodes and electrolyte and the deposition of coatings takes place. This is an economical method for achieving good quality coatings on metallic substrate at low temperatures. The electroplating method used to deposit metals like gold, silver, chromium and nickel and is used for decorative, protection and functional coatings [97]. Electrophoretic deposition is a process where charged particles are suspended in a liquid medium and migrate towards an electrode

under an electric field, forming a coating. EPD is often used to deposit ceramic or polymer coatings [98]. Electroforming is used to produce thick metal parts or intricate shapes by building up metal layers on a mold or template, which is later removed. Chuna et al. developed titanium nitride and chromium electroplated coatings to protect metallic implants from corrosion in the harsh physiological environment. These coatings provide a barrier against corrosive agents, extending the lifespan of the implant [99]. Sivakumar et al. prepared electrochemically deposited hydroxyapatite coatings on titanium and found improvement in the bone-implant bonding [100].

The mechanical methods of surface modification include blasting, surface texturing, grinding, and machining. The rough surface achieved by these processes helps in improving cell adhesion and growth and leads to improved implant fixation with the tissues [101]. Moreover, these methods clean the surfaces of the implant by removing the rust, scale, and paint. Shot peening involves bombarding the implant surface with small, spherical media (shots) to induce compressive residual stresses. Lipski & Jarzebski found the improvement fatigue life of metallic implants by shot peening, making them more durable under cyclic loading conditions typical in orthopedic applications [102]. Techniques like shot peening and laser shock peening are used to improve the fatigue life and wear resistance of joint replacements, spinal implants, and other load-bearing devices, ensuring their durability and longevity under physiological conditions [103]

The physical methods of surface modification include Physical vapor deposition (PVD), laser deposition, ion implantation, and thermal spraying. PVD encompasses several processes, including sputtering, evaporation, and arc deposition. These techniques involve the physical transfer of material from a target source to the substrate, typically in a high-vacuum environment. The deposited films can be made of metals, ceramics, or composites, tailored to enhance specific properties of the implant, such as wear resistance, corrosion resistance, and biocompatibility. Sputtering, ions (typically from a plasma) bombard a target material, causing atoms to be ejected and deposited onto the implant surface [104]. Sputtered coatings, such as titanium nitride (TiN) or hydroxyapatite (HA), are commonly applied to orthopedic implants to improve wear resistance and promote bone integration. Electron beam evaporation uses a focused beam of electrons to heat and vaporize the target material, which then condenses on the implant surface. This technique is often used to deposit biocompatible coatings like

calcium phosphate on implants to enhance osseointegration and bioactivity [105]. Ion implantation is a physical process where ions of a particular element are accelerated and directed onto the surface of an implant. The ions penetrate the surface and become embedded within the material, leading to changes in the surface composition and structure. Nitrogen ion implantation is often used to increase the surface hardness and wear resistance of titanium implants [106].

Amongst all these, thermal spraying is a widely accepted technique for surface modification of bio-implants because of its versatility, and functional biomedical coatings for addressing corrosion, wear, and biocompatibility. Also, plasma spraying has been approved by the FDA (Food and Drug Administration) USA for the deposition of coatings for bio-implant applications [51].

2.7 Thermal Spray Techniques

Thermal spraying is a coating method that involves the application of partially or fully melted materials onto the surface of the substrate. The feedstock material is melted by a heat source like an electric arc or flame which is then propelled to strike the surface of the substrate using a high-velocity stream of air or gas. When the molten particles reach the substrate surface, they get solidified to form a protective or functional coating. The schematic diagram showing the working of thermal spray processes is shown in Fig.2.5. Wide range of coating materials like metals, ceramics, polymers, and composites can be deposited by different thermal spray processes. The different process parameters like temperature, velocity of particles, pressure, carrier gas, and spray rate of various thermal spray techniques are given in Table 2.1.

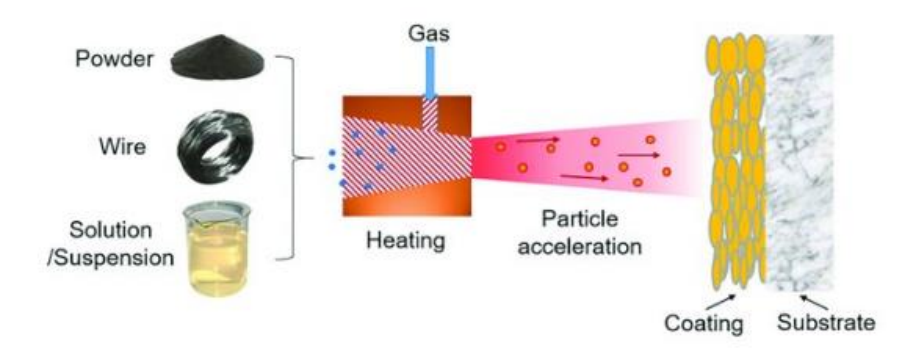


Figure 2.5 Schematic diagram showing the working principle of thermal spray processes [107]

Table 2.1 Process parameters of various thermal spray techniques [85]

Technique	Process	Carrier	Flame	Parti	Spray	Powd-
	Gases	Gas	Temperature	-cle	Distance	er Feed
			(°C)	Veloc	(mm)	Rate
				-ity		(g/min)
				(m/s)		
Flame	Oxygen,	Compress	2500-3000	50-	150-250	10-50
Spraying	Fuel	-ed Air		100		
	(Acetylene					
	, Propane)					
Detonation	Oxygen,	Oxygen	3000-4000	700-	100-150	5-20
Gun	Acetylene			1200		
Spraying						
Electric Arc	Compress	Compress	4000-5000	50-	100-200	50-300
Spraying	ed Air	-ed Air		100		
High	Oxygen,	Oxygen	2500-3200	600-	150-300	50-150
Velocity	Fuel			1000		
oxy Fuel	(Propane,					
(HVOF)	Kerosene)					
Spraying						
Plasma	Argon,	Argon	10000-15000	100-	80-150	30-150
Spraying	Helium,			300		
	Hydrogen					
Cold	Compress	Helium,	<1000	300-	10-50	50-200
Spraying	ed Gas	Nitrogen		1200		
	(Helium,					
	Nitrogen)					

2.7.1 Electric Arc Spraying

Electric arc spray was developed by M.U Scoop in 1910. In this spraying method, an electric arc is created between two consumable metal wires made up of the coating material. The wires are melted due to heat generated by the arc and then atomized into fine droplets using inert gas or compressed air. On impacting the surface it gets solidified and forms a coating. However, this process is limited to only electrically conducting materials [108]. The heat transfer from the feedstock wire to the substrate is relatively less as compared to the other thermal spray techniques because of the absence of flame or plasma. The splats formed in this process tend to be uniform in size but

coarser than other methods. The process parameters affect the size distribution of the splats [109].

2.7.2 Detonation Gun (D-Gun) Spraying

This method operates by detonating a gaseous mixture, where a combination of fuel, oxygen, and feedstock material is ignited by an electric spark inside an elongated barrel. The resulting explosion generates shock waves that heat and propel the mixture towards the open end of the barrel. This detonation process can occur at a frequency of 1 to 15 times per second. The high temperature and velocity cause the powder particles to melt and impact the substrate at supersonic speed resulting in the formation of dense and strongly adherent coatings [110]. The particle size formed during deposition is finer as compared to other processes. Further, the coatings produced with this method tend to exhibit lower oxide content due to reduced splat size and dwell time. Bulina et al. [111] utilized D-Gun spray to deposit a HA coating onto a titanium substrate and found there was no decomposition of HA because of the very small exposure time.

2.7.3 Flame Spray

In this method, a combustible gas like acetylene or hydrogen is mixed with oxygen to create a flame. The powder feedstock material is injected into the flame where it melts and forms fine droplets. These molten droplets are injected toward the surface of substrate using the inert gas or compressed air. The droplets solidify to form the coating. The fuel-to-oxygen ratio and flow rate are the key process parameters for achieving good-quality coatings. The coatings developed by this technique have high porosity and coarser microstructure [112]. Sarao et al. deposited the Titania-HA composite coatings using flame spraying on titanium substrate and reported the enhancement of corrosion resistance in simulated body fluid environment [113]. The increased porosity in coatings can enhance the cell adhesion and proliferation. The pore size between 100μm to 300μm according to cell size helps in cell migration and transport [114]. Gkomoza et al. developed porous titanium coatings by flame spraying have 34% porosity and a high fraction of pores helps in significant cell growth. The surface roughness of flame spray coatings is highest with R_a 11.19µm and has oxidized surface. The formation of spheroid globules was observed on the surface of coatings after immersion in simulated body fluid for 14 days and the Ca/P ratio was 1.61 [115].

2.7.4 High Velocity-Oxy Fuel (HVOF) Spraying

In this process, the mixture of fuel like acetylene or propane and oxygen are ignited in high pressure combustion chamber with temperature 3000°C and velocity of gas jet is around 2000m/s. The supersonic gas velocity stream carrying the melted or partially melted feedstock powder is accelerated towards the substrate. The coatings developed by this technique have low porosity and high bond strength because of higher particle velocity and lower temperature than flame spray [116]. The HVOF coatings are used in biomedical application to overcome wear and corrosion failure [117]. Melero et al. fabricated HA and HA-TiO₂ HVOF sprayed coatings to examine the corrosion resistance by performing electrochemical tests in Hanks solution for 24 hours. The addition of TiO₂ in HA can provide improved adhesion strength to Ti substrates and better mechanical properties like high hardness and low porosity [118]. The concentration of TiO₂ was increased from the upper layer of coating to the bottom layer on the substrate. This type of functionally graded coating can provide long life to implants without decreasing the bioactivity of HA [119].

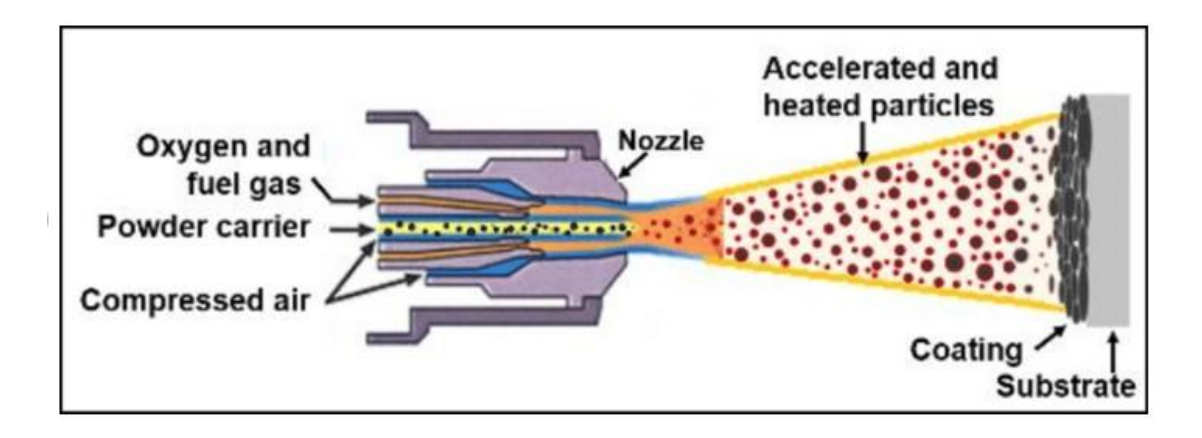


Figure 2.6 Schematic diagram illustrating the working principle of HVOF spray [120]

2.7.5 High Velocity Air Fuel (HVAF) Spraying

HVAF coatings gained attention due to its ability to produce dense, wear resistant coatings with minimal oxidation. It operates at low flame temperature (around 1,900–2,000°C) but achieves high particle velocities (up to 1,000 m/s). This unique combination results in coatings that are well-adhered, dense, and exhibit low levels of thermal degradation. The particles are in thermoplastic state and undergo simultaneously deformation while impacting the substrate and leading to effective

coating deposition [121]. The primary advantage of HVAF lies in its lower deposition temperature compared to thermal techniques, which helps prevent microstructural deterioration of the substrate and avoids melting of the deposited particles. The melting of particles can result change in the microstructure and introduce oxide inclusions in the coating. Further HVAF uses compressed air as the combustion support for spraying, leading to the reduced oxidation and lower preparation costs compared to HVOF [122].

HVAF coatings has industrial applications such as in aerospace and automotive sectors, where wear resistance and corrosion protection are critical. The use of HVAF in the surface modification of the implants has not been extensively studied. The translation of these findings to biomedical applications requires more in-depth studies on biocompatibility, long-term stability in the body, and interaction with biological tissues. Jagadeeshanayaka et al. deposited HA coatings on Ti-6Al-4V and found the retention of crystallinity of HA and enhanced compressive residual stresses and tribological performance [123].

2.7.6 Cold Spraying

Cold spraying is a solid-state process that minimizes the high-temperature reactions and can be suitable for biomedical applications. The high-pressure gas stream (He, N₂, or compressed air) containing solid feedstock powder is expanded through a convergingdiverging nozzle. The convergent part of the nozzle causes the gas stream to be compressed and attain the sonic speed at the throat area and further expanded to supersonic speed at the exit of the divergent part of the nozzle [124]. The minimum velocity required to attain the coating deposition in cold spray is called critical velocity [125]. As the cold spray always works at a temperature lower than the melting point of feedstock powder the problems associated with thermal degradation are minimized [126]. The low-pressure cold spray has a maximum pressure of 10 bar and temperature between room temperature to 1000 °C and has air as carrier gas. The high-pressure cold spray can achieve pressure up to 70 bar and temperature up to 1100 °C. With the increase in gas temperature, the particle impact temperature rises and it decreases the critical velocity. The adhesion strength of high-pressure and low-pressure cold spray copper coatings was 36 MPa and 13 MPa respectively. The thick and dense coatings can be achieved by this process. The optimization of process parameters like carrier gas

temperature and pressure, selection of carrier gas and stand-off distance can lower the critical velocity and increase the deposition efficiency [127].

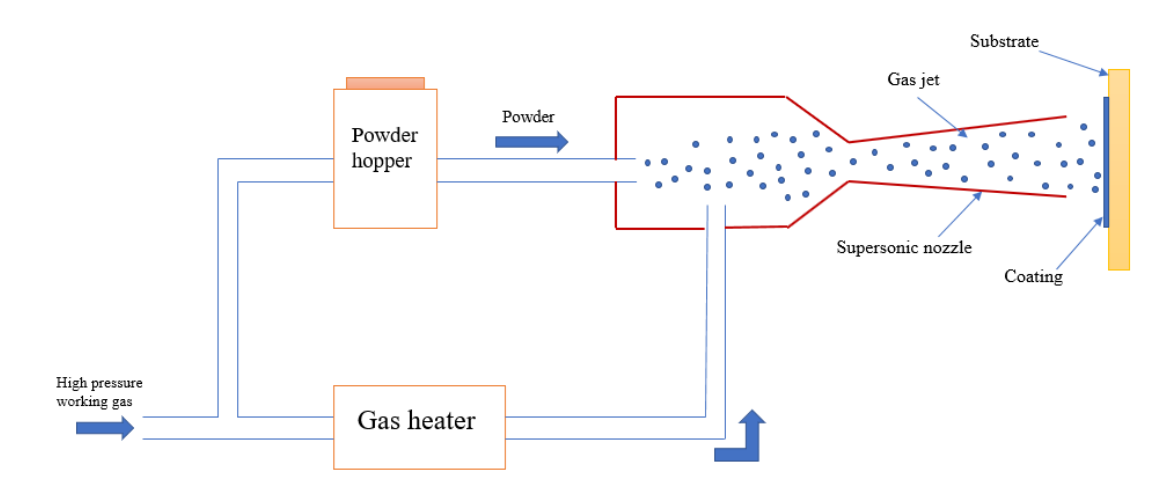


Figure 2.7 Schematic diagram of cold spray coating process [85]

The cold-sprayed Ti coatings were produced on a Co-Cr alloy substrate to examine the corrosion resistance. The coatings acted as a barrier providing the protective effect. The HA-Ti composite coatings on Ti were found to have a bond strength of 24.45 MPa. However, increasing the HA incorporation in Ti beyond 30% results in the crushing of HA particles into fragments due to the high velocity of the gas stream causing high impacts and shocks [128]. Wang et al. deposited HA-Ag coatings on Ti substrate for antibacterial applications. The antibacterial activity was improved by increasing the concentration of Ag nanopowder [129]. Kumar et al. fabricated Ti-Baghdadite (BAG) composite coatings deposited on SS316L for analyzing the corrosion resistance in simulating body fluid. BAG have better biological as well as mechanical properties. Corrosion resistance is enhanced by increasing the BAG content and thickness of coating beyond 200 µm acts as a barrier to corrosion. Further, Ti-15%BAG has the lowest wear rate where wear debris and plastic deformation is less [130]. The microhardness of this composition is best and is recommended for orthopedic implants [131]. HA has poor mechanical properties and HA-Graphene composite cold sprayed coatings are prepared on Ti substrate for load bearing and biocompatibility tests. Graphene has high mechanical strength and adding with HA enhanced elastic modulus, fracture toughness, and adhesion strength of coatings. HA-1wt% graphene enhances cell behavior and has the highest cell proliferation rate. Graphene provides more adhesion sites on the surface of coatings and the filopedia of cells incline to approach

graphene which results in improved spreading and proliferation of cells. Also, the fibronectin protein adsorbs on graphene and facilitates cell attachment [132].

2.7.7 Plasma Spraying

The plasma spray process has a wide range of applications in aircraft engines, internal combustion engines, powerplants, industrial machinery, and biomedical sectors. In aircraft engines, it protects the metallic parts from extremely corrosive surroundings. Plasma spray can melt a variety of materials including refractory ceramics. This technique has lower risk of deteriorating the coating and substrate compared to other high-temperature processes. This is attributed to the chemically inert nature of the gas in the plasma flame and the ability to maintain the target at a relatively cool temperature. Also, the plasma gun used is only a marginally cumbersome than a paint sprayer.

(a) Working Principle of Plasma Spraying

The plasma spray technique comprises two electrodes: a cone-shaped cathode positioned within a cylindrical anode, which extends beyond the cathode to create the nozzle. An inert gas argon mixed with hydrogen is passed through the gap between the electrode where it becomes ionized, forming a plasma. The feedstock powder is directed into the plasma jet generated within the nozzle via tube. To prevent the intense heat from causing melting, water circulates through the channels in both the anode and cathode.

The gun operates with the initiation of an arc across the gaps between the electrodes which is achieved by the pulse of current. As the arc is established, electrons are stripped from the gas atoms: these electrons and positively charged ions are propelled toward the cathode and anode respectively. These rapidly moving particles collide with neutral atoms or molecules in the gas, leading to the dissociation of molecules into their constituent atoms and ionization of atoms. Consequently, the gas within the arc is transformed into plasma. Repeated collisions facilitate the transfer of energy from electrons to positive ions, propelling them until the plasma attains the state of equilibrium. This leads to the formation of thermal plasma where the energy of electrons is converted into enthalpy or heat content and the temperature can reach up to 15000 °C. The addition of hydrogen in argon in a plasma gun increases the heat content of the flame and enhances the ability of the gun's power to melt refractory materials [133].

The plasma flame propels and accelerates the particles, which are melted by its high temperature and strike the surface of the substrate where they solidify and accumulate, forming a thick, firmly adhered protective coating. To have efficient coatings, the particles must absorb sufficient heat from the hot part of the flame, near to anode to fully melt but not too much that they become overheated and vaporize. Further, the droplets must not dwell in the flame for a longer time and must propelled fast enough to flatten and disperse upon impact with the target, ensuring the proper adhesion to the surface of the substrate [133].

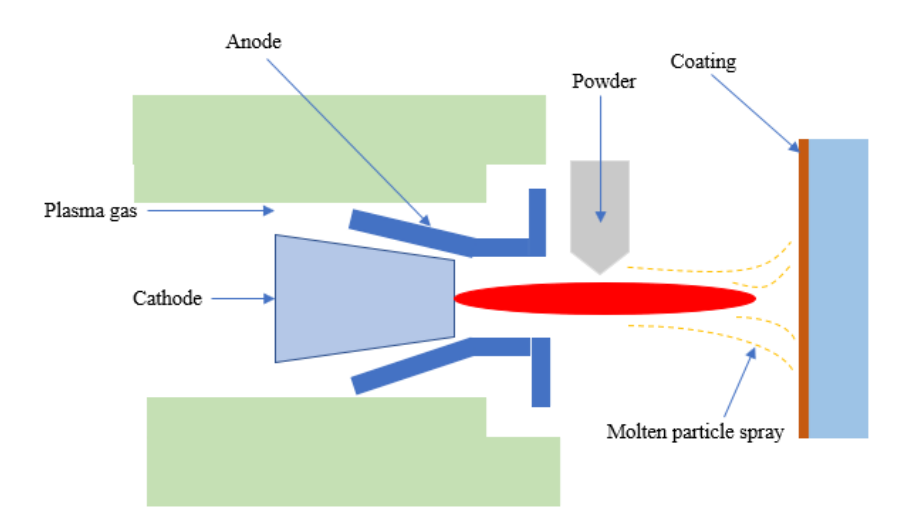


Figure 2.8 Schematic diagram representing the plasma spray coating technique [85]

Multiple variables influence particle heating and acceleration. Plasma gun design, speed of plasma flame, power output, plasma gas composition, and flow rate are the main factors affecting the plasma spray coatings. Also, the feedstock powder size and morphology are other important parameters. Each coating material and gun configuration has an optimal particle size. Particles smaller than this optimum value will overheat and vaporize, while much larger ones may fail to melt and could either disengage from the flame or bounce from the target. The manner in which the particles are introduced into the flame also influences their melting and deposition. The carrier gas pressure must be finely tuned to propel the particles into the flame without allowing them to pass through it. Additionally, the injecting angle is crucial: injecting particles in the downwind direction minimizes disruption to the flame caused by their influx and enhances their velocity, whereas the upwind injection provides the powder with more time to absorb heat from the flame. When the spraying is conducted in the air, particles

begin to cool and decelerate upon colliding with the air molecules after exciting the plasma spray. Therefore, the working distance between the gun and the coating surface is another contributing factor, which can be 5 to 10 cm for air spraying.

(b) Deposition Mechanism of Plasma Spraying

When the initial high-velocity droplets of coating material reach the target, they strike a rough surface of the substrate, made by the process of grit blasting. Upon impact, they solidify into the microscopic tortuous shape of the rough surface and adhere to its irregularities. The molten particles continue to strike at a rate of around a million per second, gradually forming a coating buildup that depends on both the surface area to be covered and the speed at which the gun transverses the surface. The isolated droplets that have solidified on the surface are known as splats. It is considered as the microscopic droplet of molten coating material that strikes the substrate surface, flattens out, and solidifies as shown in Fig. 2.9. As the droplet strikes the surface and spreads out, the substrate serves as a heat absorber, causing a solidification process to start upwards through the droplet. This results in a shallow mound of solidified material while the remaining melt spills over the edges, eventually solidifying into the raised parameter. This process is repeated millions of times and a layer of material thickness ranging from 10 micrometers to many centimeters which can also be removed from the substrate and can also be considered as a bulk material. The rough surface results the coating material to strongly adhered to it by mechanical bonding [133].

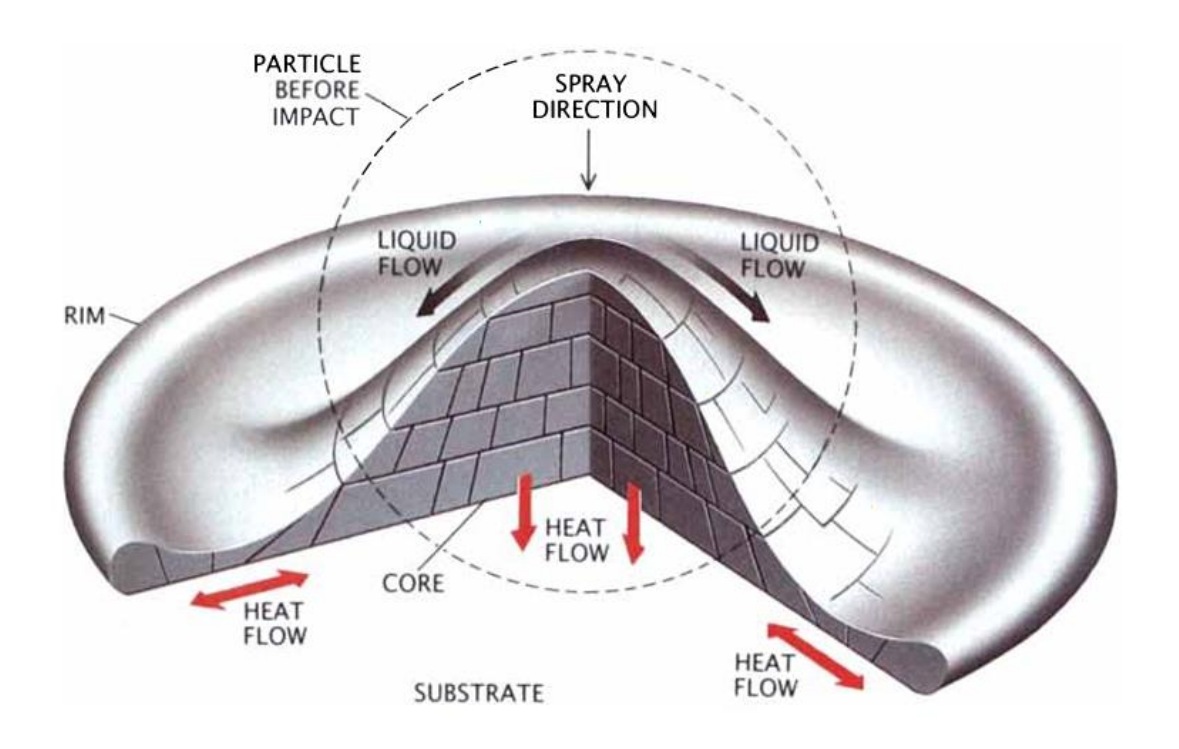


Figure 2.9 Schematic representation of plasma spray coating splat [133]

The formation of plasma sprayed coating is a complex and disordered process. The molten particles after reaching the substrate first interlocked between the irregularities and then with one another to form the coating. The formation of voids occurs due to entrapment of air within it as the coating accumulates. In certain instances, the particles may overheat in the flame, leading to oxidation, while may not melt completely and remain embedded within the coating.

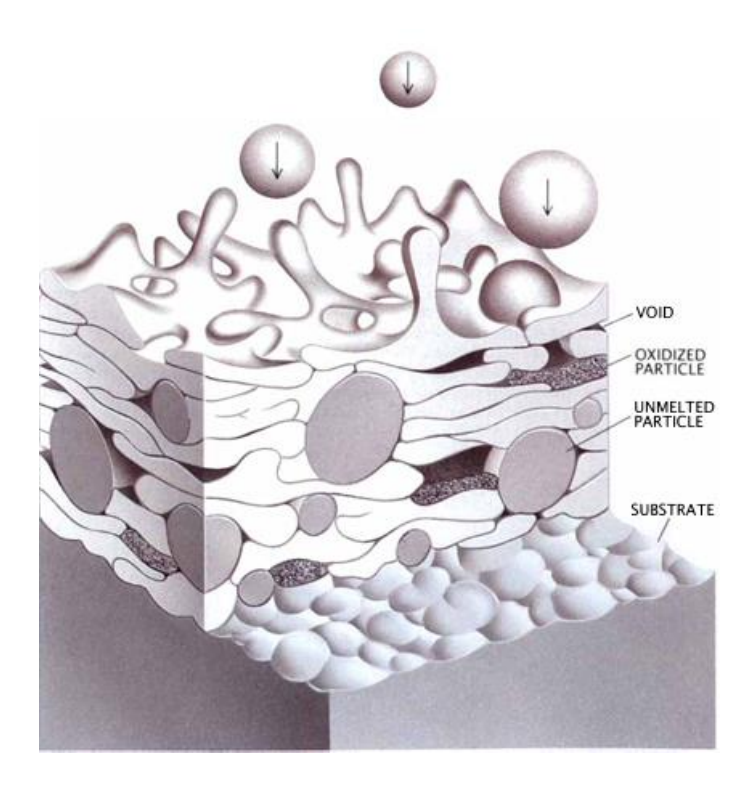


Figure 2.10 Schematic diagram illustrating the buildup of plasma spray coating showing voids, oxidized and unmelted particles [133]

Plasma spray coatings can play a significant role in biomedical applications, particularly in enhancing the performance and biocompatibility of medical implants and devices. Plasma spray coatings can deposit a wide range of materials including metals, ceramics, and composites. Many studies reported that plasma spray coatings improved corrosion and wear resistance as well as biocompatibility [134]. For the deposition of good-quality coatings, selection of the biomaterial, and optimization of process parameters are crucial.

2.8 Biomaterials used for the current study

The literature review of the different biomaterials used in the current study are given in detail as follows-

2.8.1 Hydroxyapatite (HA)

Human bone comprises three primary constituents: collagen, which is tough and flexible; bone mineral, acting as a reinforcement element within the composite structure; bone matrix which facilitates various cellular support functions [135]. The mineral component which constitutes approximately 60-70% of bone weight can be

characterized as a calcium phosphate having an apatitic structure and a composition closely resembling hydroxyapatite (Ca₁₀(PO₄)₆(OH)₂, with Ca/P ratio of approximately 1.67) [136].

HA demonstrates biocompatibility and bioactivity within the human body, integrating with various tissue types and adhering directly to the osseous, soft, and muscular tissues without requiring an intermediate layer of modified tissue [137]. Furthermore, it exhibited osteoconductivity, enabling bone formation to closely adhere to the adjacent surface which also helps in the required rapid healing. However, despite its remarkable biomaterial properties, the inherent mechanical characteristics of HA – specifically brittleness, poor tensile strength and limited impact resistance have limited its use in various load-bearing implants. Consequently, the concept of applying HA as a surface coating onto metallic implants has emerged, thereby the combination of good strength and ductility of the metal and exceptional biocompatibility and bioactivity of the HA can be utilized [138,139].

Plasma spray HA coatings have been utilized as surface treatment for metallic implants in orthopedics and dentistry since the mid-1980s [140]. The advantages of these coatings include the rapid fixation and formation of stronger bonds between the host bone and implant as well as promoting more uniform bone growth and integration at the bone-implant interface [141]. However, there are some challenges in using HA coatings concerning long-term stability. The degradation of HA coatings in the human body environment and can result in the coating disintegration. The coating delamination and disintegration can result in particulate debris formation [142].

The purity and crystallinity of HA plasma spray coatings decrease as the high temperature and sudden cooling result in the decomposition of HA. The new amorphous phases like tricalcium phosphate, tetra calcium phosphate, and calcium oxide. The formation of these amorphous phases can be reduced by controlling the spray parameters and quality of the original HA feedstock powders [143]. The microstructure and porosity can also affect the performance of HA coatings. The porosity of commercially available HA coating can vary from 1 to 10% [144]. The microstructural features have partially and unmelted particles resulting in the porosity in the coatings. In some cases, where fine feedstock powder and very high spray power levels, the microcracks can also form within the splats. With the increase in the porosity, the growth

of the bone cells on the surface of coatings increases but there is a decrease in the tribological parameters like friction and wear resistance as well as corrosion resistance. The denser microstructure of HA coating reduces the risk of bonding degradation due to cracking, spalling and delamination when exposed to the body fluids in vivo [145]. This high coating density will good adhesion strength because of continuity and integrity at the substrate-coating interface whereas the requirement of porosity will facilitates bone cell growth [146]. Therefore, controlling the porosity value is crucial for optimizing the coating performance by using appropriate plasma spray parameters.

Zheng et al. prepared the plasma-sprayed bioactive coatings for implant applications and studied the surface roughness effect on osteoblast cell adhesion and differentiation [147]. Links et al. reported titanium surfaces with an average roughness value between 4 and 7 μm, osteoblast cells showed reduced proliferation but enhanced osteogenic differentiation [148]. The plasma-sprayed coatings have micro-textured surfaces that show improved osseointegration as compared to smooth surfaces. Boyde et al. reported that osteoblast cells osteoblast cell adhere and proliferate better on rough surfaces while the epithelial and fibroblast cells prefer smooth surfaces [149]. The properties of plasma-sprayed HA coatings are also affected by the process parameters that have been investigated by various researchers [150,151]. Sun et al. [152]and Tsui et al. [138] reported a decrease in the crystallinity and purity of the plasma-sprayed HA coatings with an increase in power or current. However, Yang et al. reported an increase in crystallinity with an increase in spray current [153].

Fielding et al. prepared plasma sprayed HA coatings with the incorporation of the Ag₂O and SrO and reported the improvement in the antimicrobial activity and improved the cell proliferation and differentiation activity as compared to pure HA coatings [154]. Singh et al. developed plasma sprayed HA-niobium coatings with varying Nb % and analysed the corrosion behavior and biocompatibility. The results indicated that HA-30Nb coatings highest corrosion resistance and better cell proliferation rate [155]. Poorraesi and Afshar prepared electrodeposition HA-ZrO₂-TiO₂ nanocomposite coatings. The addition of ZrO₂ and TiO₂ nanoparticles has shown improvement in the corrosion resistance and bioactivity which is essential for bone repair and bone attachment to implant [156]. Yao et al. fabricated nanostructured HA-TiO₂ coatings by high velocity suspension flame spray. The TiO₂ additions resulted in the improvement of tensile strength, microhardness and wear properties [157]. The high velocity

suspension flame spray HA-ZrO₂ and HA-TiO₂ coatings have rough/porous surfaces with nanoparticle agglomerates and well bonded coating and substrate interface. HA-TiO₂ coatings have higher mechanical properties as compared to HA-ZrO₂ due to their higher melting degrees. Both the coatings has enhanced corrosion resistance in hank solution than SS316 L substrates [158].

2.8.2 Baghdadite (BAG)

Over the past twenty years, calcium-silicate(Ca-Si) based ceramics have been considered as promising biomaterials for bone and skeletal tissue regeneration applications [159]. The major advantages of these ceramics include their high bioactivity and biodegradability [160]. However, despite these advantages, Ca-Si-based ceramics face challenges due to their brittle nature, low strength, and high dissolution rate. The dissolution rate can affect cell growth adversely, owning to the elevated pH values, and impact the long-term stability of these materials [161]. The incorporation of Zr, which is a quadrivalent ion and ionically binds the Ca ions and improves the stability of Ca-Si ceramics [162].

BAG (Ca₃ZrSi₂O₉) is a calcium zirconium silicate material having bulk density comparable to natural minerals. The crystal structure of BAG is monoclinic and belongs to the CaO-ZrO₂-SiO₂ [163]. It is the first type of Ca-Zr-Si ceramic system which exhibits the apatite formation ability and is considered as a bioactive ceramic. In BAG ceramic, the mechanical and physiological properties are significantly improved by the presence of Zr. Further, there is no report of toxic or unfavorable consequences of incorporating the Zr in Ca-Si system [164].

In the past decade, this ceramic has gained considerable attention for its demonstrated ability to effectively promote osteogenesis and address large-scale bone defects through the release of bioactive ionic products [165]. Due to this, BAG is a promising material to be used for bone tissue repair and regeneration [166]. BAG accelerates the healing, mitigates implant rejection, and enhances various cellular processes cell adhesion, migration, proliferation, differentiation, formation of new bone, and vascularization [167]. Moreover, it forms strong biological bonds with bone tissue in vivo and emerged as a viable alternative to metallic implants for load-bearing applications [168]. The surface modification of metallic implants with BAG significantly affects the osteogenic gene expression of bone cells in vitro [169].

Schumacher et al. [170] mentioned the mechanical properties of the BAG ceramics are affected by the sintering process. The bending strength was enhanced to $98 \pm 16\,$ and $97 \pm 20\,$ MPa by adjusting the sintering temperature to $1400\,$ °C and $1450\,$ °C respectively. The Vickers hardness value at $1350\,$ °C sintering temperature was measured as $6.1 \pm 1.1\,$ GPa and it was increased to $7.9 \pm 0.2\,$ GPa at $1400\,$ °C.

Several researchers have used BAG ceramic-based composite coatings for metallic and ceramic biomaterial implants [171,172]. Liang et al. deposited plasma spray coatings with BAG feedstock particles on Ti-6Al-4V alloy substrate for hard tissue replacement applications [173]. The rapid cooling rate and intricate structure of BAG ceramic led to the baghdadite as a major phase in the coating along with a minor amorphous phase because of fast melting and sudden quenching onto the substrate surface. These BAG coatings exhibited an average surface roughness value of $9.84 \pm 1.21 \, \mu m$ and a bond strength of 28 ± 4 MPa, demonstrating superior characteristics compared to plasma-sprayed HA coatings [174]. Furthermore, the incorporation of zirconium into the crystal structure of BAG coatings resulted in significantly enhanced chemical stability when compared to calcium silicate [175].

Pham et al. evaluated the in vitro bioactivity, adhesion, degradation, microstructure, cytocompatibility, and roughness of the BAG and HA ceramic coatings. The results indicated the BAG coatings applied to the Ti-6Al-4V substrate exhibited stable microstructure and more uniform hardness (325.5 \pm 55.2 HV) compared to HA coatings (118.3 \pm 21.2 HV), attributing to the presence of Zr elements within the BAG structure. Moreover, the surface roughness of the BAG coatings showed less variability than that of HA coating with Ra values of 9.9 \pm 0.6 μ m and 10.1 \pm 0.9 μ m, respectively. Nanoindentation tests revealed that the average hardness and modulus of BAG coating were 8.2 \pm 2.9 GPa and 103.2 \pm 26.6 GPa respectively while those of the HA coatings were 3.8 \pm 3.1 GPa and 66.8 \pm 39.3 GPa respectively. In vitro investigations demonstrated superior osteointegration of MG63 cells on the BAG coating compared to both HA coating and pure Ti surfaces, suggesting the favorable biological properties of the BAG coatings are beneficial to MG63 cell proliferation [176].

Another investigation conducted by Bakhsheshirad et al. analyzed the corrosion resistance and anti-bacterial properties of Mg alloy coated with zinc oxide combined with BAG using electrophoretic deposition and physical vapor deposition. In SBF

solution ZnO/BAG coatings exhibited excellent corrosion resistance compared to both ZnO-coated and uncoated specimens shifting the corrosion potential to a noble direction. Moreover, both ZnO and ZnO/BAG coatings demonstrated significant zones of inhibition against Escherichia coli, klebsiella pneumonia, and shigella dysenteriae compared to the coated and uncoated samples. Furthermore, the authors noted that the compressive strengths of ZnO-coated and ZnO/BAG-coated samples reached 148.2 MPa and 170.6 MPa, respectively after just 10 days of immersion in SBF [177]. Kumar et al. investigated the tribological and corrosion behavior of titanium baghdadite composite coatings by cold spraying. The Ti-15 wt% BAG coatings showed significant enhancement in the wear resistance of the coatings in dry and SBF environments. Further, the corrosion rate of the coatings decreased with the increase in BAG content [178,179].

The outcomes of these investigations collectively hint at a promising future for BAG coatings in bio-implant applications. Hence, the study considered BAG, which combines both biological as well as mechanical properties as a promising material for investigation.

2.9 Carbon Reinforcement

2.9.1 Carbon nanotubes (CNT)

Discovered in 1991, by Sumio Lijima, carbon nanotubes are elongated, thin cylinders composed of carbon. These large macromolecules stand out for their distinct size, shape and extraordinary physical characteristics. They can be envisioned as a rolled-up sheet of graphite, forming a cylindrical structure. The intriguing structures of CNT have ignited considerable interest in recent years, leading to extensive research efforts dedicated to comprehending their properties. Currently, the exploration of their physical properties is still ongoing, with some aspects subject to debate. Nanotubes exhibit a wide spectrum of electronic, thermal, and structural properties which vary based on factors such as their diameter, length, and chirality. They exist in single-wall configurations (SWNT) or possess multiple walls (MWNT) with one cylinder inside the other cylinder [180].

CNT structure consists of carbon atoms arranged in a hexagonal (honeycomb) lattice, forming a single-atom thick layer known as graphene. This graphene layer is then rolled

into a cylindrical shape and bonded together to create the CNT structure. CNT has higher tensile strength than steel and Kevlar, owing to sp² bonds between individual carbon atoms which are even stronger than sp³ bonds present in diamond. When subjected to high pressure, individual nanotubes can conjoin, exchanging some sp² bonds for sp³ bonds, thus enabling the production of extended nanotube wires. The structural defects arising from atomic vacancies or rearrangement of carbon bonds can compromise the strength of CNT [180].

The atomic arrangement of CNT is such that it minimizes the collision between conduction electrons and atoms, resulting in the high electrical conductivity of CNT. The strong bonding between carbon atoms enables CNT to have higher electric conductivity than copper. The strength of atomic bonds in CNT enables them to withstand very high temperatures, making them very good thermal conductors. The thermal conductivity of CNT is influenced by both the temperature of the tubes and the surrounding environment [181].

In recent times, there has been significant interest in the distinctive biological and medical attributes of CNT and it is expected that biomaterials incorporating CNT will soon be used for clinical applications. The reinforcement of CNT will improve the strength characteristics of the biomaterials used in the treatment of fractures or arthroplasty. Numerous studies have explored the impact of CNT on osteoblast cells in vitro, indicating that CNT enhances osteoblast cell proliferation. This attribute of CNT is particularly valuable when incorporated into biomaterials intended for bone applications [182].

CNT has been considered as the potential reinforcement material for improving the fracture toughness and wear resistance of the HA composites. The CNT-reinforced HA coatings can replace the clinically used pure HA coatings because of the enhancement of mechanical and tribological properties [183].

Balani et al. prepared the CNT-reinforced HA coatings by plasma spray technique on Ti-6Al-4V substrates to improve the strength and toughness of brittle HA coatings. The HA-4wt%CNT plasma sprayed coatings increased the crystallinity by 27% and fracture toughness by 56%. The uniform dispersion of CNT results in osteoblast hFOB 1.19 cell growth and ensures the HA-CNT coatings are non-toxic. Further, CNT enhanced the mineralization and precipitation of apatite [184].

Another study by Balani et al. evaluated the tribological behavior of CNT-reinforced HA coatings in simulated body fluid environment. The wear resistance was improved with the addition of CNT. The micro-cracks induced during the abrasive wear test of HA-CNT coatings were restricted by CNT. The weight and volume loss during wear were significantly reduced for HA-CNT coatings due to the self-lubricating nature of CNT. Further, the wear debris pinning was assisted by the bridging and stretching of CNT [185].

2.9.2 Graphene

Singh et al. investigated the electrochemical behavior of graphene nanoplatelets reinforced HA plasma sprayed coatings was examined in simulated body fluid. The porosity measurement of HA coatings was 15% and with addition of 1wt% graphene it reduced to 13% and further reduced to 10% with 2wt% graphene. After plasma spraying, the defects like voids, porosity and microcracks occurs which can be minimized as graphene fills the gaps at inter-splat region and hence the porosity is reduced. Moreover, the corrosion resistance was enhanced by 67% with 1wt%graphene and by 87% with 2wt%graphene. The reason behind this can be the increased water contact angle of coating due to the hydrophobic nature of graphene [186].

Chen et al. fabricated graphene nanosheets reinforced HA plasma spray coatings for evaluating strength and toughness. The homogenous distribution of graphene in coatings was observed in the microstructure and acted as a binder between individual HA splats. Graphene nanosheets addition results in an increase in fracture toughness by 32.3% and indentation yield strength by 54.7%. The crack propagation is resisted during contact with graphene nanosheets and results in crack deflection. The strengthening mechanisms like load transfer, graphene nanosheets pull out and bridging, crack branching and inter-layer sliding of graphene nanosheets give rise to an increase in strength [187].

Khan et al. deposited plasma-sprayed HA coatings with varying wt% of graphene as 0.5%, 1%, and 5% on Ti-6Al-4V by plasma spraying for tribocorrosion behavior and biocompatibility. Mechanical properties do not change significantly with increasing graphene percentage. The shallower wear scar was observed in graphene-HA coatings which shows better tribocorrosion resistance than pure HA coating. The cell viability of HA-2wt%graphene was maximum at 89.6% as compared to 0.5wt% graphene and

5wt% graphene with cell viability of 87.3% and 85.4% respectively. The study depicted the optimum graphene wt% in HA for best biocompatibility for implants was 2wt% [188].

Table 2.2 Carbon-reinforced coatings prepared by various thermal spray techniques [85]

Author	Coating technique	Coating material	Substrate	Test perfor- med	Key finding	Remarks
Khan et al. (2023) [188]	Plasma spray	HA- Graphene Composite	Ti- 6Al- 4V	Tribocorr osion behavior	Shallow wear scar showed increase in tribocorrosio n resistance with graphene addition	2wt% graphene has shown best biocompat ibility.
Balani et al.(2007) [184]	Plasma spray	HA-CNT composite	Ti- 6Al- 4V	Fracture toughnes s and biocomp atibility	Fracture toughness increased by 56% and osteoblast hFOB1.19 cell growth occurs	Mineralis- ation and precipitat- ion of apetite
Singh et al.(2020) [186]	Plasma spray	HA- Graphene	Ti	Porosity and Corros- ion resista- nce	Porosity reduced by 5% and corrosion resistance enhanced by 87%.	Graphene fills the gaps, voids formed in coatings
Lieu et al.(2014) [132]	Cold Spray	HA- Graphene composite	Ti	Load bearing and biocom- patibility	Enhanced fracture toughness, elastic modulus and adhesion strength of coatings	Graphene-HA composite increased the attachment and proliferation of osteoblast cells

2.9 Problem Formulation

Over the past few years, there has been a rising demand for orthopedic implants to address the needs of individuals requiring such implants. The primary total hip arthroplasty and total knee arthroplasty are projected to grow to 635,000 and 1.26 million procedures respectively by 2030 [189]. With the increasing demand for orthopedic implants every year, there is a need for the development of better implants that have excellent biocompatibility as well as mechanical properties [190].

Metallic biomaterials like SS316L, cobalt-chromium alloys, and titanium-based alloys are commonly employed for repairing damaged structures because of their high strength and durability [191]. However, the lack of osteoconductivity in metallic implants is one of the major limitations that leads to poor interactions with the bone tissues and results in aseptic loosening [191,192]. Additionally, these bioimplants face challenges such as the release of metallic ions and the production of harmful wear debris. These debris generation can have effects like inflammation and damage of cell tissue and ultimately leading to the failure of bioimplants. To address these issues, bioceramic coatings on metallic implants can be applied to achieve the desired bioactivity, corrosion resistance, and mechanical properties and can help in the overall improvement of metallic implants [193,194].

Hydroxyapatite (HA, Ca₁₀(PO₄)₆(OH)₂) is a commonly used Ca-P ceramic that has chemical similarities to the mineral composition of bones and has excellent osteointegration properties. However, its intrinsic brittle nature and inadequate mechanical properties restrict its usage as a coating material, declaring it unreliable for load-bearing bioimplants [195]. Baghdadite (BAG, Ca₃ZrSi₂O₉), a Ca-Zr-Si-based bioceramic, stands out for its mechanical and biological features close to the bone tissue. The influence of baghdadite composition on its biocompatibility, bioactivity, and biodegradability, is widely acknowledged in the literature [190,196].

Plasma-spray is the most widely used coating method for bio-implants applications because of its high deposition rate, desired coating thickness, cost-effectiveness and reliability. Therefore, the Food and Drug Administration (FDA) has approved the plasma-spray coatings for orthopedic implant applications [51]. To address the defects that occurred after plasma spraying and ensure the desired wear resistance and fracture toughness for bioimplant applications, secondary reinforcing agents are added to the

bioceramic plasma-spray coatings. Carbon nanotubes (CNT) have high tensile strength, high thermal conductivity, and excellent chemical stability [197,198]. Over the past 15-20 years, CNT has emerged as a promising reinforcement material for bioimplant coating applications, contributing significantly to advancements in both mechanical and biological properties [190,199].

The CNT reinforcement in the coatings can enhance the mechanical properties, their effect on the electrochemical stability and corrosion resistance of BAG coatings was not well understood. Very few studies have investigated how CNT reinforcement affects the electrochemical behavior of BAG in SBF environment. This study explored the electrochemical properties of CNT-reinforced Baghdadite coatings and to determine their suitability for long-term implant applications.

There is insufficient data available on the biocompatibility and potential cytotoxicity of plasma sprayed CNT reinforced BAG coatings. This study discusses the biocompatibility and potential cytotoxicity of the coatings by conducting the in vitro studies particularly under conditions simulated body environments. Therefore, BAG-CNT composite coatings aim to enhance the overall performance of the coating and thereby providing new insights for the next generation biomedical implants.

The current study focuses on the development, characterization and testing of HA, BAG, and BAG reinforced with CNT coatings deposited by atmospheric plasma-spray technique. Moreover, this research work compares BAG with 1 wt% CNT and 2 wt% CNT reinforcement coatings with pure BAG and pure HA coatings. The primary aim is to evaluate how CNT reinforcement can improve the mechanical and electrochemical properties of the coatings without compromising their biological response.

2.10 Research Objectives

The central emphasis of this work is to develop bio-active coatings for better osseointegration for orthopedic implant applications. The current work has the following objectives-

- To deposit the HA, BAG, BAG-1CNT, and BAG-2CNT coatings on Ti substrates by plasma spray technique.
- To characterize the developed coatings for understanding the microstructure and phase compositions.

- To study the mechanical properties and electrochemical corrosion behavior of the coatings in a simulated body fluid environment.
- To perform the in vitro biocompatibility and cell viability analysis of coatings.

Through these research objectives novel CNT reinforced Baghdadite coatings have been development and the thus achieved improvement in mechanical properties, corrosion resistance, wear restance and bicompatibilty have been achieved.

CHAPTER 3

Experimental Methods

3.1 Introduction

This chapter focuses on the details of the materials and methods used in the present work. The main aim of this research work is to develop the bioactive coatings and the effect of CNT reinforcement in terms of mechanical, electrochemical, and biological properties. To achieve this goal, the state of art characterization tools and desired types of equipment were utilized. A brief overview of the composition of feedstock powder along with the coating technique is provided in this chapter. The characterization tools and equipment used are explained in the sequence of their usage in the research work. These are field emission scanning electron microscopy (FESEM) with energy dispersive spectroscopy (EDS), x-ray diffraction (XRD), x-ray photoelectron spectroscopy (XPS), Raman spectroscopy, plasma spray coating machine, metallography, surface roughness tester, hardness testing, scratch testing, electrochemical workstation, cell culture incubator, microplate reader and UV-Vis Spectrophotometer.

3.2 Raw Materials

3.2.1 Titanium Substrate

The current research work utilized commercially pure titanium as the substrate material for coating deposition. Ti is a commonly used material for the manufacturing of biomedical implants and has good corrosion resistance, high strength, low modulus, and inertness to the body environment. The low modulus of Ti as compared to other materials like stainless steel 316L and chromium-cobalt alloys results in a low-stress shielding effect. The size of the substrate material used is 100 x 100 mm plates with 5 mm thickness.

3.2.2 Hydroxyapatite Powder

The commercially pure hydroxyapatite (HA) powder was purchased from Nanoresearch Elements USA with more than 99% purity. HA powder has chemical composition as –

Ca-38.8 %, P- 19.8% and O- 41.4%. The particle size distribution of the HA powders was between 10 μm and 90 μm. The thermal sprayed HA coatings are commercially used for surface modification of orthopedic implants. The current study will involve different compositions of feedstock powders and the results will be compared with HA to understand the improvement in the overall performance. The feedstock powder morphology and phase identifications were analyzed with Field Emission Scanning Electron Microscopy (FESEM, JEOL, JSM-7610F plus, Japan) and X-ray Diffraction (Pananalytical, Xpert Pro MPD, Netherlands) respectively.

3.2.3 Baghdadite Powder

Baghdadite (BAG) is a calcium zirconium silicate bioceramic that promotes adhesion, growth, and proliferation of osteoblast cells and has excellent osseointegration. BAG powder (> 99% purity) was procured from Nanoresearch Elements with composition as – Ca- 29.2%, Zr- 22.1%, Si- 13.2% and O- 35.5%. The particle size distribution of the BAG powders was between 5 μ m and 30 μ m. Several reports suggest that BAG has good mechanical and biological properties and is a promising candidate for replacing HA for biomedical implants near future. FESEM and XRD analyses of BAG powders were employed for morphological and phase identifications.

3.2.4 Carbon Nanotubes

Carbon nanotubes (CNT) are well-known for their unique properties like high tensile strength, high thermal conductivity, and excellent chemical stability. CNT was incorporated as a reinforcement material in this research study to improve their mechanical as well as corrosion properties. Multi-walled CNT with a purity of 95 % was also procured from Nanoresearch elements. CNT has diameter of 50 nm and an average length of around 40 μ m. The FESEM micrographs were utilized to study the CNT morphology and will be discussed in the next chapter.

3.3 Coatings Development

3.3.1 Feedstock Powder Preparation

The BAG and CNT were mixed in different compositions to study the effect of CNT in the feedstock material on the deposition of BAG-CNT coatings. The Alphie 3D tumbler mixer machine was used for the mixing of BAG and CNT powders as shown in Fig.3.1.

The Alphie mixer is ideal for the homogeneous mixing of powders with different densities, shapes, particle sizes, and mixing proportions. It can provide homogeneity by rotary and shaking motion. The optimized mixing time of 15 min and speed of 50 rpm resulted in no segregations of different compounds. Further, there is no damage to the samples as there is no shear force applicable to the material and it involves gentle mixing. The specifications of the powder mixing machine are given in Table 3.1. The four different compositions used for the coating deposition in this work are pure HA, pure BAG, BAG reinforced with 1wt%CNT (BAG-1%CNT), and BAG reinforced with 2wt%CNT (BAG-2%CNT). Before the deposition, the powders were heated at 80°C in a hot air oven to remove the moisture trapped inside them.

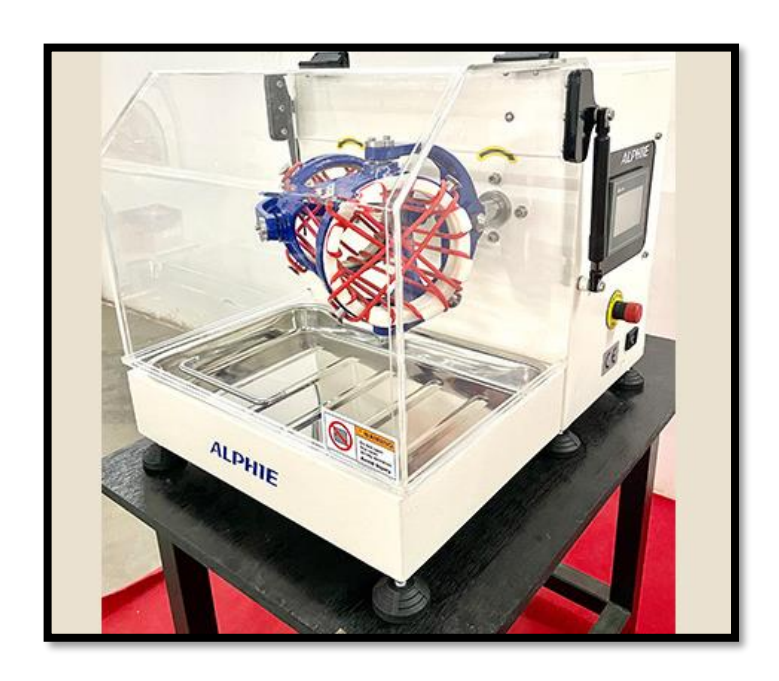


Figure 3.1 Alphie powder mixer machine used for mixing the powders [200]

Table 3.1 Specifications of powder mixing machine [200]

Capacity	2.5 L
Effective Capacity	2.0 L
Max mixing mass	5 Kg
Motor Power	0.3 hp
Power Supply	Single phase, 220 V
Container Revolution	10 – 80 rpm
Max Container Size	Dia 115 mm x 275 mm Long
Machine Weight	65 Kg

3.3.2 Substrate Preparation

To ensure the optimal adhesion strength of the coatings to the Ti substrate, the substrates were uniformly grit blasted before plasma-spray process. The pressure blasting machine was used for substrate preparation. It uses a pressurized vessel for holding the abrasive media. The blasting media was Al₂O₃ (20 mesh size) with an air pressure of 5 bar and the distance between blasting nozzle and substrate media was 6".

3.3.3 Coatings Deposition

The prepared feedstock powders were deposited using an AP 2700 "mass-flow controlled" plasma spray system. The machine is equipped with a Plasma spray gun (MF-4MB MECPL, Jodhpur) as shown in Fig.3.2. It has PLC-controlled process control, and touch screen operation, and the process fluids are equipped with mass flow controllers. The auxiliary components like the robot, powder feeder, chiller, and dust collector are integrated with the system. The plasma gun MF-4MB is a robust, widely accepted gun for depositing high-quality plasma coatings with a maximum power rating of 55kW. The primary gas used in the plasma spray system was argon, which transported the feedstock powders into the powder feeder and subsequently into the plasma gun nozzle. Hydrogen gas, used as the secondary gas, was employed to enhance the energy of the plasma for the coating process. The process parameters for plasma spray coatings are given in Table 3.2.



Figure 3.2 Plasma Spray Gun MF-4MB [200]

Table 3.2 Details of plasma-spray process parameters used for the development of coatings on Ti substrate [201]

S. No.	Parameters	Values
1.	Spray angle	90°
2.	Argon flow rate	39 nlpm
3.	Hydrogen flow rate	5 nlpm
4.	Standoff distance	110 mm
5.	Powder feed rate	30 g/min
6.	Plasma power	20 kW
7.	Current	500 A
8.	Voltage	70 V
9.	Number of passes	5

3.4 Characterization of Plasma Spray Coatings

3.4.1 Metallographic Sample Preparation

The standard guide for metallographic preparation of thermal sprayed coatings were followed as per ASTM standards E-1920-03 [202]. Samples were cut into 10 mm x10 mm using an abrasive cutter machine with a diamond wheel of 6" and 1800 rpm. The slow federate of 0.2 mm/min was kept to prevent cracks in the coatings. The samples were cold-mounted with epoxy resin as the ceramic coatings are easily damaged during hot compression mounting. Then polishing of the samples was done up to 3000 grit size emery paper followed by cloth polishing with diamond paste of $1 \mu \text{m}$.

3.4.2 Microstructural Characterization of Coatings

The coating surface and cross-sectional analysis of plasma sprayed coatings was performed using SEM-EDS. XRD analysis using Cu-K α radiation was done for the phase identification of the developed coatings. The scanning speed was set at 1kcps to record the XRD data within a 2 θ range of 20-90°. XPS (Thermofisher Scientific ESCALAB Xi+, USA) analysis was performed using a monochromatic X-ray source of Al-K α with an energy of 1486.69 eV and operating power of 150W. Avantage software was used to analyze the XPS spectrum peaks after the Shirley background subtraction

with the correction of carbon binding energy at 284.8 eV. To analyze the structural and compositional properties of HA, BAG, and to confirm CNT retention in BAG-CNT composite coatings, Raman spectroscopy (Horiba, Model - LABH RevUV-Open, Japan) was used. A laser with a wavelength of 633nm, exposure time of 10 seconds, and 4.5W power was used to obtain Raman spectra. A 100x objective lens with a 100μm slit size captured coating images, with a minimum of four areas per investigated coating [201].

Apparent surface porosity was determined by analyzing the cross-sectional SEM images of the coatings at 1000x magnification. The analysis was done by using grayscale threshold image analysis in ImageJ software. The porosity value was measured from five images per coating and then the average of the values was reported [201]. The cross-sectional SEM images of the coatings were analyzed for measuring the coating thickness.

3.5 Mechanical Testing of Coatings

3.5.1 Surface Roughness Testing

The roughness tester (HandySurf E-35-A/B, Accretech, Japan) was used to measure the surface roughness of developed coatings. Roughness parameters including the arithmetic mean deviation (R_a), root mean square average of profile heights (R_q), and maximum peaks to valley heights (R_z) were measured. Before the measurement, the equipment was calibrated by using a calibration block. The stylus of the roughness tester was made to run over the plasma-sprayed coated samples. Measurements were taken with a 2 mm cutoff length and a measuring speed of 0.25 mm/s. The roughness parameters were reported as an average of ten values for each coating.

3.5.2 Microhardness Testing

Vickers microhardness tester (ZHV μ , Vickers tester, Germany) was used for measuring the microhardness at coating cross-sections as shown in Fig.3.3. The load applied was 300 gf and dwell time was taken as 10 sec. Micro indentations at coating cross sections are located at a distance greater than 3 times the diagonal length. The average of 10 micro indentations was taken to evaluate the HV value [190].

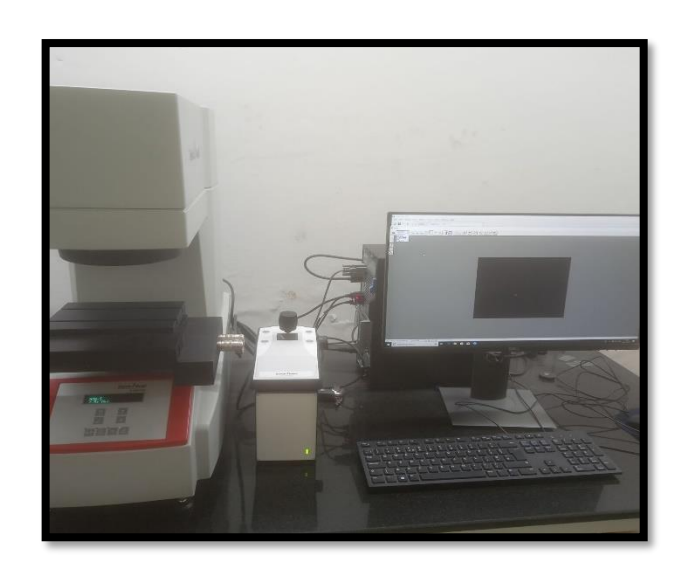


Figure 3.3 Vickers microhardness setup

3.5.3 Scratch Testing

Micro-scratch tester (DUCOM, TR-101, India) was used to evaluate the scratch resistance of plasma-sprayed coatings as shown in Fig.3.4. The scratch was created on the surface of the coatings with a spherical stylus of tip size 200 μm. Progressive scratching mode with a normal load from 20 N to 120 N over a scratch length of 5 mm with 0.1 mm/s scratch velocity was employed. A minimum of three scratch tests were conducted and instantaneous friction force was recorded. The variation in penetration depth was measured using a surface roughness tester and post-scratch morphology was observed using FESEM [190].

The scratch wear rate (S_R) was calculated by following eqn. (1) [203]-

$$S_R = \frac{W_{vol}}{FL} \tag{1}$$

where F is the average normal load during progressive load scratching and L is the scratch length and wear volume loss, W_{vol} was calculated by using eqn. (2) [203] -

$$W_{vol} = A L \tag{2}$$

where A is the horizontal projected contact area and is calculated by using eqn. (3) [204]-

$$A = R^{2} \cos^{-1} \{1 - d/R\} - (R - d)\sqrt{2Rd - d^{2}}$$
(3)

where d is the penetration depth of scratch and R is the Rockwell indenter radius (0.2 mm). The scratch hardness was also estimated by using eqn. (4) [204]-

$$H_S = \frac{8F_N}{\pi w^2} \tag{4}$$

where w is maximum scratch width and F_N is the normal load.



Figure 3.4 Scratch testing setup

3.6 Electrochemical Corrosion Studies

3.6.1 Potentiodynamic Polarization Tests

The developed coatings were evaluated for their anticorrosive properties through the use of open circuit potential (OCP) and potentiodynamic polarization testing (ASTM Standard F1089-02). To conduct the tests, a three-electrode cell assembly was used, consisting of a saturated calomel electrode (SCE), graphite electrode, and coating samples as the reference, counter, and working electrode respectively. These tests were performed at a temperature of 37°C by using an electrochemical workstation (Autolab, M204) as shown in Fig. 3.5. The Ringer's solution having ion concentrations approximately equal to human blood was used as an electrolyte medium. The reagents used for preparing the ringer solution are given in Table 3.3 [201].

The coated face of Ti substrate was exposed to the electrolyte medium whereas the other faces were masked with the use of masking tape. Therefore, the exposed area of coatings in a corrosive medium was 1 cm². The required circuit connections were completed and the samples were dipped into the solution. The reference electrode tip is placed near to the surface of the working electrode to minimize the solution resistance drop. Before initiating the polarization test, the open circuit potential of the coatings was stabilized by immersing each coating individually in simulated body fluid (SBF) for a duration of 1 hour. An anodic polarization test was performed by scanning the coated samples from cathodic region -0.5 V to anodic region 0.5 V with a scan rate of 100 mV/min at OCP condition. The Nova 2.1 software was used for the data analysis. The corrosion current density and corrosion potential were determined from the polarization curves of plasma sprayed coated samples by Tafel exploration method.

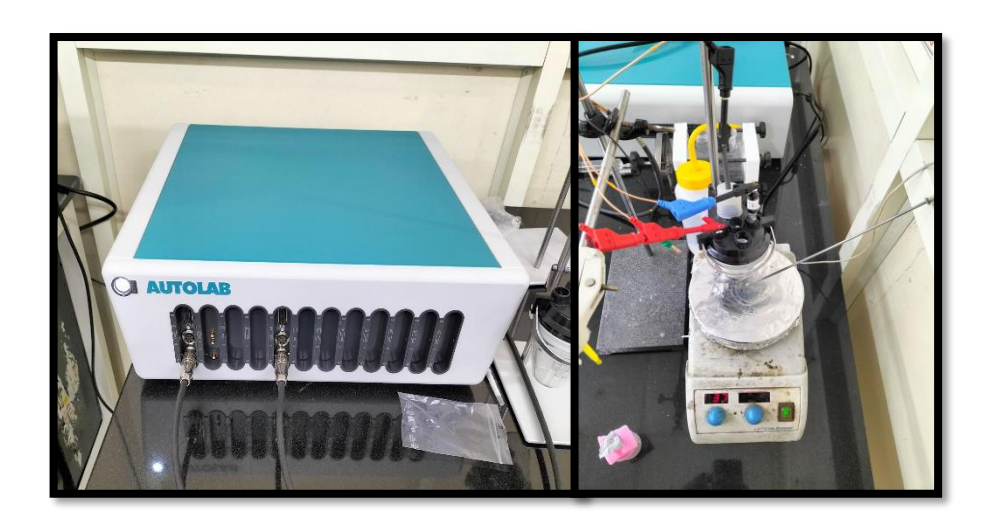


Figure 3.5 Electrochemical Corrosion Workstation setup

Table 3.3 Ringer's solution reagents and compositions [201]

S. No.	Reagent	Composition (g/l)
1.	NaCl	9
2.	CaCl ₂	0.24
3.	NaHCO ₃	0.2
4.	KC1	0.42

3.6.2 Electrochemical Impedance Spectroscopy (EIS)

The EIS analysis is useful in studying the deterioration of coating on metal substrates caused by the exposure of electrolytes. The coating degradation may result in the corrosion of the underlying substrate by the electrolyte medium. EIS can quantitatively measure the capacitances and resistances in the electrochemical cell. Resistance is associated with the electron transfer processes like corrosion. The resistance offered by the electrolyte medium connecting the reference and working electrode is called electrolyte resistance. The capacitance of the coating changes with the deterioration of the coating with time during exposure to electrolyte. The capacitance of the coating is related to the impedance magnitude and is given as-

$$|Z| = \frac{1}{2\pi f C_{coating}} \tag{5}$$

Where, f = frequency of applied AC voltage

The resistance due to the presence of micropores in the coating is called pore resistance. When the electrolyte penetrates inside the pores of the coatings, the pore resistance is very high initially and gradually decreases with electrolyte exposure time. The polarization resistance describes the corrosion rate of metal substrate underneath the coating. The metal electrolyte surface separates the charge in electrolyte and charge on the metal electrode. This interface is called double layer and the corresponding capacitance is called double layer capacitance (C_{dl}). C_{dl} can be related to the coating delamination especially in the coatings with good adhesion strength that will not allow the electrolyte-metal contact.

The EIS analysis was conducted under open circuit potential (OCP) conditions. The frequency range used for this analysis was 100 kHz to 10 mHz, with an applied AC excitation potential of 10 mV.

3.6.3 Post-Corrosion Analysis

After the electrochemical corrosion testing, the samples were analyzed to study the corrosion mechanism of plasma-sprayed coatings. The microstructural changes in the corroded samples were analyzed by FESEM. Raman spectroscopy was also done to confirm the presence of CNT in BAG-1CNT and BAG-2CNT plasma sprayed coatings. The proposed mechanism of corrosion will be discussed in detail in Chapter no. 5.

3.7 Biocompatibility Testing of Coatings

An In-vitro cytocompatibility assay has been done to determine the coating's biomedical applicability. For this, cell adhesion, viability, and proliferation assays were performed according to standard protocols [205].

MC3T3-E1 Maintenance: It is an osteoblast precursor cell line derived from *Mus musculus* (subclone-4) were purchased from ATCC. These cells were cultured in a minimal essential media alpha (MEM-α, Gibco, USA) with 10% fetal bovine serum (FBS, Gibco Co., USA) and 2% antibiotic antimycotic solution (Himedia, India). Before usage in the experiment, cells were grown under a 5% CO₂ atmosphere at 37 °C in a cell culture incubator (Thermo Scientific, USA (Fig.3.6)) and examined following standard procedure [190,206].

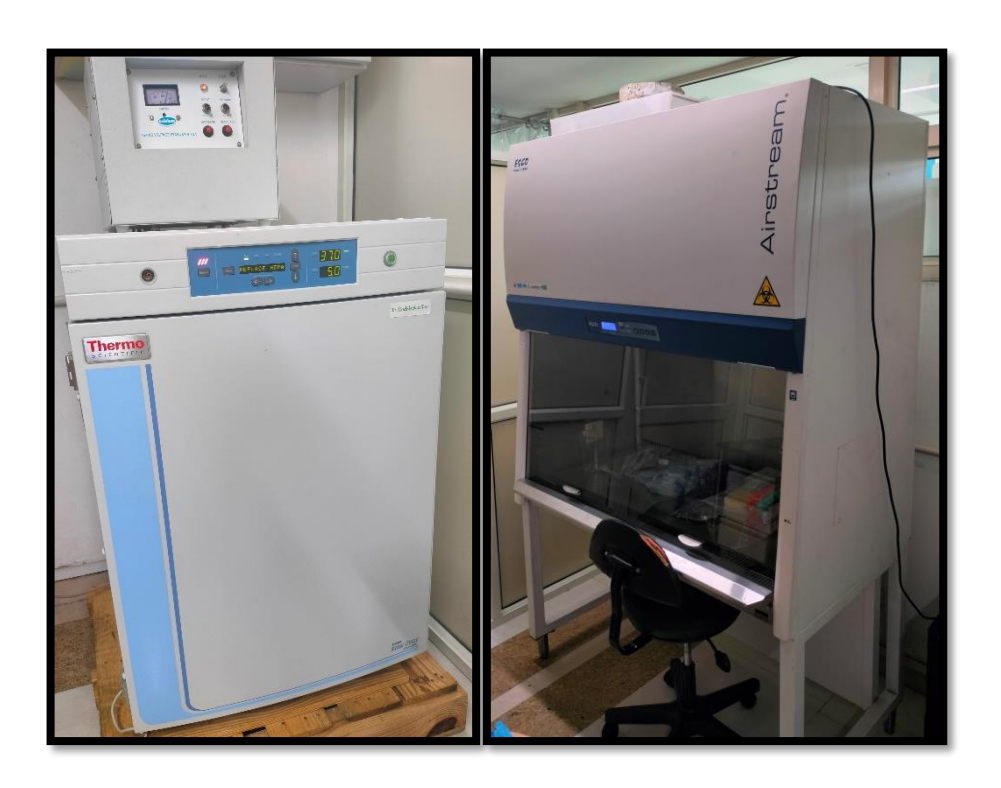


Figure 3.6 Cell culture incubator and hood used for biocompatibility tests

3.7.1 Cells Adhesion and Growth

The samples of 10 mm x 10 mm size were firstly sterilized by dipping them in 70% ethanol in 24 well cell culture plate under UV for 30 min on one side and 30 min other side [207]. Then, they were washed with phosphate buffer saline (PBS, 1X, Loba Chemie, India pH 7.4) 3 times 10 min in each. The samples were kept in a cell culture

incubator for 12 hr after soaking in MEM- α complete media. The sample was then washed once again with complete media and it was ready for cell seeding. The MC3T3-E1 suspension was formed using an earlier protocol and samples were seeded with 2 × 10 ⁴ cells/mL [208]. The culture medium was changed every 3rd day. After growth of 1, 3, and 7th days, samples were prepared for visualization in electron microscopy with slight modification to observe sample adhesion capabilities and cell morphology [209]. For this, media was discarded from the sample, washed twice with PBS, and fixed with 4% paraformaldehyde at 4 $^{\circ}$ C for 20 min. After that, samples were washed with PBS 2 times for 10 min each, gradient alcohol washed for 30 min each, and dried in a desiccator for 2 hr. Afterward, sputter coating of gold was done and the surfaces were investigated by FESEM [190,210].

3.7.2 Cell Viability and Proliferation

A quantitative method (EZCountTM MTT Cell Assay kit, Himedia) was used which is prescribed according to manufacturer protocol with slight modification to determine the cell viability and proliferation on the sample surface [211]. The samples of 10 mm × 10 mm were sterilized and incubated using the protocol described above. The samples were seeded with MC3T3-E1 suspension with 2 × 10 ⁴ cells/mL along with control (n=3). The media was changed at a specific time. At a predefined time, the 3-[4, 5-dimethylthiazol-2-yl]-2, 5-diphenyl tetrazolium bromide (MTT) solution 5 mg/mL was added to each well followed by a covered plate with aluminum foil. After incubation of 4 hr in an incubator in dark conditions, the supernatant was discarded and dimethyl sulfoxide solution (DMSO) was added to each well to dissolve formazan crystals. Strong agitation for 10 min on a plate reader, followed by a read of absorbance at 570 nm in UV-Vis Spectrophotometer (Infinite® M Plex, multimode microplate reader) was taken [190,212].

$$Cell \ Viability\% = \frac{absorbance \ of \ sample}{absorbance \ of \ control} \times 100 \tag{6}$$

3.7.3 Zr Toxicity Analysis

The plasma-sprayed BAG, BAG-1CNT and BAG-2CNT coated samples (10x10 mm size) were immersed in SBF (1mL) at 37 °C for 7 days. The normal human dermal fibroblast cell line was used to study the toxicity of Zr present in the BAG bioceramic. The cells were seeded in 96 well plate with 20000 cells/mL. The cells were kept in the

incubator (5% CO₂ and 37 °C) for 24 hrs to obtain cell confluency. The SBF extract were collected and were autoclaved to achieve sterilization. Further SBF extract with various concentrations from 10μL/mL to 150μL/mL (n=3) used to study its toxicity for 1 and 3 days. The cell morphology was analyzed using optical microscope (Life Technology-EVOS) and cell viability percentage was also calculated with quantitative method (EZCountTM MTT Cell Assay kit, Himedia).

The identification and concentration of Zr ions in SBF were also examined by XPS analysis. The plasma-sprayed BAG coated samples were immersed in SBF for 3 and 7 days. After that, the samples were removed and SBF extract was collected and drop cast on a glass slide for the XPS study. The concentration of the Zr ions was analyzed based on the weight % in the XPS analysis.

3.8 Summary of the Chapter

The above-mentioned methods and testing carried out in this research work have been summarized using a flow chart represented in Fig.3.7.

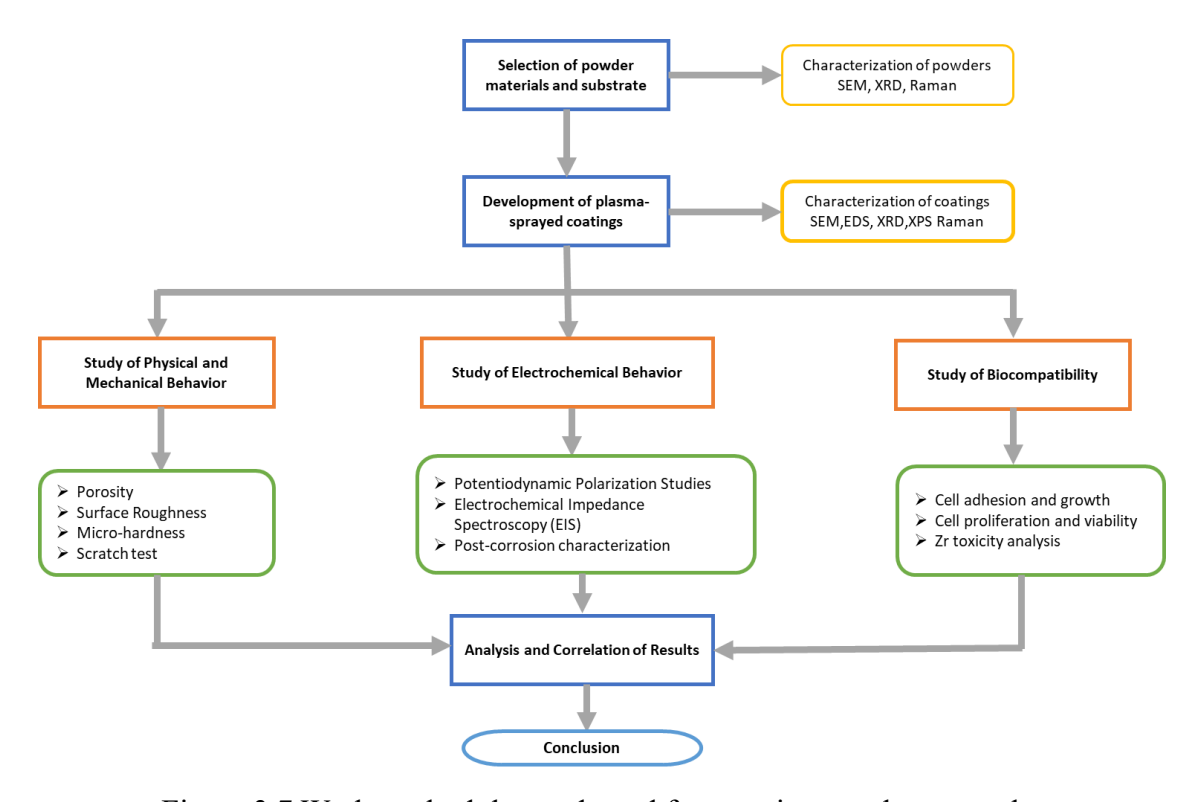


Figure 3.7 Work methodology adopted for carrying out the research

CHAPTER 4

Feedstock Powder and Coatings Characterization

4.1 Introduction

In the present chapter, the characterization of feedstock powder and coating has been discussed in detail. The microstructural features of the coatings and CNT distribution in the BAG matrix have been analyzed by field emission scanning electron microscopy (FESEM). The cross-sectional analysis of coatings along with their EDS maps have been provided and used for coating thickness measurement and porosity analysis. The x-ray diffraction (XRD) and x-ray photoelectron spectroscopy (XPS) analysis has been done for phase identification of the coatings. Raman Spectroscopy has also been done for the feedstock powders and the coatings.

4.2 Feedstock Powder Characterization

4.2.1 FESEM Analysis of Powders

The HA, BAG, and CNT were used as feedstock materials for plasma spraying. FESEM images depict the morphological characteristics of spray powders as shown in Fig.4.1. The HA powder (Fig.4.1(a)) exhibited the particle size distribution between 10 μ m and 90 μ m, showcasing a spherical shape advantageous to optimal flowability and resistance against injection blockage during plasma spraying. In contrast, BAG particles (Fig.4.1(b)) displayed an irregular shape with particle size distribution between 5 μ m and 30 μ m. Non-spherical particles have a lower tendency for elastic rebound from the substrate compared to spherical particles. Furthermore, they possess greater drag coefficient resulting in higher impact velocity and enhanced spreading mechanisms on the substrate [213]. Fig.4.1(c) represents the high magnification micrograph of CNT powder having a diameter of less than 50 nm and a length of around 40-50 μ m. The original entangled and twisted state of CNT was observed and agglomeration was absent

which may help in uniformity and stability in improvement of mechanical properties [190].

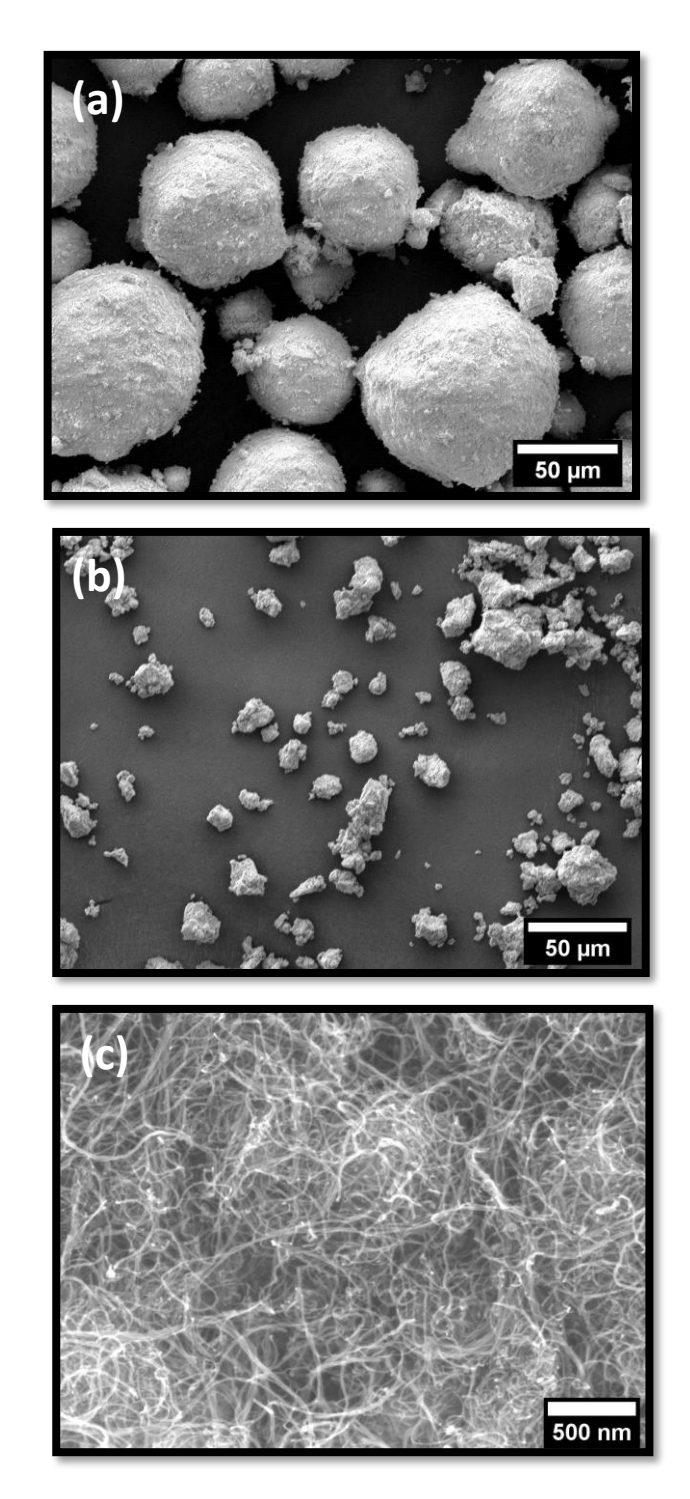


Figure 4.1 FESEM micrographs of feedstock powders (a) HA (b) BAG, and (c) CNT used for the deposition of plasma-sprayed coatings on Ti substrate [190]

The homogeneous mixing of BAG powders and CNT was achieved by the use of Alphie 3D tumbler machine. The specification and working of powder mixing machine is given

in detail in the chapter-3. The distribution of CNT in BAG-1CNT and BAG-2CNT powders after mixing is shown in Fig.4.2. The high-magnification images showed the uniform dispersion of CNT in BAG-1CNT and BAG-2CNT powders. This uniform distribution of CNT suggests the potential for enhanced mechanical properties of the resulting coatings.

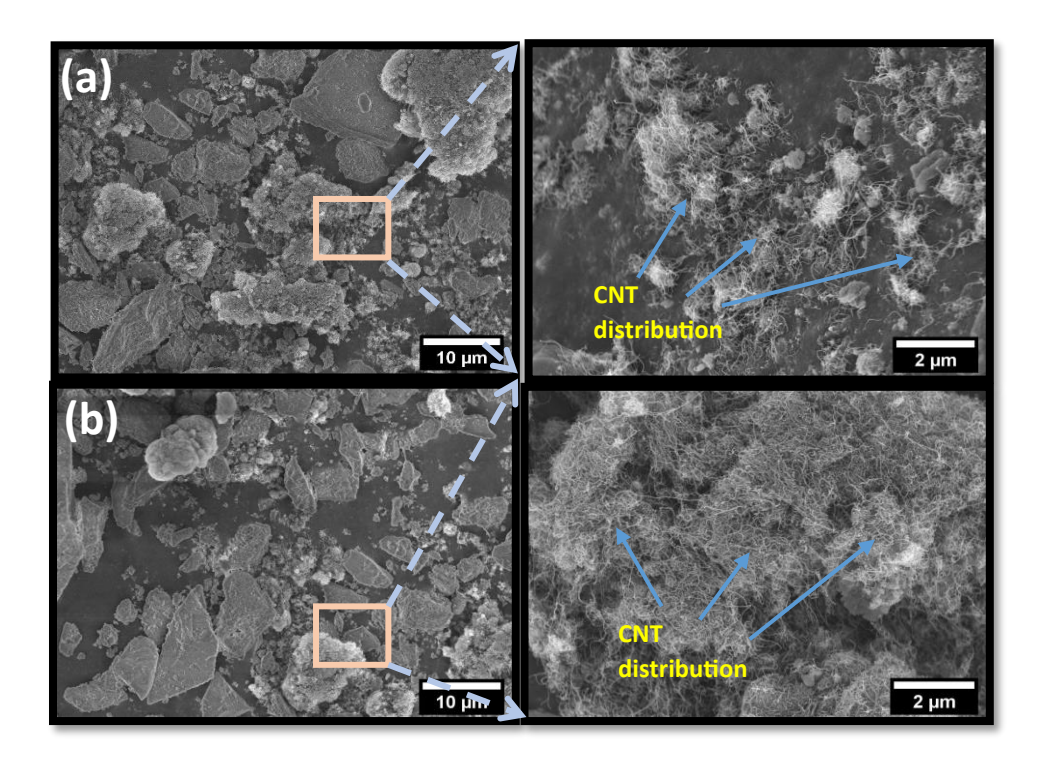


Figure 4.2 FESEM micrographs of blended (a) BAG-1CNT and (b) BAG-2CNT with high magnification images showing CNT distribution [190]

4.2.2 XRD Analysis of Powders

The XRD peaks of HA and BAG powders was analysed to study the presence of initial phases in the feedstock powders and presented in Fig. 4.3. The HA powders have all the peaks corresponding to hydroxyapatite phase which indicates the absence of other phases like tricalcium phosphate and calcium oxide. However, the BAG powders have baghdadite as the major phase along with the minor phases of calcium silicate and zirconium oxide. The presence of these minor phases depends upon the preparation methods of the BAG powders. The absence of impurities was confirmed as there was no foreign peaks detected in the XRD spectrum.

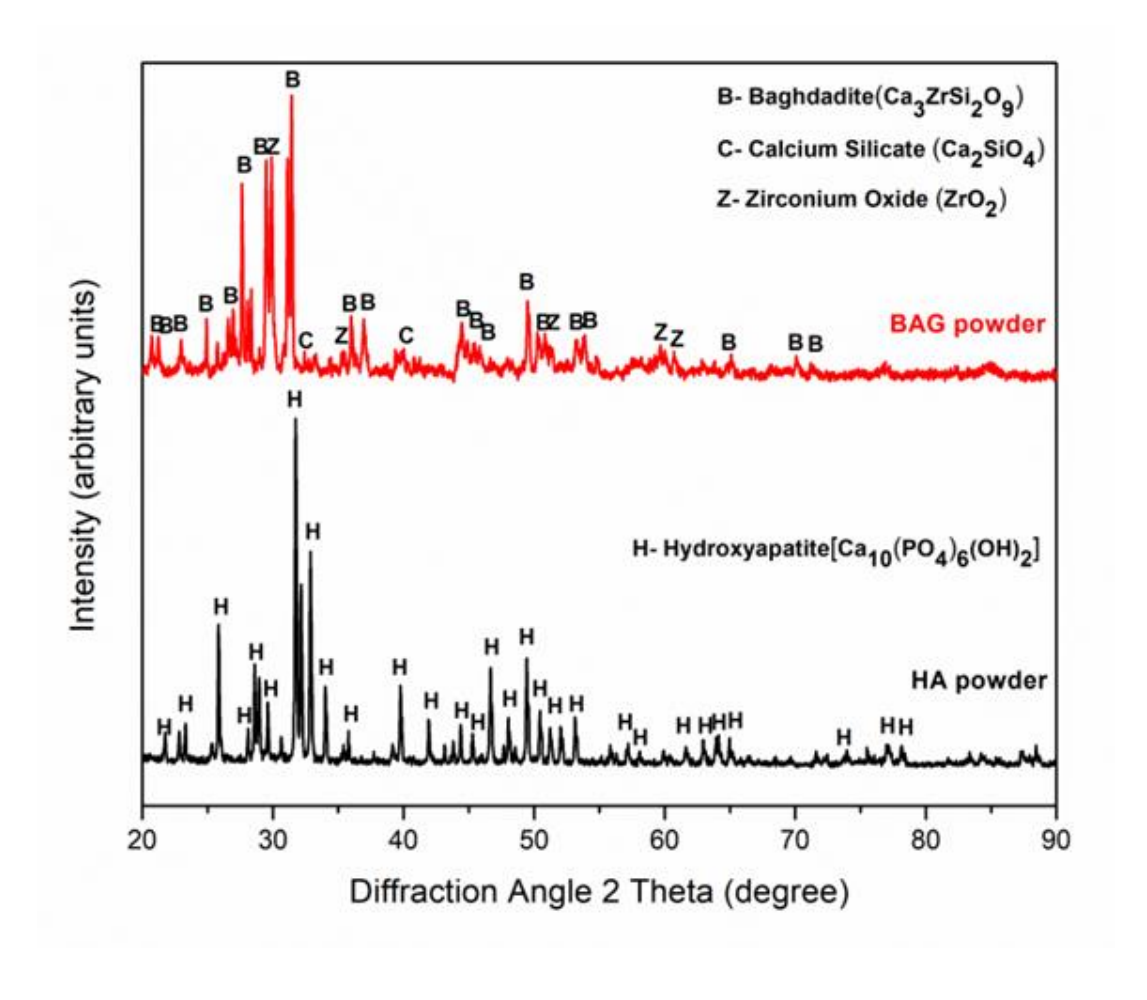


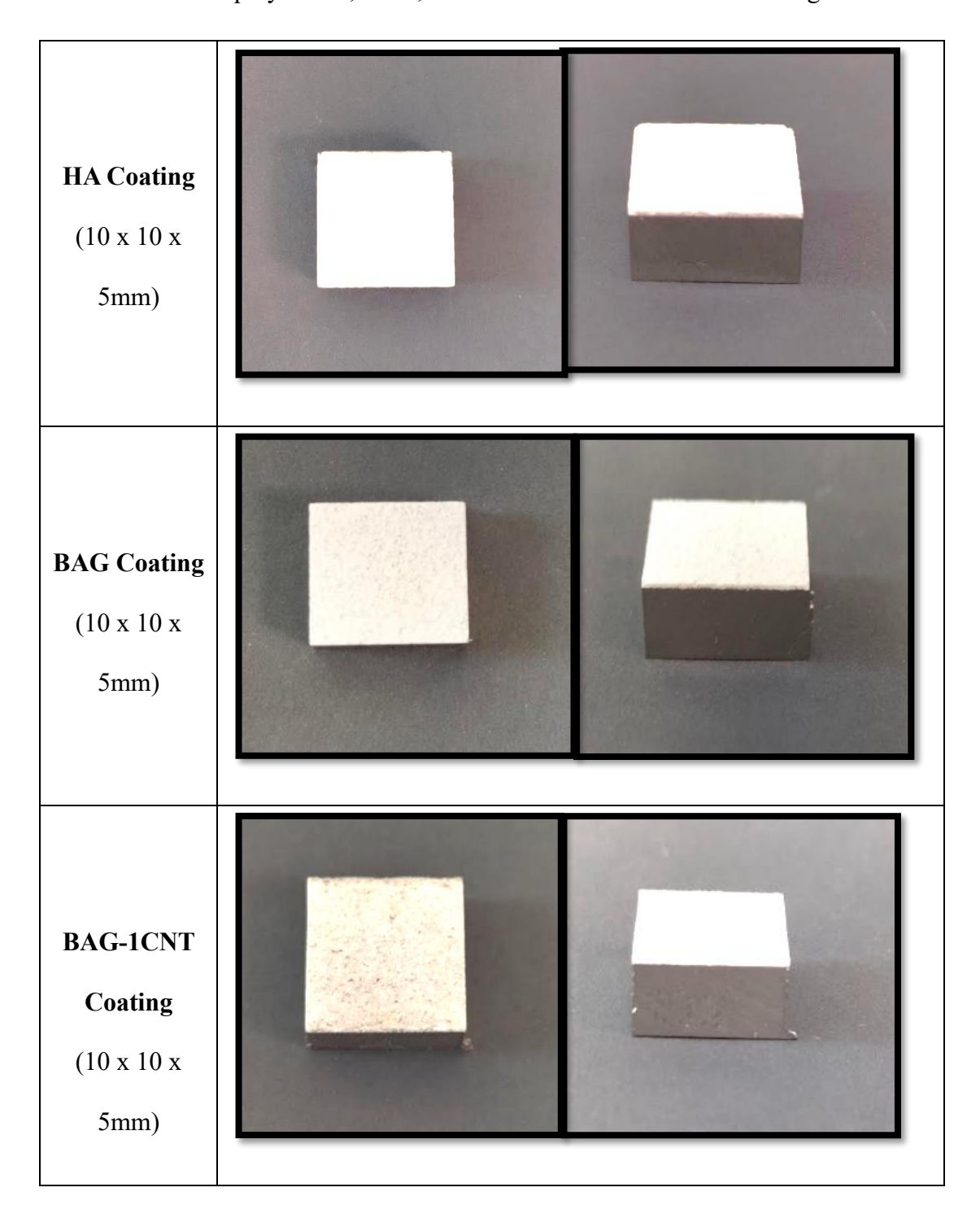
Figure 4.3 XRD analysis of HA and BAG powders used for plasma spray coatings

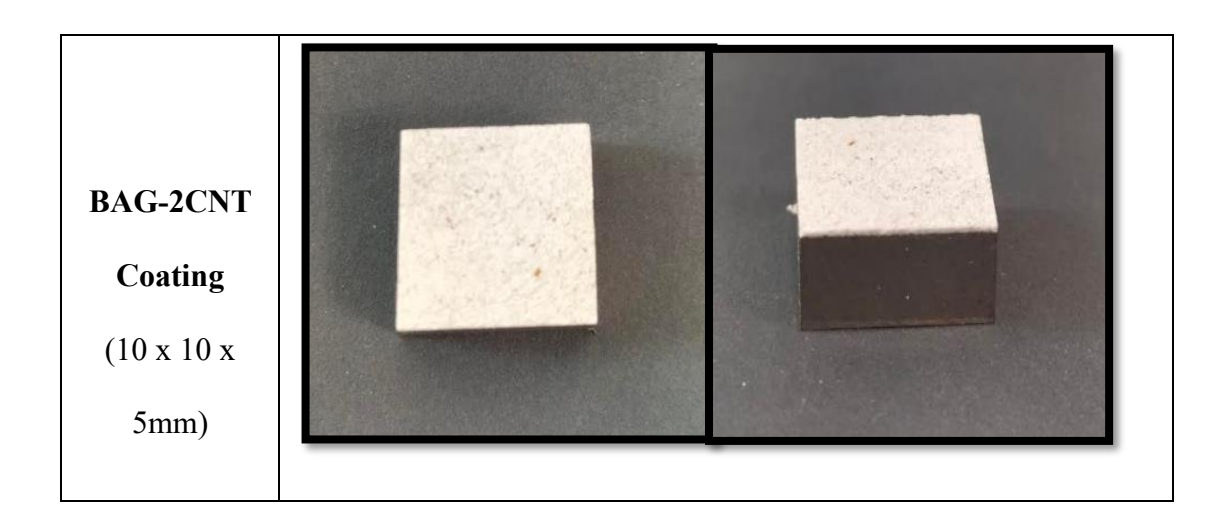
4.3 Microstructural Characterization of Coatings

4.3.1 Deposition of Coatings

The different compositions of feedstock powder- HA, BAG, BAG-1CNT and BAG-2CNT coatings was deposited using AP-2700 "mass flow controlled" plasma spray system. The details of the equipment and process parameters are given in chapter-3. Before deposition of coatings, Ti substrate was grit blasted involving the striking of alumina particles to ensure optimal adhesion strength of the coatings. The actual deposited coatings are shown in Table. 4.1. The visual examination of all the coatings indicate the coatings were thick.

Table 4.1 Plasma sprayed HA, BAG, BAG-1CNT and BAG-2CNT coatings





4.3.2 FESEM-EDS Analysis of Coatings

The surfaces of plasma-sprayed HA, BAG, BAG-1CNT and BAG-2CNT coatings on the Ti substrate are shown in Fig. 4.4. Well-formed interconnected splats are observed in the microstructure of HA and BAG coatings. The splats within BAG coatings display enhanced uniformity compared to those in HA coatings. Both HA and BAG coatings reveal the presence of voids or pores, which are less predominant in CNT-reinforced coatings. Some microcracks are observed in HA coatings which may be due to thermal contraction caused by instant cooling of splats. However, there are no microcracks detected in the other coatings as depicted by FESEM images (Fig. 4.4). The partially or unmelted particles may have spherical shapes in all the coatings.

The BAG coatings exhibit a more fully melted region as compared to HA coating. This can be attributed to the effective fusion of irregularly shaped BAG particles, leading to the formation of well-melted splats [214]. The BAG-1CNT reveals a denser and smoother microstructure as observed in SEM images (Fig. 4.4(c)). Furthermore, BAG-1CNT and BAG-2CNT coatings show uneven surfaces with fewer voids in comparison to HA and BAG coatings. The uniform dispersion of CNT in the BAG matrix can be observed from the FESEM images (Fig. 4.4 (d)) and it can be incorporated in the intersplat regions of coatings to minimize the post-plasma spray defects like microcracks and pores.

The presence of CNT is evident in BAG-2CNT coatings as reinforcement and the size of the individual splats looks bigger in this coating. The uniform distribution of CNT and formation of flake-like structure growing outwardly over the surface is observed.

The results from EDS analysis revealed that the HA coatings mainly consist of calcium (Ca), phosphorus (P), and oxygen (O) elements while the BAG coatings exhibit Ca, zirconium (Zr), silicon (Si), and O as the main elements which is similar as the feedstock powders. The EDS analysis on the surface of HA coatings has the Ca/P atomic wt% ratio as 1.80 which indicated the presence of HA or tetra calcium phosphate phase. The Ca/Si atomic wt% ratio in BAG, BAG-1CNT and BAG-2CNT coatings is 0.72, 0.93 and 0.88 respectively. The BAG coating elemental analysis shows the homogeneous distribution of Ca, Zr and Si across the surface. The presence of high atomic wt% of Zr and O can indicate the formation of ZrO₂ along with BAG phase. A small amount of C atomic wt% is also detected in the EDS elemental analysis in the CNT-reinforced BAG coatings [201].

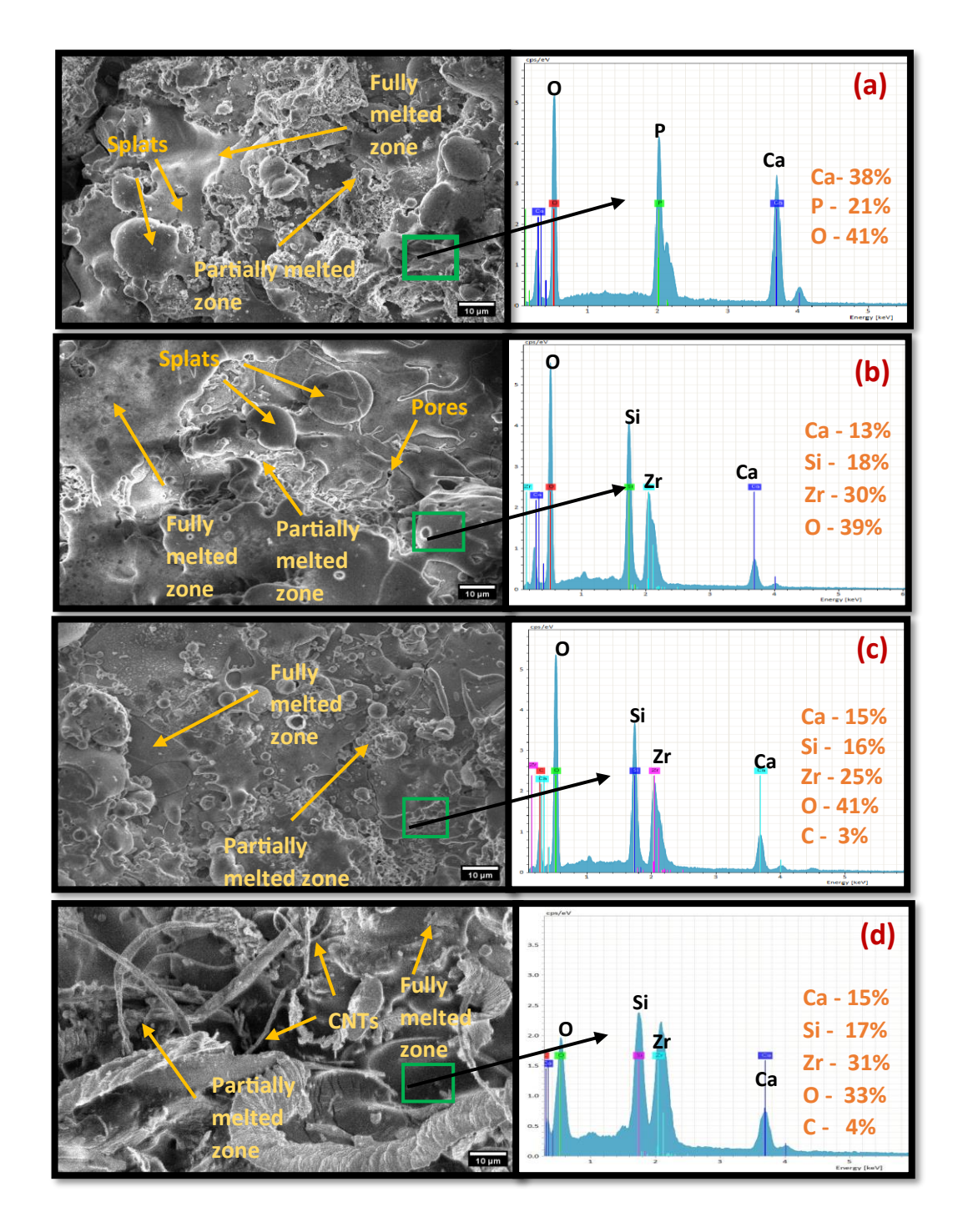


Figure 4.4 FESEM-EDS images of (a) HA (b) BAG (c) BAG-1CNT and (d) BAG-2CNT plasma sprayed coatings on Ti substrate [201]

The distribution of CNT in BAG coatings is given in Fig. 4.5 The uniform dispersion of CNT observed in FESEM images, indicates the successful resistance of CNT to withstand high temperature and impact conditions of the plasma spray process. Further, the high-magnification images show the CNT anchoring and splat bridging at various

sites in the brittle bioceramic matrix which can lead to the enhancement in the mechanical properties of the coatings [190,215].

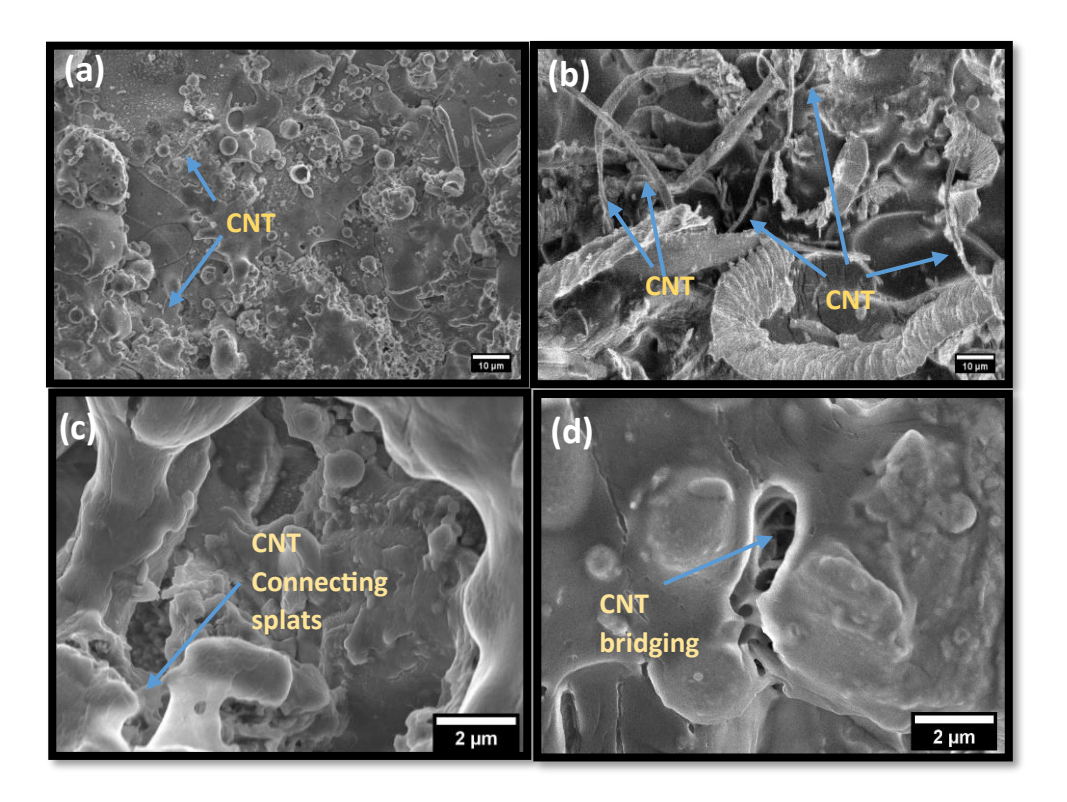


Figure 4.5 FESEM images of CNT distribution on (a) BAG-1CNT and (b) BAG-2CNT plasma sprayed coatings and magnified images showing (c) CNT connecting splats and (d) CNT bridging on the fracture surface of BAG-2CNT coatings [201]

The EDS mapping of BAG-2CNT coatings indicates the uniform distribution of Ca, Si, Zr, O, and C as shown in Fig. 4.6. The C distribution can indicate the effectiveness of mechanical mixing used for this study.

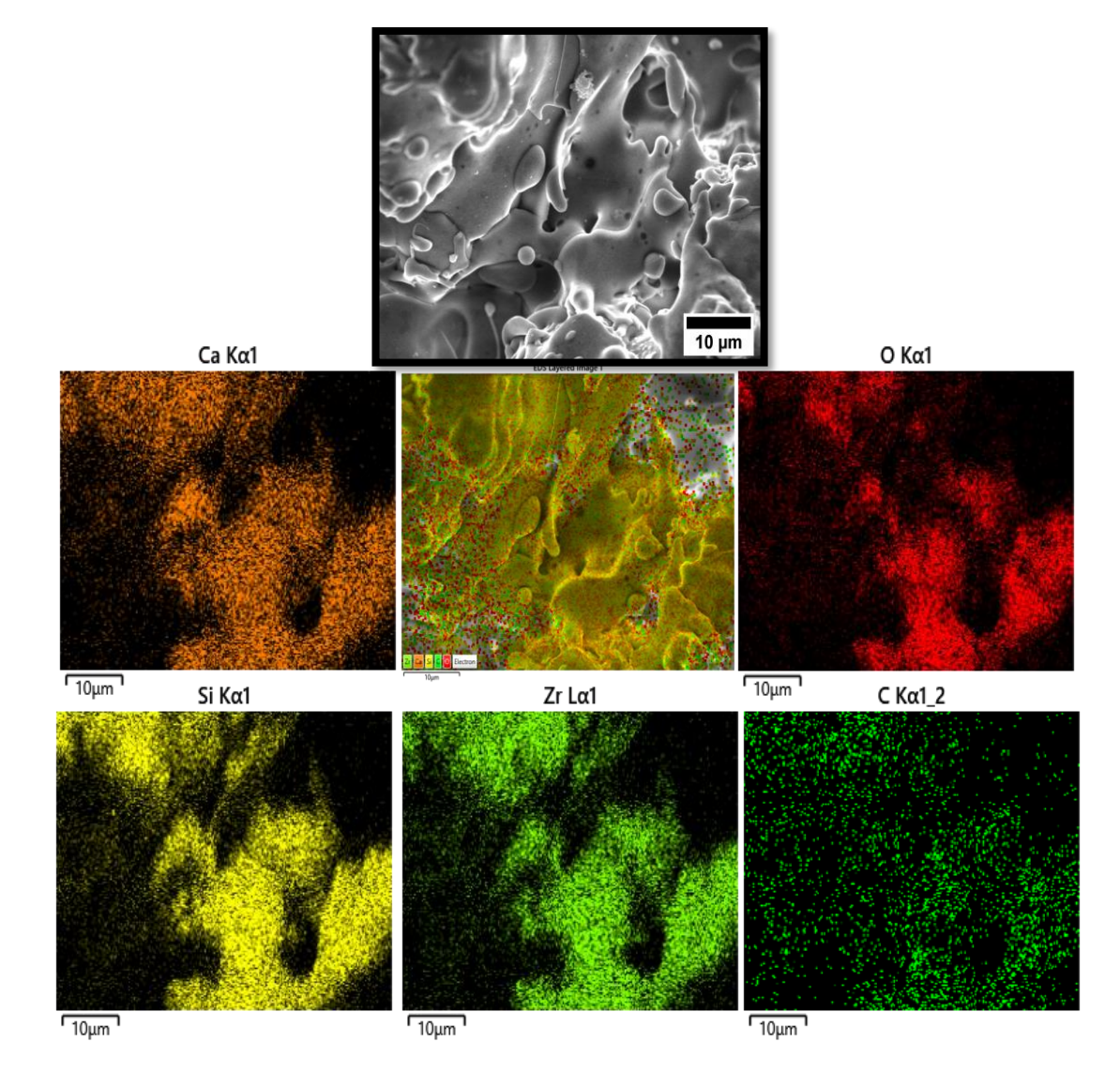


Figure 4.6 EDS mapping of plasma sprayed BAG-2CNT coatings [190]

4.3.3 XRD Analysis of Coatings

XRD data of plasma-sprayed HA, BAG, BAG-1CNT, and BAG-2CNT coatings are shown in Fig. 4.7. The crystallinity of the developed coatings is lower in comparison to their respective powder forms. This reduction in crystallinity can be attributed to the rapid heating of the feedstock powders at elevated temperatures and their subsequent rapid melting, which occurs within a short timeframe of 5-8 milliseconds between the plasma torch and the substrate. This rapid cooling process leads to the formation of splats in the plasma-sprayed coatings, ultimately resulting in the observed decrease in crystallinity [216].

HA along with minor phase tricalcium phosphate (TCP) [Ca₃(PO₄)₂] are observed from the XRD data of HA coating (Fig. 4.7). The formation of this TCP phase is a result of

heating the powders to temperatures above 1500°C. At higher temperatures, HA undergoes decomposition, resulting in the formation of TCP, tetra-calcium phosphate (TTCP, (Ca₄(PO₄)₂O)) and CaO phase. The powders contain a low concentration of CaO and TTCP, which may not attain the decomposition temperature during plasma spray. As a result, these compounds are not detected in the XRD peaks [217].

The XRD analysis of BAG coating shows the BAG as the major phase along with the minor phases of calcium silicate (Ca₂SiO₄), zirconium oxide (ZrO₂), and silicon oxide (SiO₂). The phase compositions of the CaO-SiO₂-ZrO₂ system are affected by the specific weight fractions of the starting components, primarily CaO, SiO₂, and ZrO₂ [218]. Similar phases are observed in XRD patterns of BAG-1CNT and BAG-2CNT coatings. The intensity of peaks is reduced, and no carbon phases are observed in XRD data due to the very low content of CNT.

In this study, the crystallinity values of HA and BAG powders are 82.1% and 70.4% while the HA, BAG, BAG-1CNT and BAG-2CNT coatings have crystallinity values as 65.4%, 29.3%, 23.4% and 35.2% respectively. The crystallinity level requirement of plasma sprayed coatings for orthopedic implants is 65-70% crystalline. In the present study, the crystallinity level of BAG coatings is lesser as compared to the HA coatings and this may be attributed to the more intricate crystal structure of BAG and will have more complex recrystallization. Therefore, post-heat treatment is one of the methods to increase the crystallinity [201].

The plasma spray process often results in a significant rise in the amorphous phases within coatings. This is majorly due to the rapid change in temperature of feedstock powder to the formation of splats, leading to a substantial decrease in crystallinity levels. Comparatively, BAG coatings show lower crystallinity levels compared to HA coatings. BAG coatings possess a more complex crystal structure and feature Ca-Si ceramic bonds, which require a complex recrystallization process when compared with HA coatings [201,219].

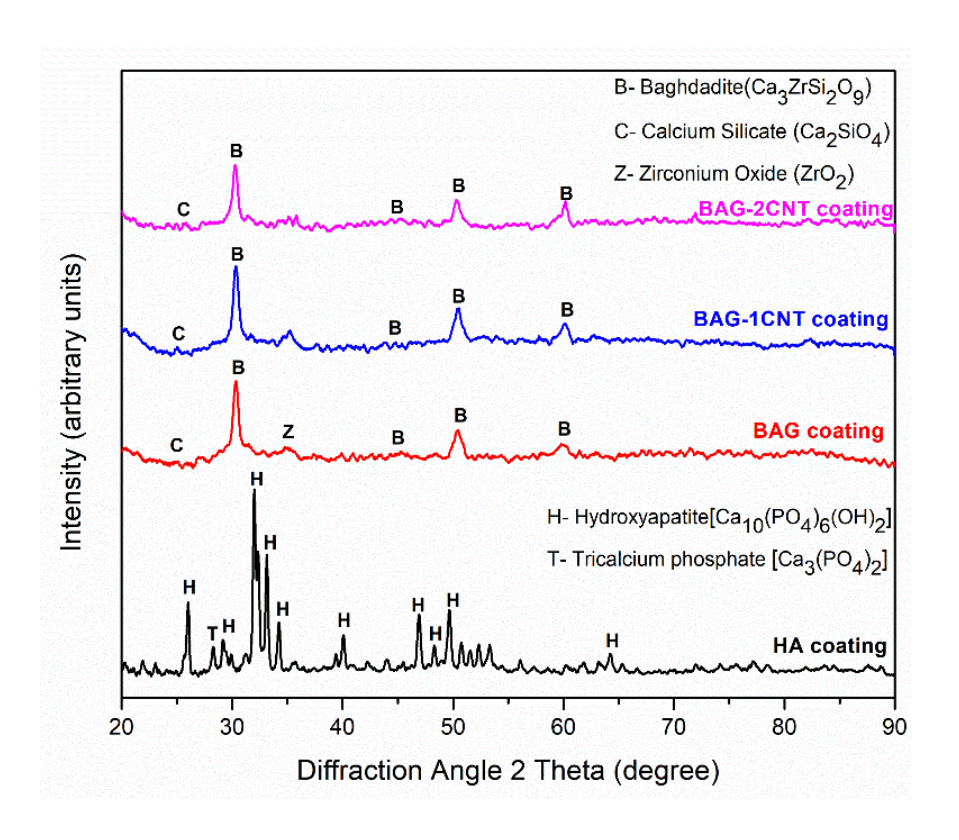


Figure 4.7 XRD peaks of HA, BAG, BAG-1CNT and BAG-2CNT plasma sprayed coatings on Ti substrate [190]

4.3.4 XPS Analysis of Coatings

The XPS spectrum of HA, BAG, BAG-1CNT, and BAG-2CNT plasma sprayed coatings was presented in Fig. 4.8. The main elements Ca, P, and O were observed in the XPS spectrum of HA coatings. The presence of tricalcium phosphate is confirmed by the atomic ratio of Ca/P, which is determined to be 1.5. The XPS plot reveals the binding energy of Ca 2p and Ca 2s to be 345.9 and 437.5 eV, respectively. Furthermore, Ca 2p represents a doublet of Ca 2p3/2 and Ca 2p1/2, and the presence of CaO is indicated by Ca2p3/2. The P 2p, O 1s, and O 2s peaks are observed at a binding energy of 131.9, 530.1, and 25.3 eV, respectively. The PO₄³⁻ and metal oxides presence is confirmed by the binding energy of P and oxygen, respectively [220].

The primary elements of BAG, namely Ca, Si, Zr, and O are observed in the XPS spectrum. The high-resolution scans reveal specific peaks of Zr at 180.8 and 181.7 eV, and for Si at 101.3 and 102.3 eV. The formation of ZrO_2 on the coating surface is confirmed by the binding energy of Zr, while the formation of orthosilicate (SiO_4^-) and pyrosilicate ($Si_2O_7^{6-}$) is confirmed by the binding energy of Si. These are characteristic functional groups of BAG and calcium silicate (Ca_2SiO_4) [220]. Therefore, the different

phases of BAG are confirmed by the XPS technique. The BAG-1CNT and BAG-2CNT exhibit peaks corresponding to different phases of BAG, with the intensity of C 1s is higher compared to BAG.

The XPS spectrum of HA, BAG, BAG-1CNT, and BAG-2CNT plasma sprayed coatings was presented in Fig. 4.8. The main elements Ca, P, and O were observed in the XPS spectrum of HA coatings. The presence of tricalcium phosphate is confirmed by the atomic ratio of Ca/P, which is determined to be 1.5. The XPS plot reveals the binding energy of Ca 2p and Ca 2s to be 345.9 and 437.5 eV, respectively. Furthermore, Ca 2p represents a doublet of Ca 2p3/2 and Ca 2p1/2, and the presence of CaO is indicated by Ca2p3/2. The P 2p, O 1s, and O 2s peaks are observed at a binding energy of 131.9, 530.1, and 25.3 eV, respectively. The PO₄³⁻ and metal oxides presence is confirmed by the binding energy of P and oxygen, respectively [220].

The primary elements of BAG, namely Ca, Si, Zr, and O are observed in the XPS spectrum. The high-resolution scans reveal specific peaks of Zr at 180.8 and 181.7 eV, and for Si at 101.3 and 102.3 eV. The formation of ZrO₂ on the coating surface is confirmed by the binding energy of Zr, while the formation of orthosilicate (SiO₄-) and pyrosilicate (Si₂O₇⁶-) is confirmed by the binding energy of Si. These are characteristic functional groups of BAG and calcium silicate (Ca₂SiO₄) [220]. Therefore, the different phases of BAG are confirmed by XPS technique. The BAG-1CNT and BAG-2CNT exhibit peaks corresponding to different phases of BAG, with the intensity of C 1s is higher compared to BAG [190].

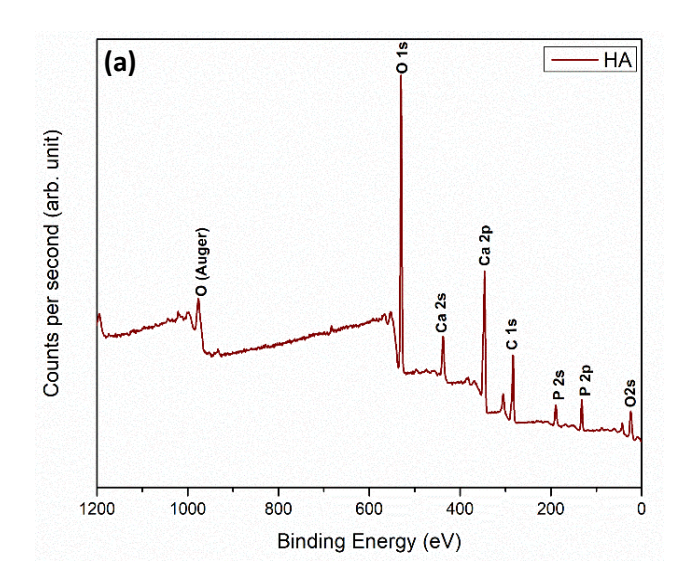


Figure 4.8 (a) XPS peaks of HA plasma sprayed coatings on Ti substrate

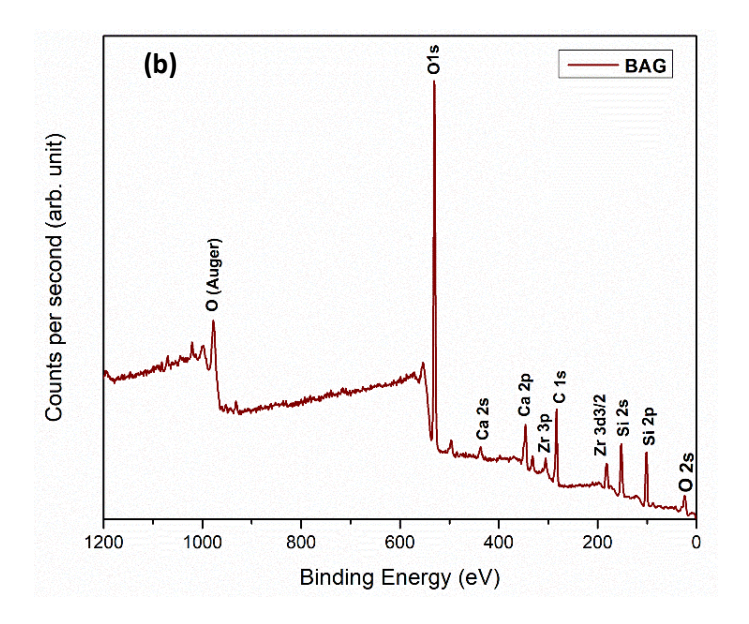


Figure 4.8 (b) XPS peaks of BAG plasma sprayed coatings on Ti substrate

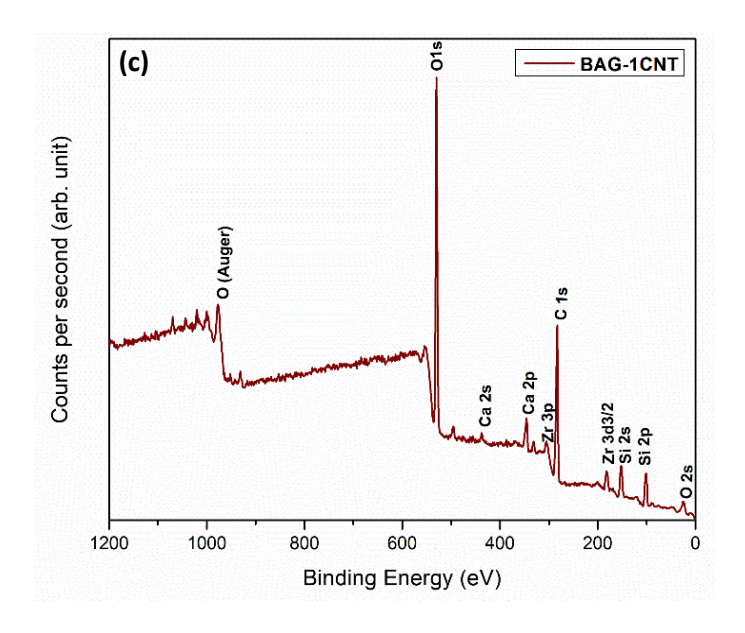


Figure 4.8 (c) XPS peaks of BAG-1CNT plasma sprayed coatings on Ti substrate

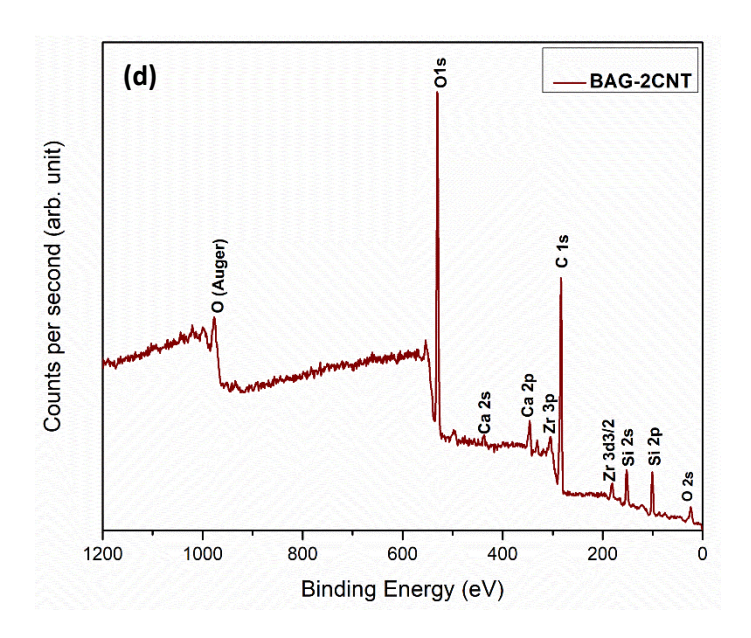


Figure 4.8 (d) XPS peaks of BAG-2CNT plasma sprayed coatings on Ti substrate [190]

4.3.5 Raman Spectroscopy Analysis

The Raman spectrum of HA and BAG in both powder and coating forms are shown in Fig. 4.9. It clearly indicates that the peak intensities of coatings are much less and wider as compared to their respective powders. Apart from that, the BAG coating peak intensities are much less than HA coatings. The powders and coatings have slight variations in the Raman shift as shown in Fig. 4.9. This is attributed to the change in crystallinity and sudden cooling during the plasma spray process. The manufacturing processes of powders can influence their crystalline structure and result in a change in Raman shifts of powders used for coating development [221]. The contamination in the powder manufacturing process can cause additional peaks at 892cm⁻¹ and 1035cm⁻¹ in BAG powders. No evidence of a new phase formation is observed in HA coating.

The HA powder and coating have a dominant vibration of PO₄³⁻. The Raman spectrum shows a strong peak at 962cm⁻¹ which is the symmetric stretching mode of P-O bond in PO₄³⁻ group. The other peaks in HA powders are two peaks at 432cm⁻¹ for double degenerate O-P-O bending mode, three peaks at 588cm⁻¹ for triply degenerate O-P-O bending mode, and three peaks at 1050 cm⁻¹ representing the triply degenerate and triply asymmetric P-O stretching mode. The peak at 3572cm⁻¹ is observed in HA powder indicating the presence of O-H stretching mode of OH⁻ group resulting in the formation of Ca(OH)₂ from the CaO phase [222].

The BAG powder and coating exhibit vibration, bending, rotation, and stretching groups, indicating the presence of all the functional groups of BAG [221]. The vibration is due to the Si-O-Zr group while the groups of Si-O-Si, O-Si-O, Si-O-Zr, O-Zr-O, and Zr-O-Zr represent the bending group. The rotational group is represented by SiO₄ tetrahedral group. The stretching groups are observed as symmetric and anti-symmetric stretching. The symmetric stretching functional groups are the Zr-O(Zr), Si-O(Si), Si-O(Zr), and Si-O(Ca) while the Si-O(Ca) represents both symmetric and anti-symmetric functional states. The high-intensity peaks present at 624cm⁻¹ are observed in BAG powders and 630cm⁻¹ in BAG coatings representing Zr-O-Zr bending mode. The symmetric stretching of Si-O-(Zr) at 945cm⁻¹ and 947cm⁻¹ in BAG powder and coating and Zr-O-(Zr) at 669cm⁻¹ only in BAG powders [221].

The Raman spectra of BAG-1CNT and BAG-2CNT coatings clearly identify the retention of CNT after the rigorous high-temperature plasma spray process for a short time interval. The distinct D, G, and 2D bands of CNT are observed in both coatings. However, the presence of an intense D band at 1350cm⁻¹ indicates the disordered or flattened CNT which is associated with the amount of sp³ hybridized phonon scattering sites in CNT. It may also be due to the difference in temperature of the plasma plume and substrate, causing an instant quenching of CNT. The G band was also present at 1580cm⁻¹ which is associated with sp² bonded carbon atoms tangential lattice vibrations. The presence of CNT reinforced in BAG plasma-sprayed coatings can be confirmed by the intense G band [223]. A small intensity 2D band is also observed at 2670cm⁻¹ due to two phonon vibration processes and it does not constitute any defects [201,224].

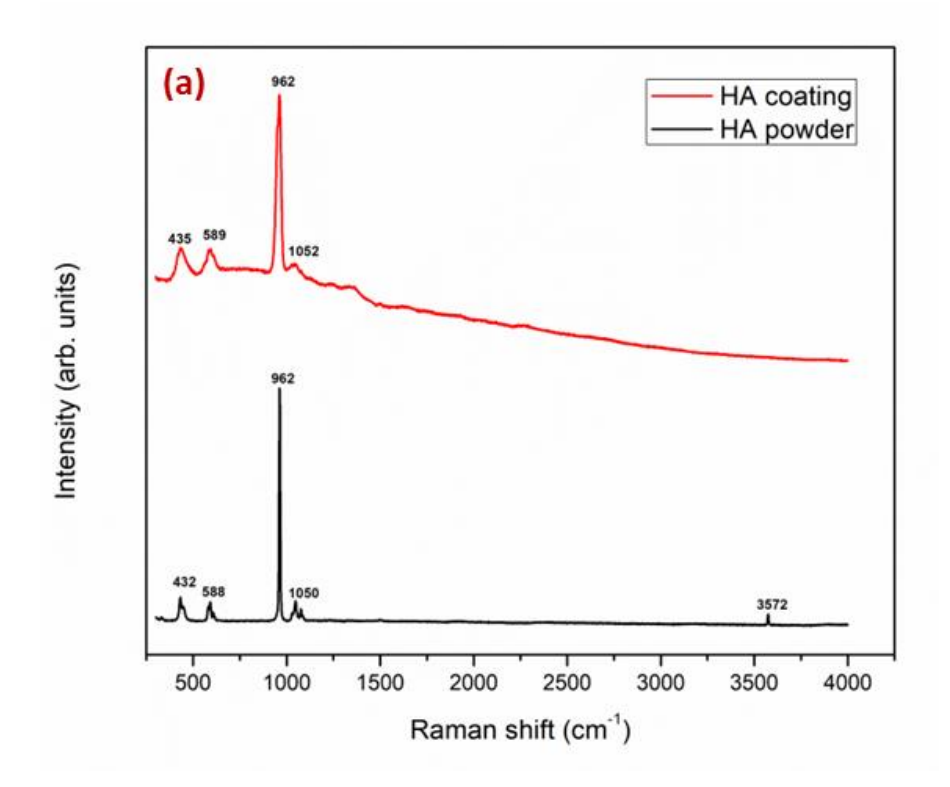


Figure 4.9 (a). Raman spectroscopy of HA powder and coating on Ti substrates [201]

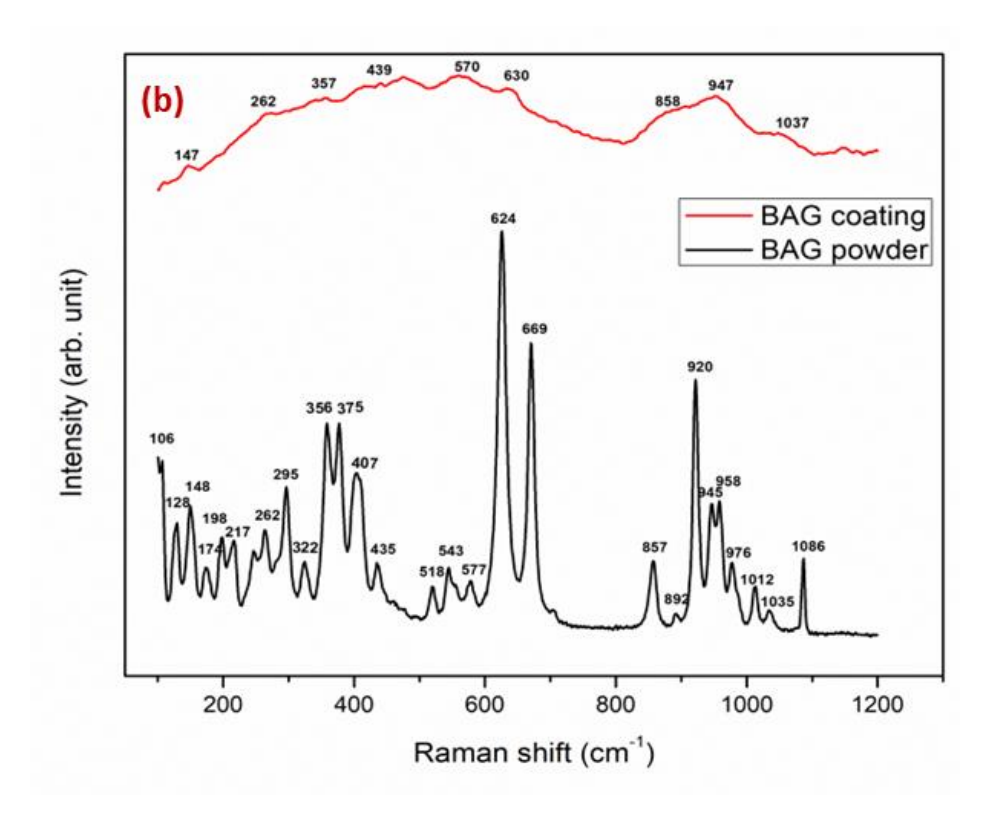


Figure 4.9 (b). Raman spectroscopy of BAG powder and coating on Ti substrates [201]

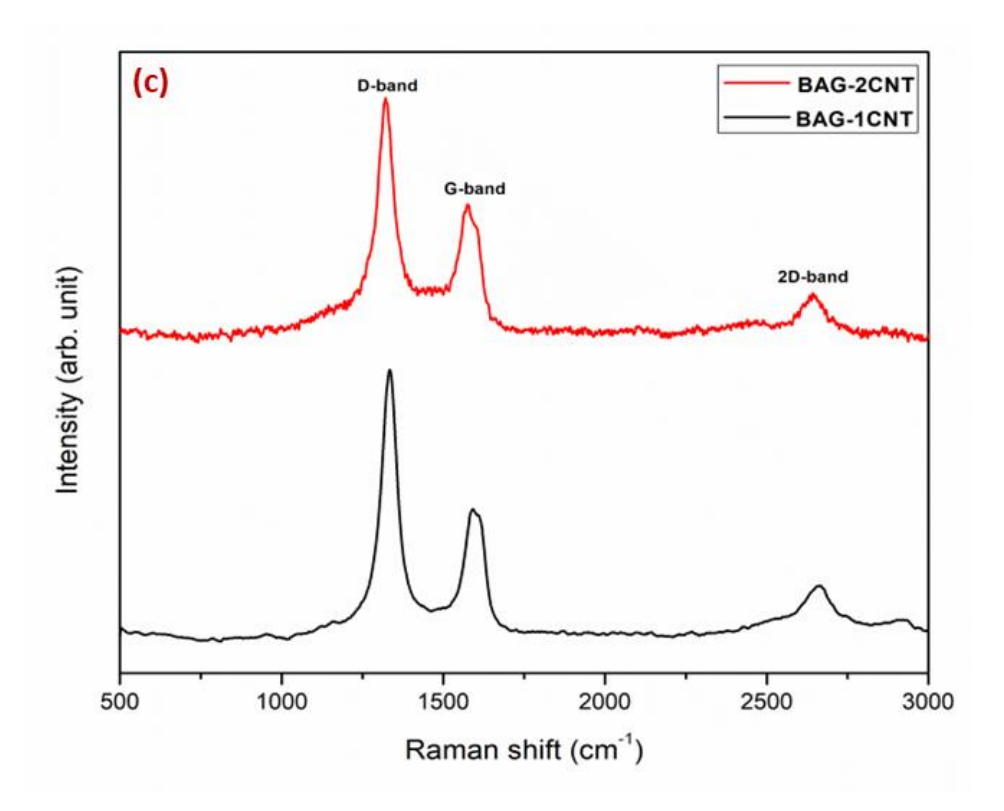


Figure 4.9 (c). Raman spectroscopy of BAG-1CNT and BAG-2CNT coating on Ti substrates [201]

4.3.6 Cross-sectional Analysis of Coatings

The polished cross-sectional view of plasma-sprayed HA, BAG, BAG-1CNT, and BAG-2CNT are shown in Fig. 4.10. FESEM cross-sectional images reveal several typical characteristics of plasma-sprayed coatings. These include the presence of lamellar structures containing pores and microcracks [225]. All the coatings contain some unmelted particles which can be clearly seen in high magnification images (Fig. 4.10). The fully molten particles can also be observed (Fig. 4.10), which may act as a binder between unmelted particles and result in good cohesion of the coatings. The sudden cooling of splats in plasma spray may cause thermal contraction and can be seen as microcracks. BAG coatings have less average particle size but the variation the particle size in HA and BAG is broader, consisting of particles of varying sizes from fine to relatively course. During the plasma spraying process, particles of different sizes can melt and solidify at different rates. This variation in size of HA and BAG particles lead to non-uniform cooling and solidification within the coating, which may introduce thermal stresses. Fine particles may cool and solidify more rapidly than coarse ones, leading to differential shrinkage and the formation of microcracks. The lesser size

distribution in the BAG leads to more consistent melting, solidification, and cooling, resulting in a more uniform coating with fewer internal stresses and, results in fewer microcracks. Larger particles of HA may create stress concentrations at the interfaces with smaller particles, where microcracks are more likely to initiate. These microcracks affects the mechanical properties of the coatings, potentially compromising their performance in biomedical applications [176]. The microcracks are bigger in size in HA coating as compared to BAG coating and it may be because of the difference in cooling rate of particles of different sizes and morphology of HA and BAG powders. Some unmelted particles are seen in FESEM images (Fig. 4.10) of CNT-reinforced coatings but the fully melted region is more predominant. It may be because of the higher thermal conductivity of the CNT leading to an increase in heat transfer rate. For instance, Jambagi et al. prepared the plasma-sprayed ceramic coatings with the incorporation of the CNT and reported the enhancement of coating cohesion. Moreover, CNT was found to bridge the splats due to high thermal conductivity and uniform heat transfer [226]. The heat capacity of molten feedstock was found to increase due to the presence of CNT and it ensured the proper melting of the powders. The well-molten feedstock also ensured a decrease in the porosity [201,226].

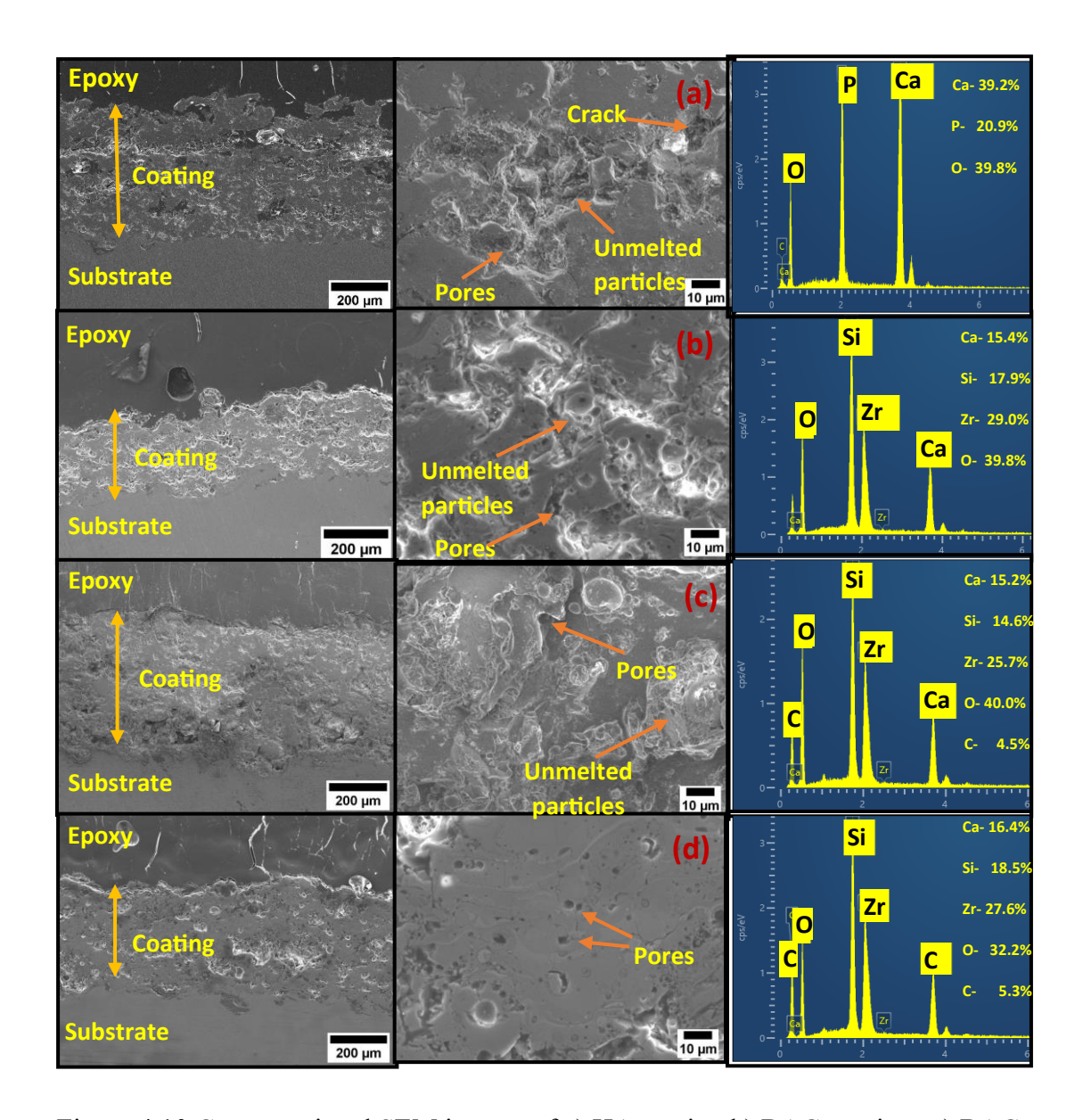


Figure 4.10 Cross-sectional SEM images of a) HA coating b) BAG coatings c) BAG-1CNT d) BAG-2CNT along with magnified images (middle) and their EDS analysis respectively [201]

The cross-sectional EDS mapping of all the investigated coatings is shown in Fig. 4.11. The mappings reveal the presence of Ca, P, O and Ca, Zr, Si, O as the main elements in HA and BAG coatings respectively. The homogeneous distribution of Ca, Zr, and Si is observed in all the BAG coatings. The presence of any foreign elements is not observed in all of the investigated coatings [201].

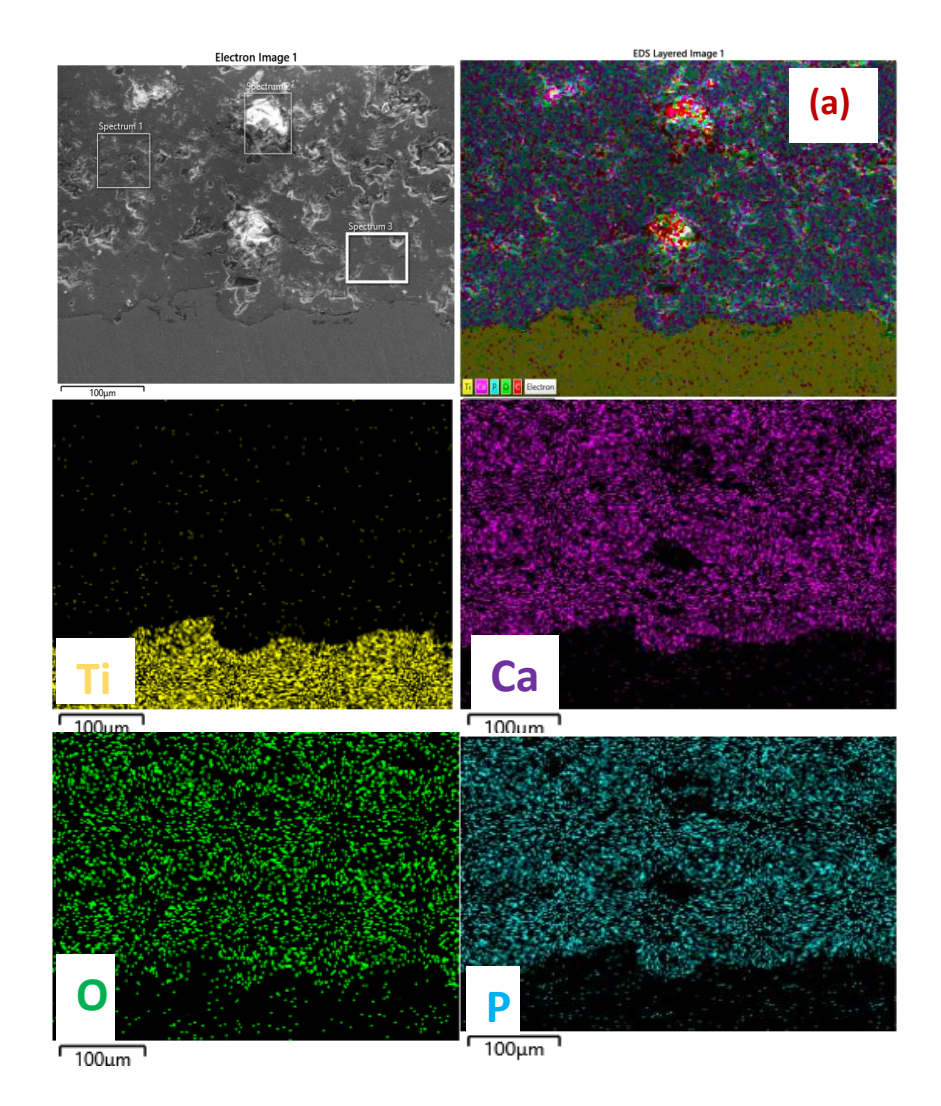


Figure 4.11 (a) Cross-sectional EDS mappings of plasma-sprayed HA coating on Ti substrate [201]

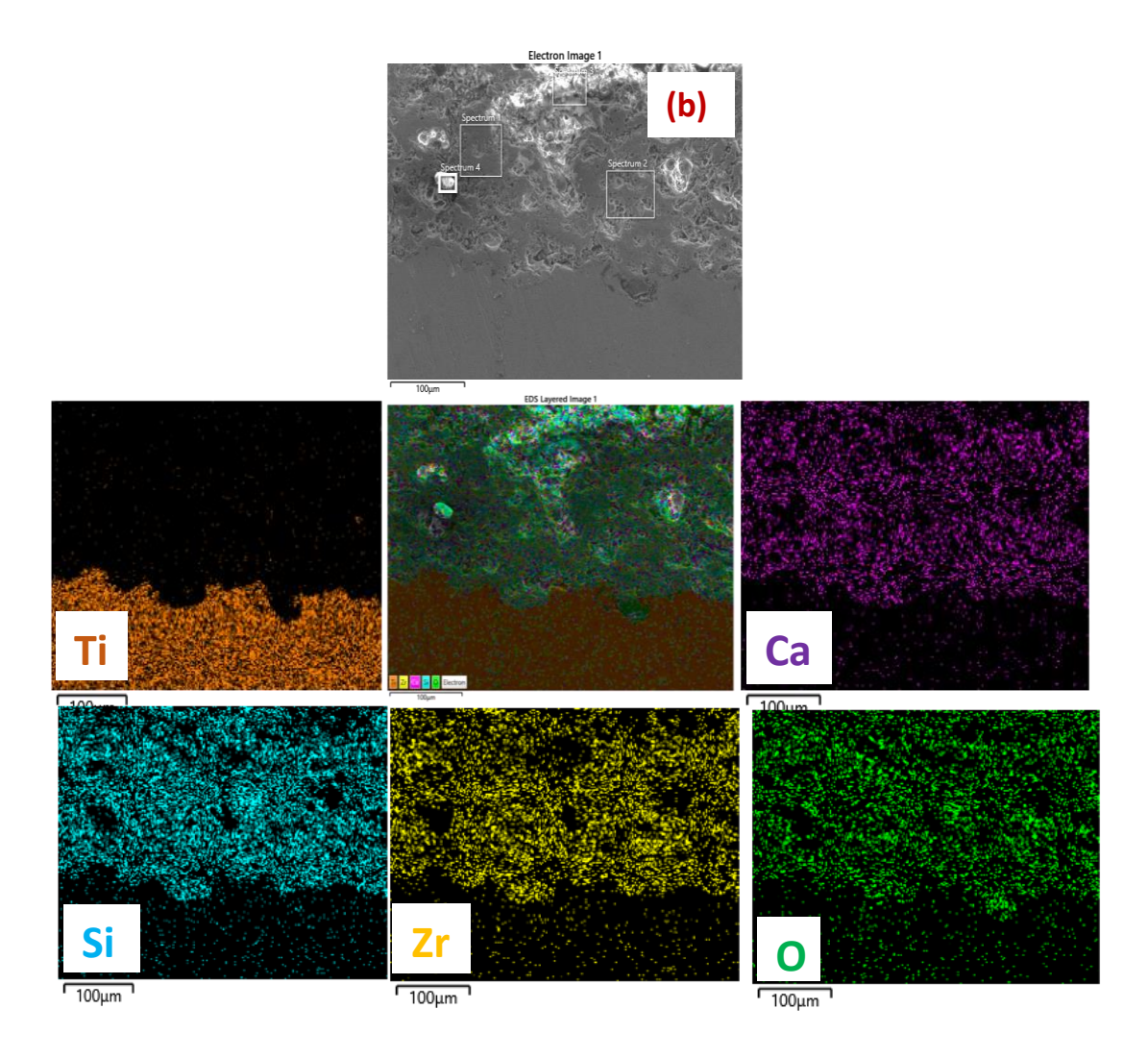


Figure 4.11 (b) Cross-sectional EDS mappings of plasma-sprayed BAG coating on Ti substrate [201]

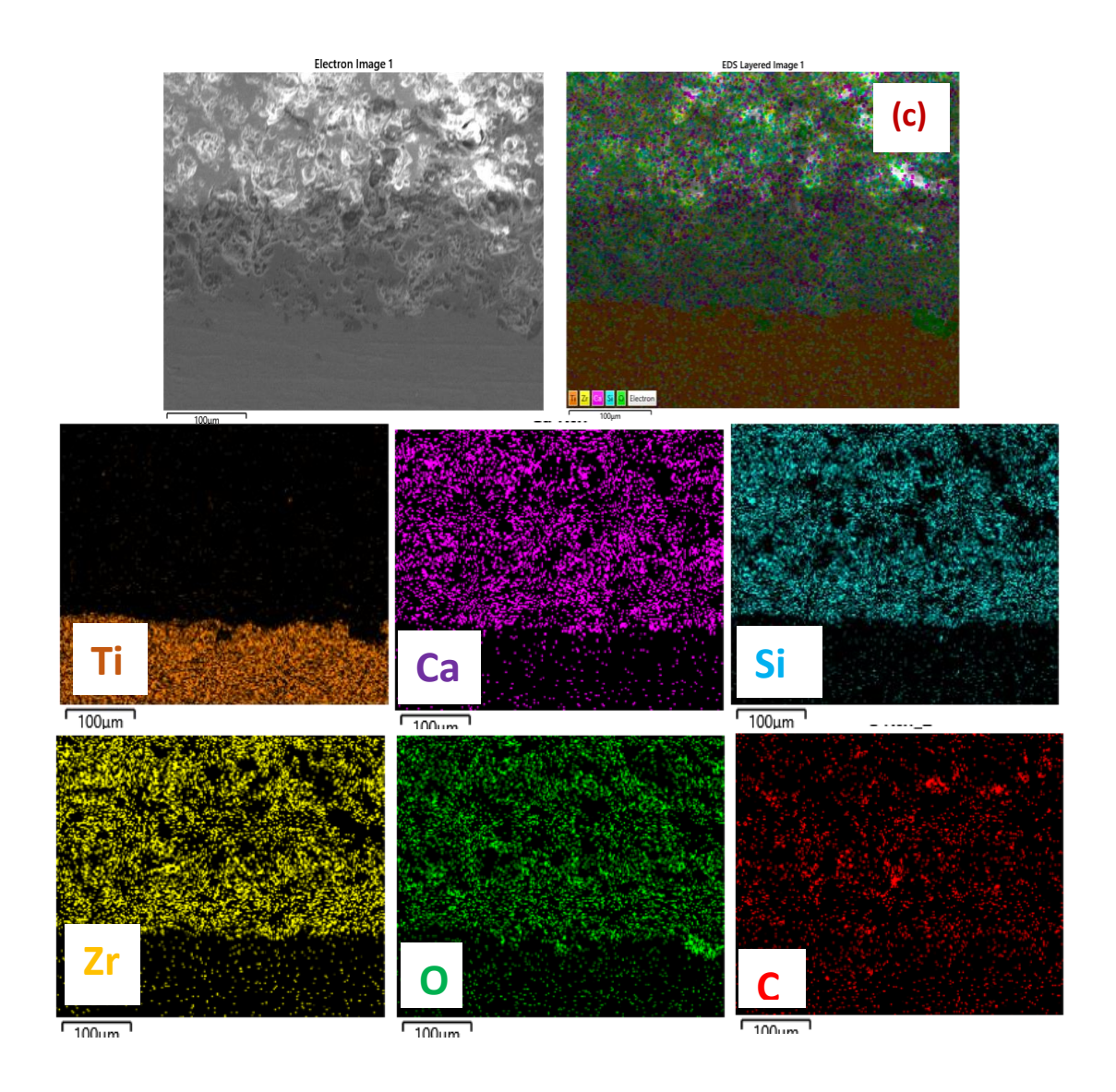


Figure 4.11 (c) Cross-sectional EDS mappings of plasma-sprayed BAG-1CNT coating on Ti substrate [201]

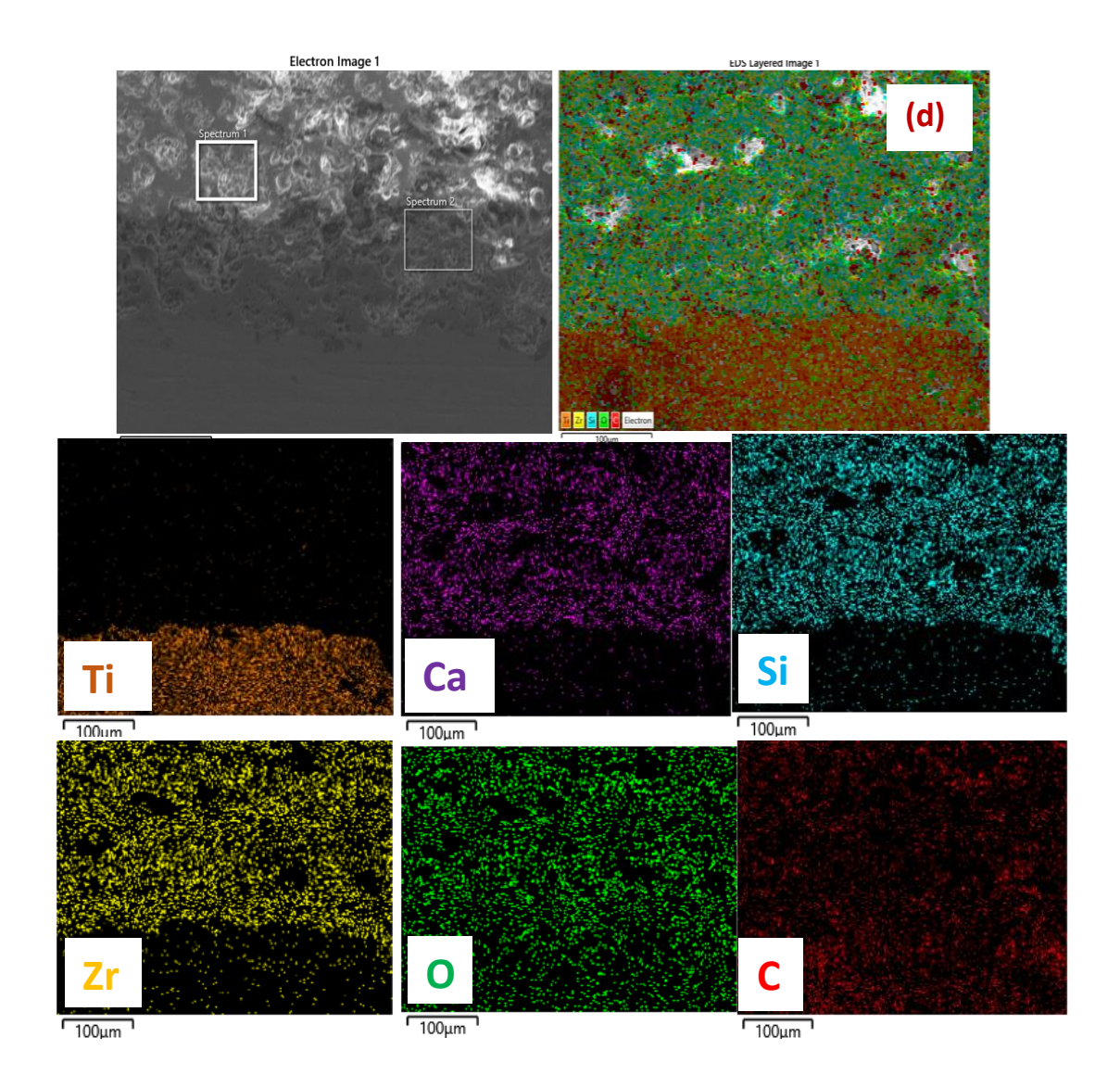


Figure 4.11 (d) Cross-sectional EDS mappings of plasma-sprayed BAG-2CNT coating on Ti substrate [201]

4.4 Coating Thickness Measurement

The FESEM cross-sectional images were used to calculate the thickness of the coatings. All the coatings have thickness in the range of 350-450 µm and is given in Table 4.2. Thick coatings increase implant stability by a long-lasting biological effect. Large-scale bone regeneration requirement is not sufficiently sustained by thin coatings. Hence, thick coatings are needed to stimulate bone regeneration over longer times. Clinical evidence has shown that thin HA coatings have lesser chances of survival than thick coatings [227]. Therefore, the coating thickness plays an important role in biological applications [201].

Table 4.2 Plasma-sprayed HA, BAG, BAG-1CNT, and BAG-2CNT coating thickness values [201].

Sr. no.	Coating type	Thickness of coatings (in µm)
1.	НА	420 ± 20
2.	BAG	340 ± 10
3.	BAG-1CNT	390 ± 15
4.	BAG-2CNT	375 ± 15

4.5 Porosity Analysis of Coatings

ImageJ, an imaging software was used to calculate the porosity of the coatings. The apparent porosity of HA, BAG, BAG-1CNT, and BAG-2CNT coatings is 5.94%, 6.77%, 3.67%, and 2.34% respectively as shown in Fig. 4.12. The BAG coating has more porosity value as compared to HA. The melting point of BAG is around 1450 °C which is slightly lower than that of HA with 1670 °C. However, the lower melting temperature may not always result in the better melting during plasma spray. The other factors like thermal properties of BAG including thermal conductivity and specific capacity, might lead to less efficient heat absorption and retention during spraying, which result in the higher porosity. Further, BAG has more complex phase composition and phase stability than HA. During the sudden cooling process after plasm spray, BAG might undergo phase transformation and formation of amorphous phases can contribute to porosity.

However, the porosity decreased with the addition of CNT reinforcement in the BAG coatings. The pores develop at intersplat contact due to the fast solidification of lamellae and fragmentation of molten splats occurs. The reduction in the porosity with CNT reinforcement can be attributed to the ability of CNT to infiltrate the inter-lamellar spaces and fill the gaps at the intersplat region. The well-distribution of CNT within the coating is important for achieving a reduction in porosity. Another contributing factor is the high thermal conductivity of CNT, which can help in instant and steady heat transfer from plasma plume to BAG matrix and increase the number of particles melting. The CNT have a high thermal conductivity of 3000-3500 W/mK. The addition of 1-2% CNT could potentially enhance the thermal conductivity of the composite

coating. This improved thermal conductivity can lead to more efficient heat distribution during the plasma spraying process, promoting more uniform melting and solidification of the BAG matrix. Hence, it leads to the reduction in the porosity values and improving coating integrity [201].

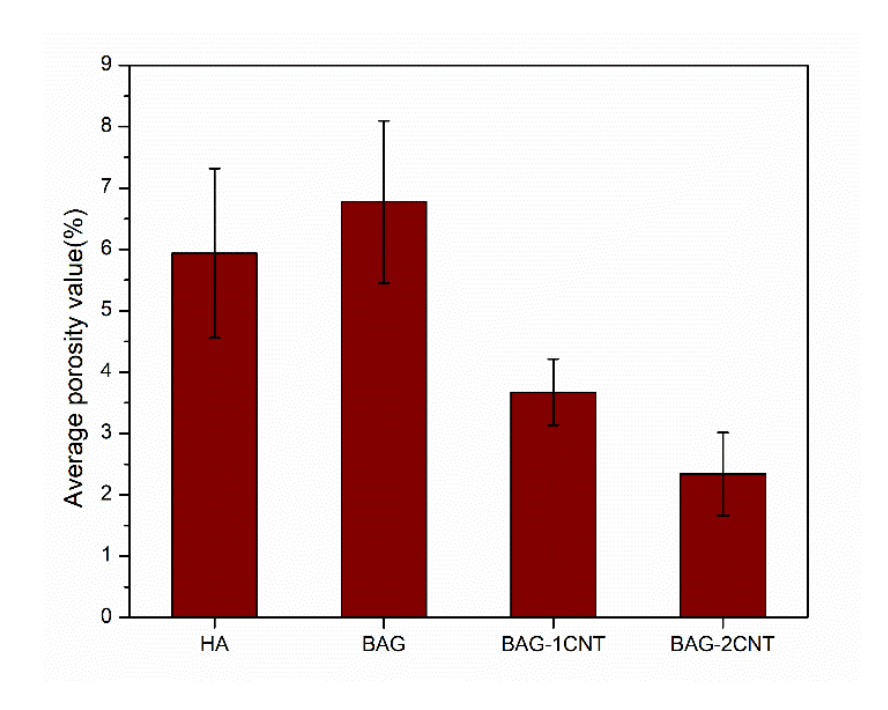


Figure 4.12 Porosity analysis of plasma-sprayed HA, BAG, BAG-1CNT, and BAG-2CNT plasma sprayed coatings on Ti substrates [201]

4.6 Summary of the Chapter

The plasma-sprayed HA, BAG, BAG-1CNT, and BAG-2CNT coatings have been successfully deposited on the Ti substrate. The surface FESEM analysis of the coatings indicated the presence of micropores, partially melted, and fully melted zones. The EDS spectrum showed the Ca, P, and O elements in the HA coating while the Ca, Zr, Si, and O elements were in the BAG coatings. The uniform distribution of CNT was observed in the CNT-reinforced BAG coatings. The XRD analysis indicated the drop in crystallinity in the plasma spray coatings to their respective powders. HA coatings have a major phase as hydroxyapatite along with a minor phase of TCP while the BAG coatings have baghdadite as the major phase along with the minor phases of Ca₂SiO₄, ZrO₂, and SiO₂. These minor phases present in HA and BAG coatings were also confirmed in the XPS analysis. However, the presence of CaO and phosphate oxides in small quantities was also indicated by peaks of the XPS spectrum.

The Raman spectroscopy analysis showed wider and lesser peak intensities of the coatings as compared to their respective powders. The presence of distinct D, G, and 2D bands in the BAG-1CNT and BAG-2CNT coatings confirmed the retention of CNT after the high-temperature plasma spray process.

Based on the cross-sectional evaluation of the coatings, the plasma spray characteristics of voids, microcracks, and irregular melting regions were observed from the FESEM micrographs. The reinforcement of CNT in BAG has resulted in an increase in the fully melted regions. The cross-sectional EDS mapping indicated the homogenous distribution of the elements in HA and BAG coatings. The thickness of the coatings was in the range of 340- 420 μ m and were well-adhered to the substrate. The coating thickness values of HA, BAG, BAG-1CNT, and BAG-2CNT were 420, 340, 390 and 375 μ m. The BAG coatings have maximum porosity value of 6.77% and there was a decrease in the value to 2.34% with the addition of 2wt% of CNT in BAG coatings.

Mechanical and Electrochemical Corrosion Studies

5.1 Introduction

The mechanical and electrochemical corrosion behavior of the developed plasma spray coatings has been investigated in detail in this chapter. Under mechanical characterization, surface roughness, micro-hardness and scratch testing of the coatings have been conducted. Post-scratch testing analyses were performed to calculate the scratch wear rate and scratch hardness. The electrochemical corrosion testing was performed in a simulated body fluid environment at 37 °C. After corrosion, the samples were analyzed using FESEM and Raman Spectroscopy. The proposed corrosion inhibition mechanism by the reinforcement of carbon nanotubes in the baghdadite coatings have also been discussed.

5.2 Mechanical Characterization

5.2.1 Surface Roughness Testing

The surface roughness is an important parameter in biomedical coatings as it will affect the implant tissue interaction. The higher the surface roughness value more the cell adhesion and growth as it will increase the coating and body fluid interface [228,229].

Surface roughness parameters such as arithmetic mean deviation (R_a), root mean square average of profile heights (R_q), and maximum peaks to valley heights (R_z) of the coatings were measured and shown in Fig.5.1. The mean of R_a values for HA, BAG, BAG-1CNT, and BAG-2CNT plasma-sprayed coatings are 8.58, 13.88, 15.18 and 16.10 μ m respectively. The R_q and R_z values of HA, BAG, BAG-1CNT, and BAG-2CNT are 10.54 μ m and 46.38 μ m, 16.93 μ m and 69.66 μ m, 18.36 μ m and 75.76 μ m and 19.25 μ m and 77.28 μ m respectively. The average surface roughness value of around 10.5 μ m is considered beneficial in promoting the timely fixation of implants along with mechanical stability [230]. The graph in Fig.5.1 showing the R_a values indicates that the surface roughness values of BAG coatings is higher than HA coating. This can be

attributed to the non-uniform melting of BAG due to the variation in the particle size distribution and differences in the thermal properties. Even with the smaller average particle size, incomplete melting and differential cooling can lead to the increase in the surface irregularities and resulting in higher surface roughness. Further, when the core of an unmelted particle lacks sufficient strength, it can fragment upon impact with the surface. This can cause the spreading of crystalline particulate on the surface of the coating. Conversely, the fully melting regions will result in a smooth surface as the liquid will spread evenly on the coating surface [201,231].

The increase in surface roughness values with the reinforcement of CNT can be attributed to various reasons related to the properties and behavior of CNT. The CNT reinforcement can increase the overall surface area of the coating and changes in the microstructure can introduce additional peaks and valleys. Apart from the above, the CNT has high thermal stability and electrical conductivity which can interact with the plasma arc and influence the deposition process causing irregularities on the surface. The CNT act as a mechanical interlock within the structure which creates irregular surface topography as CNT protrude from the BAG matrix at the surface.

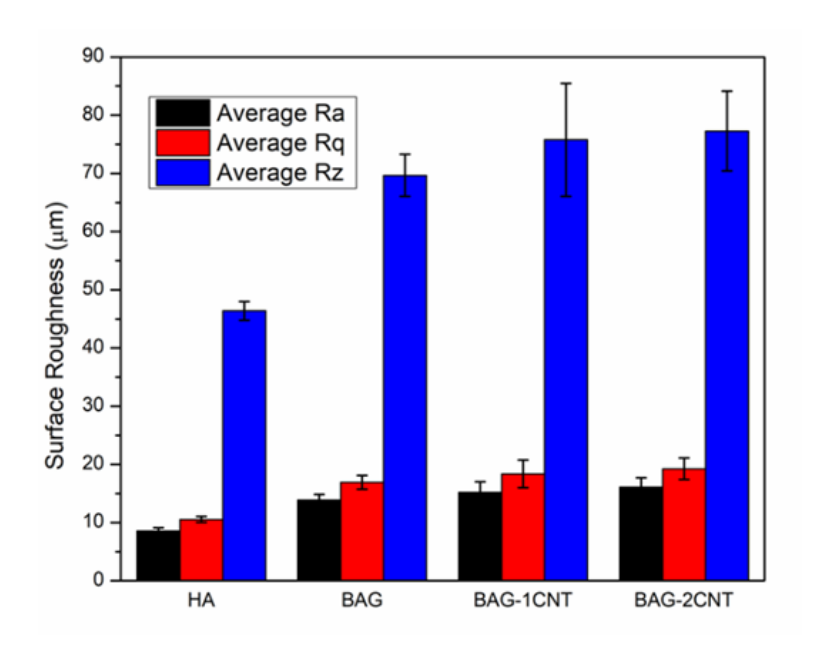


Figure 5.1 Surface roughness measurement of HA, BAG, BAG-1CNT and BAG-2CNT plasma sprayed coated samples [201]

5.2.2 Micro-Hardness Testing

Average micro-hardness values for HA, BAG, BAG-1CNT, and BAG-2CNT coating are 110, 160, 189 and 222 HV respectively, and are shown in Fig.5.2. BAG coating exhibits higher hardness than HA coating, because of the presence of Zr in BAG structure. Zirconium is tetravalent and has exceptional biocompatibility and mechanical properties. Further, the stability of Ca-Si structure is supported by the presence of Zr in BAG [232]. Schumacher et al. and Pham et al. corroborate these findings, highlighting BAG's superior mechanical properties compared to HA [170,176]. Fig.5.2 shows a trend of increasing micro-hardness with the reinforcement of CNT in BAG coatings. The 1 wt% CNT and 2 wt% CNT reinforcement in BAG led to micro-hardness increases of 18.1% and 38.7%, respectively. Bakshi et al. also observed the similar trend of increase in hardness by 44% and 80% with 5 wt% and 10 wt% CNT-reinforcement [233]. The observed increase in micro-hardness is attributed to reduced porosity, uniform CNT distribution, and effective anchoring within the ceramic matrix, promoting enhanced mechanical properties [190,234].

Pham et al. deposited the plasma sprayed HA and BAG coatings and measured the microhardness values at the cross-section of the coatings at a load of 300gf. Microhardness values of the HA and BAG coatings reported as 118.3 ± 21.2 HV and 325.5 ± 55.2 HV respectively [176]. Another study by Hasan et al. studied the effect of applied load, indent location and measurement direction on the microhardness values on plasma sprayed hydroxyapatite coatings. The microhardness value at coating cross-section at 300gf at denser and porous area was found to be 200 HV and 160 HV respectively [235]. The microhardness values depend upon various factors like plasma spray parameters and powder size and distribution. The BAG coatings have lower microhardness value in comparison to reported in the literature which could be attributed to differences in particle size distribution, porosity, and the specific plasma spraying parameters used.

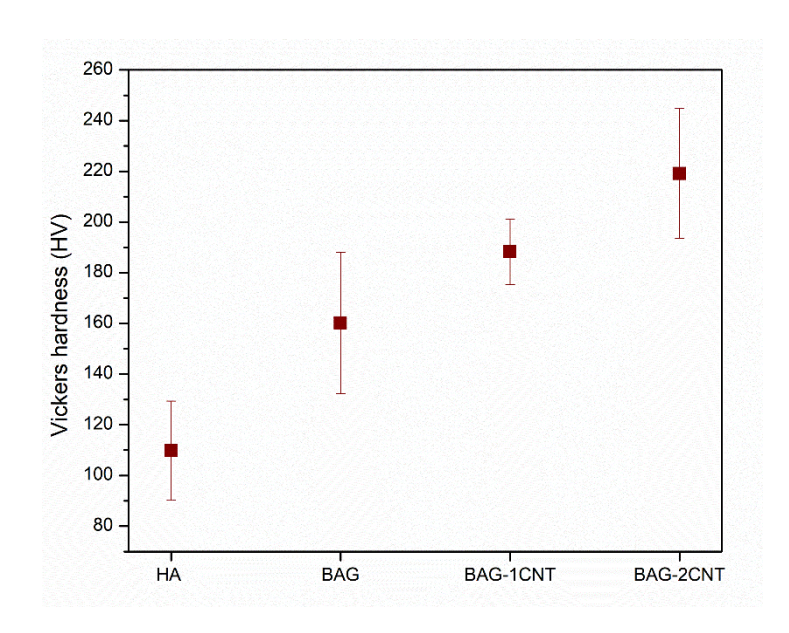


Figure 5.2 Microhardness values of HA, BAG, BAG-1CNT and BAG-2CNT plasma sprayed coated samples [190]

5.2.3 Scratch Testing

The scratch test results of the developed plasma-sprayed coatings are shown in Fig.5.3. The data is plotted as frictional force vs normal force for progressively increasing load of 20 N to 140 N. The critical load (L_c) is defined as the load at which the fracture or delamination of the coating surface occurs. It provides a qualitative indication of the adhesion strength between the coating and the substrate [236]. From Fig.5.3, it is observed that at the initial loads from 20-30 N, all prepared coatings exhibit minimal fluctuations in frictional force. This phenomenon is attributed to the gradual wear of the upper coating layer against the scratch tip under low normal loads. The consistent frictional force variation indicates a controlled wear process without any chipping or flaking. The relative motion of the scratch tip against the surface of the coating leads to abrasion wear, resulting in progressive loss of coating at the surface [237]. However, beyond 30 N, the fluctuations in the frictional force tend to increase and these fluctuations become more intense after 50 N of normal force for all the coatings. At higher normal loads, wear mechanisms like ploughing, flaking, and chipping of the coatings occur which is the main reason for the sudden variation of the frictional force. These findings provide insights into the dynamic behavior of the coatings under varying scratch loads, elucidating on the critical load threshold and the associated modes of wear [190].

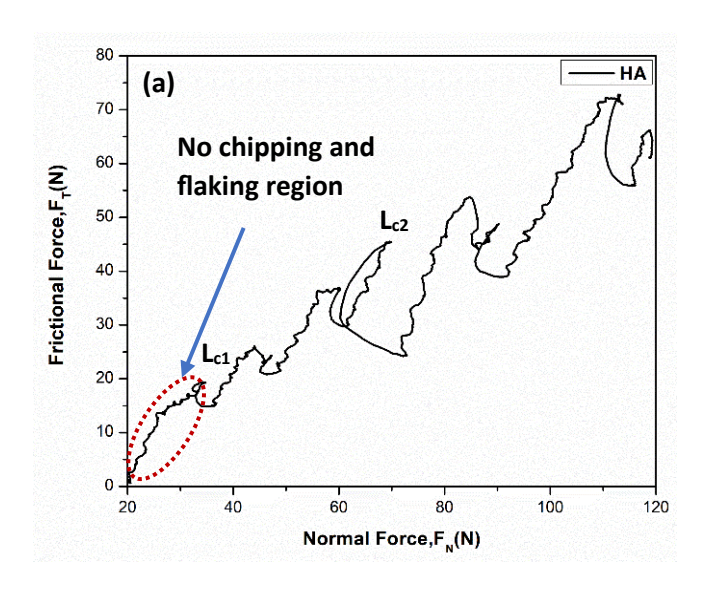


Figure 5.3 (a) Frictional force during the progressive scratch test of HA plasma sprayed coatings

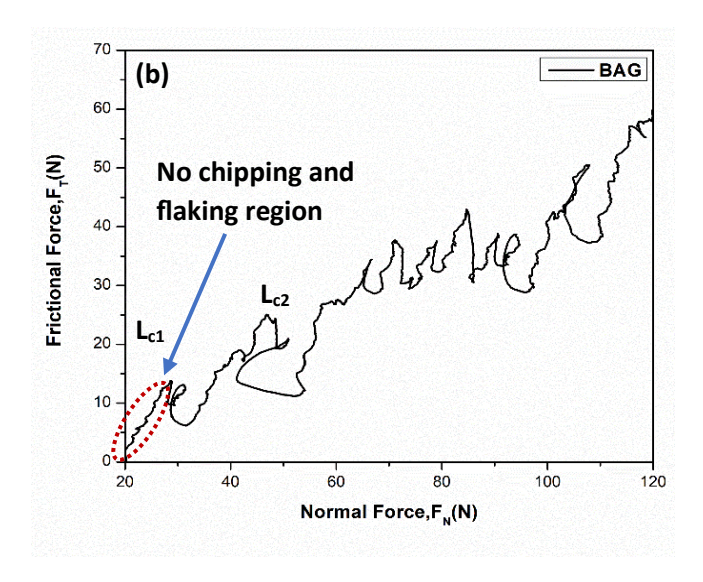


Figure 5.3 (b) Frictional force during the progressive scratch test of BAG plasma sprayed coatings

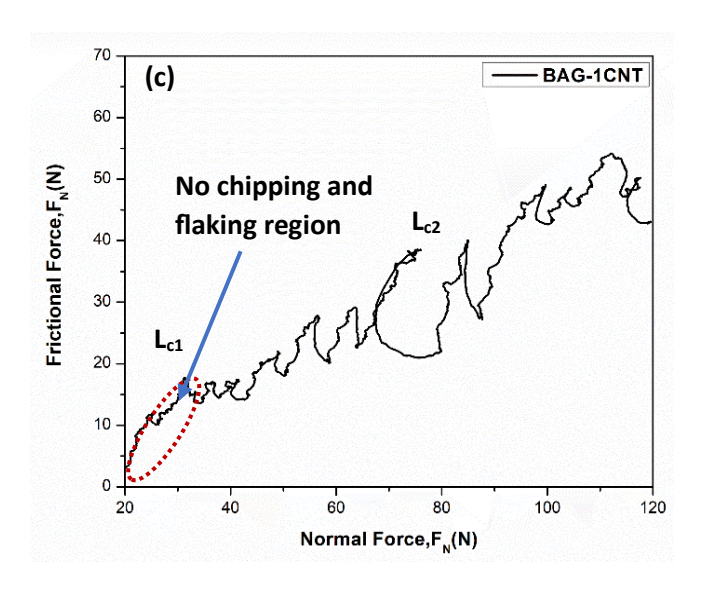


Figure 5.3 (c) Frictional force during the progressive scratch test of BAG-1CNT plasma sprayed coatings

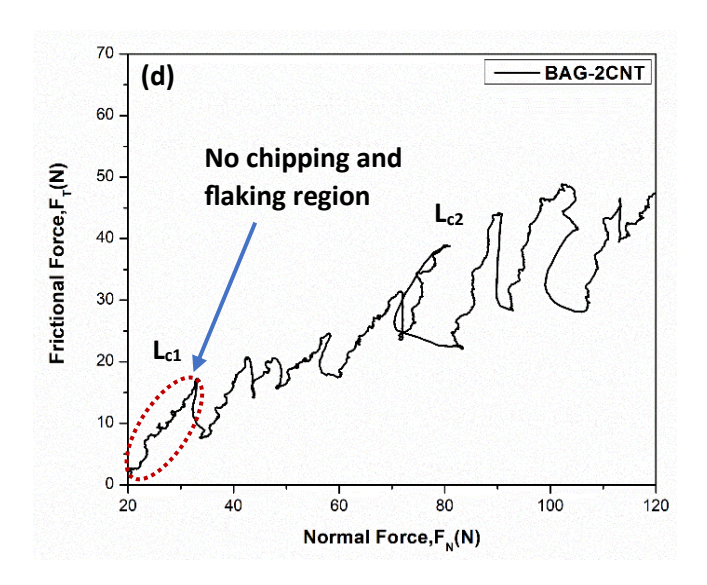


Figure 5.3 (d) Frictional force during the progressive scratch test of BAG-2CNT plasma sprayed coatings [190]

Table 5.1 presents the first critical load (L_{c1}), and the final critical load (L_{c2}), These critical loads serve as indicators of adhesion strength, playing a pivotal role in coating failure mechanisms such as flaking, chipping, and lamellae delamination. The L_{c1} and L_{c2} values for HA are 32.55 N and 69.29 N while for BAG it is 28.93 N and 47.19 N.

The critical load values correspond to the specific points during the test where different types of failure mechanisms occur in the coatings. The L_{c1} corresponds to the load where the no chipping and flaking region ends and at which the first microcrack or minor chipping of the material appears within the coating. It signifies the ability of the coating

material to withstand mechanical stresses without breaking apart. The L_{c1} for HA coatings is higher than BAG coatings which shows the HA coating have better initial resistance to scratch induced failure. This can be attributed to the lesser porosity, dense and higher thickness of HA coatings as compare to the BAG coatings.

The L_{c2} represents the load at which there is loss or delamination of the coating material and can result in the spallation or detachment of the coating. It is marked by the sudden increase in the fluctuations in the frictional force plots. The CNT reinforcement does not influence L_{c1} which shows it has not changed the point at which initial damage occurs. At this point the coating ability to withstand initial scratches depends more on the fundamental bonding and adhesion properties rather than internal reinforcement. However, CNT have a more pronounced effect on L_{c2} because it improves the overall mechanical properties like hardness, toughness and fracture resistance. As the applied load increases the CNT enhance the coating resistance to severe damage, leading to increase in L_{c2}. The incorporation of CNT reinforcements acts as a resistance against various failure modes like chipping, flaking, and crack propagation. Consequently, it results in the enhancement of critical load values in both compositions of BAG-CNT coatings. The CNT bridging and CNT pull-out are the toughening mechanisms that lead to decreasing of frictional force and overall improvement in the scratch resistance life of the coatings from failure [190,203].

Table 5.1 First critical load and final critical load of HA, BAG, BAG-1CNT and BAG-2CNT plasma sprayed coatings [190]

Sample	L _{C1} (N)	L _{C2} (N)
НА	32.55	69.29
BAG	28.93	47.19
BAG-1CNT	31.90	75.50
BAG-2CNT	33.59	80.51

The FESEM images in Fig.5.4 depict the surfaces of plasma-sprayed coatings, namely HA, BAG, BAG-1CNT, and BAG-2CNT after the scratch test. The scratch grooves on the coating surfaces after the progressive load scratching are visible across all the coatings. At lower normal loads, minimal damage occurs with narrower scratch widths and a lack of chipping and flaking. The HA coatings may have weak adhesion between

coating layers and to substrate leading to significant material removal. The mechanical properties of the coatings such as hardness, toughness influence the scratch behavior. The HA coatings have poor mechanical properties causing it to deform or fail under scratching resulting in wider scratches. The CNT-reinforced coatings exhibit larger chipping and flaking free regions compared to BAG and HA coatings. With the increase in normal load, the scratch width also increases, unveiling coating failure modes like ploughing, chipping, and flaking. Among the investigated coatings, the HA coating shows the maximum chipping and wear debris formation. The formation of flakes and debonding in the coatings induces a sudden drop in frictional force, which is also noticed in the frictional force graphs (Fig.5.3). The incorporation of CNT-reinforcement in BAG coatings contributes to an increase in hardness and interfacial strength. This improvement can be attributed to mechanisms like CNT pull-out and bridging, offering insights into the enhanced scratch behavior of the coatings [190,238].

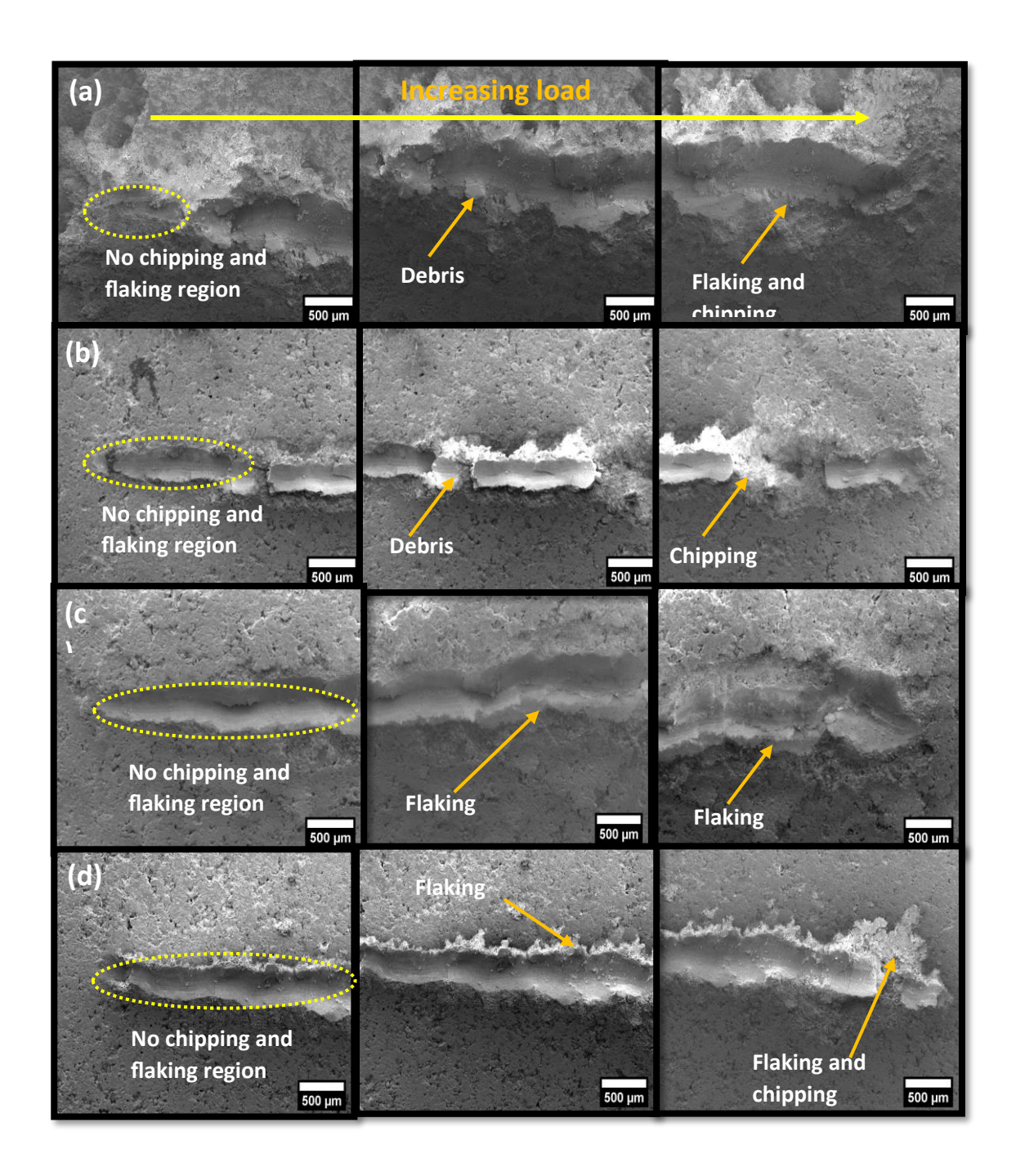


Figure 5.4 FESEM images of scratch groves on (a) HA (b) BAG (c) BAG-1CNT and (d) BAG-2CNT plasma sprayed coatings after progressive load scratching [190]

The surface element mapping of the coatings after the scratch test is shown in Fig. 5.5. The CNT-reinforced coatings have uniform elemental distribution at the scratched part of the coatings. Moreover, the substrate is not exposed after the end of the scratch.

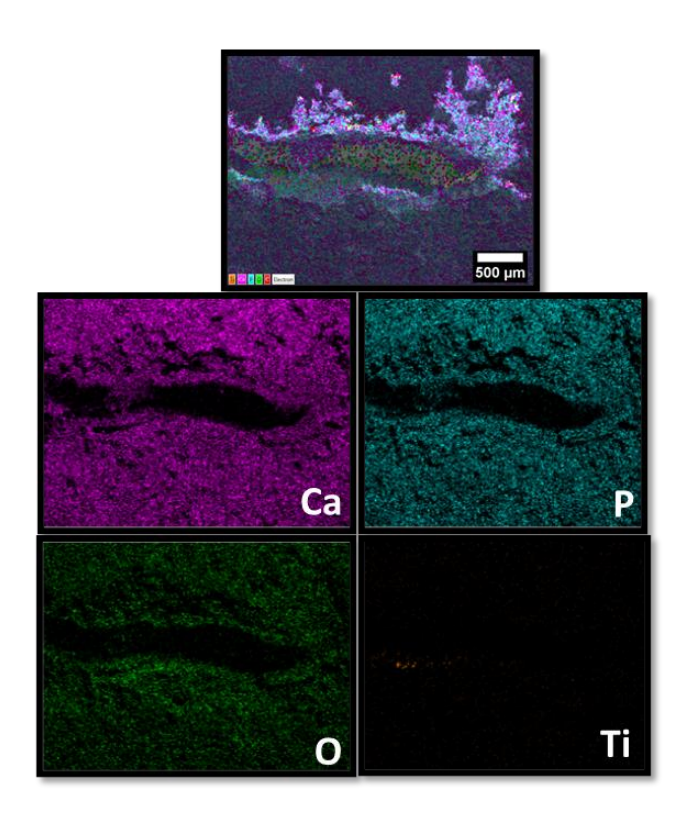


Figure 5.5 (a) Surface element mapping of plasma sprayed HA coatings after scratch test

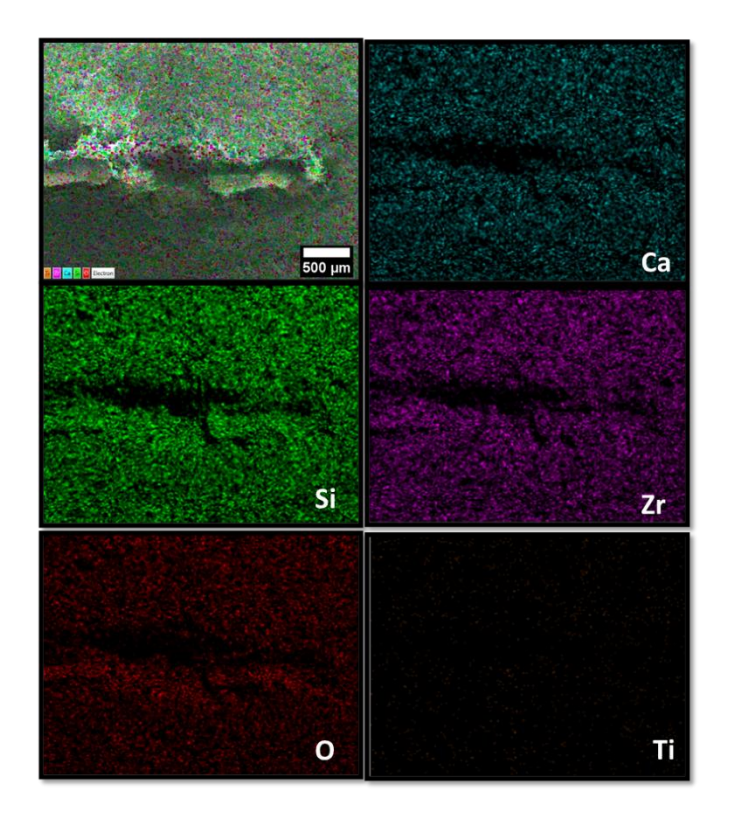


Figure 5.5 (b) Surface element mapping of plasma sprayed BAG coatings after scratch test

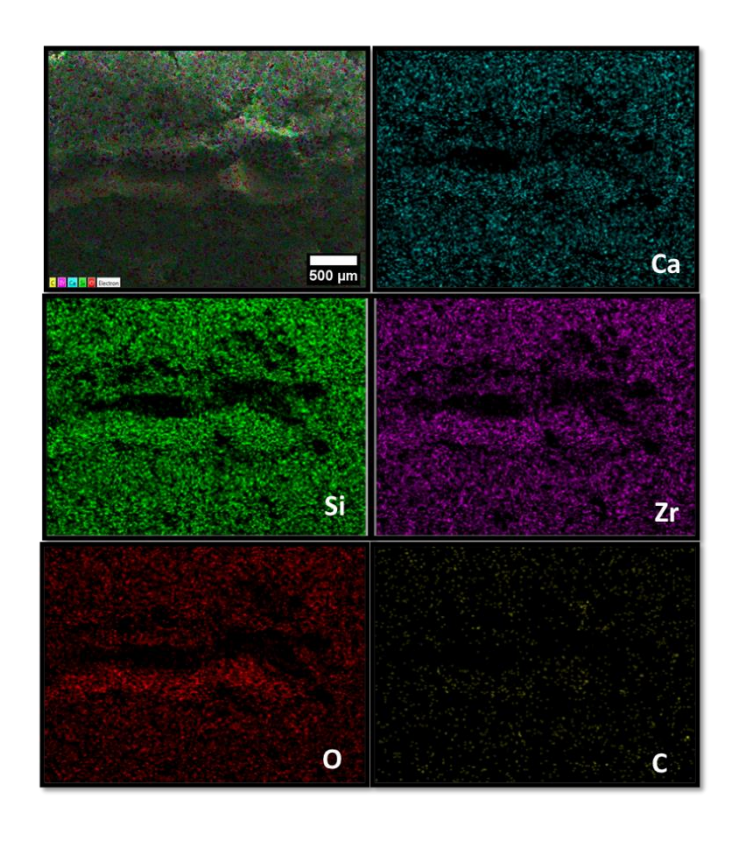


Figure 5.5 (c) Surface element mapping of plasma sprayed BAG-1CNT coatings after scratch test

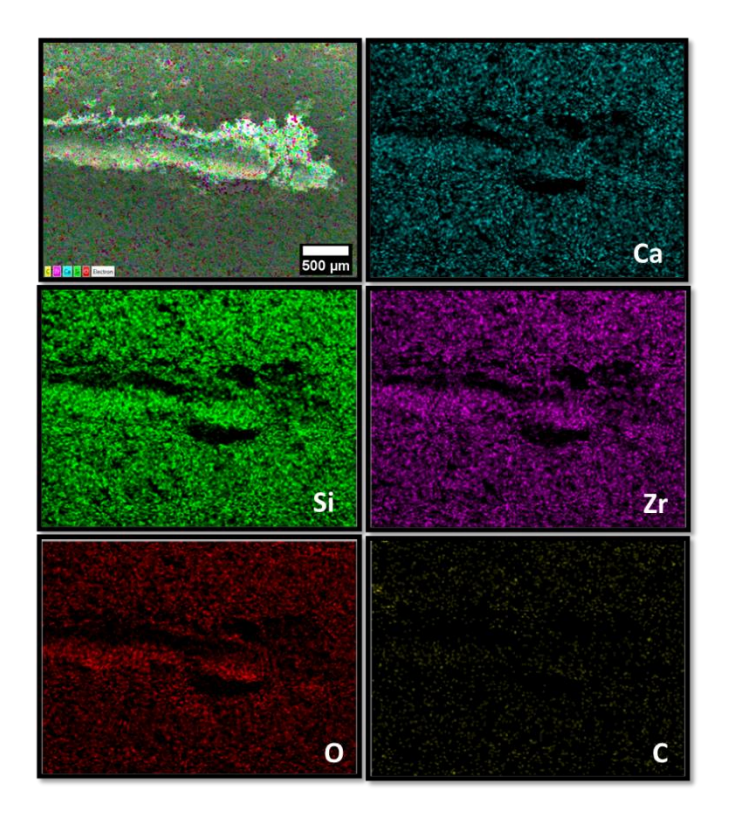


Figure 5.5 (d) Surface element mapping of plasma sprayed BAG-2CNT coatings after scratch test

The penetration depth of the scratches measured using a profilometer for the developed coatings under progressive loading conditions is shown in Fig.5.6. The penetration depth is directly related to the scratch groove volume and is employed to evaluate the scratch resistance of the investigated coatings. The maximum penetration depth and scratch width at the highest normal load are given in Table 5.2. The penetration depth of HA, BAG, BAG-1CNT, and BAG-2CNT is 182 μm, 151 μm, 119 μm, and 108 μm, respectively. The changes in penetration depth are attributed to the hardness of the coatings. HA coating is characterized by minimum hardness and exhibits maximum depth of penetration during scratching. Similarly, BAG-2CNT coating exhibits minimum penetration depth because of its highest hardness. The BAG and BAG-1CNT coatings exhibit intermediate values of penetration depth between HA and BAG-2CNT coatings. Also, the scratch groove width, w is higher for HA coatings (545 µm) than BAG coatings (384 µm). The scratch groove width experiences a marginal reduction in BAG-1CNT (365 μ m) and BAG-2CNT (340 μ m) coatings. The wear volume loss (W_{vol}) and scratch rate (W_R) with the corresponding values are given in Table 5.2. HA coating exhibits the highest wear volume loss (16.832 mm³) and scratch rate (48.244 mm³N⁻¹m⁻¹ 1). The wear volume loss and scratch rate decreases in BAG coating (15.051 mm³ and 43.262 mm³N⁻¹m⁻¹) and further diminish in BAG-1CNT (13.206 mm³ and 37.971 mm³N⁻¹m⁻¹) and BAG-2CNT (12.574 mm³ and 36.172 mm³N⁻¹m⁻¹) coatings. Overall, the incorporation of 2wt% CNT in BAG coatings reduces the scratch rate by 16.38% compared to pure BAG coatings. This improvement is attributed to decreased porosity and increased micro-hardness resulting from CNT addition, highlighting their significant role in enhancing scratch resistance of BAG-2CNT coatings.

The scratch hardness (H_S) of the developed coatings is also calculated based on the maximum width of the scratch and normal load, with results reported in Table 5.2. The scratch hardness of HA, BAG, BAG-1CNT, and BAG-2CNT coatings is 1.028 GPa, 2.072 GPa, 2.293 GPa, and 2.643 GPa, respectively. The incorporation of 2 wt% CNT enhances the scratch hardness by 27.55% compared to pure BAG coating. The improvement in scratch hardness in CNT-reinforced BAG coatings is attributed to the strong bonding of CNT in the BAG matrix [190].

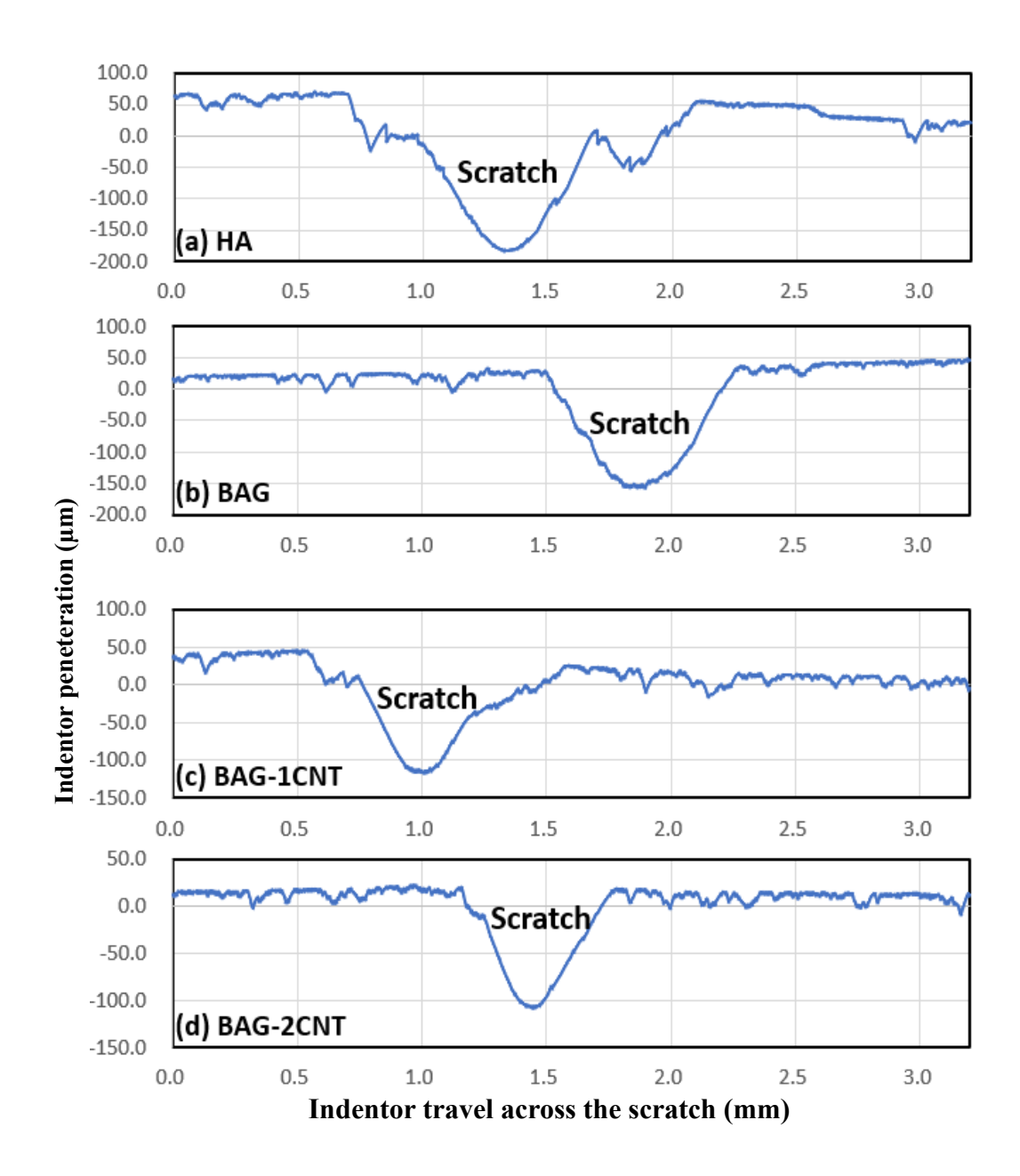


Figure 5.6 Scratch profile of (a) HA (b) BAG (c) BAG-1CNT and (d) BAG-2CNT plasma sprayed coatings after scratch test under progressive loading conditions [190]

Table 5.2 Coefficient of friction (COF), penetration depth (P_d), maximum frictional force ($F_{T(max)}$), maximum scratch width (w), wear volume loss (W_{vol}), scratch rate (W_R) and scratch hardness (H_s) of HA, BAG, BAG-1CNT, and BAG-2CNT plasma sprayed coatings [190]

Sample	COF	Pd	F _T (Max.)	W	W _{vol} (mm ³)	$W_R(mm^3N^{-1})$	H _S (GPa)
		(µm)	(N)	(µm)		m ⁻¹)	
НА	0.519	182	73.1	545	16.832	48.244	1.028
BAG	0.4016	151	59.5	384	15.051	43.262	2.072
BAG-	0.4184	119	54.28	365	13.206	37.971	2.293
1CNT							
BAG-	0.3690	108	49.15	340	12.574	36.172	2.643
2CNT							

During the scratch test, the load is transmitted from the stylus to a well-bonded CNT within the coating. Splats are the fundamental building blocks of coatings. It is considered that stronger and more adhering splats will enhance the function of the coating in a wear environment.

The addition of CNT has been found to decrease in porosity and microcracks in plasma-sprayed BAG coatings [201]. The presence of pores and microcracks may lead to higher fluctuations in the coefficient of friction plots of the coatings (Fig.5.3). When a pore comes directly below the scratch indenter, it collapses and the indentor slips over a small vertical distance reported by Ghabchi et al [239]. While scratching, the coating in front of the advancing stylus experiences compression, whereas the scratch region at the trailing edge of the stylus is subjected to tension which can lead to tensile crack formation. With the increase in the normal load, the cracks can propagate within the coating along with the splat boundary which is the weakest part in the thermal spray coatings. The cohesive strength of the coating is tested during this crack propagation. Ultimately the small portion of the coating is detached from the top layer. The CNT reinforcement has led to the resistance of crack propagation and resulted in the enhancement of the critical load values. The increase in cohesion strength of CNT-reinforced coatings is attributed to the improved interlocking and mechanical anchorage

among the splats provided by CNT [240]. The presence of CNT at the inter-splat boundary and filling up the pores and microcracks are shown in Fig.5.7 [190].

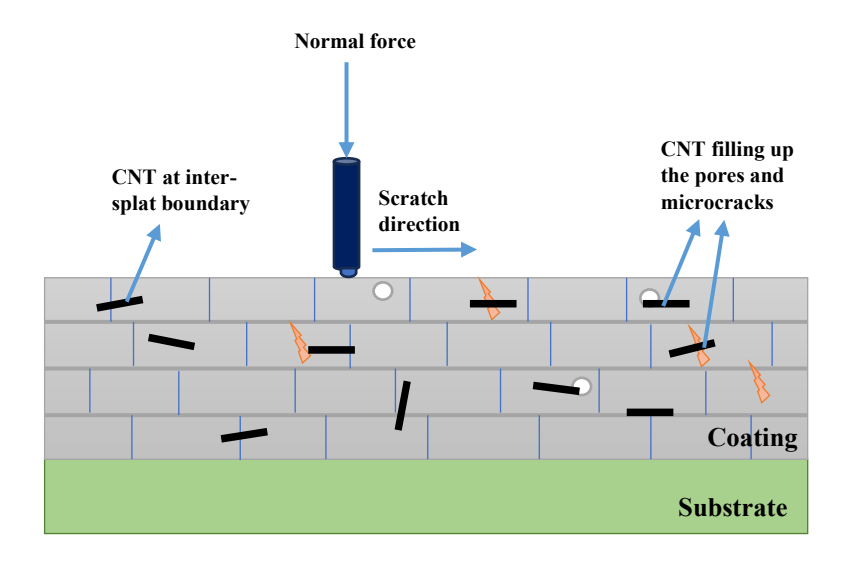


Figure 5.7 Schematic diagram of the effect of CNT reinforcement on plasma sprayed BAG coatings during scratch testing [190]

5.3 Electrochemical Corrosion Testing

5.3.1 Open Circuit Potential Measurements

The OCP as a function of time is measured for all the investigated coatings in SBF. The OCP graphs are shown in Fig.5.8. and values are given in Table 5.3. The OCP is recorded for 1 hr to attain steady state. From the OCP graph, it is observed that the samples having CNT as reinforcement show better results under SBF. The OCP of HA and BAG coatings are -0.411 V and -0.399 V respectively. With the addition of 1wt% and 2wt% of CNT in BAG coating, the OCP value shifts to -0.393 V and -0.391 V respectively. The shift in OCP towards the noble direction indicates the improvement in electrochemical corrosion performance. The presence of pores in HA and BAG coatings can be the main reason for their lower OCP values. With CNT addition, the reduction in porosity and uniformity of splats in their microstructure shifts the OCP to more positive values [201].

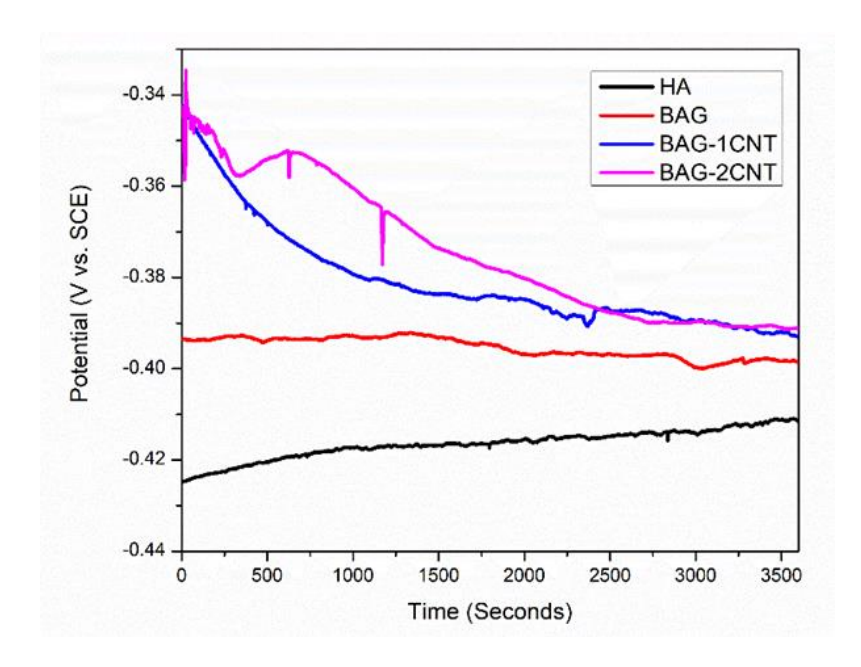


Figure 5.8 Open Circuit Potential (OCP) of HA, BAG, BAG-1CNT, and BAG-2CNT plasma-sprayed coatings on Ti substrate [201]

5.3.2 Potentiodynamic polarisation studies

Potentiodynamic scans of HA, BAG, BAG-1CNT, and BAG-2CNT coatings on Ti substrates in SBF are shown in Fig.5.9(a). The corrosion current density (I_{corr}), corrosion potential (E_{corr}), polarization resistance (R_p), anodic Tafel slope b_a , and cathodic Tafel slope b_c are measured from potentiodynamic curves using the Tafel extrapolation method and reported in Table 5.3. The I_{corr} and E_{corr} for all the investigated coatings are displayed in Fig.5.9(b).

It is evident from the results that E_{corr} follows a similar trend to that of OCP of the investigated coatings under SBF. There is a notable improvement in the E_{corr} of BAG-1CNT and BAG-2CNT as compared to pure HA and pure BAG coatings. The BAG coating exhibits the highest I_{corr} value and is more prone to corrosion than other investigated coatings. The reason may be that BAG coating has the highest porosity value so there are chances that the electrolyte medium might have travelled inside and reached the Ti substrate. However, the HA coating is thicker and denser and has better corrosion resistance compared to BAG coating. The BAG-2CNT coatings show the lowest I_{corr} , indicating the highest resistance to corrosion. This could be attributed to the accumulation of CNT inside the voids and gaps of the BAG matrix, leading to a significant drop in I_{corr} value [201].

Table 5.3 Electrochemical parameters of HA, BAG, BAG-1CNT, and BAG-2CNT coatings on Ti [201].

Sample	OCP (V)	Icorr	Ecorr(V)	Rpol	ba	b _c (V/dec)
		(µA/cm²)		(kΩ)	(V/dec)	
HA-coated	-0.411	6.056	-0.429	2.228	0.035	0.272
BAG coated	-0.402	9.789	-0.428	2.265	0.061	0.303
BAG-1CNT coated	-0.393	6.181	-0.422	2.454	0.075	0.709
BAG-2CNT coated	-0.391	1.927	-0.423	10.909	0.064	0.192

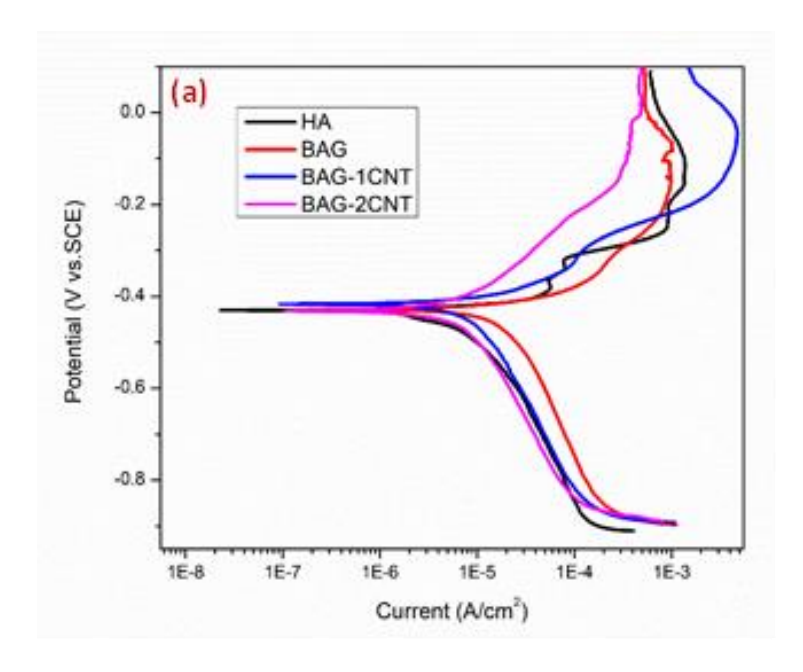


Figure 5.9 (a) Potentiodynamic polarization curves for HA, BAG, BAG-1CNT and BAG-2CNT plasma-sprayed coatings and Ti substrate

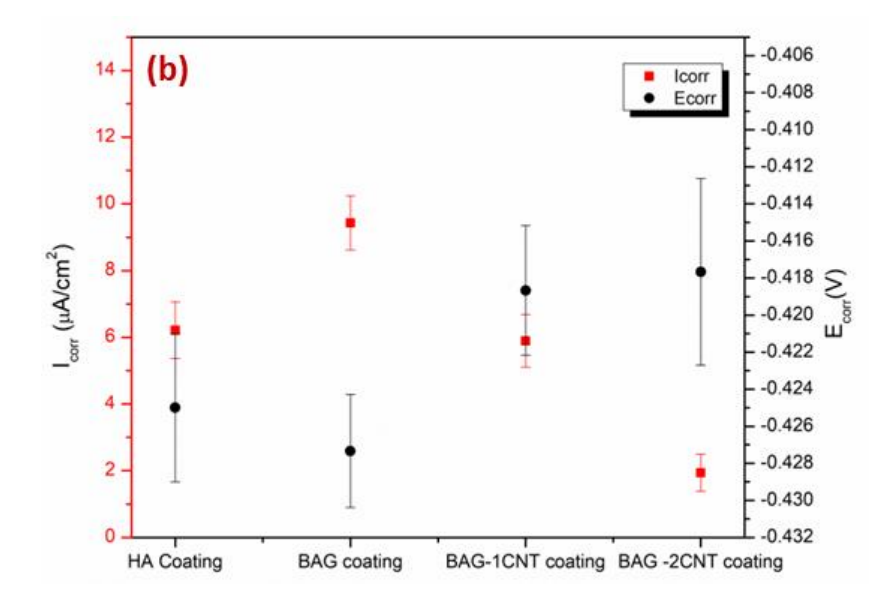


Figure 5.9 (b) I_{corr} and E_{corr} values for HA, BAG, BAG-1CNT and BAG-2CNT plasma-sprayed coatings and Ti substrate [201]

The existing literature also reveals that the reinforcement in HA coatings has led to the reduction in the porosity of coatings and enhanced the corrosion behavior of coatings [201]. The plasma-sprayed graphene nanoplatelets reinforced HA coatings were deposited on Ti substrates. The addition of 2wt% of graphene nanoplatelets reduced the corrosion rate upto 87% [241]. Gopi et al. also found similar results in CNT-reinforced HA composite coatings on Ti substrates under SBF solution [242].

5.3.3 Electrochemical Impedance Spectroscopy (EIS) Studies

The EIS analysis of the HA, BAG, BAG-1CNT, and BAG-2CNT coatings is performed in SBF at OCP condition. The Nyquist, bode, and phase plots with equivalent circuit are shown in Fig.5.10. In the circuit, R_s represents the solution resistance, R_p represents the resistance of pores in the coating, and CPE represents the constant phase element of the coatings. The nature of impedance (Z) of CPE is given by formula-

$$Z_{CPE} = Y_0^{-1} (k\omega)^{-n} \tag{1}$$

where Y_0 is the CPE constant, k is an arbitrary unit, ω is the angular frequency and n is the CPE exponent between 0 and 1. If n=1,0 or -1 then Y_0 is the capacitance, resistance or inductance respectively. The use of CPE instead of the capacitor can better fit the equivalent circuit and is considered as an imperfect capacitor. EIS-fitted circuit values are given in Table 5.4.

The Nyquist curve depicts real vs. imaginary impedance for the investigated coatings as shown in Fig.5.10(a). These curves take the form of a semi-circle for all the coatings. It is observed from the results that BAG coatings reinforced with CNT exhibit higher arc diameters compared to pure BAG and HA coatings. From Table 5.4, the R_p value which is a measure of resistance to charge transfer through pores is lower in pure HA and pure BAG coatings compared to BAG coatings reinforced with CNT. However, there is not much difference in R_p values of BAG-1CNT and BAG-2CNT coatings. The pure BAG coatings exhibit R_p value of 3.112k Ω which significantly increases to 8.647k Ω with the addition of 1wt% CNT. The pure HA and BAG-2CNT coatings show R_p values of 5.483k Ω and 8.126k Ω respectively. It indicates that pure BAG coatings show relatively lower stability in the corrosive medium. The reason attributed to this is the high porosity and lower thickness of pure BAG coatings. The reinforcement of CNT in BAG coatings leads to a substantial increase in the semi-circle diameter, indicating the enhancement of coating stability and resistance to corrosion.

The Bode impedance plot for all the investigated coatings is shown in Fig.5.10(b). At very low frequencies, the impedance of the capacitor is very high as it varies inversely with frequency for all the coatings. The effective impedance is the sum of electrolyte resistance (R_s) and resistance through pores (R_p). As the frequency increases, the impedance of the capacitor decreases, allowing current to flow through it and reducing the overall impedance. With a further increase in frequency, the impedance of the capacitor becomes very low, finally reaching to zero ohms. This stage will be called as short circuit or zero-ohm impedance, and the impedance will be determined due to R_s only. It leads to the resistive behavior at high frequency and the curve runs the parallel to x-axis as observed in the impedance plot (Fig.5.10(b)). At intermediate frequencies, the impedance will lie in between the R_s value and the sum of R_s and R_p. From the bode plot, the lowest impedance is observed in BAG coatings. Furthermore, these plots clearly indicate that the incorporation of CNT leads to higher impedance values compared to pure HA and BAG coatings.

The Bode phase plot is shown in Fig.5.10(c). The phase is nearly zero both at very low and high frequencies indicating the resistive behavior. The phase angle starts to approach -90° at the intermediate frequencies of all the coatings. The BAG-1CNT and BAG-2CNT coatings show the lowest phase angle indicating the capacitive behavior at a higher frequency range compared to the pure HA and BAG coatings [243]. The

equivalent circuit model for fitting of plasma-sprayed HA, BAG, BAG-1CNT, and BAG-2CNT coatings on Ti substrates is shown in Fig.510(d) [201].

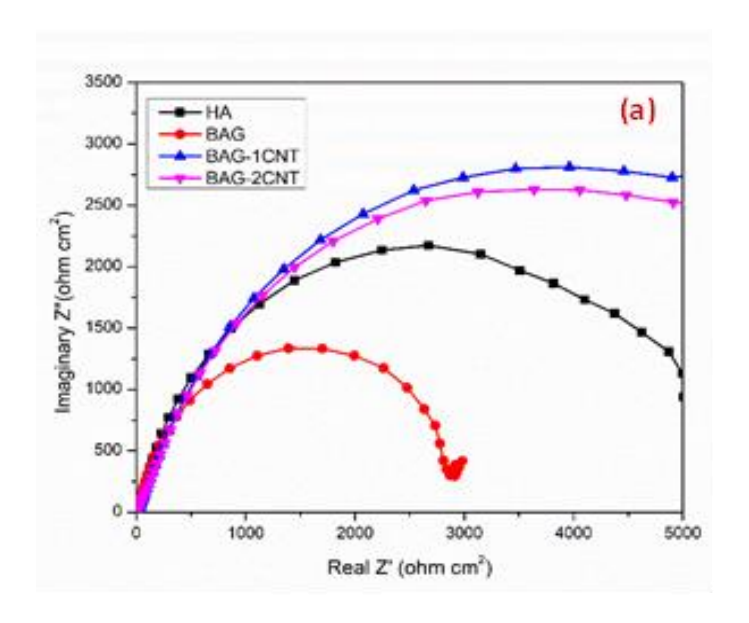


Figure 5.10 (a) Nyquist plot of HA, BAG, BAG-1CNT and BAG-2CNT plasma spray coatings on Ti substrates

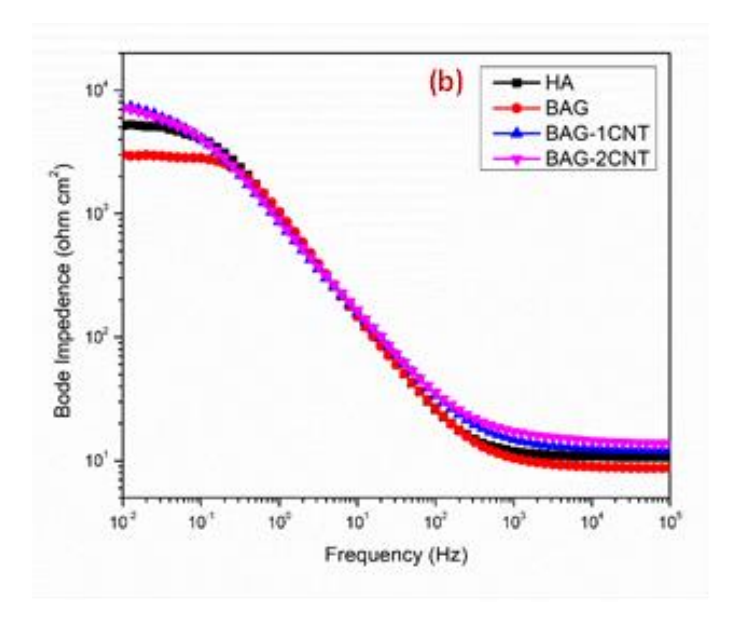


Figure 5.10 (b) Bode impedance plot of HA, BAG, BAG-1CNT and BAG-2CNT plasma-sprayed coatings on Ti substrates

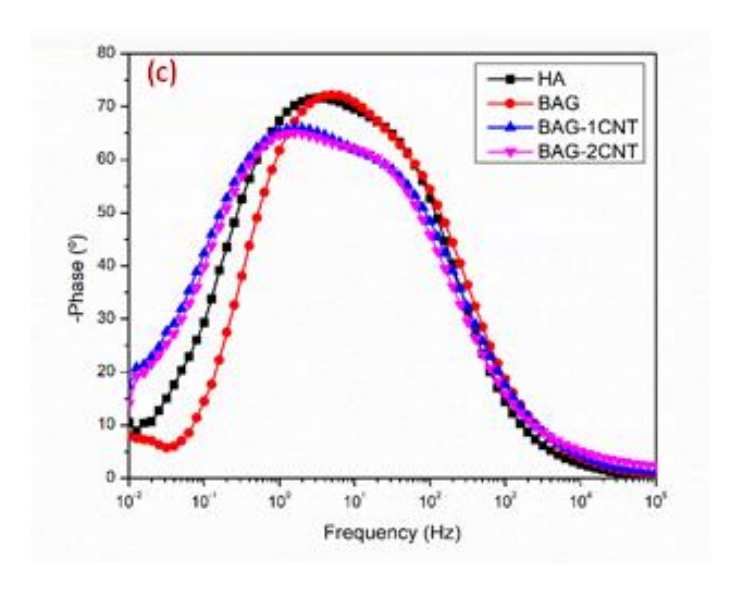


Figure 5.10 (c) Bode Phase plot of HA, BAG, BAG-1CNT and BAG-2CNT plasmasprayed coatings on Ti substrates

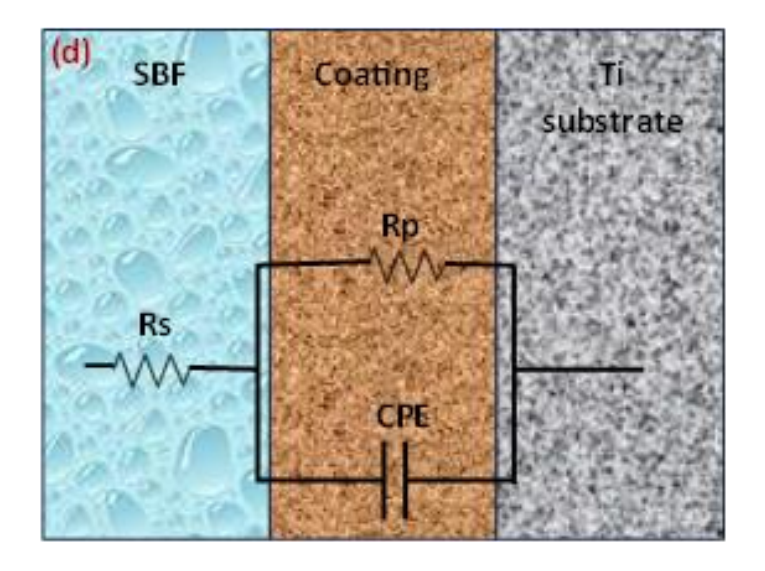


Figure 5.10 (d) Equivalent circuit model for fitting of HA, BAG, BAG-1CNT and BAG-2CNT plasma-sprayed coatings on Ti substrates [201]

Table 5.4 EIS circuit element values for plasma-sprayed HA, BAG, BAG-1CNT, and BAG-2CNT coatings on Ti substrates [201].

Sample	Rs (Ω)	Rp (kΩ)	CPE Y ₀ (μMho*s^N)	N
HA coated	10.746	5.483	199	0.848
BAG coated	8.99	3.112	182	0.858
BAG-1CNT coated	12.3	8.647	273	0.762
BAG-2CNT coated	14.3	8.126	262	0.764

The anodic polarization curve and EIS analysis indicate that corrosion resistance has improved with the reinforcement of CNT in the coatings. The reduction in porosity values can be considered as the major reason for enhancing the corrosion resistance of BAG-2CNT coatings. Apart from that, CNT may serve as an inert chemical barrier to SBF and restrict its passage deep inside the coatings and preventing contact with the substrate. It should also be noted that the homogeneous dispersion of CNT is important in the BAG matrix and random orientation of wrinkled CNT onto the surface for being effective in the corrosive medium [241].

5.3.4 Post-corrosion analysis

The surface morphology of the coated samples after corrosion is shown in Fig.5.11. The number of defects like pores, and microcracks is observed from the SEM images after the corrosion test. The HA and BAG coatings show microcracks as evident from Fig.5.11. However, these defects are minimized in the CNT-reinforced coatings. These defects may act as a passage for the electrolyte to penetrate inside the coating and ultimately reach to the substrate. This can lead to localized corrosion as SBF penetrates through pores and attacks the coating-substrate interface. The pure BAG and HA coatings exhibit higher porosity, which results in poor corrosion resistance. From Fig.5.11(c) and (d) it is observed that some small pores are present in the BAG-1CNT and BAG-2CNT coatings but microcracks are absent. The reduction in defects in CNT-reinforced coatings can be attributed as the major reason for the enhancement of corrosion resistance. The addition of CNT in the coatings results in lower pore

formation, because of their higher thermal conductivity and uniform dispersion into the BAG matrix. Higher thermal conductivity of CNT promotes homogeneous heat dissipation in the BAG matrix, then reducing porosity. The growth of corrosive pits is prevented by the uniform dispersion of the CNT in the BAG matrix. Also, there are no signs of potential fluctuations during the corrosion test, thereby indicating that the substrate remained unaffected [201].

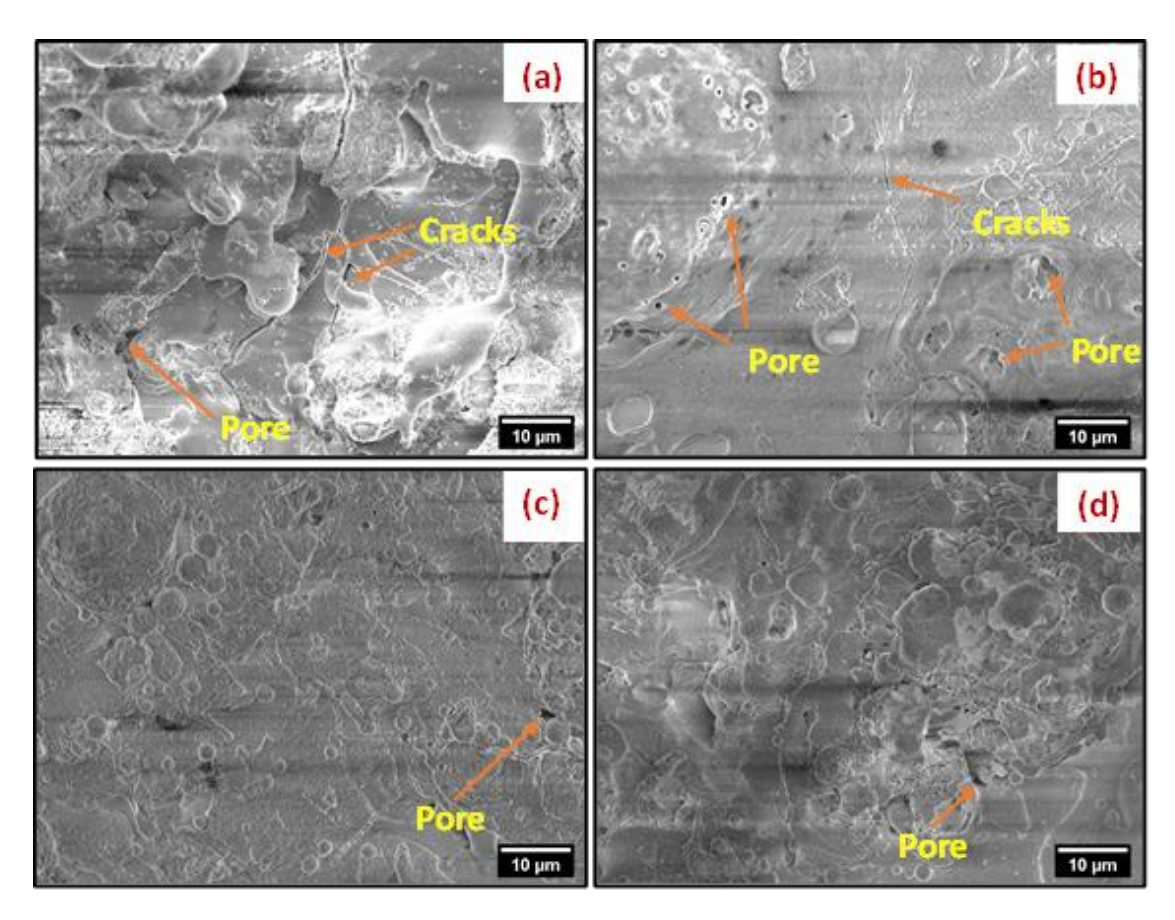


Figure 5.11 Pits and crack formation in the surface of (a) HA (b) BAG (c) BAG-1CNT and (d) BAG-2CNT coatings after corrosion [201]

The Raman spectroscopy of plasma-sprayed BAG-1CNT and BAG-2CNT coatings has been performed to confirm the presence of CNT in the coatings after corrosion tests are shown in Fig.5.12. In the case of BAG-2CNT coatings, the D and G-band are clearly visible at 1350cm⁻¹ and 1580cm⁻¹ respectively which was also evident before corrosion tastings. The G-band confirmed the presence of CNT in the coatings, while the D-band some defects in the structure that occurred after corrosion. However, in BAG-1CNT coatings the presence of D and G-band is less evident and difficult to observe from the peaks. The lower amount of CNT in the matrix may result in weak bands and may lead to coating defects. This can provide a passage for electrolytic ions to penetrate deeper

into the coatings, whereas 2wt% CNT may prevent the electrolytic ions from penetrating either by repelling them from the surface or absorbing them [201,241].

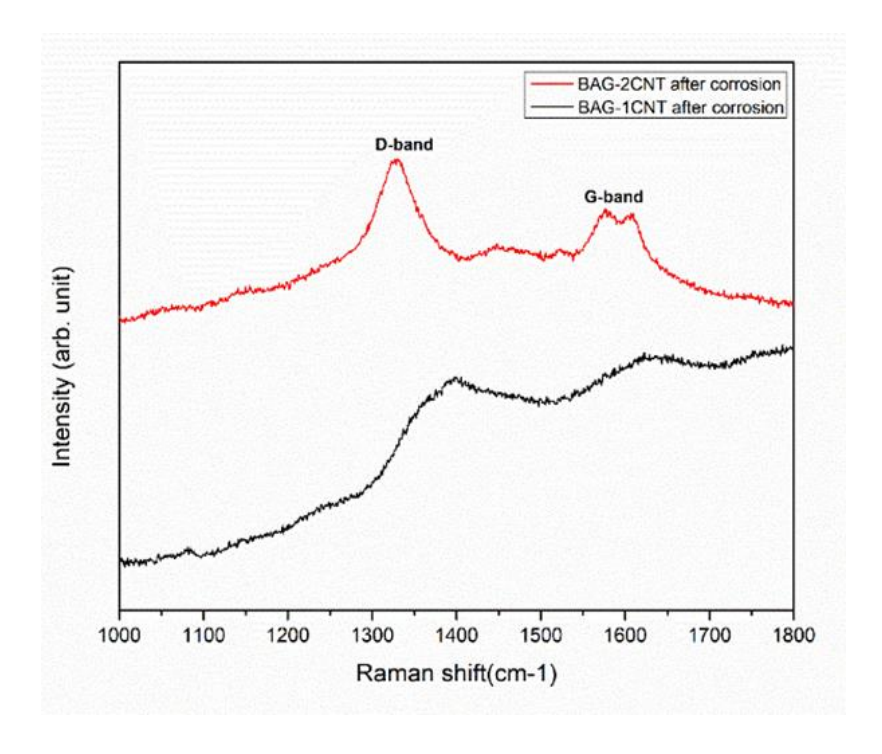


Figure 5.12 Raman spectroscopy of CNT reinforced coatings after corrosion test [201]

The schematic illustration of the corrosion mechanism is shown in Fig.5.13 after investigating the microstructural features of coatings. As discussed previously, the microstructural features consist of defects like pores and microcracks which are caused by sudden quenching of feedstock powders after coating layer deposition (Fig.5.13(a)). The CNT reinforcement fills up the defects as shown in Fig.5.13(b). When the coatings are exposed to SBF solution the ions start penetrating through these defects (Fig.5.13(c)) and the CNT reinforcement acts as a barrier to these ions and inhibits the corrosion response by the reduction of these defects (Fig.5.13(d)).

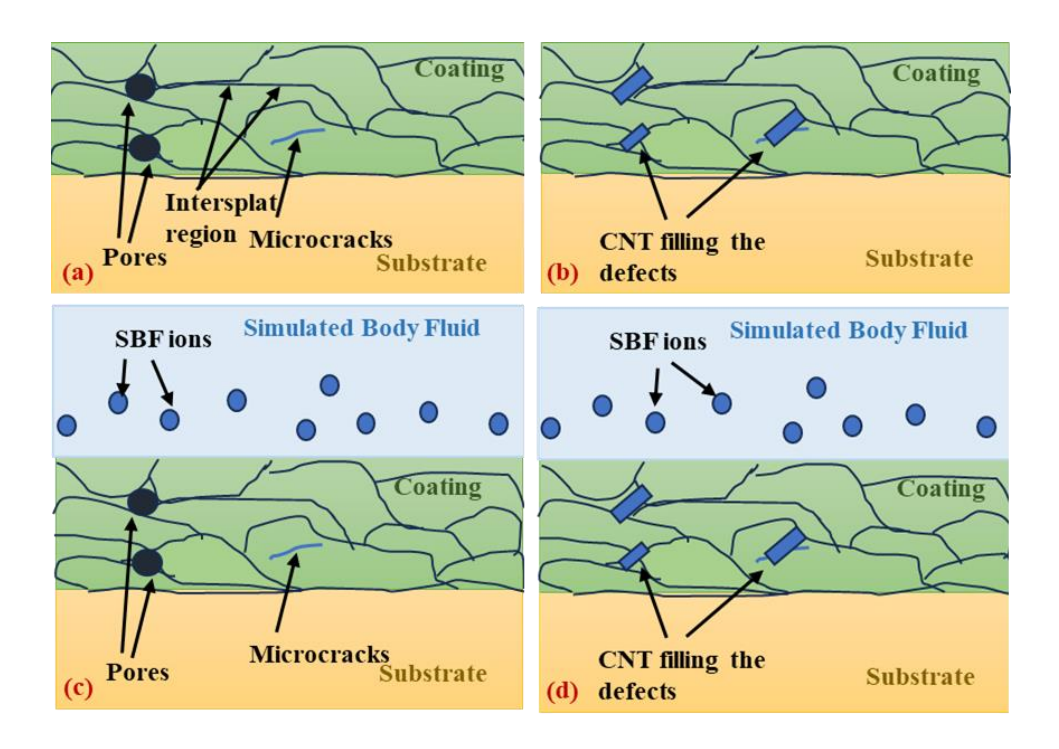


Figure 5.13 Schematic illustrations of corrosion inhibiting nature of CNT-reinforced plasma-sprayed coatings [201]

5.4 Summary of the Chapter

In this chapter, surface roughness, micro-hardness, and scratch testing have been evaluated as the mechanical characterization of the coatings. The average surface roughness value of HA and BAG were $8.58~\mu m$ and $13.88~\mu m$ and it increased to $15.18~\mu m$ and $16.10~\mu m$ with the reinforcement of 1wt% and 2 wt% of CNT in the BAG coatings. The plasma-sprayed BAG coatings have higher microhardness than HA coatings while the additition of 2wt% CNT in BAG coatings leads to the increase in microhardness value by 38.75%.

Scratch test results indicated the increase in critical load values with the incorporation of CNT in the coating. The wear mechanisms like ploughing, chipping, and flaking of the coatings occur at higher values of normal load. The decrease in the penetration depth and scratch width with CNT addition resulted in a decrease in the wear volume loss and scratch rate. The scratch rate of BAG coatings was 43.262 mm³N⁻¹m⁻¹ while it decreased to 36.172 mm³N⁻¹m⁻¹ for BAG-2CNT coatings. Further, the scratch hardness increased by 27.55% for BAG-2CNT coatings as compared to BAG coatings.

In electrochemical corrosion testing of the coatings, the OCP value was shifted to the noble direction for BAG-2CNT coatings as compared to other coatings. The BAG

coatings have highest I_{corr} value (9.789 $\mu A/cm^2$) due to maximum porosity while the BAG-2CNT have the least I_{corr} value (1.927 $\mu A/cm^2$). The EIS analysis also indicated the increase in the resistance value with the CNT addition in BAG coating. The reduction in the porosity values and CNT acting as an inert barrier to the SBF are the major reasons for the enhancement of corrosion resistance .

In-vitro Biocompatibility Studies

6.1 Introduction

This chapter deals with the in-vitro cell culture studies of the developed coatings. The MC3T3-E1 mouse osteoblast cell line was used for testing the biocompatibility of the coatings by following the standard protocols. The cell adhesion and growth of the MC3T3-E1 cells on the surfaces of the coatings were analyzed from FESEM images at different magnifications. The study was done on 1, 3, and 7 days to understand the cell growth and proliferation. Further, the cell viability percentage of all the samples was calculated after 1, 3 and 7 days to evaluate the cytotoxicity effects of coating on the cells. The effect of CNT reinforcement in the coatings on the cell culture studies have been discussed in this chapter. The simulated body fluid extract after immersing the samples was also analyzed by assessing the cell morphology and cell viability percentage.

6.2 Cell Adhesion and Growth

FESEM micrographs of MC3T3-E1 mouse osteoblast cells on the plasma sprayed HA, BAG, BAG-1CNT, and BAG-2CNT coatings are shown in Fig.6.1. The growth and adhesion of the cells inside the microstructures of the coatings after 1 day incubation is clearly observed. The cells on the CNT reinforced BAG coatings exhibit elongated spindle and flattened morphology and spreading of the cells over large area. Further, it is observed that the filopodia stretching out from the edge of the cells indicates more adhesion sites on BAG-CNT coating. The addition of CNT leads to enhanced cell spreading and stronger adhesion between the cells and the surfaces of the coatings [201].

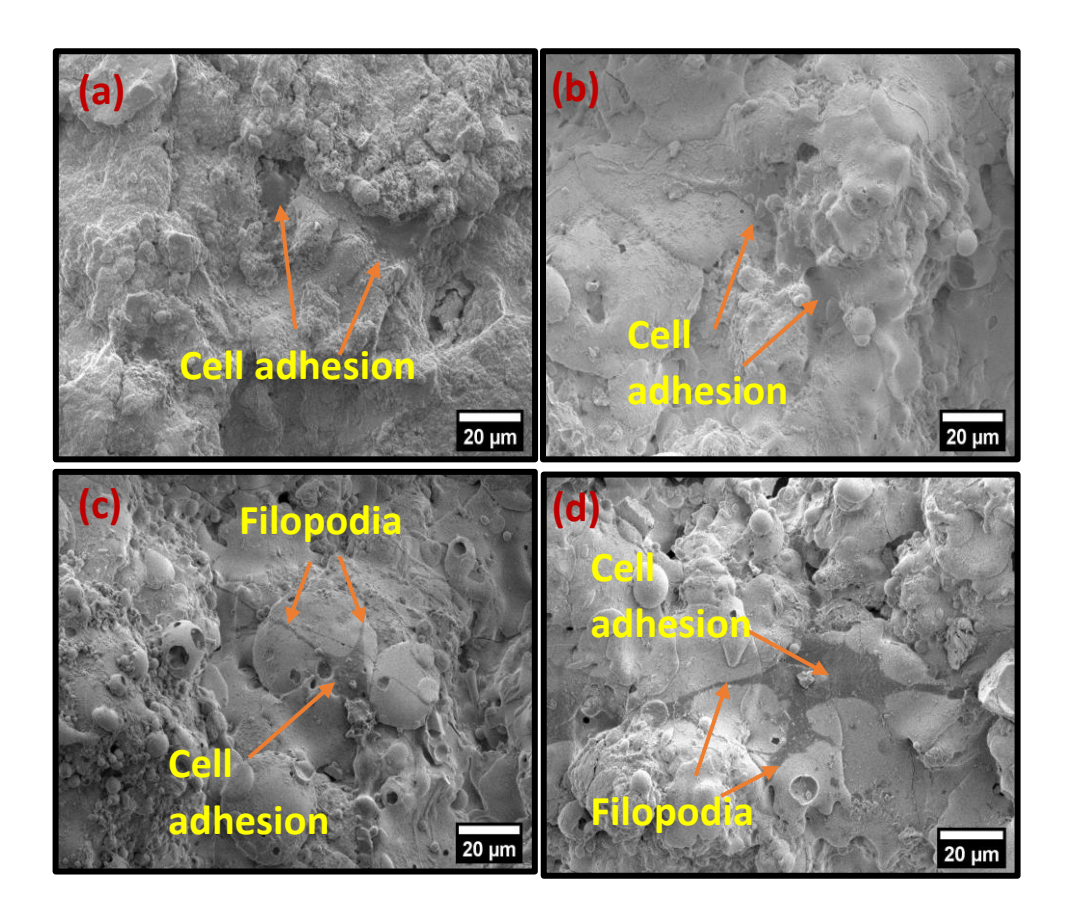


Figure 6.1 FESEM images showing successful adhesion of MC3T3-E1 cells on the surfaces of (a) HA (b) BAG (c) BAG-1CNT and (d) BAG-2CNT plasma sprayed coatings [201]

The FESEM micrographs represent the morphological features of MC3T3-E1 cell line on the developed coatings after 1, 3, and 7 days of culturing periods are shown in Fig.6.2. The images revealed good cell attachment, growth, and spreading on the surface of the coatings on all the days. The lateral spreading of the cells is observed after 3 days, which is favorable. After a period of 7 days, the cells exhibit a stretched and flattened morphology, resulting in the formation of a dense and contiguous cellular monolayer that covers a significant portion of the substrate surface. Moreover, there is penetration of the MC3T3-E1 cells in the microstructure of the coatings. The process of cell attachment and spreading on biomaterial surfaces is a key phenomenon that occurs at the early stage of cellular response. This behavior plays a crucial role in facilitating subsequent cell proliferation and differentiation[244]. Particularly, when the duration of culture increases, the MC3T3-E1 cells exhibit growth and proliferation, resulting in the coverage of nearly the entire coated surface after a period of 7 days. Hence, the results indicate the healthy development of MC3T3-E1 cells on all the coating surfaces

including the CNT-reinforced BAG coatings. In summary, the addition of CNT in BAG coatings exhibits no cytotoxicity effect on the MC3T3-E1 cells.

Pham et al. reported the colonisation of osteoblast cells on the surfaces of plasma sprayed HA and BAG coatings after one day incubation. The cells were adhered, proliferate and elongate on the coating surface at the end of day 3 and 5 [176]. Balani et al. reported the plasma sprayed HA-CNT composite coatings showed the cell growth and proliferation during cell culture studies. It demonstrated that HA-CNT coatings are non-toxic to bone cells [245]. Singh et al. fabricated the HA-TiO₂ coatings by plasma sprayed technique. The in vitro cell culture results indicated the adhesion and growth of MG-63 osteoblast cells on the surfaces of HA-30%TiO₂ coatings [246].

Cell adhesion and proliferation get affected by the surface topological features like surface roughness, surface chemistry, porosity and surface energy, as reported in the literature [247,248]. These factors contribute to the ultimate clinical success of the orthopedic implants. Surface roughness of the bio-implant is considered as one of the main factors in affecting the cellular response [249,250]. The developed coatings exhibit average surface roughness values between 8 μ m to 15 μ m. The slight increase in average surface roughness with CNT reinforcement has positively impacted cellular response, ensuring the mechanical stability by early fixation of the bioimplants [230].

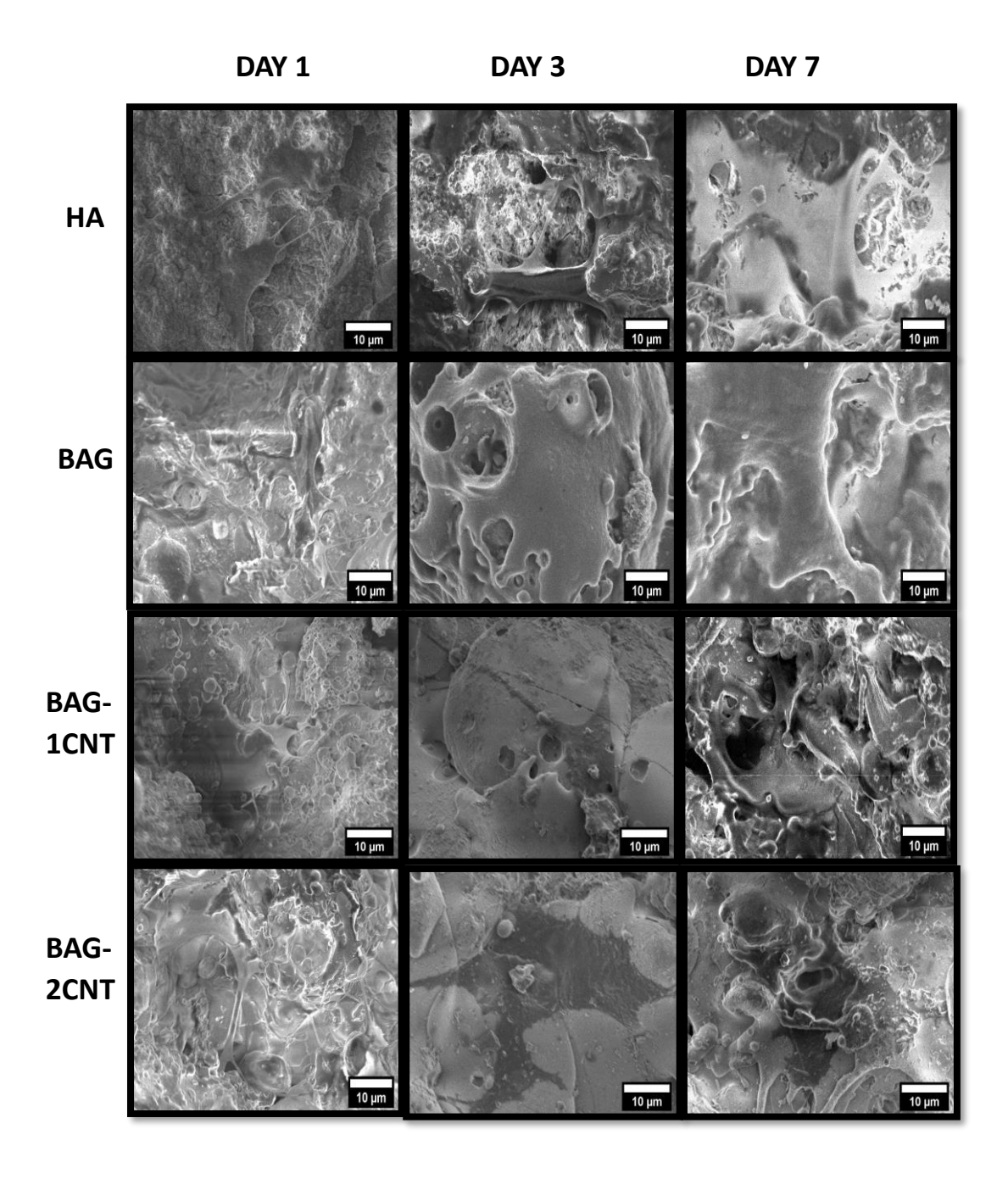


Figure.6.2 FESEM images of MC3T3-E1 cell morphology on HA, BAG, BAG-1CNT and BAG-2CNT plasma sprayed coatings after incubation periods of 1,3 and 7 days [190]

Previous research has highlighted the positive impact of CNT on promoting cell adhesion in-vitro, in both osteoblasts and fibroblasts [251]. In addition, several in vivo investigations have demonstrated the favorable compatibility of CNT with bone tissue, indicating their potential utility in bone healing [252].

FESEM images show the filopodia development of MC3T3-E1 cells on the surfaces of plasma-sprayed HA, BAG, BAG-1CNT, and BAG-2CNT coatings, as shown in Fig.6.3. Filopodia are cellular extensions composed of actin filaments that project outward from the periphery of the cell. The formation of filopodia serves as a crucial indicator of the effective colonization and spreading of cells on implant surfaces [253]. The filopodia formation of MC3T3-E1 cells on the surfaces of CNT-reinforced BAG coatings indicates the normal development of the cells [190].

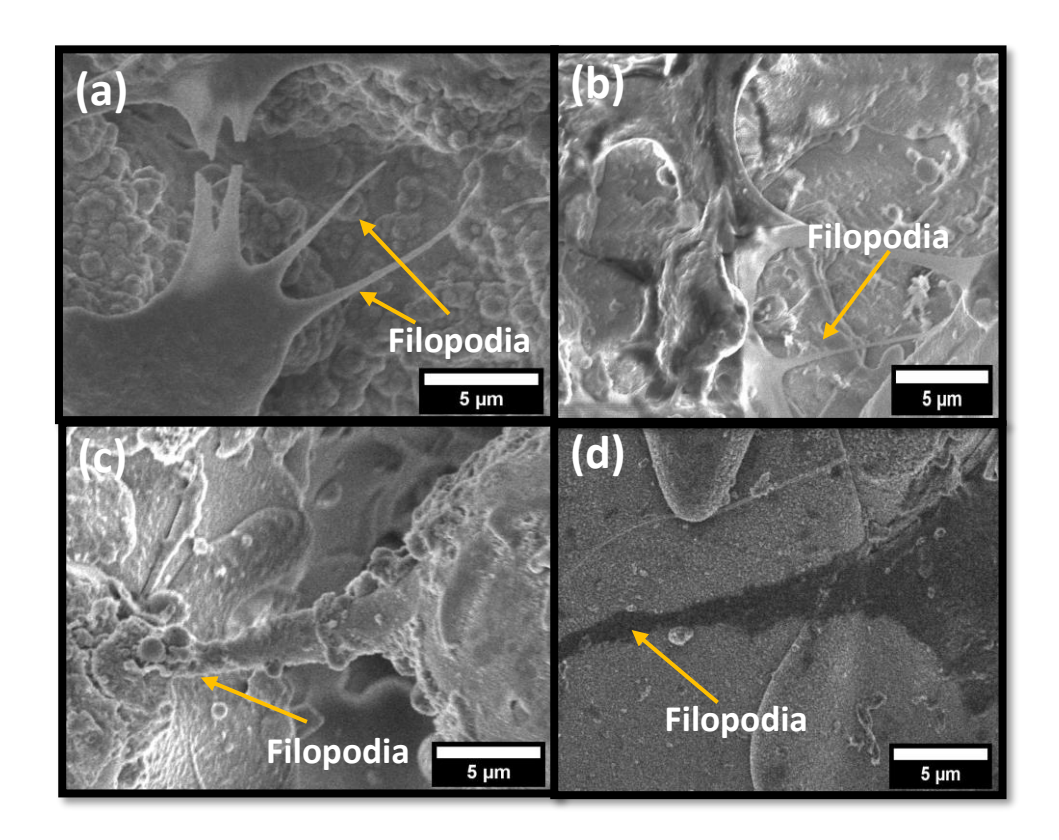


Figure 6.3 Filopodia developments of MC3T3-E1 cells on the surfaces of (a) HA (b) BAG (c) BAG-1CNT and (d) BAG-2CNT plasma sprayed coatings [190]

6.3 Cell Viability Analysis

Further, the percentage of cell viability after 1, 3, and 7 days of incubation period on HA, BAG, BAG-1CNT, and BAG-2CNT coatings is shown in Fig.6.4. The graph clearly indicates that all the samples exhibit cell viability percentage above 60% at the end of day 7. Further, the BAG-2CNT coatings exhibit the highest cell viability percentage for all the days, indicating enhanced growth rate of MC3T3-E1 cells.

The cytotoxicity of CNT has been studied by many researchers indicating the positive response of CNT to bone cells [254]. Kalmodia et al. prepared CNT-reinforced composites and reported good adhesion and growth of cells [255]. The osteoblast cells showed normal growth and proliferation on the CNT-reinforced surfaces. This is attributed to the selective absorption and attachment of proteins from cell culture medium due to the presence of C-C bonds [256,257]. The bioactive nature and high surface area of CNT contribute to better proliferation and viability of osteoblast cells [258]. The filopodia protrusions have also been observed along with the active spreading of MC3T3-E1 osteoblast cells on the surfaces of CNT-reinforced BAG coatings. However, with the increase in CNT concentration, there is a chance of a cytotoxic effect due to the presence of metallic catalyst particles and CNT agglomeration [259,260]. Khalid et. al. studied the CNT-reinforced HA composites and their interaction with human osteoblast cells. They reported a decline in cell viability percentage with the increase in CNT content, indicating potential cytotoxic at higher concentrations of CNT [261]. In conclusion, the incorporation of CNT in the coatings enhances biocompatibility without inducing cytotoxic effects, as evidenced by the results [190].

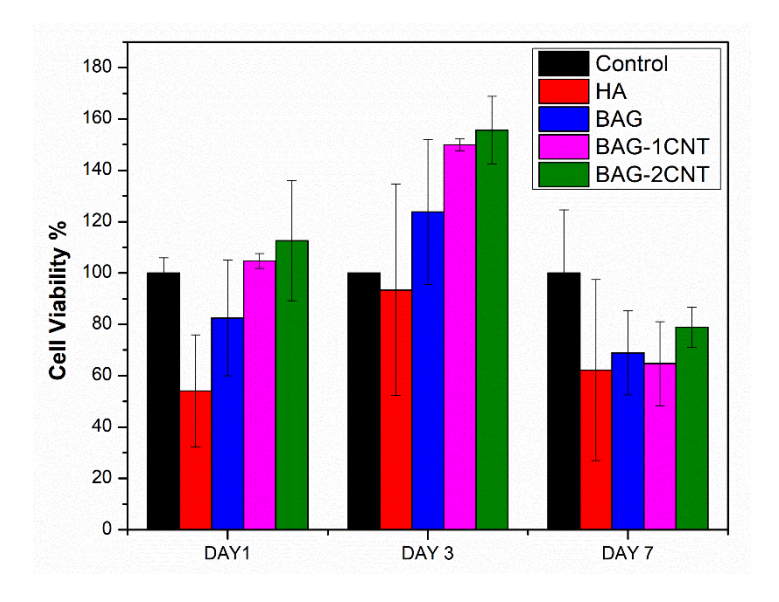


Figure 6.4 Cell viability % of MC3T3-E1 cells on HA, BAG, BAG-1CNT and BAG-2CNT plasma-sprayed coatings

6.4 Zr Toxicity Analysis

The presence of Zr in baghdadite (BAG) ceramic plays an important role in the biological properties and improves the structural stability of calcium-silicate ceramics [164]. The Zr ions are anyway present at trace levels in the range of 2–20 mg/kg body weight in the human bones and tissues with an average daily intake of 3.5 mg. In BAG ceramic, the Zr ions are released in more controllable concentrations in the range of 10-100 μ M into SBF [262]. On the other hand, a study reveals that Zr did not reduce the proliferation of osteoblast cells below concentrations of 0.1 mM [263]. The in-vitro studies indicated that Zr can improve the proliferation and differentiation of human osteoblasts due to up-regulation of BMP2 expression and increased BMP signaling. Further, the Zr ions have novel osteogenic activity on primary human osteoblast and enhance their differentiation into osteoblasts and mineralized bone matrix [262,264].

Several studies reported the Zr-incorporated ceramic may have a crucial function in promoting the proliferation of bone marrow stromal cells (BMSCs) and have the capability of inducing angiogenesis in biological conditions [265,266]. Pahlevanzadeh et al. prepared the bone cement of polymethyl methacrylate (PMMA) and BAG and reported the release of Zr ions in SBF led to the formation of Zr-OH. This increased the nucleation of new apatite and enhanced the bioactivity in BAG groups [267]. Therefore, based on the literature it can be concluded that the released Zr ions positively affected cell adhesion, proliferation, and differentiation. Another in vivo study confirmed that the BAG stimulates osteogenesis [268].

The toxicity due to Zr ions release was tested by analyzing the SBF extract. The optical images showed no change in the morphology of the fibroblast cells as shown in Fig. 6.5. Further, a gradual increase in the number of cells was observed at the end of day 3 similar to control. The cell viability percentage graph for 1 and 3-day studies is presented in Fig.6.6. The graph indicates the percentage of viable cells was above 70% in all the samples. Based on the above results, it can be concluded that the presence of Zr in BAG has no cytotoxicity effects on the cells.

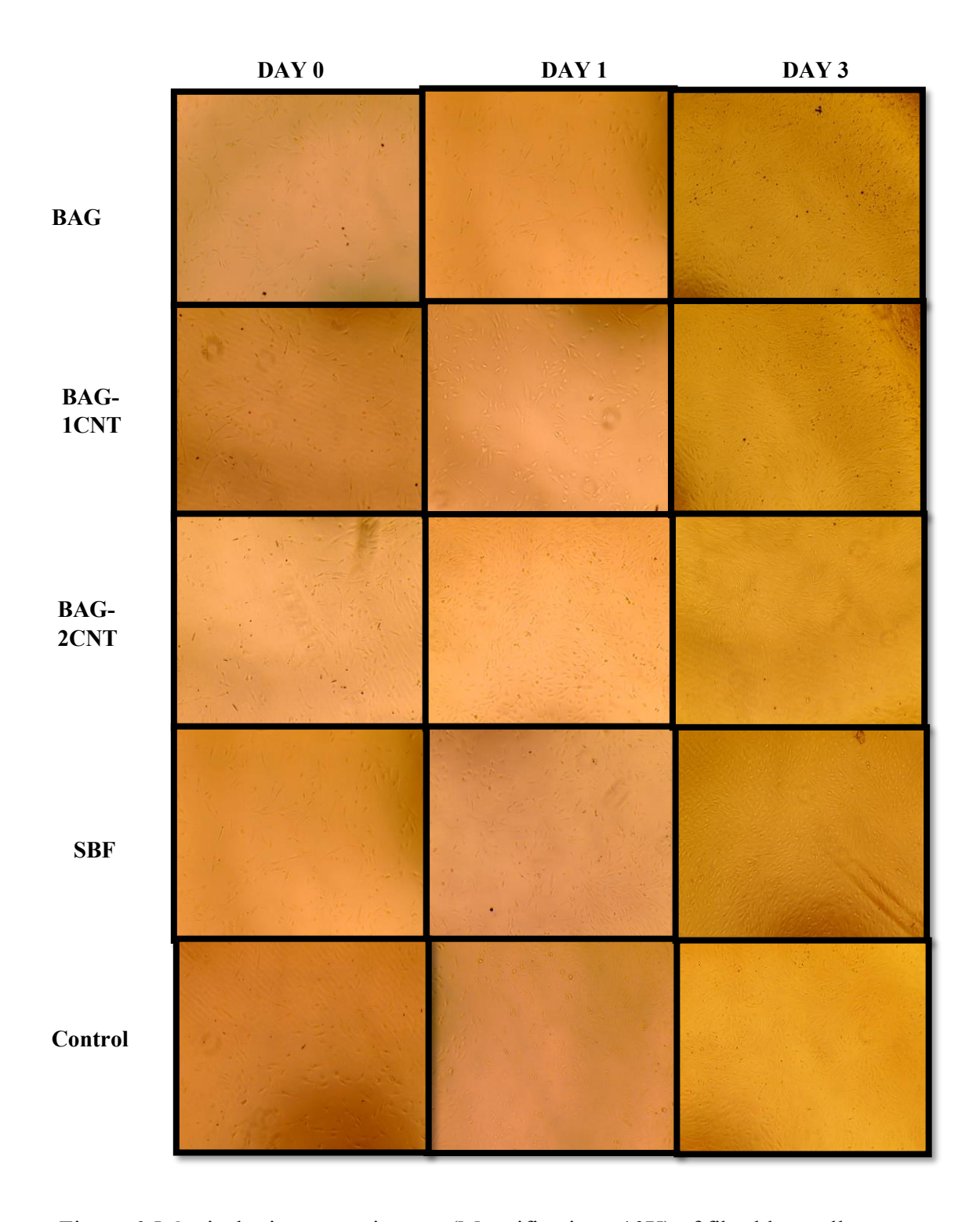


Figure 6.5 Optical microscopy images (Magnification= 10X) of fibroblast cells on plasma sprayed BAG, BAG-1CNT and BAG-2CNT coatings compared with SBF and control

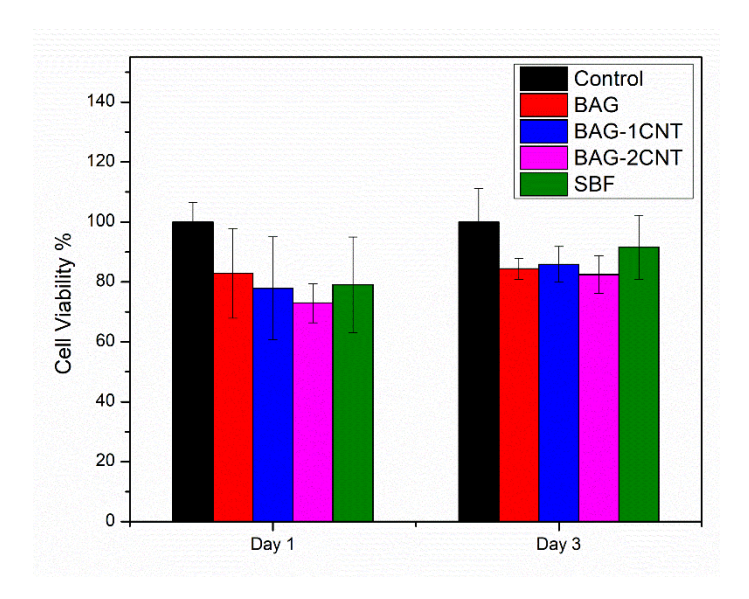
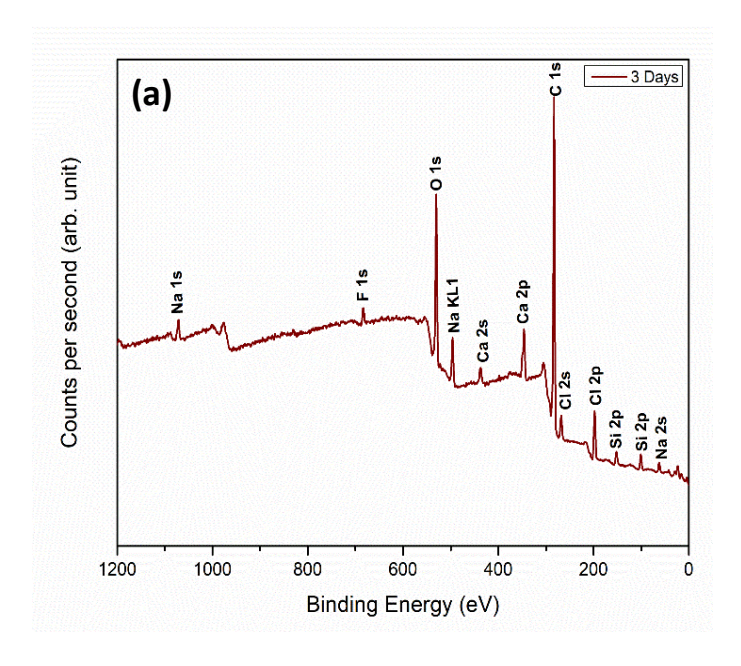


Figure 6.6 Cell viability % of BAG, BAG-1CNT and BAG-2CNT coatings compared with SBF and control

The XPS peaks of the SBF extract of BAG coated samples after 3 and 7 days is shown in Fig.6.7. The Ca and Si peaks have been observed in the spectrum of 3 and 7 days. The Ca 2p and Ca 2s peaks are at 346 and 437eV binding energies respectively while the Si 2p are at 101 and 152 eV. The Na 1s, Na 2s, Cl 2s and Cl 2p peaks have been observed due to the presence of NaCl in the SBF. However, no Zr peaks were observed in the spectrum of both 3 days and 7 days. The results indicate negligible release of Zr ions in SBF after 7 days which is desirable to avoid any potential carcinogenicity and inflammatory responses.



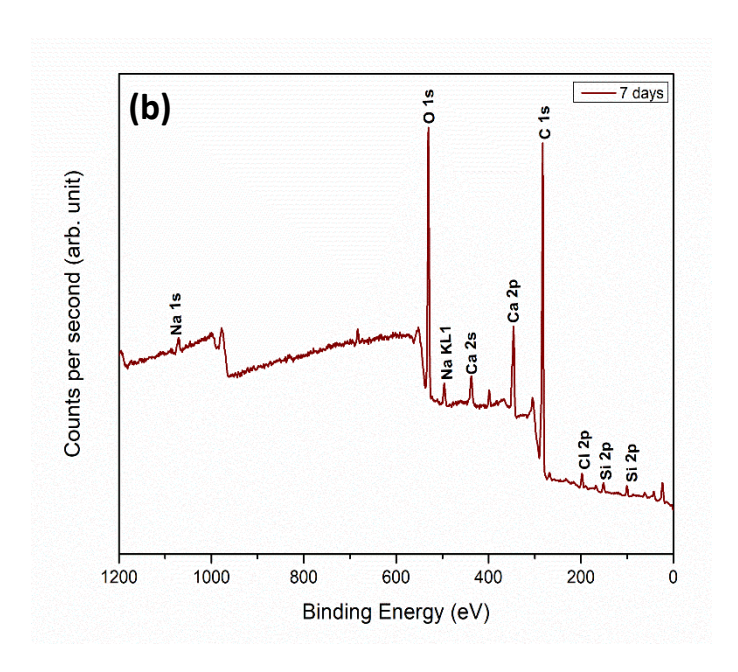


Figure 6.7 XPS graphs of SBF extract of plasma sprayed BAG coatings immersed for (a) 3 days and (b) 7 days

6.5 Summary of the Chapter

The in-vitro cell culture studies of HA, BAG, BAG-1CNT, and BAG-2CNT plasma spray coatings have been evaluated. The FESEM micrographs of MC3T3-E1 cell line morphological features on the coatings after 1, 3, and 7 days of culturing, showed good cell attachment, growth, and spreading. The dense cellular monolayer covering the substrate after the end of day 7 indicated healthy cell development. The CNT addition in the coatings does not exhibit cytotoxic effects while the increase in the surface roughness with CNT reinforcement positively impacts the cellular response and ensures mechanical stability for early bioimplant fixation.

The good cell viability % of all the developed coatings was observed after 1, 3 and 7 days of incubation period. The cell proliferation rate was increased with the CNT addition as BAG-2CNT coatings have the highest value of cell viability %.

Conclusion and Future Work

7.1 Conclusions

In the current study, novel CNT-reinforced BAG plasma sprayed coatings have been developed for biomedical implant applications to improve mechanical, electrochemical, and biological properties. The investigated properties have been comprehensively compared with pure HA and BAG coatings. The following conclusions have been drawn from the results-

7.1.1 Coatings Development and Characterization

- 1. The plasma-sprayed HA, BAG, BAG-1CNT and BAG-2CNT coatings have been successfully deposited on the Ti substrate. All the coatings remained fully intact on their respective substrates.
- 2. The microstructure, morphology, and phases present before and after coating deposition have been studied by SEM-EDS and XRD. The BAG coatings have exhibited a more fully melted region due to the effective fusion of irregularly shaped BAG particles.
- 3. Microstructural observations revealed both partially and fully melted regions, with a uniform distribution of CNT in BAG-CNT coatings.
- 4. The HA coating has Ca, P, and O as the primary elements while the BAG coating has Ca, Zr, Si, and O as major elements.
- 5. XRD analysis indicated the Hydroxyapatite and Baghdadite as the major phases in the HA and BAG coatings respectively.
- 6. Raman spectroscopy has confirmed the retention of CNT in BAG-1CNT and BAG-2CNT coatings.
- 7. The cross-sectional analysis of the coatings revealed the homogenous distribution of the elements and the thickness of the coatings in the range of $350-450 \ \mu m$.

8. Porosity analysis has indicated that the addition of 2wt% CNT to BAG coatings significantly reduced porosity. This reduction may be associated with the filling of gaps in the intersplat area by the CNT.

7.1.2 Mechanical and Electrochemical Behavior of the Developed

Coatings

- Surface roughness parameters (R_a, R_q, and R_z) have been measured for all
 the coatings and it is found that pure BAG coating has exhibited higher
 surface roughness than pure HA coatings because of large size particle
 distributions. The roughness values further increase with the addition of
 CNT in BAG coatings.
- 2. The reinforcement of 2 wt% CNT in BAG coatings has resulted an increase in microhardness by 38.75%. It can be attributed to reduced porosity, uniform CNT distribution, and effective anchoring within the BAG ceramic matrix.
- 3. Scratch testing results indicated a reduction in wear volume loss by 16.45% and scratch rate by 16.38% with the reinforcement of 2 wt% CNT in BAG coatings. Further, BAG-2CNT coatings exhibited the highest scratch hardness among all the investigated coatings.
- 4. The CNT reinforcement resulted in the reduction of penetration depth and scratch width of the coatings. Moreover, the increase in critical load values in BAG-2CNT coatings indicated the enhancement of the cohesion strength of the coatings. It can be attributed to the improved interlocking and mechanical anchorage among the splats provided by CNT.
- 5. The electrochemical corrosion testing has revealed an 80% reduction in I_{corr} for BAG-2CNT coatings in comparison to pure BAG coating.
- 6. EIS analysis has shown the addition of CNT improved the corrosion performance of the coatings. This can be attributed to the reduction in porosity and CNT acting as a chemical barrier to SBF.

7.1.3 In-vitro biocompatibility studies of the coatings

- 1. In-vitro cell culture studies of HA, BAG and CNT-reinforced coatings revealed good cell attachment, adhesion and growth of the MC3T3-E1 osteoblast cell line.
- 2. The filopodia development of MC3T3-E1 cells on the surfaces of the coatings indicated the effective colonization and spreading of the cells.
- 3. The cell viability % of the coatings was above 60% at the end of day 7. Further, BAG-2CNT coatings exhibited the highest cell viability % after 1, 3, and 7 days of observation which showed no cytotoxicity caused by the CNT reinforcement.
- 4. The cell morphology and cell viability % SBF extract after the immersion of samples for 7 days showed cell growth and proliferation. The XPS analysis indicated the negligible release of Zr in BAG coatings.

Overall, this work demonstrates the use of plasma-sprayed BAG coatings reinforced with CNT exhibits favourable mechanical properties, electrochemical properties and biocompatibility. Hence, it can be considered a promising candidate for orthopedic implant applications [190].

7.2 Future Work

- Optimization of coating properties- The process parameters of plasma spraying
 can be further refined to enhance the mechanical, electrochemical, and
 biological properties of the coatings including adhesion strength, porosity
 control, and phase purity.
- Surface modification- Investigating surface modification techniques such as surface modification techniques such as surface roughening, functionalization or coating with bioactive molecules to further improve the bioactivity and osseointegration of BAG coatings with host tissue.
- In-vivo studies- BAG ceramic is still in the experimental stage. Several in vivo
 animal studies can be conducted for evaluating the tissue response, and
 inflammatory reactions to assess the safety and long-term performance of these
 coatings.
- 4. Degradation behavior- Understanding the degradation behavior of plasma sprayed baghdadite coatings in physiological environments, including the effect

- of coating thickness, microstructure, and exposure conditions on their long-term stability and bioresorption kinetics.
- 5. *Multi-functional coatings* Apart from CNT, the incorporation of therapeutic agents, growth factors, or antibacterial agents into BAG coatings can be investigated which will impart additional functionalities such as enhanced tissue regeneration, controlled drug release, and infection prevention.
- 6. CNT reinforcement optimization- Several other compositions of CNT reinforcement can be studied to find the optimum quantity to enhance the desired properties while minimizing the agglomeration and defects.
- 7. Advanced coating techniques- BAG-CNT composite coatings can be developed by advanced thermal spray techniques like cold spray and can be compared with the developed plasma sprayed coatings.
- 8. *Post-processing of coatings* The heat treatment of the coatings can be studied to optimize the crystallinity, phase composition and microstructure of the BAG matrix. This will result in the enhancement of mechanical strength, chemical stability and bioactivity of the coatings.

References

- [1] A. Arsiwala, P. Desai, V. Patravale, Recent advances in micro/nanoscale biomedical implants, Journal of Controlled Release 189 (2014) 25–45. https://doi.org/10.1016/j.jconrel.2014.06.021.
- [2] G. Manivasagam, D. Dhinasekaran, A. Rajamanickam, Biomedical Implants: Corrosion and its Prevention A Review, Recent Patents on Corrosion Science 2 (2010) 40–54. https://doi.org/10.2174/1877610801002010040.
- [3] D.R. Holmes, D.J. Kereiakes, S. Garg, P.W. Serruys, G.J. Dehmer, S.G. Ellis, D.O. Williams, T. Kimura, D.J. Moliterno, Stent Thrombosis, J Am Coll Cardiol 56 (2010) 1357–1365. https://doi.org/10.1016/j.jacc.2010.07.016.
- [4] K.E. Hammermeister, G.K. Sethi, W.G. Henderson, C. Oprian, T. Kim, S. Rahimtoola, A Comparison of Outcomes in Men 11 Years after Heart-Valve Replacement with a Mechanical Valve or Bioprosthesis, New England Journal of Medicine 328 (1993) 1289–1296. https://doi.org/10.1056/NEJM199305063281801.
- [5] M. Esposito, Y. Ardebili, H. V Worthington, Interventions for replacing missing teeth: different types of dental implants, Cochrane Database of Systematic Reviews (2014). https://doi.org/10.1002/14651858.CD003815.pub4.
- [6] L. Gaviria, J.P. Salcido, T. Guda, J.L. Ong, Current trends in dental implants, J Korean Assoc Oral Maxillofac Surg 40 (2014) 50. https://doi.org/10.5125/jkaoms.2014.40.2.50.
- [7] A.L. Benabid, S. Chabardes, J. Mitrofanis, P. Pollak, Deep brain stimulation of the subthalamic nucleus for the treatment of Parkinson's disease, Lancet Neurol 8 (2009) 67–81. https://doi.org/10.1016/S1474-4422(08)70291-6.
- [8] W.M. Grill, S.E. Norman, R. V. Bellamkonda, Implanted Neural Interfaces: Biochallenges and Engineered Solutions, Annu Rev Biomed Eng 11 (2009) 1–24. https://doi.org/10.1146/annurev-bioeng-061008-124927.
- [9] J. Howatt, A.S. Liew, G. Wilkin, Patellar Fractures, Journal of Bone and Joint Surgery 103 (2021) 2237–2246. https://doi.org/10.2106/JBJS.20.01478.
- [10] R. Dimitriou, E. Jones, D. McGonagle, P. V Giannoudis, Bone regeneration: current concepts and future directions, BMC Med 9 (2011) 66. https://doi.org/10.1186/1741-7015-9-66.
- [11] J.C. Mora, R. Przkora, Y. Cruz-Almeida, Knee osteoarthritis: Pathophysiology and current treatment modalities, J Pain Res 11 (2018) 2189–2196. https://doi.org/10.2147/JPR.S154002.
- [12] THE GLOBAL BURDEN OF DISEASE, n.d.
- [13] J.A. Buckwalter, Sports, Joint Injury, and Posttraumatic Osteoarthritis, 2003. www.jospt.org.

- [14] S. V. Garstang, T.P. Stitik, Osteoarthritis, Am J Phys Med Rehabil 85 (2006) S2–S11. https://doi.org/10.1097/01.phm.0000245568.69434.1a.
- [15] H.A. Wieland, M. Michaelis, B.J. Kirschbaum, K.A. Rudolphi, Osteoarthritis an untreatable disease?, Nat Rev Drug Discov 4 (2005) 331–344. https://doi.org/10.1038/nrd1693.
- [16] E. Qvistgaard, R. Christensen, S. Torp-Pedersen, H. Bliddal, Intra-articular treatment of hip osteoarthritis: a randomized trial of hyaluronic acid, corticosteroid, and isotonic saline, Osteoarthritis Cartilage 14 (2006) 163–170. https://doi.org/10.1016/j.joca.2005.09.007.
- [17] M. Wathier, B.A. Lakin, P.N. Bansal, S.S. Stoddart, B.D. Snyder, M.W. Grinstaff, A Large-Molecular-Weight Polyanion, Synthesized via Ring-Opening Metathesis Polymerization, as a Lubricant for Human Articular Cartilage, J Am Chem Soc 135 (2013) 4930–4933. https://doi.org/10.1021/ja400695h.
- [18] Courtney Philip, Doherty Michael, Intra-articular corticosteroid injection for osteoarthritis, Int J Clin Rheumtol 4 (2009).
- [19] J.C. Van Egmond, H. Verburg, N.M.C. Mathijssen, The first 6 weeks of recovery after total knee arthroplasty with fast track, Acta Orthop 86 (2015) 708–713. https://doi.org/10.3109/17453674.2015.1081356.
- [20] https://www.medfin.in/blog/orthopaedic/total-knee-replacement/impact-of-tkr-surgery-on-quality-life/, (n.d.).
- [21] A.J. Tande, R. Patel, Prosthetic Joint Infection, Clin Microbiol Rev 27 (2014) 302–345. https://doi.org/10.1128/CMR.00111-13.
- [22] M.P. Ast, M.P. Abdel, Y. Lee, S. Lyman, A. V. Ruel, G.H. Westrich, Weight Changes After Total Hip or Knee Arthroplasty, Journal of Bone and Joint Surgery 97 (2015) 911–919. https://doi.org/10.2106/JBJS.N.00232.
- [23] P.F. Sharkey, P.M. Lichstein, C. Shen, A.T. Tokarski, J. Parvizi, Why Are Total Knee Arthroplasties Failing Today—Has Anything Changed After 10 Years?, J Arthroplasty 29 (2014) 1774–1778. https://doi.org/10.1016/j.arth.2013.07.024.
- [24] D.F. Williams, On the nature of biomaterials, Biomaterials 30 (2009) 5897–5909. https://doi.org/10.1016/j.biomaterials.2009.07.027.
- [25] J.B. Park, J.D. Bronzino, eds., Biomaterials, CRC Press, 2002. https://doi.org/10.1201/9781420040036.
- [26] M.B. Nasab, M.R. Hassan, Metallic Biomaterials of Knee and Hip-A Review, 2010. http://www.sbaoi.org.
- [27] J. Alvarado, R. Maldonado, J. Marxuach, R. Otero, BIOMECHANICS OF HIP AND KNEE PROSTHESES 1, 2003. http://www.ece.uprm.edu/~m goyal/home.htm.

- [28] M. Geetha, A.K. Singh, R. Asokamani, A.K. Gogia, Ti based biomaterials, the ultimate choice for orthopaedic implants A review, Prog Mater Sci 54 (2009) 397–425. https://doi.org/10.1016/j.pmatsci.2008.06.004.
- [29] W. Cui, L. Cao, X. Zhang, Bioceramics: materials, properties, and applications, in: Ceramic Science and Engineering, Elsevier, 2022: pp. 65–110. https://doi.org/10.1016/B978-0-323-89956-7.00017-6.
- [30] T. Ayode Otitoju, P. Ugochukwu Okoye, G. Chen, Y. Li, M. Onyeka Okoye, S. Li, Advanced ceramic components: Materials, fabrication, and applications, Journal of Industrial and Engineering Chemistry 85 (2020) 34–65. https://doi.org/10.1016/j.jiec.2020.02.002.
- [31] M.N. Rahaman, A. Yao, B.S. Bal, J.P. Garino, M.D. Ries, Ceramics for Prosthetic Hip and Knee Joint Replacement, Journal of the American Ceramic Society 90 (2007) 1965–1988. https://doi.org/10.1111/j.1551-2916.2007.01725.x.
- [32] A. Ershad-Langroudi, N. Babazadeh, F. Alizadegan, S. Mehdi Mousaei, G. Moradi, Polymers for implantable devices, Journal of Industrial and Engineering Chemistry 137 (2024) 61–86. https://doi.org/10.1016/J.JIEC.2024.03.030.
- [33] D.F. Williams, Biomaterials On the nature of biomaterials q, Biomaterials 30 (2009) 5897–5909. https://doi.org/10.1016/j.biomaterials.2009.07.027.
- [34] C.R. Arciola, D. Campoccia, P. Speziale, L. Montanaro, J.W. Costerton, Biofilm formation in Staphylococcus implant infections. A review of molecular mechanisms and implications for biofilm-resistant materials, Biomaterials 33 (2012) 5967–5982. https://doi.org/10.1016/j.biomaterials.2012.05.031.
- [35] N. Eliaz, Corrosion of Metallic Biomaterials: A Review, Materials 12 (2019) 407. https://doi.org/10.3390/ma12030407.
- [36] B.N. Popov, Corrosion Engineering: Principles and Solved Problems, Elsevier, 2015. https://doi.org/10.1016/C2012-0-03070-0.
- [37] J.J. JACOBS, J.L. GILBERT, R.M. URBAN, Corrosion of Metal Orthopaedic Implants*, J Bone Joint Surg Am 80 (1998) 268–282. https://doi.org/10.2106/00004623-199802000-00015.
- [38] Q. Chen, G.A. Thouas, Metallic implant biomaterials, Materials Science and Engineering: R: Reports 87 (2015) 1–57. https://doi.org/10.1016/j.mser.2014.10.001.
- [39] J. Pouilleau, D. Devilliers, F. Garrido, S. Durand-Vidal, E. Mahé, Structure and composition of passive titanium oxide films, Materials Science and Engineering: B 47 (1997) 235–243. https://doi.org/10.1016/S0921-5107(97)00043-3.

- [40] D.G. Olmedo, G. Duffó, R.L. Cabrini, M.B. Guglielmotti, Local effect of titanium implant corrosion: an experimental study in rats, Int J Oral Maxillofac Surg 37 (2008) 1032–1038. https://doi.org/10.1016/j.ijom.2008.05.013.
- [41] B. Tritschler, B. Forest, J. Rieu, Fretting corrosion of materials for orthopaedic implants: a study of a metal/polymer contact in an artificial physiological medium, Tribol Int 32 (1999) 587–596. https://doi.org/10.1016/S0301-679X(99)00099-7.
- [42] F.M.S. Soares, C.N. Elias, E.S. Monteiro, M.E.R. Coimbra, A.I.C. Santana, Galvanic Corrosion of Ti Dental Implants Coupled to CoCrMo Prosthetic Component, Int J Biomater 2021 (2021) 1–11. https://doi.org/10.1155/2021/1313343.
- [43] D.L. Levine, R.W. Staehle, Crevice corrosion in orthopedic implant metals, J Biomed Mater Res 11 (1977) 553–561. https://doi.org/10.1002/jbm.820110410.
- [44] S. Jafari, S.E. Harandi, R.K. Singh Raman, A Review of Stress-Corrosion Cracking and Corrosion Fatigue of Magnesium Alloys for Biodegradable Implant Applications, JOM 67 (2015) 1143–1153. https://doi.org/10.1007/s11837-015-1366-z.
- [45] W.H. Harris, Wear and Periprosthetic Osteolysis, Clin Orthop Relat Res 393 (2001) 66–70. https://doi.org/10.1097/00003086-200112000-00007.
- [46] J. Hembus, L. Lux, M. Jackszis, R. Bader, C. Zietz, Wear analysis of cross-linked polyethylene inserts articulating with alumina and ion-treated cobalt-chromium femoral heads under third-body conditions, Wear 402–403 (2018) 216–223. https://doi.org/10.1016/j.wear.2018.02.017.
- [47] W. Toh, X. Tan, A. Bhowmik, E. Liu, S. Tor, Tribochemical Characterization and Tribocorrosive Behavior of CoCrMo Alloys: A Review, Materials 11 (2017) 30. https://doi.org/10.3390/ma11010030.
- [48] M.T. Mathew, P. Srinivasa Pai, R. Pourzal, A. Fischer, M.A. Wimmer, Significance of Tribocorrosion in Biomedical Applications: Overview and Current Status, Advances in Tribology 2009 (2009) 1–12. https://doi.org/10.1155/2009/250986.
- [49] J.L. Katz, Anisotropy of Young's modulus of bone, Nature 283 (1980) 106–107. https://doi.org/10.1038/283106a0.
- [50] D.R. Sumner, T.M. Turner, R. Igloria, R.M. Urban, J.O. Galante, Functional adaptation and ingrowth of bone vary as a function of hip implant stiffness, J Biomech 31 (1998) 909–917. https://doi.org/10.1016/S0021-9290(98)00096-7.
- [51] L. Sun, Thermal Spray Coatings on Orthopedic Devices: When and How the FDA Reviews Your Coatings, Journal of Thermal Spray Technology 27 (2018) 1280–1290. https://doi.org/10.1007/s11666-018-0759-2.

- [52] G. Manivasagam, D. Dhinasekaran, A. Rajamanickam, Biomedical Implants: Corrosion and its Prevention A Review, Recent Patents on Corrosion Science 2 (2010) 40–54. https://doi.org/10.2174/1877610801002010040.
- [53] Corrosion of metals and alloys Basic terms and definitions, (1999).
- [54] Y. Liu, D. Zhu, D. Pierre, J.L. Gilbert, Fretting initiated crevice corrosion of 316LVM stainless steel in physiological phosphate buffered saline: Potential and cycles to initiation, Acta Biomater 97 (2019) 565–577. https://doi.org/10.1016/j.actbio.2019.07.051.
- [55] B. Aksakal, Ö.S. Yildirim, H. Gul, Metallurgical Failure Analysis of Various Implant Materials Used in Orthopedic Applications, Journal of Failure Analysis & Prevention 4 (2004) 17–23. https://doi.org/10.1361/15477020419794.
- [56] Q. Wang, F. Eltit, R. Feng, D. Garbuz, C. Duncan, B.A. Masri, N. Greidanus, M.E. Cox, R. Wang, Nature of fretting corrosion products in CoCrMo hip implants from in vivo study to in vitro simulation, Materialia (Oxf) 22 (2022) 101433. https://doi.org/10.1016/j.mtla.2022.101433.
- [57] J.L. Gilbert, C.A. Buckley, J.J. Jacobs, K.C. Bertin, M.R. Zernich, Intergranular corrosion-fatigue failure of cobalt-alloy femoral stems. A failure analysis of two implants, J Bone Joint Surg 76 (1994).
- [58] K. Merritt, S.A. Brown, Release of hexavalent chromium from corrosion of stainless steel and cobalt—chromium alloys, J Biomed Mater Res 29 (1995) 627–633. https://doi.org/10.1002/jbm.820290510.
- [59] P.R. Walker, J. LeBlanc, M. Sikorska, Effects of aluminum and other cations on the structure of brain and liver chromatin, Biochemistry 28 (1989) 3911–3915. https://doi.org/10.1021/bi00435a043.
- [60] B.C. Costa, C.K. Tokuhara, L.A. Rocha, R.C. Oliveira, P.N. Lisboa-Filho, J. Costa Pessoa, Vanadium ionic species from degradation of Ti-6Al-4V metallic implants: In vitro cytotoxicity and speciation evaluation, Materials Science and Engineering: C 96 (2019) 730–739. https://doi.org/10.1016/j.msec.2018.11.090.
- [61] Willert H, L. Brobäck, G. Buchhorn, P.H. Jensen, G. Köster, I. Lang, P. Ochsner, R. Schenk, Crevice Corrosion of Cemented Titanium Alloy Stems in Total Hip Replacements, Clin Orthop Relat Res (1996).
- [62] M. NAKAGAWA, S. MATSUYA, K. UDOH, Corrosion Behavior of Pure Titanium and Titanium Alloys in Fluoride-containing Solutions., Dent Mater J 20 (2001) 305–314. https://doi.org/10.4012/dmj.20.305.
- [63] C.T. dos Santos, C. Barbosa, M. de J. Monteiro, I. de C. Abud, I.M.V. Caminha, C.R. de M. Roesler, Fretting corrosion tests on orthopedic plates and screws made of ASTM F138 stainless steel, Research on Biomedical Engineering 31 (2015) 169–175. https://doi.org/10.1590/2446-4740.0710.
- [64] R.A. Cooper, C.M. McAllister, L.S. Borden, T.W. Bauer, Polyethylene debrisinduced osteolysis and loosening in uncemented total hip arthroplasty, J

- Arthroplasty 7 (1992) 285–290. https://doi.org/10.1016/0883-5403(92)90050-Z.
- [65] S.A. Syggelos, A.J. Aletras, I. Smirlaki, S.S. Skandalis, Extracellular Matrix Degradation and Tissue Remodeling in Periprosthetic Loosening and Osteolysis: Focus on Matrix Metalloproteinases, Their Endogenous Tissue Inhibitors, and the Proteasome, Biomed Res Int 2013 (2013) 1–18. https://doi.org/10.1155/2013/230805.
- [66] relationship of acetabular wear to osteolysis and 18, (n.d.).
- [67] A. Wennerberg, T. Albrektsson, Effects of titanium surface topography on bone integration: a systematic review, Clin Oral Implants Res 20 (2009) 172–184. https://doi.org/10.1111/j.1600-0501.2009.01775.x.
- [68] D. Roe, B. Karandikar, N. Bonn-Savage, B. Gibbins, J.-B. Roullet, Antimicrobial surface functionalization of plastic catheters by silver nanoparticles, Journal of Antimicrobial Chemotherapy 61 (2008) 869–876. https://doi.org/10.1093/jac/dkn034.
- [69] S. Govender, C. Csimma, H.K. Genant, A. Valentin-Opran, COPYRIGHT © 2002 BY THE JOURNAL OF BONE AND JOINT SURGERY, INCORPORATED Recombinant Human Bone Morphogenetic Protein-2 for Treatment of Open Tibial Fractures A PROSPECTIVE, CONTROLLED, RANDOMIZED STUDY OF FOUR HUNDRED AND FIFTY PATIENTS BY THE BMP-2 EVALUATION IN SURGERY FOR TIBIAL TRAUMA (BESTT) STUDY GROUP, 2002. http://journals.lww.com/jbjsjournal.
- [70] M.P. Staiger, A.M. Pietak, J. Huadmai, G. Dias, Magnesium and its alloys as orthopedic biomaterials: A review, Biomaterials 27 (2006) 1728–1734. https://doi.org/10.1016/j.biomaterials.2005.10.003.
- [71] C.G. Ambrose, T.O. Clanton, Bioabsorbable Implants: Review of Clinical Experience in Orthopedic Surgery, Ann Biomed Eng 32 (2004) 171–177. https://doi.org/10.1023/B:ABME.0000007802.59936.fc.
- [72] T. Duerig, A. Pelton, D. Stöckel, An overview of nitinol medical applications, Materials Science and Engineering: A 273–275 (1999) 149–160. https://doi.org/10.1016/S0921-5093(99)00294-4.
- [73] J. KELLY, I. DENRY, Stabilized zirconia as a structural ceramic: An overview★, Dental Materials 24 (2008) 289–298. https://doi.org/10.1016/j.dental.2007.05.005.
- [74] A. Bandyopadhyay, I. Mitra, S.B. Goodman, M. Kumar, S. Bose, Improving biocompatibility for next generation of metallic implants, Prog Mater Sci 133 (2023) 101053. https://doi.org/10.1016/j.pmatsci.2022.101053.
- [75] M. Guazzato, M. Albakry, S.P. Ringer, M. V Swain, Strength, fracture toughness and microstructure of a selection of all-ceramic materials. Part II.

- Zirconia-based dental ceramics, Dental Materials 20 (2004) 449–456. https://doi.org/10.1016/j.dental.2003.05.002.
- [76] M. Long, H.J. Rack, Titanium alloys in total joint replacement—a materials science perspective, Biomaterials 19 (1998) 1621–1639. https://doi.org/10.1016/S0142-9612(97)00146-4.
- [77] H.J. Rack, J.I. Qazi, Titanium alloys for biomedical applications, Materials Science and Engineering: C 26 (2006) 1269–1277. https://doi.org/10.1016/j.msec.2005.08.032.
- [78] G.E. Ryan, A.S. Pandit, D.P. Apatsidis, Porous titanium scaffolds fabricated using a rapid prototyping and powder metallurgy technique, Biomaterials 29 (2008) 3625–3635. https://doi.org/10.1016/j.biomaterials.2008.05.032.
- [79] S. Suresh, Graded Materials for Resistance to Contact Deformation and Damage, Science (1979) 292 (2001) 2447–2451. https://doi.org/10.1126/science.1059716.
- [80] X. Liu, P.K. Chu, C. Ding, Surface nano-functionalization of biomaterials, in: Materials Science and Engineering R: Reports, 2010: pp. 275–302. https://doi.org/10.1016/j.mser.2010.06.013.
- [81] R. Bosco, J. Van Den Beucken, S. Leeuwenburgh, J. Jansen, Surface Engineering for Bone Implants: A Trend from Passive to Active Surfaces, Coatings 2 (2012) 95–119. https://doi.org/10.3390/coatings2030095.
- [82] S. Dosta, N. Cinca, A.M. Vilardell, I.G. Cano, J.M.G. Guilemany, Cold spray coatings for biomedical applications, in: Cold-Spray Coatings: Recent Trends and Future Perspectives, Springer International Publishing, 2017: pp. 533–557. https://doi.org/10.1007/978-3-319-67183-3 19.
- [83] J.C. Silva, C.S. Moura, N. Alves, J.M.S. Cabral, F.C. Ferreira, Effects of Different Fibre Alignments and Bioactive Coatings on Mesenchymal Stem/Stromal Cell Adhesion and Proliferation in Poly (ε-caprolactone) Scaffolds towards Cartilage Repair, Procedia Manuf 12 (2017) 132–140. https://doi.org/10.1016/J.PROMFG.2017.08.034.
- [84] M. Salwiczek, Y. Qu, J. Gardiner, R.A. Strugnell, T. Lithgow, K.M. McLean, H. Thissen, Emerging rules for effective antimicrobial coatings, Trends Biotechnol 32 (2014) 82–90. https://doi.org/10.1016/j.tibtech.2013.09.008.
- [85] S. Singh, H. Singh, K. Rakha, A Comprehensive Review on Carbon-Based Thermal Sprayed Coatings for Orthopedic Implants, Journal of Thermal Spray and Engineering 4 (2024) 126–131. https://doi.org/10.52687/2582-1474/408.
- [86] Z.A. Uwais, M.A. Hussein, M.A. Samad, N. Al-Aqeeli, Surface Modification of Metallic Biomaterials for Better Tribological Properties: A Review, Arab J Sci Eng 42 (2017) 4493–4512. https://doi.org/10.1007/s13369-017-2624-x.
- [87] K. Choy, Chemical vapour deposition of coatings, Prog Mater Sci 48 (2003) 57–170. https://doi.org/10.1016/S0079-6425(01)00009-3.

- [88] Y.L. Su, S.H. Yao, Z.L. Leu, C.S. Wei, C.T. Wu, Comparison of tribological behavior of three films—TiN, TiCN and CrN—grown by physical vapor deposition, Wear 213 (1997) 165–174. https://doi.org/10.1016/S0043-1648(97)00182-8.
- [89] M Ohring, Materials Science of Thin Films: Deposition and Structure, Academic press, 2002.
- [90] Corbella C, Sanchez O, Albella J M, Plasma enhanced chemical vapor deposition of thin films, in: Jenny Stanford Publishing, 2021: p. 37.
- [91] J. Corona-Gomez, S. Shiri, M. Mohammadtaheri, Q. Yang, Adhesion enhancement of DLC on CoCrMo alloy by diamond and nitrogen incorporation for wear resistant applications, Surf Coat Technol 332 (2017) 120–127. https://doi.org/10.1016/j.surfcoat.2017.10.050.
- [92] Lusvardi G, Malavasi G, Menabue L, Aina V, Morterra C, Verne E, Zirconium nitride coating of titanium implants: mechanical and corrosion resistance studies, J Biomed Mater Res Part A (2010) 1576–1583.
- [93] H.-W. Kim, Y.-H. Koh, L.-H. Li, S. Lee, H.-E. Kim, Hydroxyapatite coating on titanium substrate with titania buffer layer processed by sol–gel method, Biomaterials 25 (2004) 2533–2538. https://doi.org/10.1016/j.biomaterials.2003.09.041.
- [94] Brinker C J, Scherer G W, Sol-Gel Science: The Physics and Chemistry of Sol-Gel Processing, Academic Press, 1990.
- [95] Q. Chen, S. Liang, G.A. Thouas, Elastomeric biomaterials for tissue engineering, Prog Polym Sci 38 (2013) 584–671. https://doi.org/10.1016/j.progpolymsci.2012.05.003.
- [96] Catauro M, Bollino F, Papale F, Piccolela S, Pacifico S, Sol–gel synthesis and characterization of SiO2/CaO/P2O5 glass coatings on titanium substrates: Bioactivity, biocompatibility, and drug delivery tests, J Biomed Mater Res A (2004) 2877–2887.
- [97] Schlesinger M., Paunovic M, Modern electroplating, John Wiley & Sons, 2011.
- [98] A.R. Boccaccini, I. Zhitomirsky, Application of electrophoretic and electrolytic deposition techniques in ceramics processing, Curr Opin Solid State Mater Sci 6 (2002) 251–260. https://doi.org/10.1016/S1359-0286(02)00080-3.
- [99] Cunha J P, Paiva O C, Silva C J, Tavares C J, Alves E, Cavaleiro A, Titanium nitride coatings for biomedical applications: A short review., Vacuum 86 (2012) 1777–1790.
- [100] Sivakumar M, Swaminathan T, Rao K P, Electrodeposition of hydroxyapatite coatings on titanium and its alloy for biomedical applications, Surf Coat Technol 146 (2001) 321–327.

- [101] L. Le Guehennec, M.A. Lopez-Heredia, B. Enkel, P. Weiss, Y. Amouriq, P. Layrolle, Osteoblastic cell behaviour on different titanium implant surfaces, Acta Biomater 4 (2008) 535–543. https://doi.org/10.1016/J.ACTBIO.2007.12.002.
- [102] Lipski A, Jarzebski J, Fatigue strength of orthopedic implants after shot peening, J Biomed Mater Res B Appl Biomater 87 (2008) 243–250.
- [103] Y. Sano, Laser Peening without Coating as a Surface Enhancement Technology, Journal of Laser Micro/Nanoengineering 1 (2006) 161–166. https://doi.org/10.2961/jlmn.2006.03.0002.
- [104] Mattox D M, Handbook of Physical Vapor Deposition (PVD) Processing (2nd ed.), 2010.
- [105] Ratner B D, Hoffman A S, Schoen F J, Lemons J E, Biomaterials Science: An Introduction to Materials in Medicine (3rd ed.), (n.d.).
- [106] K. Gan, H. Liu, L. Jiang, X. Liu, X. Song, D. Niu, T. Chen, C. Liu, Bioactivity and antibacterial effect of nitrogen plasma immersion ion implantation on polyetheretherketone, Dental Materials 32 (2016) e263–e274. https://doi.org/10.1016/j.dental.2016.08.215.
- [107] D. Wu, Z. Yuan, S. Liu, J. Zheng, X. Wei, C. Zhang, Recent Development of Corrosion Factors and Coating Applications in Biomass Firing Plants, Coatings 10 (2020) 1001. https://doi.org/10.3390/coatings10101001.
- [108] J.N. Ndumia, M. Kang, B.V. Gbenontin, J. Lin, S.M. Nyambura, A Review on the Wear, Corrosion and High-Temperature Resistant Properties of Wire Arc-Sprayed Fe-Based Coatings, Nanomaterials 11 (2021) 2527. https://doi.org/10.3390/nano11102527.
- [109] S. Amin, H. Panchal, A Review on Thermal Spray Coating Processes, 2016. http://www.ijcter.com.
- [110] Davis J R, Handbook of thermal spray technology, 2004.
- [111] N. V. Bulina, D.K. Rybin, S. V. Makarova, D. V. Dudina, I.S. Batraev, A. V. Utkin, I.Yu. Prosanov, M. V. Khvostov, V.Yu. Ulianitsky, Detonation Spraying of Hydroxyapatite on a Titanium Alloy Implant, Materials 14 (2021) 4852. https://doi.org/10.3390/ma14174852.
- [112] J.N. Ndumia, M. Kang, B.V. Gbenontin, J. Lin, S.M. Nyambura, A Review on the Wear, Corrosion and High-Temperature Resistant Properties of Wire Arc-Sprayed Fe-Based Coatings, Nanomaterials 11 (2021) 2527. https://doi.org/10.3390/nano11102527.
- [113] T.P.S. Sarao, H.S. Sidhu, H. Singh, Characterization and In Vitro Corrosion Investigations of Thermal Sprayed Hydroxyapatite and Hydroxyapatite-Titania Coatings on Ti Alloy, Metallurgical and Materials Transactions A 43 (2012) 4365–4376. https://doi.org/10.1007/s11661-012-1175-8.

- [114] V. Karageorgiou, D.K. Ã, Porosity of 3D biomaterial scaffolds and osteogenesis, 26 (2005) 5474–5491. https://doi.org/10.1016/j.biomaterials.2005.02.002.
- [115] P. Gkomoza, G.S. Lampropoulos, M. Vardavoulias, D.I. Pantelis, P.N. Karakizis, Surface & Coatings Technology Microstructural investigation of porous titanium coatings, produced by thermal spraying techniques, using plasma atomization and hydride- dehydride powders, for orthopedic implants, Surf Coat Technol 357 (2019) 947–956. https://doi.org/10.1016/j.surfcoat.2018.10.072.
- [116] J. Kawakita, S. Kuroda, T. Fukushima, H. Katanoda, Dense titanium coatings by modified HVOF spraying, 201 (2006) 1250–1255. https://doi.org/10.1016/j.surfcoat.2006.01.056.
- [117] M. Oksa, E. Turunen, T. Suhonen, T. Varis, S. Hannula, Optimization and Characterization of High Velocity Oxy-fuel Sprayed Coatings: Techniques, Materials, and Applications, (2011) 17–52. https://doi.org/10.3390/coatings1010017.
- [118] H.C. Melero, R.T. Sakai, C.A. Vignatti, A.V. Benedetti, J.M. Guilemany, P.H. Suegama, U. De Barcelona, Corrosion Resistance Evaluation of HVOF Produced Hydroxyapatite and TiO 2 hydroxyapatite Coatings in Hanks 'Solution, 21 (2018).
- [119] J.H.M.C.J. Hincapie-bedoya, PEER REVIEWED HVOF Hydroxyapatite / Titania-Graded Coatings: Microstructural, Mechanical, and In Vitro Characterization, (2018) 1302–1321. https://doi.org/10.1007/s11666-018-0811-2.
- [120] https://www.corrosionprotectionindia.com/hvof-spray-process.html, (n.d.).
- [121] E. Sadeghi, S. Joshi, Chlorine-induced high-temperature corrosion and erosion-corrosion of HVAF and HVOF-sprayed amorphous Fe-based coatings, Surf Coat Technol 371 (2019) 20–35. https://doi.org/10.1016/J.SURFCOAT.2019.01.080.
- [122] H. Yin, W. Ge, R. Li, L. Zhou, F. Yin, H. Sun, J. Sun, J. Zhao, Microstructure and properties of AlCrFeNiMoNb high-entropy alloys coating on ZM5 magnesium alloy prepared by high-velocity air fuel (HVAF) spray, Journal of Materials Research and Technology 26 (2023) 8704–8720. https://doi.org/10.1016/J.JMRT.2023.09.125.
- [123] N. Jagadeeshanayaka, S.N. Kele, S.C. Jambagi, An Investigation into the Relative Efficacy of High-Velocity Air-Fuel-Sprayed Hydroxyapatite Implants Based on the Crystallinity Index, Residual Stress, Wear, and In-Flight Powder Particle Behavior, Langmuir 39 (2023) 17513–17528. https://doi.org/10.1021/acs.langmuir.3c02840.

- [124] R. Lupoi, W.O. Neill, Surface & Coatings Technology Powder stream characteristics in cold spray nozzles, Surf Coat Technol 206 (2011) 1069–1076. https://doi.org/10.1016/j.surfcoat.2011.07.061.
- [125] R.N. Raoelison, Y. Xie, T. Sapanathan, M.P. Planche, R. Kromer, S. Costil, C. Langlade, Cold gas dynamic spray technology: A comprehensive review of processing conditions for various technological developments till to date, Addit Manuf 19 (2018) 134–159. https://doi.org/10.1016/j.addma.2017.07.001.
- [126] Y. Xie, C. Chen, M.P.S. Deng, Strengthened Peening Effect on Metallurgical Bonding Formation in Cold Spray Additive Manufacturing, Journal of Thermal Spray Technology 28 (2019) 769–779. https://doi.org/10.1007/s11666-019-00854-4.
- [127] T. Schmidt, F. Ga, H. Assadi, H. Kreye, Development of a generalized parameter window for cold spray deposition, 54 (2006) 729–742. https://doi.org/10.1016/j.actamat.2005.10.005.
- [128] S. Dosta, N. Cinca, A.M. Vilardell, I.G. Cano, Cold Spray Coatings for Biomedical Applications, (2018).
- [129] X. Wang, L. Zhang, X. Zhou, W. Wu, X. Jie, Surface & Coatings Technology Corrosion behavior of Al 2 O 3 -reinforced graphene encapsulated Al composite coating fabricated by low pressure cold spraying, Surf Coat Technol 386 (2020) 125486. https://doi.org/10.1016/j.surfcoat.2020.125486.
- [130] A. Kumar, H. Singh, R. Kant, N. Rasool, Development of Cold Sprayed Titanium/Baghdadite Composite Coating for Bio-implant Applications, Journal of Thermal Spray Technology 30 (2021) 2099–2116. https://doi.org/10.1007/s11666-021-01269-w.
- [131] A. Kumar, R. Kant, H. Singh, Surface & Coatings Technology Tribological behavior of cold-sprayed titanium / baghdadite composite coatings in dry and simulated body fluid environments, Surf Coat Technol 425 (2021) 127727. https://doi.org/10.1016/j.surfcoat.2021.127727.
- [132] Y. Liu, Z. Dang, Y. Wang, J. Huang, H. Li, Hydroxyapatite / graphene-nanosheet composite coatings deposited by vacuum cold spraying for biomedical applications: Inherited nanostructures and enhanced properties, Carbon N Y 67 (2013) 250–259. https://doi.org/10.1016/j.carbon.2013.09.088.
- [133] H. Herman, Plasma-sprayed Coatings, 259 (1988) 112–117. https://doi.org/10.2307/24989234.
- [134] G. Singh, H. Singh, B.S. Sidhu, Corrosion behavior of plasma sprayed hydroxyapatite and hydroxyapatite-silicon oxide coatings on AISI 304 for biomedical application, Appl Surf Sci 284 (2013) 811–818. https://doi.org/10.1016/j.apsusc.2013.08.013.
- [135] Hulbert SF, Hench LL, Wilson J, An introduction to bioceramics., World Scientific Pub, Singapore (1993) 25.

- [136] M. Grynpas, Age and disease-related changes in the mineral of bone, Calcif Tissue Int 53 (1993) S57–S64. https://doi.org/10.1007/BF01673403.
- [137] De Lange G, De Putter C, Structure of the bone interface to dental implants in vivo, J Oral Implantol 19 (1993) 123–35.
- [138] Y.C. Tsui, C. Doyle, T.W. Clyne, Plasma sprayed hydroxyapatite coatings on titanium substrates Part 1: Mechanical properties and residual stress levels, Biomaterials 19 (1998) 2015–2029. https://doi.org/10.1016/S0142-9612(98)00103-3.
- [139] C.C. Berndt, G.N. Haddad, A.J.D. Farmer', K.A. Gross, THERMAL SPRAYING FOR BIOCERAMIC APPLICATIONS, 1990.
- [140] R. Furlong, J. Osborn, Fixation of hip prostheses by hydroxyapatite ceramic coatings, J Bone Joint Surg Br 73-B (1991) 741–745. https://doi.org/10.1302/0301-620X.73B5.1654336.
- [141] P.K. Stephenson, M.A.R. Freeman, P.A. Revell, J. Germain, M. Tuke, C.J. Pirie, The effect of hydroxyapatite coating on ingrowth of bone into cavities in an implant, J Arthroplasty 6 (1991) 51–58. https://doi.org/10.1016/S0883-5403(06)80157-9.
- [142] J.P. Collier, V.A. Surprenant, M.B. Mayor, M. Wrona, R.E. Jensen, H.P. Surprenant, Loss of hydroxyapatite coating on retrieved, total hip components, J Arthroplasty 8 (1993) 389–393. https://doi.org/10.1016/S0883-5403(06)80037-9.
- [143] L. Sun, C.C. Berndt, K.A. Gross, A. Kucuk, Material Fundamentals and Clinical Performance of Plasma-Sprayed Hydroxyapatite Coatings: A Review, (2001). https://doi.org/10.1002/jbm.xxxx.
- [144] G. Magyar, S. Toksvig-Larsen, A. Moroni, HYDROXYAPATITE COATING OF THREADED PINS ENHANCES FIXATION, J Bone Joint Surg Br 79-B (1997) 487–489. https://doi.org/10.1302/0301-620X.79B3.0790487.
- [145] C.Y. Yang, B.C. Wang, E. Chang, B.C. Wu, Bond degradation at the plasma-sprayed HA coating/Ti-6AI-4V alloy interface: an in vitro study, J Mater Sci Mater Med 6 (1995) 258–265. https://doi.org/10.1007/BF00120268.
- [146] O. Graßmann, R.B. Heimann, Compositional and microstructural changes of engineered plasma-sprayed hydroxyapatite coatings on Ti6Al4V substrates during incubation in protein-free simulated body fluid, J Biomed Mater Res 53 (2000) 685–693. https://doi.org/10.1002/1097-4636(2000)53:6<685::AID-JBM11>3.0.CO;2-B.
- [147] B. Zhang, D. Myers, G. Wallace, M. Brandt, P. Choong, Bioactive Coatings for Orthopaedic Implants—Recent Trends in Development of Implant Coatings, Int J Mol Sci 15 (2014) 11878–11921. https://doi.org/10.3390/ijms150711878.
- [148] J. Lincks, B.D. Boyan, C.R. Blanchard, C.H. Lohmann, Y. Liu, D.L. Cochran, D.D. Dean, Z. Schwartz, Response of MG63 osteoblast-like cells to titanium

- and titanium alloy is dependent on surface roughness and composition, Biomaterials 19 (1998) 2219–2232. https://doi.org/10.1016/S0142-9612(98)00144-6.
- [149] A. Boyde, A. Corsi, R. Quarto, R. Cancedda, P. Bianco, Osteoconduction in large macroporous hydroxyapatite ceramic implants: evidence for a complementary integration and disintegration mechanism, Bone 24 (1999) 579–589. https://doi.org/10.1016/S8756-3282(99)00083-6.
- [150] R. Gadow, A. Killinger, N. Stiegler, Hydroxyapatite coatings for biomedical applications deposited by different thermal spray techniques, Surf Coat Technol 205 (2010) 1157–1164. https://doi.org/10.1016/j.surfcoat.2010.03.059.
- [151] X. Bai, K. More, C.M. Rouleau, A. Rabiei, Functionally graded hydroxyapatite coatings doped with antibacterial components, Acta Biomater 6 (2010) 2264–2273. https://doi.org/10.1016/j.actbio.2009.12.002.
- [152] L. Sun, C.C. Berndt, C.P. Grey, Phase, structural and microstructural investigations of plasma sprayed hydroxyapatite coatings, Materials Science and Engineering: A 360 (2003) 70–84. https://doi.org/10.1016/S0921-5093(03)00439-8.
- [153] C.Y. Yang, B.C. Wang, E. Chang, J.D. Wu, The influences of plasma spraying parameters on the characteristics of hydroxyapatite coatings: a quantitative study, J Mater Sci Mater Med 6 (1995) 249–257. https://doi.org/10.1007/BF00120267.
- [154] G.A. Fielding, M. Roy, A. Bandyopadhyay, S. Bose, Antibacterial and biological characteristics of silver containing and strontium doped plasma sprayed hydroxyapatite coatings, Acta Biomater 8 (2012) 3144–3152. https://doi.org/10.1016/j.actbio.2012.04.004.
- [155] B. Singh, G. Singh, B.S. Sidhu, Investigation of the in vitro corrosion behavior and biocompatibility of niobium (Nb)-reinforced hydroxyapatite (HA) coating on CoCr alloy for medical implants, J Mater Res 34 (2019) 1678–1691. https://doi.org/10.1557/jmr.2019.94.
- [156] M. Poorraeisi, A. Afshar, The study of electrodeposition of hydroxyapatite-ZrO2-TiO2 nanocomposite coatings on 316 stainless steel, Surf Coat Technol 339 (2018) 199–207. https://doi.org/10.1016/j.surfcoat.2018.02.030.
- [157] H.-L. Yao, H.-T. Wang, X.-B. Bai, G.-C. Ji, Q.-Y. Chen, Improvement in mechanical properties of nano-structured HA/TiO2 multilayer coatings deposited by high velocity suspension flame spraying (HVSFS), Surf Coat Technol 342 (2018) 94–104. https://doi.org/10.1016/j.surfcoat.2018.02.058.
- [158] H.-L. Yao, X.-Z. Hu, X.-B. Bai, H.-T. Wang, Q.-Y. Chen, G.-C. Ji, Comparative study of HA/TiO2 and HA/ZrO2 composite coatings deposited by high-velocity suspension flame spray (HVSFS), Surf Coat Technol 351 (2018) 177–187. https://doi.org/10.1016/j.surfcoat.2018.07.082.

- [159] C. Wu, J. Chang, A review of bioactive silicate ceramics, Biomedical Materials 8 (2013) 032001. https://doi.org/10.1088/1748-6041/8/3/032001.
- [160] W. Xue, X. Liu, X. Zheng, C. Ding, In vivo evaluation of plasma-sprayed wollastonite coating, Biomaterials 26 (2005) 3455–3460. https://doi.org/10.1016/j.biomaterials.2004.09.027.
- [161] P. Siriphannon, Y. Kameshima, A. Yasumori, K. Okada, S. Hayashi, Formation of hydroxyapatite on CaSiO3 powders in simulated body fluid, J Eur Ceram Soc 22 (2002) 511–520. https://doi.org/10.1016/S0955-2219(01)00301-6.
- [162] Y. Xie, X. Liu, X. Zheng, C. Ding, P.K. Chu, Improved stability of plasma-sprayed dicalcium silicate/zirconia composite coating, Thin Solid Films 515 (2006) 1214–1218. https://doi.org/10.1016/j.tsf.2006.07.124.
- [163] S. Mehrafzoon, S.A. Hassanzadeh-Tabrizi, A. Bigham, Synthesis of nanoporous Baghdadite by a modified sol-gel method and its structural and controlled release properties, Ceram Int 44 (2018) 13951–13958. https://doi.org/10.1016/j.ceramint.2018.04.244.
- [164] Y. Ramaswamy, C. Wu, A. Van Hummel, V. Combes, G. Grau, H. Zreiqat, The responses of osteoblasts, osteoclasts and endothelial cells to zirconium modified calcium-silicate-based ceramic, Biomaterials 29 (2008) 4392–4402. https://doi.org/10.1016/J.BIOMATERIALS.2008.08.006.
- [165] S.I. Roohani-Esfahani, C.R. Dunstan, B. Davies, S. Pearce, R. Williams, H. Zreiqat, Repairing a critical-sized bone defect with highly porous modified and unmodified baghdadite scaffolds, Acta Biomater 8 (2012) 4162–4172. https://doi.org/10.1016/J.ACTBIO.2012.07.036.
- [166] H.R. Bakhsheshi-Rad, E. Hamzah, A.F. Ismail, M. Aziz, Z. Hadisi, M. Kashefian, A. Najafinezhad, Novel nanostructured baghdadite-vancomycin scaffolds: In-vitro drug release, antibacterial activity and biocompatibility, Mater Lett 209 (2017) 369–372. https://doi.org/10.1016/J.MATLET.2017.08.027.
- [167] F. Tavangarian, C.A. Zolko, S. Sadeghzade, M. Fayed, K. Davami, Fabrication, Mechanical Properties and In-Vitro Behavior of Akermanite Bioceramic, Materials 13 (2020) 4887. https://doi.org/10.3390/ma13214887.
- [168] S. Punj, J. Singh, K. Singh, Ceramic biomaterials: Properties, state of the art and future prospectives, Ceram Int 47 (2021) 28059–28074. https://doi.org/10.1016/J.CERAMINT.2021.06.238.
- [169] D.Q. Pham, C.C. Berndt, J. Cizek, U. Gbureck, H. Zreiqat, Z. Lu, A.S.M. Ang, Baghdadite coating formed by hybrid water-stabilized plasma spray for bioceramic applications: Mechanical and biological evaluations, Materials Science and Engineering: C 122 (2021) 111873. https://doi.org/10.1016/J.MSEC.2021.111873.
- [170] T.C. Schumacher, E. Volkmann, R. Yilmaz, A. Wolf, L. Treccani, K. Rezwan, Mechanical evaluation of calcium-zirconium-silicate (baghdadite) obtained by a

- direct solid-state synthesis route, J Mech Behav Biomed Mater 34 (2014) 294–301. https://doi.org/10.1016/J.JMBBM.2014.02.021.
- [171] A. Arefpour, M. Kasiri-Asgarani, A. Monshi, S. Karbasi, A. Doostmohammadi, Baghdadite/Polycaprolactone nanocomposite scaffolds: preparation, characterisation, and in vitro biological responses of human osteoblast-like cells (Saos-2 cell line), Materials Technology 35 (2020) 421–432. https://doi.org/10.1080/10667857.2019.1692161.
- [172] F. Soleymani, R. Emadi, S. Sadeghzade, F. Tavangarian, Bioactivity Behavior Evaluation of PCL-Chitosan-Nanobaghdadite Coating on AZ91 Magnesium Alloy in Simulated Body Fluid, Coatings 10 (2020) 231. https://doi.org/10.3390/coatings10030231.
- [173] Y. Liang, Y. Xie, H. Ji, L. Huang, X. Zheng, Excellent stability of plasma-sprayed bioactive Ca 3 ZrSi 2 O 9 ceramic coating on Ti-6Al-4V, Appl Surf Sci 256 (2010) 4677–4681. https://doi.org/10.1016/j.apsusc.2010.02.071.
- [174] K.A. Khor, C.S. Yip, P. Cheang, Ti- 6Al-4V/hydroxyapatite composite coatings prepared by thermal spray techniques, Journal of Thermal Spray Technology 6 (1997) 109–115. https://doi.org/10.1007/BF02646320.
- [175] X. Wang, Y. Zhou, L. Xia, C. Zhao, L. Chen, D. Yi, J. Chang, L. Huang, X. Zheng, H. Zhu, Y. Xie, Y. Xu, K. Lin, Fabrication of nano-structured calcium silicate coatings with enhanced stability, bioactivity and osteogenic and angiogenic activity, Colloids Surf B Biointerfaces 126 (2015) 358–366. https://doi.org/10.1016/j.colsurfb.2014.11.044.
- [176] D.Q. Pham, C.C. Berndt, U. Gbureck, H. Zreiqat, V.K. Truong, A.S.M. Ang, Mechanical and chemical properties of Baghdadite coatings manufactured by atmospheric plasma spraying, Surf Coat Technol 378 (2019). https://doi.org/10.1016/j.surfcoat.2019.124945.
- [177] H.R. Bakhsheshi-Rad, E. Hamzah, A.F. Ismail, M. Aziz, M. Kasiri-Asgarani, E. Akbari, S. Jabbarzare, A. Najafinezhad, Z. Hadisi, Synthesis of a novel nanostructured zinc oxide/baghdadite coating on Mg alloy for biomedical application: In-vitro degradation behavior and antibacterial activities, Ceram Int 43 (2017) 14842–14850. https://doi.org/10.1016/j.ceramint.2017.07.233.
- [178] A. Kumar, H. Singh, R. Kant, N. Rasool, Development of Cold Sprayed Titanium/Baghdadite Composite Coating for Bio-implant Applications, Journal of Thermal Spray Technology 30 (2021) 2099–2116. https://doi.org/10.1007/s11666-021-01269-w.
- [179] A. Kumar, R. Kant, H. Singh, Tribological behavior of cold-sprayed titanium/baghdadite composite coatings in dry and simulated body fluid environments, Surf Coat Technol 425 (2021). https://doi.org/10.1016/j.surfcoat.2021.127727.
- [180] C. Scoville, R. Cole, J. Hogg, O. Farooque, A. Russell, Carbon Nanotubes, n.d. http://www.answers.com/topic/timeline-of-carbon-nanotubes?cat=technology.

- [181] Physical properties of carbon nanotubes. http://www.pa.msu.edu/cmp/csc/ntproperties/, (n.d.).
- [182] N. Saito, Y. Usui, K. Aoki, N. Narita, M. Shimizu, K. Hara, N. Ogiwara, K. Nakamura, N. Ishigaki, H. Kato, S. Tarut, M. Endo, Carbon nanotubes: Biomaterial applications, Chem Soc Rev 38 (2009) 1897–1903. https://doi.org/10.1039/b804822n.
- [183] D. Lahiri, S. Ghosh, A. Agarwal, Carbon nanotube reinforced hydroxyapatite composite for orthopedic application: A review, Materials Science and Engineering C 32 (2012) 1727–1758. https://doi.org/10.1016/j.msec.2012.05.010.
- [184] K. Balani, R. Anderson, T. Laha, M. Andara, J. Tercero, E. Crumpler, A. Agarwal, Plasma-sprayed carbon nanotube reinforced hydroxyapatite coatings and their interaction with human osteoblasts in vitro, 28 (2007) 618–624. https://doi.org/10.1016/j.biomaterials.2006.09.013.
- [185] K. Balani, Y. Chen, S.P. Harimkar, N.B. Dahotre, Tribological behavior of plasma-sprayed carbon nanotube-reinforced hydroxyapatite coating in physiological solution, 3 (2007) 944–951. https://doi.org/10.1016/j.actbio.2007.06.001.
- [186] S. Singh, K.K. Pandey, A. Islam, A.K. Keshri, Corrosion behaviour of plasma sprayed graphene nanoplatelets reinforced hydroxyapatite composite coatings in simulated body fl uid, Ceram Int 46 (2020) 13539–13548. https://doi.org/10.1016/j.ceramint.2020.02.139.
- [187] Y. Chen, J. Ren, Y. Sun, W. Liu, X. Lu, S. Guan, Ef fi cacy of graphene nanosheets on the plasma sprayed hydroxyapatite coating: Improved strength, toughness and in-vitro bioperformance with osteoblast, Mater Des 203 (2021) 109585. https://doi.org/10.1016/j.matdes.2021.109585.
- [188] P.A. Khan, A.K. Thoutam, V. Gopal, A. Gurumallesh, S. Joshi, A. Palaniappan, N. Markocsan, G. Manivasagam, Influence of Graphene Nanoplatelets on the Performance of Axial Suspension Plasma-Sprayed Hydroxyapatite Coatings, (2023) 1–22.
- [189] J. Gao, D. Xing, S. Dong, J. Lin, The primary total knee arthroplasty: A global analysis, J Orthop Surg Res 15 (2020). https://doi.org/10.1186/s13018-020-01707-5.
- [190] S. Singh, A. Kumar, M. Kamboj, B. Das, H. Singh, K. Rakha, Scratch resistance and in-vitro biocompatibility of plasma-sprayed baghdadite coatings reinforced with carbon nanotubes, Surf Coat Technol 481 (2024) 130670. https://doi.org/10.1016/j.surfcoat.2024.130670.
- [191] W.S.W. Harun, R.I.M. Asri, J. Alias, F.H. Zulkifli, K. Kadirgama, S.A.C. Ghani, J.H.M. Shariffuddin, A comprehensive review of hydroxyapatite-based coatings adhesion on metallic biomaterials, Ceram Int 44 (2018) 1250–1268. https://doi.org/10.1016/J.CERAMINT.2017.10.162.

- [192] D. Lahiri, S. Ghosh, A. Agarwal, Carbon nanotube reinforced hydroxyapatite composite for orthopedic application: A review, Materials Science and Engineering: C 32 (2012) 1727–1758. https://doi.org/10.1016/J.MSEC.2012.05.010.
- [193] G. Graziani, M. Bianchi, E. Sassoni, A. Russo, M. Marcacci, Ion-substituted calcium phosphate coatings deposited by plasma-assisted techniques: A review, Materials Science and Engineering: C 74 (2017) 219–229. https://doi.org/10.1016/J.MSEC.2016.12.018.
- [194] R.B. Heimann, Thermal spraying of biomaterials, Surf Coat Technol 201 (2006) 2012–2019. https://doi.org/10.1016/J.SURFCOAT.2006.04.052.
- [195] A. Kumar, K. Biswas, B. Basu, On the toughness enhancement in hydroxyapatite-based composites, Acta Mater 61 (2013) 5198–5215. https://doi.org/10.1016/J.ACTAMAT.2013.05.013.
- [196] S.I. Roohani-Esfahani, C.R. Dunstan, B. Davies, S. Pearce, R. Williams, H. Zreiqat, Repairing a critical-sized bone defect with highly porous modified and unmodified baghdadite scaffolds, Acta Biomater 8 (2012) 4162–4172. https://doi.org/10.1016/J.ACTBIO.2012.07.036.
- [197] S.C. Jambagi, S. Kar, P. Brodard, P.P. Bandyopadhyay, Characteristics of plasma sprayed coatings produced from carbon nanotube doped ceramic powder feedstock, Mater Des 112 (2016) 392–401. https://doi.org/10.1016/J.MATDES.2016.09.095.
- [198] A. Bor, B. Ichinkhorloo, B. Uyanga, J. Lee, H. Choi, Cu/CNT nanocomposite fabrication with different raw material properties using a planetary ball milling process, Powder Technol 323 (2018) 563–573. https://doi.org/10.1016/J.POWTEC.2016.06.042.
- [199] Y. Chen, Y.Q. Zhang, T.H. Zhang, C.H. Gan, C.Y. Zheng, G. Yu, Carbon nanotube reinforced hydroxyapatite composite coatings produced through laser surface alloying, Carbon N Y 44 (2006) 37–45. https://doi.org/10.1016/J.CARBON.2005.07.011.
- [200] https://www.alphiemixer.com/products/laboratory-mixer/, (n.d.).
- [201] S. Singh, A. Kumar, M. Kamboj, B. Das, K. Rakha, H. Singh, Corrosion behaviour of plasma-sprayed baghdadite bioceramic coatings reinforced with carbon nanotubes, J Alloys Compd 976 (2024) 173094. https://doi.org/10.1016/J.JALLCOM.2023.173094.
- [202] Standard Guide for Metallographic Preparation of Thermal Sprayed Coatings, (n.d.). https://doi.org/10.1520/E1920-03R21.
- [203] A. S, R. Maurya, Assessment of plasma sprayed carbon nanotube reinforced Al2O3-based nanocomposite with micro-scratching, Surf Coat Technol 418 (2021) 127216. https://doi.org/10.1016/J.SURFCOAT.2021.127216.

- [204] A.T. Akono, N.X. Randall, F.J. Ulm, Experimental determination of the fracture toughness via microscratch tests: Application to polymers, ceramics, and metals, J Mater Res 27 (2012) 485–493. https://doi.org/10.1557/jmr.2011.402.
- [205] S. Singh, C. Prakash, H. Singh, Deposition of HA-TiO2 by plasma spray on β-phase Ti-35Nb-7Ta-5Zr alloy for hip stem: Characterization, mechanical properties, corrosion, and in-vitro bioactivity, Surf Coat Technol 398 (2020). https://doi.org/10.1016/j.surfcoat.2020.126072.
- [206] N. Rasool, D. Negi, Y. Singh, Thiol-Functionalized, Antioxidant, and Osteogenic Mesoporous Silica Nanoparticles for Osteoporosis, ACS Biomater Sci Eng 9 (2023) 3535–3545. https://doi.org/10.1021/acsbiomaterials.3c00479.
- [207] T. Roy, P.P. Maity, A.P. Rameshbabu, B. Das, A. John, A. Dutta, S.K. Ghorai, S. Chattopadhyay, S. Dhara, Core-shell nanofibrous scaffold based on polycaprolactone-silk fibroin emulsion electrospinning for tissue engineering applications, Bioengineering 5 (2018). https://doi.org/10.3390/bioengineering5030068.
- [208] P.K. Srivas, K. Kapat, B. Das, P. Pal, P.G. Ray, S. Dhara, Hierarchical surface morphology on Ti6Al4V via patterning and hydrothermal treatment towards improving cellular response, Appl Surf Sci 478 (2019) 806–817. https://doi.org/10.1016/j.apsusc.2019.02.039.
- [209] P. Pal, P.K. Srivas, P. Dadhich, B. Das, D. Maulik, S. Dhara, Nano-/Microfibrous Cotton-Wool-Like 3D Scaffold with Core-Shell Architecture by Emulsion Electrospinning for Skin Tissue Regeneration, ACS Biomater Sci Eng 3 (2017) 3563–3575. https://doi.org/10.1021/acsbiomaterials.7b00681.
- [210] J. Guillem-Marti, N. Cinca, M. Punset, I.G. Cano, F.J. Gil, J.M. Guilemany, S. Dosta, Porous titanium-hydroxyapatite composite coating obtained on titanium by cold gas spray with high bond strength for biomedical applications, Colloids Surf B Biointerfaces 180 (2019) 245–253. https://doi.org/10.1016/j.colsurfb.2019.04.048.
- [211] B. Das, A. Girigoswami, A. Dutta, P. Pal, J. Dutta, P. Dadhich, P.K. Srivas, S. Dhara, Carbon Nanodots Doped Super-paramagnetic Iron Oxide Nanoparticles for Multimodal Bioimaging and Osteochondral Tissue Regeneration via External Magnetic Actuation, ACS Biomater Sci Eng 5 (2019) 3549–3560. https://doi.org/10.1021/acsbiomaterials.9b00571.
- [212] N. Chauhan, P. Gupta, L. Arora, D. Pal, Y. Singh, Dexamethasone-loaded, injectable pullulan-poly(ethylene glycol) hydrogels for bone tissue regeneration in chronic inflammatory conditions, Materials Science and Engineering C 130 (2021). https://doi.org/10.1016/j.msec.2021.112463.
- [213] A. Nouri, A. Sola, Powder morphology in thermal spraying, J Adv Manuf Process 1 (2019). https://doi.org/10.1002/amp2.10020.

- [214] G. Singh, H. Singh, B.S. Sidhu, In vitro corrosion investigations of plasmasprayed hydroxyapatite and hydroxyapatite-calcium phosphate coatings on 316L SS, 2014.
- [215] W.T. Lin, Z.W. Lin, T.Y. Kuo, C.S. Chien, J.W. Huang, Y.L. Chung, C.P. Chang, M.Z. Ibrahim, H.T. Lee, Mechanical and biological properties of atmospheric plasma-sprayed carbon nanotube-reinforced tantalum pentoxide composite coatings on Ti6Al4V alloy, Surf Coat Technol 437 (2022) 128356. https://doi.org/10.1016/J.SURFCOAT.2022.128356.
- [216] C. Berndt, M. Fahad Hasan, U. Tietz, K. Schmitz, M. Hasan, A Review of Hydroxyapatite Coatings Manufactured by Thermal Spray, (n.d.). https://doi.org/10.1007/978-3-642-53980-0__9.
- [217] K.A. Gross, C.C. Bernd, P. Stephens, R. Dinnebier, Oxyapatite in hydroxyapatite coatings, 1998.
- [218] S.Y. Kwon, W.Y. Kim, P. Hudon, I.H. Jung, Thermodynamic modeling of the CaO-SiO2-ZrO2 system coupled with key phase diagram experiments, J Eur Ceram Soc 37 (2017) 1095–1104. https://doi.org/10.1016/j.jeurceramsoc.2016.10.011.
- [219] A. Najafinezhad, M. Abdellahi, H. Ghayour, A. Soheily, A. Chami, A. Khandan, A comparative study on the synthesis mechanism, bioactivity and mechanical properties of three silicate bioceramics, Materials Science and Engineering C 72 (2017) 259–267. https://doi.org/10.1016/j.msec.2016.11.084.
- [220] J.F. Moulder, W.F. Stickle, P.E.' Sobol, K.D. Bomben, J. Chastain, Handbook of X-ray Photoelectron Spectroscopy AReference Book of Standard Spectra for Identification and Interpretation of XPS Data, n.d.
- [221] K. Dul, A. Kolezyński, M. Sitarz, D. Madej, Vibrational spectra of a baghdadite synthetic analogue, Vib Spectrosc 76 (2015) 1–5. https://doi.org/10.1016/j.vibspec.2014.11.001.
- [222] P.N. De Aza, F. Guitiá, C. Santos, S. De Aza, R. Cuscó, L. Artú, Vibrational Properties of Calcium Phosphate Compounds. 2. Comparison between Hydroxyapatite and-Tricalcium Phosphate, 1997. https://pubs.acs.org/sharingguidelines.
- [223] A. Abouelsayed, B. Anis, S. Hassaballa, A.S.G. Khalil, U.M. Rashed, K.A. Eid, E. Al-Ashkar, W. El hotaby, Preparation, characterization, Raman, and terahertz spectroscopy study on carbon nanotubes, graphene nano-sheets, and onion like carbon materials, Mater Chem Phys 189 (2017) 127–135. https://doi.org/10.1016/j.matchemphys.2016.12.065.
- [224] P.A. Khan, A.K. Thoutam, V. Gopal, A. Gurumallesh, S. Joshi, A. Palaniappan, N. Markocsan, G. Manivasagam, Influence of Graphene Nanoplatelets on the Performance of Axial Suspension Plasma-Sprayed Hydroxyapatite Coatings, Bioengineering 10 (2023). https://doi.org/10.3390/bioengineering10010044.

- [225] P. Fauchais, Understanding plasma spraying, J Phys D Appl Phys 37 (2004). https://doi.org/10.1088/0022-3727/37/9/R02.
- [226] S.C. Jambagi, S. Kar, P. Brodard, P.P. Bandyopadhyay, Characteristics of plasma sprayed coatings produced from carbon nanotube doped ceramic powder feedstock, Mater Des 112 (2016) 392–401. https://doi.org/10.1016/J.MATDES.2016.09.095.
- [227] R.B. Heimann, Plasma-Sprayed Hydroxylapatite-Based Coatings: Chemical, Mechanical, Microstructural, and Biomedical Properties, Journal of Thermal Spray Technology 25 (2016) 827–850. https://doi.org/10.1007/s11666-016-0421-9.
- [228] L. Sun, C.C. Berndt, K.A. Gross, A. Kucuk, Material Fundamentals and Clinical Performance of Plasma-Sprayed Hydroxyapatite Coatings: A Review, (2001). https://doi.org/10.1002/jbm.xxxx.
- [229] T.M. Lee, R.S. Tsai, E. Chang, C.Y. Yang, M.R. Yang, The cell attachment and morphology of neonatal rat calvarial osteoblasts on the surface of Ti-6Al-4V and plasma-sprayed HA coating: Effect of surface roughness and serum contents, n.d.
- [230] L. Le Guéhennec, A. Soueidan, P. Layrolle, Y. Amouriq, Surface treatments of titanium dental implants for rapid osseointegration, Dental Materials 23 (2007) 844–854. https://doi.org/10.1016/J.DENTAL.2006.06.025.
- [231] K.A. Gross, M. Babovic, Influence of abrasion on the surface characteristics of thermally sprayed hydroxyapatite coatings, 2002.
- [232] Y. Ramaswamy, C. Wu, A. Van Hummel, V. Combes, G. Grau, H. Zreiqat, The responses of osteoblasts, osteoclasts and endothelial cells to zirconium modified calcium-silicate-based ceramic, Biomaterials 29 (2008) 4392–4402. https://doi.org/10.1016/J.BIOMATERIALS.2008.08.006.
- [233] S.R. Bakshi, V. Singh, S. Seal, A. Agarwal, Aluminum composite reinforced with multiwalled carbon nanotubes from plasma spraying of spray dried powders, Surf Coat Technol 203 (2009) 1544–1554. https://doi.org/10.1016/J.SURFCOAT.2008.12.004.
- [234] J.G. Thakare, C. Pandey, R.S. Mulik, M.M. Mahapatra, Mechanical property evaluation of carbon nanotubes reinforced plasma sprayed YSZ-alumina composite coating, Ceram Int 44 (2018) 6980–6989. https://doi.org/10.1016/J.CERAMINT.2018.01.131.
- [235] M.F. Hasan, J. Wang, C. Berndt, Evaluation of the mechanical properties of plasma sprayed hydroxyapatite coatings, Appl Surf Sci 303 (2014) 155–162. https://doi.org/10.1016/j.apsusc.2014.02.125.
- [236] I. Ratha, P. Datta, N. Chand Reger, H. Das, V.K. Balla, K.B. Devi, M. Roy, S.K. Nandi, B. Kundu, In vivo osteogenesis of plasma sprayed ternary-ion doped hydroxyapatite coatings on Ti6Al4V for orthopaedic applications, Ceram Int 48 (2022) 11475–11488. https://doi.org/10.1016/J.CERAMINT.2022.01.004.

- [237] T. Arai, H. Fujita, M. Watanabe, 387 EVALUATION OF ADHESION STRENGTH OF THIN HARD COATINGS*, 1987.
- [238] S. Ariharan, A. Nisar, N. Balaji, S.T. Aruna, K. Balani, Carbon nanotubes stabilize high temperature phase and toughen Al2O3-based thermal barrier coatings, Compos B Eng 124 (2017) 76–87. https://doi.org/10.1016/J.COMPOSITESB.2017.05.032.
- [239] A. Ghabchi, S. Sampath, K. Holmberg, T. Varis, Damage mechanisms and cracking behavior of thermal sprayed WC–CoCr coating under scratch testing, Wear 313 (2014) 97–105. https://doi.org/10.1016/J.WEAR.2014.02.017.
- [240] S.C. Jambagi, P.P. Bandyopadhyay, Plasma sprayed carbon nanotube reinforced splats and coatings, J Eur Ceram Soc 37 (2017) 2235–2244. https://doi.org/10.1016/J.JEURCERAMSOC.2017.01.028.
- [241] S. Singh, K.K. Pandey, A. Islam, A.K. Keshri, Corrosion behaviour of plasma sprayed graphene nanoplatelets reinforced hydroxyapatite composite coatings in simulated body fluid, Ceram Int 46 (2020) 13539–13548. https://doi.org/10.1016/j.ceramint.2020.02.139.
- [242] D. Gopi, E. Shinyjoy, M. Sekar, M. Surendiran, L. Kavitha, T.S. Sampath Kumar, Development of carbon nanotubes reinforced hydroxyapatite composite coatings on titanium by electrodeposition method, Corros Sci 73 (2013) 321–330. https://doi.org/10.1016/j.corsci.2013.04.021.
- [243] A. Zeng, E. Liu, I.F. Annergren, S.N. Tan, S. Zhang, P. Hing, J. Gao, EIS capacitance diagnosis of nanoporosity effect on the corrosion protection of DLC films, 2002.
- [244] K. Anselme, Osteoblast adhesion on biomaterials, Biomaterials 21 (2000) 667–681. https://doi.org/10.1016/S0142-9612(99)00242-2.
- [245] K. Balani, R. Anderson, T. Laha, M. Andara, J. Tercero, E. Crumpler, A. Agarwal, Plasma-sprayed carbon nanotube reinforced hydroxyapatite coatings and their interaction with human osteoblasts in vitro, 28 (2007) 618–624. https://doi.org/10.1016/j.biomaterials.2006.09.013.
- [246] S. Singh, C. Prakash, H. Singh, Deposition of HA-TiO2 by plasma spray on β-phase Ti-35Nb-7Ta-5Zr alloy for hip stem: Characterization, mechanical properties, corrosion, and in-vitro bioactivity, Surf Coat Technol 398 (2020). https://doi.org/10.1016/j.surfcoat.2020.126072.
- [247] A. Okumura, M. Goto, T. Goto, M. Yoshinari, S. Masuko, T. Katsuki, T. Tanaka, Substrate affects the initial attachment and subsequent behavior of human osteoblastic cells (Saos-2), Biomaterials 22 (2001) 2263–2271. https://doi.org/10.1016/S0142-9612(00)00415-4.
- [248] C. Wu, M. Chen, T. Zheng, X. Yang, Effect of surface roughness on the initial response of MC3T3-E1 cells cultured on polished titanium alloy, Biomed Mater Eng 26 (2015) S155–S164. https://doi.org/10.3233/BME-151301.

- [249] R.A. Gittens, T. McLachlan, R. Olivares-Navarrete, Y. Cai, S. Berner, R. Tannenbaum, Z. Schwartz, K.H. Sandhage, B.D. Boyan, The effects of combined micron-/submicron-scale surface roughness and nanoscale features on cell proliferation and differentiation, Biomaterials 32 (2011) 3395–3403. https://doi.org/10.1016/J.BIOMATERIALS.2011.01.029.
- [250] R.A. Gittens, R. Olivares-Navarrete, Z. Schwartz, B.D. Boyan, Implant osseointegration and the role of microroughness and nanostructures: Lessons for spine implants, Acta Biomater 10 (2014) 3363–3371. https://doi.org/10.1016/J.ACTBIO.2014.03.037.
- [251] M.A. Correa-Duarte, N. Wagner, J. Rojas-Chapana, C. Morsczeck, M. Thie, M. Giersig, Fabrication and biocompatibility of carbon nanotube-based 3D networks as scaffolds for cell seeding and growth, Nano Lett 4 (2004) 2233–2236. https://doi.org/10.1021/nl048574f.
- [252] N. Saito, Y. Usui, K. Aoki, N. Narita, M. Shimizu, K. Hara, N. Ogiwara, K. Nakamura, N. Ishigaki, H. Kato, S. Tarut, M. Endo, Carbon nanotubes: Biomaterial applications, Chem Soc Rev 38 (2009) 1897–1903. https://doi.org/10.1039/b804822n.
- [253] G. Jacquemet, H. Hamidi, J. Ivaska, Filopodia in cell adhesion, 3D migration and cancer cell invasion, Curr Opin Cell Biol 36 (2015) 23–31. https://doi.org/10.1016/J.CEB.2015.06.007.
- [254] Y. Usui, K. Aoki, N. Narita, N. Murakami, I. Nakamura, K. Nakamura, N. Ishigaki, H. Yamazaki, H. Horiuchi, H. Kato, S. Taruta, Y.A. Kim, M. Endo, N. Saito, Carbon nanotubes with high bone-tissue compatibility and bone-formation acceleration effects, Small 4 (2008) 240–246. https://doi.org/10.1002/smll.200700670.
- [255] S. Kalmodia, S. Goenka, T. Laha, D. Lahiri, B. Basu, K. Balani, Microstructure, mechanical properties, and in vitro biocompatibility of spark plasma sintered hydroxyapatite–aluminum oxide–carbon nanotube composite, Materials Science and Engineering: C 30 (2010) 1162–1169. https://doi.org/10.1016/J.MSEC.2010.06.009.
- [256] T. Akasaka, A. Yokoyama, M. Matsuoka, T. Hashimoto, F. Watari, Thin films of single-walled carbon nanotubes promote human osteoblastic cells (Saos-2) proliferation in low serum concentrations, Materials Science and Engineering: C 30 (2010) 391–399. https://doi.org/10.1016/J.MSEC.2009.12.006.
- [257] W.C. Lee, C.H.Y.X. Lim, H. Shi, L.A.L. Tang, Y. Wang, C.T. Lim, K.P. Loh, Origin of enhanced stem cell growth and differentiation on graphene and graphene oxide, ACS Nano 5 (2011) 7334–7341. https://doi.org/10.1021/nn202190c.
- [258] Y.P. Guo, Y.B. Yao, C.Q. Ning, L.F. Chu, Y.J. Guo, Fabrication of mesoporous carbonated hydroxyapatite/carbon nanotube composite coatings by microwave irradiation method, Mater Lett 65 (2011) 1007–1009. https://doi.org/10.1016/J.MATLET.2010.12.036.

- [259] H.X. Ren, X. Chen, J.H. Liu, N. Gu, X.J. Huang, Toxicity of single-walled carbon nanotube: How we were wrong?, Materials Today 13 (2010) 6–8. https://doi.org/10.1016/S1369-7021(10)70002-X.
- [260] M.A. Hussain, M.A. Kabir, A.K. Sood, On the cytotoxicity of carbon nanotubes, 2009.
- [261] P. Khalid, M.A. Hussain, P.D. Rekha, A.B. Arun, Carbon nanotube-reinforced hydroxyapatite composite and their interaction with human osteoblast in vitro, Hum Exp Toxicol 34 (2015) 548–556. https://doi.org/10.1177/0960327114550883.
- [262] Y. Chen, S.I. Roohani-Esfahani, Z.F. Lu, H. Zreiqat, C.R. Dunstan, Zirconium ions up-regulate the BMP/SMAD signaling pathway and promote the proliferation and differentiation of human osteoblasts, PLoS One 10 (2015). https://doi.org/10.1371/journal.pone.0113426.
- [263] N.J. Hallab, S. Anderson, T. Stafford, T. Glant, J.J. Jacobs, Lymphocyte responses in patients with total hip arthroplasty, Journal of Orthopaedic Research 23 (2005) 384391. https://doi.org/10.1016/j.orthres.2004.09.001.
- [264] A. Moghanian, M. Zohourfazeli, M.H.M. Tajer, The effect of zirconium content on in vitro bioactivity, biological behavior and antibacterial activity of sol-gel derived 58S bioactive glass, J Non Cryst Solids 546 (2020) 120262. https://doi.org/10.1016/J.JNONCRYSOL.2020.120262.
- [265] Y. Zhu, Y. Zhang, C. Wu, Y. Fang, J. Yang, S. Wang, The effect of zirconium incorporation on the physiochemical and biological properties of mesoporous bioactive glasses scaffolds, Microporous and Mesoporous Materials 143 (2011) 311–319. https://doi.org/10.1016/J.MICROMESO.2011.03.007.
- [266] Y.J. No, T. Nguyen, Z. Lu, M. Mirkhalaf, F. Fei, M. Foley, H. Zreiqat, Development of a bioactive and radiopaque bismuth doped baghdadite ceramic for bone tissue engineering, Bone 153 (2021) 116147. https://doi.org/10.1016/J.BONE.2021.116147.
- [267] E. Karamian, A. Nasehi, S. Saber-Samandari, A. Khandan, Fabrication of hydroxyapatite-baghdadite nanocomposite scaffolds coated by PCL/Bioglass with polyurethane polymeric sponge technique, J (Basel) 4 (2017) 177–183. https://doi.org/10.22038/nmj.2017.8959.
- [268] S. Sadeghzade, J. Liu, H. Wang, X. Li, J. Cao, H. Cao, B. Tang, H. Yuan, Recent advances on bioactive baghdadite ceramic for bone tissue engineering applications: 20 years of research and innovation (a review), Mater Today Bio 17 (2022). https://doi.org/10.1016/j.mtbio.2022.100473.